



HAL
open science

ILLUMINATING FAULT SLIP WITH INSAR: STRAIN RELEASE ALONG THE CHAMAN PLATE BOUNDARY

Manon Dalaison

► To cite this version:

Manon Dalaison. Illuminating fault slip with InSAR: Strain release along the Chaman plate boundary. Earth Sciences. Université PSL (Paris Sciences & Lettres); Ecole Normale Supérieure de Paris - ENS Paris, 2021. English. NNT: . tel-04107602v1

HAL Id: tel-04107602

<https://theses.hal.science/tel-04107602v1>

Submitted on 23 Feb 2023 (v1), last revised 26 May 2023 (v2)

HAL is a multi-disciplinary open access archive for the deposit and dissemination of scientific research documents, whether they are published or not. The documents may come from teaching and research institutions in France or abroad, or from public or private research centers.

L'archive ouverte pluridisciplinaire **HAL**, est destinée au dépôt et à la diffusion de documents scientifiques de niveau recherche, publiés ou non, émanant des établissements d'enseignement et de recherche français ou étrangers, des laboratoires publics ou privés.



Distributed under a Creative Commons Attribution - NonCommercial 4.0 International License



THÈSE DE DOCTORAT
DE L'UNIVERSITÉ PSL

Préparée à l'École Normale Supérieure

**Mesurer le glissement le long des failles par interférométrie
radar : étude de la frontière de plaques de Chaman**

illuminating fault slip with InSAR: Strain release along the
Chaman plate boundary

Soutenue par

Manon DALAISON

Le 7 décembre 2021

École doctorale n°560

**Sciences de la Terre et
de l'Environnement et
Physique de l'Univers**

Spécialité

**Sciences de la Terre et de
l'Environnement**

Composition du jury :

Roland BÜRGMANN Professeur, University of California	<i>Rapporteur</i>
Virginie PINEL Chargé de recherche, Université de Grenoble	<i>Rapporteuse</i>
Laetitia LE POURHIET Professeur, Sorbonne Universités	<i>Examinatrice, Présidente du jury</i>
Raphaël GRANDIN Maître de conférences, IPGP	<i>Examineur</i>
Jessica C. HAWTHORNE Professeur, University of Oxford	<i>Examinatrice</i>
Romain JOLIVET Maître de conférences, ENS	<i>Directeur de thèse</i>
Cécile LASSERRE Directeur de recherche, Université de Lyon	<i>Invitée</i>



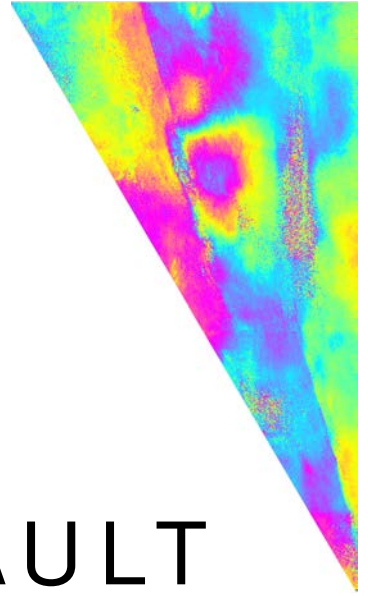
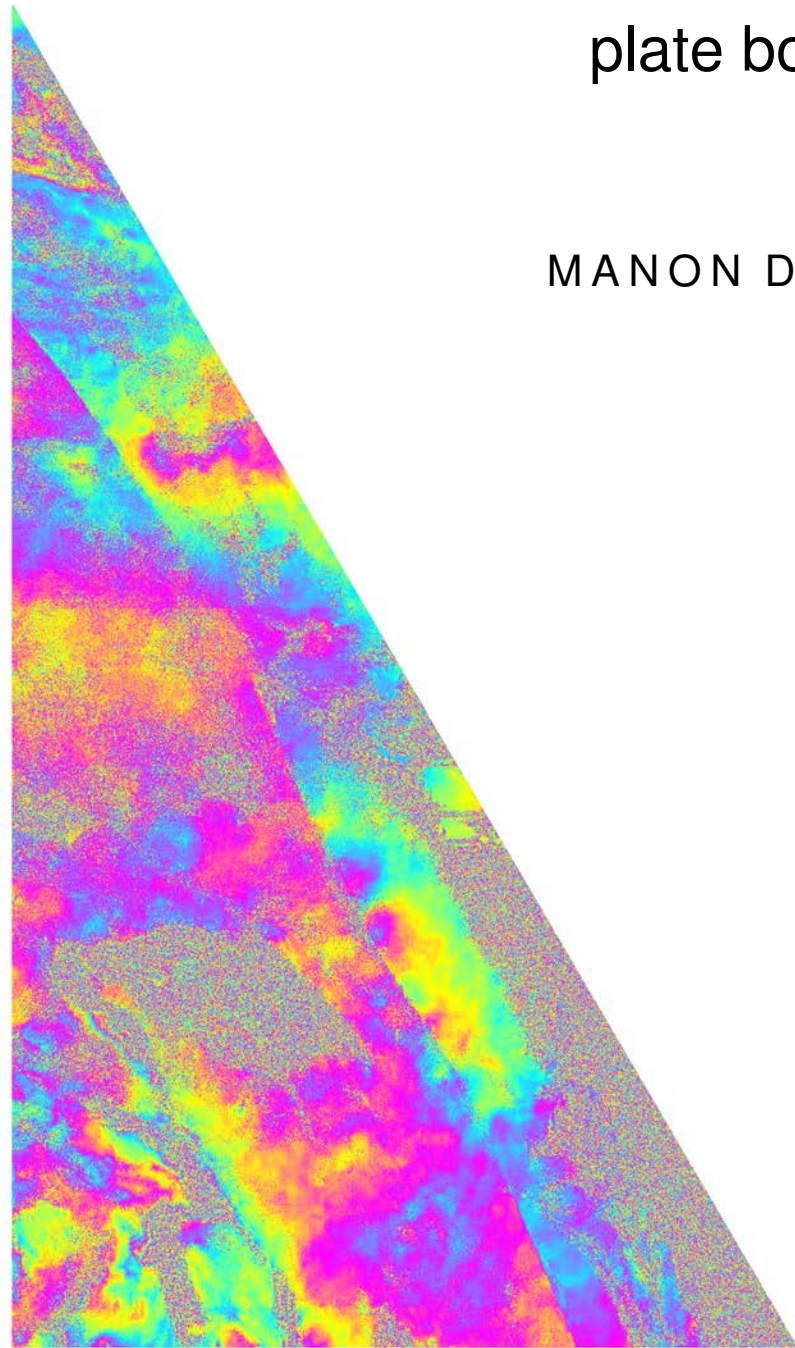
THÈSE DE DOCTORAT

ILLUMINATING FAULT SLIP WITH INSAR

Strain release along the Chaman
plate boundary

MANON DALAISON

École Normale Supérieure,
Paris Sciences et Lettres



Copyright © 2021 Manon Dalaison

PUBLISHED BY ÉCOLE NORMALE SUPÉRIEURE, PARIS SCIENCES ET LETTRES

TUFTE-LATEX.GITHUB.IO/TUFTE-LATEX

Tufte-latex template is licensed under the Apache License, Version 2.0. Title page illustrations are subsets of a six-year-long interferogram over the Chaman plate boundary.

First printing, December 2021

RÉSUMÉ

Comment une faille accumule-t-elle l'énergie nécessaire à la rupture sismique ? L'Interférométrie radar à synthèse d'ouverture (InSAR) permet de mesurer avec une précision millimétrique les déplacements du sol le long des failles continentales entre les passages successifs des satellites au même endroit. Dans cette thèse, j'identifie quand et comment la déformation est accommodée à travers la frontière de plaque de Chaman entre l'Inde et l'Eurasie au Pakistan et en Afghanistan, une région touchée par de grands séismes qui reste énigmatique. De nos jours, les satellites acquièrent des images haute-résolution en continu ayant le potentiel de nous informer sur l'évolution de la déformation en temps (presque) réel, un défi pour les techniques classiques de traitement.

Dans cette thèse, je présente une nouvelle méthode de calcul de séries temporelles InSAR, nommée KFTS, qui permet de mettre à jour itérativement une série temporelle préexistante par la combinaison appropriée des données, du modèle et de leurs incertitudes respectives, au fur et à mesure que les images satellite sont disponibles. La méthode est testée sur des données synthétiques ainsi que sur des réseaux d'interférogrammes sur l'Etna (Italie) et sur la frontière de plaque de Chaman. KFTS estime des délais de phase et des vitesses de déformation en accord avec les méthodes couramment utilisées et calcule également les incertitudes associées.

Ensuite, j'interprète des séries temporelles InSAR le long de la frontière de plaque de Chaman entre 2014 et 2020. Je constate que la majeure partie de la faille de Chaman (FC) glisse de manière asismique et continue avec un taux de chargement compris entre 0,7 et 1,2 cm/an et trois sections qui glissent continuellement et asismiquement de 80 à 130 km de long. Je propose une nouvelle segmentation de la FC et discute de l'interaction entre les séismes, le glissement asismique et la géométrie du tracé de faille. J'étudie trois séismes de magnitude modérée, qui présentent un glissement asismique induit important.

A l'aide des vitesses InSAR, je cartographie les gradients de déformation dans la ceinture de faille-plissement à l'est de la FC. Ils sont interprétés comme l'expression en surface du glissement décrochant sénestre sur trois ou quatre failles verticales. Il s'avère que la majeure partie de la déformation actuelle de la limite de plaques se concentre à l'est de la FC, dans le prolongement de la faille d'Ornach Nal au sud et le long de la faille de Quetta-Kalat qui aurait été le siège du séisme de Quetta en 1935, de magnitude 7,7. Notre description du partitionnement est en accord avec la géologie et suggère une migration vers l'est de la frontière de plaque.

SUMMARY

How does a fault accumulate the energy necessary for seismic rupture? Synthetic Aperture Radar Interferometry (InSAR) can measure with a millimetre-precision ground displacements along continental faults between successive passes of satellites at the same location. In this thesis, I identify when and how strain is accommodated across the Chaman plate boundary between India and Eurasia in Pakistan and Afghanistan, a region struck by large earthquakes that remains enigmatic. Nowadays, satellites acquire continuous high-resolution images with the potential to inform us about the evolution of deformation in (almost) real time, a challenge for classic processing techniques.

In this thesis, I present a new method for computing InSAR time series, named KFTS, which allows us to iteratively update a pre-existing time series through the appropriate combination of data, models and their respective uncertainties, as satellite images become available. The method is tested on synthetic data as well as interferometric networks on Etna (Italy) and on the Chaman plate boundary. KFTS estimates phase delays and strain rates in agreement with commonly used methods and also computes associated uncertainties.

Subsequently, I interpret InSAR time series along the Chaman plate boundary between 2014 and 2020. I find that most of the Chaman fault (CF) slides aseismically and continuously with a loading rate between 0.7 and 1.2 cm/yr and three 80-130 km-long creeping sections. I propose a new segmentation of the CF and discuss the interplay between earthquakes, aseismic slip and fault trace geometry. I image three moderate magnitude earthquakes, which exhibit significant induced aseismic slip.

Using InSAR velocities, I map deformation gradients in the fault and fold belt east of the CF. They are interpreted as the surface expression of left-lateral strike-slip on three to four vertical faults. It turns out that most of the current plate boundary deformation focusses to the east of the CF, along the continuation of the Ornach Nal fault to the south and along the Quetta-Kalat fault which is thought to have hosted the 1935 Quetta earthquake of magnitude 7.7. Our description of partitioning is consistent with the geology and suggests an eastward migration of the plate boundary.

Contents

	Page
1 INTRODUCTION	1
1.1 Imaging the Seismic cycle	4
1.1.1 The genesis of earthquakes	4
1.1.2 Geophysical observables for slip on faults	7
1.1.3 Inferring the characteristics of the source	10
1.2 The observed diversity of slip on continental faults	11
1.2.1 Earthquakes coseismic deformation and structural control	11
1.2.2 Postseismic signal	13
1.2.3 Interseismic strain	16
1.2.4 Creeping faults and slow slip events	17
1.2.5 Earthquake precursory phase	19
1.3 InSAR : theory and current issues	20
1.3.1 How InSAR works	21
1.3.2 The challenge of dealing with error and biases	23
1.3.3 The evolution of phase change	25
1.4 Towards systematic InSAR time series : the Chaman plate boundary natural laboratory	26
1.4.1 Describing active faults and learning from SAR data	26
1.4.2 The appeal of the Chaman plate boundary	28
1.4.3 Aims and structure of the thesis	32
2 A KALMAN FILTER TIME SERIES ANALYSIS METHOD FOR INSAR	33
2.1 Introduction	35
2.2 A Kalman filter-based approach for times series analysis	37
2.2.1 Data description and formulation of the problem	37
2.2.2 Formulation and set-up	39
2.2.3 Configuring parameters	41
2.3 Applications of the Kalman filter time series analysis (KFTS)	42
2.3.1 Synthetic tests	42
2.3.1.1 Reference case set-up	42
2.3.1.2 Performance with optimal configuration	44
2.3.1.3 Sensitivity analysis to predefined errors	47
2.3.2 Application to the Etna Volcano on Envisat Asar images	49
2.3.3 Application to the Chaman fault on Sentinel 1 images	52
2.4 Discussion	55
2.4.1 Guideline to choose parameters	55
2.4.2 Efficiency	57
2.4.3 Limitation and perspectives	58

2.5	Conclusion	59
3	THE INTERPLAY BETWEEN SEISMIC AND ASEISMIC SLIP ALONG THE CHAMAN FAULT ILLUMINATED BY INSAR	61
3.1	Introduction	63
3.2	Tectonic context and seismicity	66
3.2.1	Activity and geometry of the fault	66
3.2.2	Seismic record	67
3.3	Method	68
3.3.1	Interferometric processing	69
3.3.2	Iterative time series analysis incorporating coseismic displacements	69
3.3.3	Combining InSAR tracks	71
3.3.4	Measuring fault slip	72
3.3.5	Slip inversion for 3 earthquakes	73
3.4	Results: InSAR-derived deformation	74
3.4.1	Ground velocity	74
3.4.2	Slip along the Chaman fault	76
3.4.3	Seismic events	79
3.4.3.1	Surface displacement fields	79
3.4.3.2	Results of the slip inversion	82
3.5	Discussion	83
3.5.1	A decadal perspective on Chaman fault slip	83
3.5.2	Postseismic signal characteristics in comparison with coseismic deformation	86
3.5.3	Variations in slip behaviour, implications for rheology and fault system orientation	89
3.6	Conclusion	92
4	PARTITIONING ALONG THE CHAMAN PLATE BOUNDARY: OBSERVATIONS TOWARDS A MIGRATING TRANSFORM PLATE BOUNDARY	93
4.1	Introduction	95
4.2	Current understanding of the plate boundary	96
4.3	Materials and method	98
4.3.1	Obtaining velocities from InSAR	98
4.3.2	Defining an appropriate model for InSAR velocities	99
4.3.3	Modelling parallel strike-slip faults	100
4.3.4	A priori knowledge on parameters	101
4.4	Results	102
4.5	Discussion	106
4.5.1	Partitioning of slip and mapped earthquake ruptures	106
4.5.2	Inset from Geology	108
4.5.3	Long-term evolution of the plate boundary	110
4.6	Conclusion	112
5	OPEN QUESTIONS, REMARKS AND PERSPECTIVES	113
5.1	How time series analysis can be further improved for the study of tectonic deformation?	115
5.2	What is the detection limit of InSAR?	117
5.2.1	Geometry of acquisition and sensitivity	117
5.2.2	Flirting with the limits: comparison with creepmeter data	119
5.2.3	Automatic denoising of time series	120

5.3	How peculiar is the Chaman slip distribution ?	121
5.4	Seismic hazard along the Chaman plate boundary	123
5.5	Final Conclusion	125
APPENDICES		131
A.1	Review of published slip rates along the Chaman plate boundary	131
A.2	Explicit formulation of an example for KFTS	133
A.3	Illustration of KFTS parametrization tests for Chapter 2	134
A.4	Structure of interferometric networks	145
A.5	Additional details on Chapter 3 methodology	147
A.5.1	On the earthquake step amplitude <i>a priori</i>	147
A.5.2	On the parameterization of the dislocation screw inversion	147
A.5.3	On the uncertainty propagation from interferograms to surface fault slip	148
A.5.4	On earthquake slip inversion	149
A.6	Additional results for Chapter 3	152
A.7	Parametrisation of the partitioning model and additional results for Chapter 4	166
BIBLIOGRAPHY		173

List of Figures

1.1	Idealised model of a crustal block during the Earthquake cycle. Example of a left-lateral fault.	4
1.2	Earth's tectonic plates, seismicity and faults	6
1.3	Observing earthquakes: the case study of the 2019 Ridgecrest (California, USA) earthquake	9
1.4	New York Times article on the seismic wave record of the 1906 San Francisco earthquake	12
1.5	The 1992 $M_w7.2$ Landers earthquake: interferogram and rupture geometry.	13
1.6	Example of postseismic deformation and models	14
1.7	Examples of recorded slow slip events with InSAR	17
1.8	Past, current and future SAR satellite missions	21
1.9	Schematics of the acquisition geometry of repeated SAR images for interferometric SAR.	22
1.10	Examples of atmospheric artifacts observed in interferograms	23
1.11	Graphical representation of interferometric phase unwrapping	24
1.12	Schematics of time series analysis for a network of small baseline interferograms	26
1.13	Faults and significant earthquakes since the end of the 19th century in the Chaman plate boundary	29
1.14	Slow slip along the Chaman plate boundary viewed by InSAR	30
2.1	Scheme of the temporal evolution of the state vector as a function of assimilation time and available data	40
2.2	Performance of the Kalman filter time series analysis for a two-dimensional synthetic deformation field	43
2.3	Time series for one pixel with temporal evolution of the model on a synthetic set of InSAR data for one pixel	45
2.4	Maps of three of the model parameters : velocity, slow slip amplitude and quake amplitude	46
2.5	Temporal evolution of model functional parameters at each assimilation step for the reference pixel in our synthetic test	46
2.6	Errors in estimated model parameters and phases) from the Kalman filter time series analysis as a function of the standard deviation of the mismodeling noise and the standard deviation of interferometric network misclosure	47
2.7	Map of cumulative phase change and associated uncertainty between 2003 and 2010 over Mt Etna	50
2.8	Overlay of GPS and InSAR time series of relative deformations	51
2.9	Maps of cumulative phase change between late 2014 and early 2019 over the Chaman plate boundary and comparison of KFTS with the NSBAS solution	52
2.10	Time series for 3 selected pixels of Figure 2.9	54
2.11	Variations of the gain in phase and model parameter estimates and of the standard deviation of those estimates as a function of the error terms used to initialize KFTS	56
3.1	Tectonic setting and seismicity of the Chaman fault system	64
3.2	InSAR Velocity fields in ascending and descending directions and estimated coseismic displacement	75

3.3	Velocity field along the Chaman fault projected in fault-parallel direction and across-fault profiles	76
3.4	Temporal evolution of surface slip along the Chaman fault in line of sight	77
3.5	Geometry, measured slip rates and seismicity along the Chaman fault	80
3.6	Surface horizontal displacement induced by each of the three earthquakes close to the town of Chaman during their coseismic and postseismic periods combining ascending and descending InSAR observations	82
3.7	Modelled earthquakes slip on the fault plane and associated surface displacement fields . . .	83
3.8	Earthquake frequency against magnitude near the Chaman fault	84
3.9	Temporal and spatial footprint of coseismic and postseismic deformation for earthquakes on the Chaman fault	88
4.1	Tectonic setting and current seismicity along the southern Chaman fault system	97
4.2	Velocity in ascending and descending directions computed with InSAR	100
4.3	Inferred velocities, fault locations and locking depths on the topographic map	103
4.4	Slip and locking depth statistics per fault for the Chaman fault, Ghazaband fault and East fault	104
4.5	Statistics for the Nushki segment of the Chaman fault	105
4.6	Plate boundary geology and faults	107
4.7	Schematic interpretation of the plate boundary cinematic and long-term evolution	110
5.1	Coseismic deformation for the 12 August 2020 earthquake from InSAR	115
5.2	Coseismic deformation for the 14 November 2020 earthquake from InSAR	116
5.3	Multiplicative coefficients between Sentinel 1 LOS and horizontal ground motion	117
5.4	Synthetic horizontal surface deformation field as predicted by the solution of the 13 May 2016 earthquake from different viewing geometries.	118
5.5	Creepmeter time series in Amir Khan (Chaman fault)	119
5.6	Close up on InSAR-derived surface slip and potential identification of a micro-slip event recorded by a creepmeter	119
5.7	Performance of the autonomous denoising algorithm for InSAR time series	120
5.8	Application of the denoising algorithm to real InSAR data over the North Anatolian fault (Turkey)	122
5.9	Coseismic and postseismic deformation for the two earliest earthquakes	123
5.10	6-year-long interferogram on ascending track 42 capturing most spatial features of the surface deformation discussed in this thesis	126

REMERCIEMENTS

TOUT D'ABORD, je tiens à remercier les membres de mon jury de thèse de l'intérêt qu'ils portent à mes travaux de recherche.

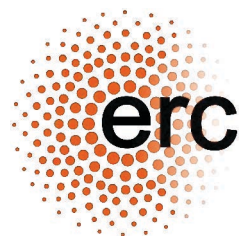
JE VOUDRAIS aussi remercier les personnes qui m'ont soutenues et aider pour me permettre de finalement conclure ces travaux de thèse en décembre 2021, 39 mois après les avoir commencés. C'est à mon superviseur, Romain Jolivet, que vont mes premières pensées. Je le remercie beaucoup pour son enthousiasme permanent, sa passion communicative pour la science, sa disponibilité et sa générosité. J'espère qu'aux 10 mois supplémentaires prévus au laboratoire de Géologie de l'ENS s'ajouteront de nombreuses années de collaboration.

C'est justement dans ce laboratoire, avec les étudiants et chercheurs qui le peuplent que je me sens bien. C'est une histoire d'amitiés d'abord, mais aussi de confort matériel, de liberté d'organiser son temps et de bienveillance générale. Un Grand merci donc à mes co-bureaux du présent et du passé : Dr. Amin, Alexandre, Bryan (a.k.a. les chouquettes), Philippe, Théo, Lisa, Johanne, Léa et, bien sûr, à mon co-salon de pandémie, Stéphane. Merci aussi à tous mes buddy doctorants à l'ENS : Ariel, Léo, Valentine, Claudia, Samson, Ludivine, Arnaud, Sung-Pin, Thomas, Cédric, Hugo, Augustin, Antoine, Jérôme, Simon, Chao, Clément. Une dédicace toute particulière à Arefeh et Eva qui auront aussi très prochainement le soulagement d'avoir achevé Le manuscrit. Ainsi qu'à mes amis de promo de l'IPGP (ou de plus loin) : Solène, Guillaume, Sophie, Luc, Flore, Quentin et Louise.

JE REMERCIE les chercheurs de mon comité de thèse Kristel Chanard, Alexandre Fournier et Jean-Arthur Olive d'avoir suivi avec intérêt la progression de ma thèse. Je remercie les chercheurs avec qui j'ai travaillé pendant la thèse : Angélique Benoit, Bertrand Rouet-Leduc, Flore Sergeant, Sylvain Michel, Elenora van Rijsingen, Théo Rebert, Claudia Hulbert, Jorge Jara, Laetitia Le Pourhiet et Arthur Hauck.

Je remercie chaleureusement Rhodri Davies qui m'a transmis une passion et une méthode scientifique qui m'accompagne depuis mon départ de l'Australian National University; ainsi qu'Emmanuel David, Paul Tregoning et Eric Calais qui m'ont recommandée auprès de leurs pairs.

FINALEMENT, je remercie du fond du coeur Maman, Bruce, Mamie, Flavien et Stéphane pour leur soutien inconditionnel et indispensable depuis de nombreuses années.



This thesis received funding from the European Research Council (ERC) under the European Union's Horizon 2020 research and innovation program (Geo-4D project, grant agreement 758210)

"Mon intention n'est pas de démontrer que j'ai eu raison
jusqu'alors mais de chercher à savoir si j'ai raison. Je vous le dis:
laissez toute espérance vous qui entrez dans l'observation"
La vie de Galilée, *Bertolt Brecht*

Chapter 1

INTRODUCTION

Each Chapter of this thesis is first summarized in french (blue text).

Introduction

LE CYCLE SISMIQUE est la répétition cyclique de tremblements de terre, ou séismes, sur une même faille. Comment la faille accumule-t-elle l'énergie nécessaire à la rupture sismique ? Que se passe-t-il entre chaque séisme ? Les failles actives se situent principalement le long des frontières de plaques tectoniques (Figure 1.2), qui se déplacent les unes par rapport aux autres à des vitesses de quelques centimètres par an. Le modèle classique d'un chargement élastique des failles nous dit qu'une faille ne glisse pas pendant de longues périodes dites inter-sismiques, allant de quelques dizaines d'années à plusieurs siècles, durant lesquelles la faille accumule de l'énergie qui est ensuite rapidement (en quelques secondes) relâchée lors de séismes (Figure 1.1). Si les ondes sismiques émises lors de cette libération d'énergie sont la source de nombreux dégâts, elles nous informent aussi sur l'origine du séisme et ses propriétés. Une autre observation permettant de caractériser un séisme est la déformation pérenne en surface causée par la rupture (Figure 1.3).

LES SYSTÈMES de positionnement par satellites (ex. GPS) et les méthodes d'Interférométrie radar à synthèse d'ouverture (InSAR) permettent de mesurer avec une précision allant jusqu'à quelques millimètres les déplacements du sol, que leur origine soit sismique, hydrologique ou anthropique. Alors que le positionnement par satellites requiert l'installation de récepteurs au sol et ne fournit en conséquence que des mesures locales du déplacement, les images Radar à Synthèse d'Ouverture (SAR) prises par satellite couvrent actuellement l'intégralité des terres émergées (excepté les pôles). Elles contiennent l'amplitude et la phase de l'onde radar initialement émise par le satellite, réfléchi sur le sol et finalement réceptionnée par l'antenne du satellite.

L'InSAR combine en un interférogramme deux images SAR de la même surface continentale prises à des instants différents (Figure 1.9), de sorte qu'un motif spatial émerge de la différence entre les phases

réfléchies qui prises individuellement paraissent aléatoires. Les différences de phases contiennent la déformation du sol entre les deux passages des satellites dans la direction de visée, parmi de nombreux autres signaux indésirables pour l'étude des failles. Une des sources de bruit la plus problématique provient de l'interaction entre l'onde radar et l'atmosphère turbulente¹ (Figure 1.10).

UN RÉSEAU d'interférogrammes reliant les passages successifs des satellites au même endroit permet de reconstituer l'évolution de la déformation au cours du temps, à travers une analyse en série temporelle. Bien que simple numériquement, cette analyse est un défi puisqu'elle considère un volume important d'images en haute-résolution et donc de données. Celles-ci contiennent de plus, du bruit et des biais, souvent corrélés, qui doivent être pris en compte dans les estimations d'incertitudes. Comment peut-on obtenir l'évolution de la déformation du sol et son incertitude de manière efficace (en minimisant l'utilisation des ressources numériques) ? Le Chapitre 2 tente d'apporter des éléments de réponse à cette question.

LES OBSERVATIONS depuis la fin du XIX^{ème} siècle (Figure 1.4) mettent en évidence la diversité des processus induisant la libération de l'énergie accumulée au niveau des failles. Les séismes en sont la manifestation la plus spectaculaire et destructrice : les plus gros (ceux qui ont une magnitude de moment, M_w , supérieure à 7) impliquent souvent plusieurs failles ou segments de failles (Figure 1.5) et sont suivis d'une période post-sismique de sismicité induite ("aftershocks"), de glissement asismique ("afterslip") et de relaxation viscoélastique et poro-élastique (Figure 1.6). Comment la géométrie de faille influence l'initiation, la propagation et l'arrêt des ruptures ? Quelle est la quantité d'énergie relâchée lors de la période post-sismique relativement au séisme principal ?

LA PÉRIODE inter-sismique est la plus longue et donc celle pour laquelle nous avons le plus de données. Bien que calme en apparence, plusieurs phénomènes y sont observables. Au premier ordre, on mesure la déformation en champ-lointain qui s'accumule sur une ou plusieurs failles sur des largeurs d'une vingtaine à centaine de kilomètres. En se rapprochant des failles, il ressort que certaines failles glissent de manière asismique proche de la surface (Figure 1.7) ou en profondeur, comme la partie centrale de la faille de San Andreas très étudiée. Ce glissement lent apparaît, essentiellement, continu et constant dans le temps. Néanmoins, une analyse détaillée des séries temporelles et des enregistrements sismiques (qui contiennent des signaux induits par le glissement en majorité asismique) nous révèle des événements transitoires, durant quelques minutes à quelques années. Quelle est la fréquence du glissement asismique, sa signature spatio-temporelle et son rôle dans la libération d'énergie ?

¹ les variations de pression, température et d'hygrométrie dans l'atmosphère qui ne sont pas dans les modèles météorologiques, contrairement aux variations liées à l'atmosphère stratifiée

DANS CETTE THÈSE, j'aborde ces questions fondamentales à travers l'étude de la zone de faille de Chaman, à la frontière occidentale entre les plaques Indienne et Eurasienne en Afghanistan et au Pakistan (Figure 1.13). Les modèles globaux de cinématique des plaques prédisent 23 à 36 mm/an de glissement sénestre moyen entre l'Inde et l'Eurasie. Pourtant, peu de grands séismes ont été enregistrés le long de cette frontière de plaques au cours de l'histoire récente (depuis 1880) (Figure 1.13). Sommes-nous dans une phase d'accumulation d'énergie en vue d'un grand séisme ? Ou est-ce que l'énergie liée au déplacement entre l'Inde et l'Eurasie est relâchée de manière asismique ?

Les mesures InSAR sur la période 2003-2011 indiquent que la faille de Chaman glisse de manière asismique proche de la surface. Néanmoins, elle n'a pour l'instant jamais été étudiée sur toute sa longueur (~ 800 km), et la signature temporelle de ce glissement reste inconnu. Des glissements post-sismiques importants déclenchés par des séismes de taille modérée contribueraient à un ratio asismique sur sismique élevé (Figure 1.14). Le Chapitre 3 a pour objectif de caractériser les variations spatio-temporelles du glissement asismique le long de la faille de Chaman à l'aide des images SAR prises par la mission Sentinel 1 entre 2014 et 2020.

NÉANMOINS, la faille de Chaman en elle-même ne semble pas glisser à plus de 12 mm/an et, bien qu'ayant une signature très nette dans la topographie et la géologie, le plus gros séisme enregistré n'est qu'un M_w 6.5-6.7 et date de 1892. Des chaînes de montagnes longent la faille de Chaman à l'est et contiennent de nombreuses failles, dont certaines ont connu de grands séismes décrochants, dont le séisme de Quetta en 1935 de M_w 7.7. La déformation de frontière de plaques est-elle distribuée entre plusieurs failles ? Quel est le rôle des failles à l'est de Chaman ? Ces questions sont abordées au Chapitre 4.

POUR FINIR, le Chapitre 5 contient une discussion des résultats présentés dans les sections précédentes avec une attention particulière sur la sensibilité et les limites de l'InSAR et les futurs projets.

YOU PROBABLY HEARD in the news of the most recent earthquakes at unexpected times and often surprising places. In the southeast of France, on November 11, 2019, Le Teil earthquake damaged several century old buildings which had probably never felt a nearby earthquake before. More dramatically, the August 14, 2021, Haiti earthquake recalled the disaster of the 2010 earthquake near Port-au-Prince. Most recently (September 21, 2021), the Melbourne earthquake which damaged old Victorian era pubs oriented the spotlight on this natural event, which in fact is less exceptional than it appears: there are about 300 earthquakes of similar size in the world every year. The physics and origin of earthquakes is the long and continuous story of the deformation of the superficial layer of our planet. Slip on faults in

fault systems along tectonic plate boundaries account for most of the deformation and it is the object of interest of this thesis.

1.1 Imaging the Seismic cycle

1.1.1 The genesis of earthquakes

PARADOXICALLY, although most earthquakes are located in well-identified seismogenic regions, principally tectonic plate boundaries, they constantly surprise seismologist. Out of a few rare exceptions, individual earthquakes are unexpected. Experts were not able to predict their times and locations, sometimes at the cost of many lives (e.g. Sumatra earthquake in 2004). Is this the result of a misunderstanding of the physical causes leading to an earthquakes, or of incomplete observation, or, lastly, the result of an inherently unpredictable chaotic system? In this thesis, as a step towards answering this driving question for seismologists, I investigate deformation as measured from radar satellites, before, during and after earthquakes at length-scales ranging from a few meters to hundreds of kilometres.

EARTHQUAKES correspond to the release of tectonic stress through sudden and fast slip within a limited area of a fault surface [e.g. *Reid, 1910; Scholz, 2002*]. Earthquakes radiate seismic waves, which dissipate significant energy and may induce severe ground shaking, one of the greatest threat to natural and human environments. The recurrence of earthquakes on a fault plane is termed seismic cycle [e.g. *Tse and Rice, 1986*] (Figure 1.1). Tectonic stress results from the relative motion of lithospheric plates at centimetres to millimetres per year [e.g. *Le Pichon, 1968; DeMets et al., 2010*], which is driven by the thermo-chemical convection in Earth's mantle, the solid and viscous layer extending from the lithosphere to 2900 km below our feet [*Davies, 1999*]. Lithospheric plates are essentially rigid, so that current differential plate motion is well described by a rotation at a constant rate on the spherical Earth around an Euler pole [e.g. *McKenzie and Morgan, 1969; Chase, 1978; DeMets et al., 1990*]. Global plate models such as MORVEL [*DeMets et al., 2010*] or the reference frame ITRF2014 [*Altamimi et al., 2017*] combine measurements of deformation from geodesy and geology to infer plate rotation for Earth's 15 to 20 tectonic plates (Figure 1.2). The residual misfit of global plate models with data confirm that deformation focuses around plate boundaries, and can locate around a single fault on a width no greater than 50 km (e.g. across the Dead Sea fault) or extend to 1000s km like across the Tibetan plateau where India meets Eurasia and where numerous faults and folds come into play [*Jolivet et al., 1990; Meade and Hager, 2005; Zheng et al., 2017*].

FAULTING is the classical way of accommodating stress (i.e. force per unit surface) and strain (i.e. deformation) in a brittle medium such

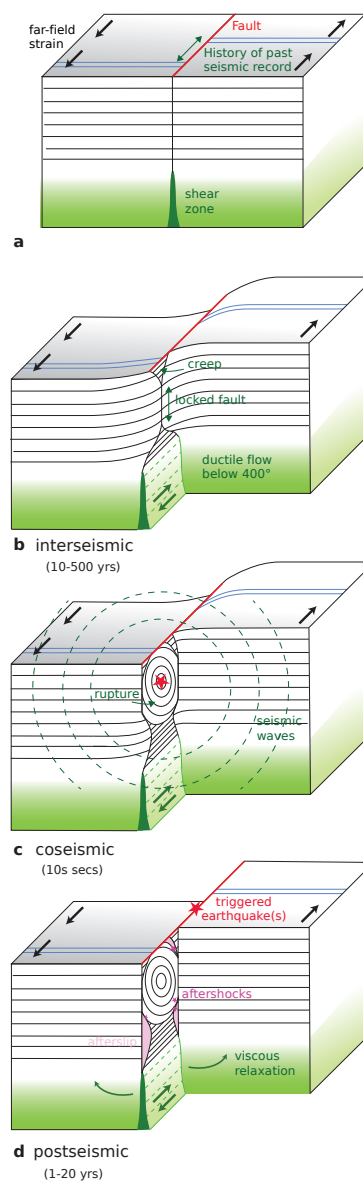


Figure 1.1: Idealised model of a crustal block during the Earthquake cycle. Example of a left-lateral fault.

as the lithosphere in the pressure-temperature condition of the surface down to 10-30 km depth, also called the seismogenic zone [Byerlee, 1968; Marone and Scholz, 1988; Scholz, 1988, 2002]. Theoretically, the orientation of stress determines the geometry of new faults and sliding directions [Anderson, 1905]: thrust faults accommodate compression, normal faults extension and vertical strike-slip faults horizontal motion. Pre-existing faults are planes of weakness and generally host slip preferentially. Therefore, major faults hosted numerous and repetitive earthquakes across geological times (several thousand to million years) [e.g. Schwartz and Coppersmith, 1984; Sieh and Jahns, 1984; Manighetti et al., 2007].

Figure 1.1 pictures the typical story of a seismogenic fault loaded elastically due to far-field strain accumulation [Gu et al., 1984; Marone, 1997]. In its simplest form, an earthquake corresponds to the elastic rebound, that releases in a few seconds (the coseismic period) the strain accumulated during decades to centuries (the interseismic period) [Reid, 1910, 1911; Benioff, 1964]. Apparently, the interseismic period is a period of quiet far-field strain accumulation. Nevertheless, there are observable processes partially releasing strain on the fault plane, like continuous shallow aseismic slip (i.e. creep) or transient slow slip [e.g. Beroza and Ide, 2011; Bürgmann, 2018]. Before some earthquake, a pre-seismic phase is recorded with an acceleration of seismic activity and other precursory signals of critical importance in the perspective of early warning. In the coseismic phase, fast slip generates seismic waves, which are mechanical waves travelling at the surface and through Earth's interior at speeds between 3 and 5 km/s. Because earthquakes have finite size, local stress drop on the ruptured patch is associated with stress increase around it, which may induce nearby earthquakes (i.e. aftershocks), slow slip (i.e. afterslip) and viscous relaxation at depth during the postseismic period [e.g. Dietz and Ellsworth, 1990; Hauksson et al., 1993; Stein, 1999]. Observational evidences of the seismic cycle and the diversity of associated processes are presented in Section 1.2. Ultimately, slow and fast slip on the fault plane sum up to a long-term strain equal to the far field strain. If far-field strain is known, this concept allows to quantify slip-deficit on a fault plane, an important quantity for seismic risk estimates [Avouac, 2015; Michel et al., 2017].

HISTORICALLY, physical relationships for fault slip arose from theoretical work and the observation of stressed rocks under controlled conditions in the laboratory [Paterson, 1958; Jaeger, 1959; Brace and Byerlee, 1966]. The strength of unbroken rock sample governs the way they deform [e.g. Griggs, 1936; Mogi, 1966], while faulted rock deformation depends on friction². The stability of friction determines whether fault slip can be fast-enough to generate seismic waves (i.e. seismic event) or not (i.e. aseismic slip) [Scholz, 2002]. The stick-slip pattern (i.e. long period of quiescence separated by rapid slip) analogous to the seismic cycle requires a weakening mechanism dropping friction in

² "Friction is the resistance to motion that occurs when a body is slid tangentially to a surface on which it contacts another body" Scholz [2002]

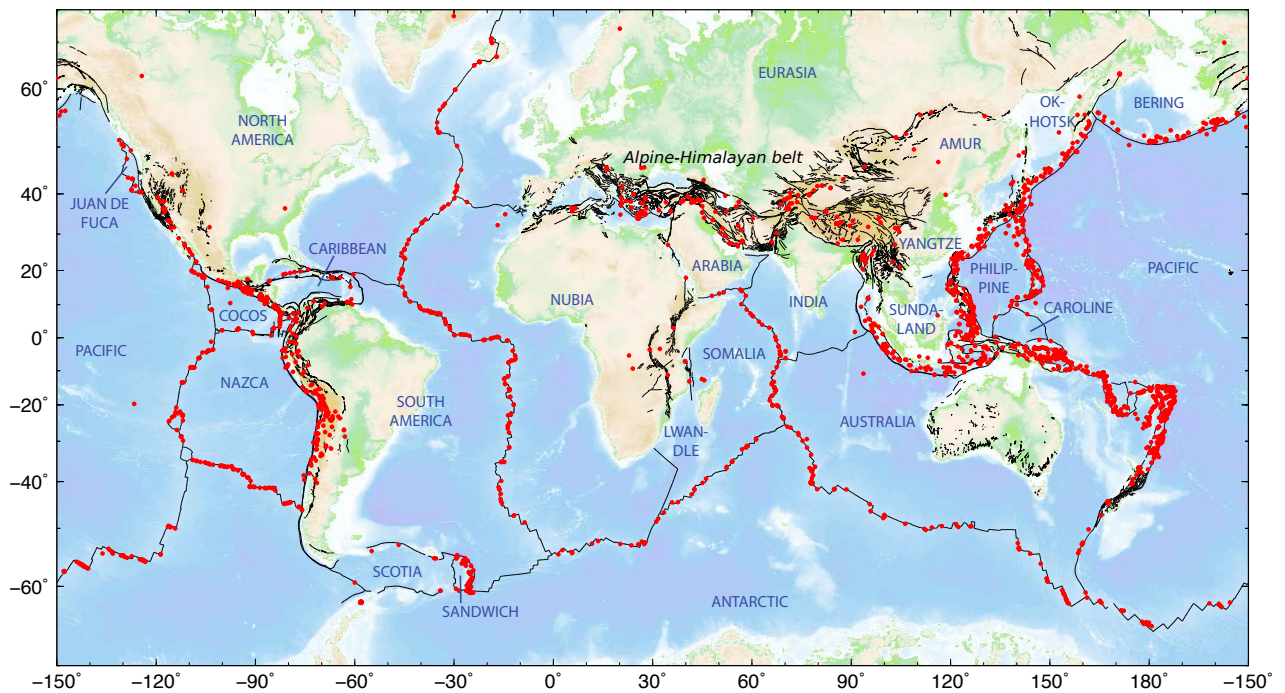


Figure 1.2: Earth's tectonic plates. Black lines are active faults from the Global Earthquake Model. The epicentre of all 2020 $M_w > 5$ earthquakes in the Global Centroid Moment Tensor (GCMT) catalogue are red dots. Global topography is from ETOPO1 [Amante and Eakins, 2009].

dynamic regime compare to static conditions, to allow fast slip acceleration [Brace and Byerlee, 1966; Byerlee and Brace, 1968; Noda and Lapusta, 2013; Udías *et al.*, 2014]. Alternatively, under rate-strengthening conditions frictional resistance increases during sliding, thus preventing spontaneous slip acceleration (earthquakes and transient slow slips) and favouring slow and stable sliding.

A typical continental fault is rate-strengthening below a certain depth where pressure-temperature conditions prevent earthquakes ($> 400^\circ\text{C}$) [Blanpied *et al.*, 1998; Scholz, 1998]. At shallower depth, models and experiments in controlled conditions outline the key role of the fault mineralogy and fluids in determining the seismogenic potential of a fault [e.g. Segall *et al.*, 2010; Brantut *et al.*, 2011]. More specifically, velocity strengthening minerals such as serpentine, clay-rich sediments or hydrothermal alteration in the fault zone promote slow slip [e.g. Avouac, 2015; Bürgmann, 2018]. The rate-and-state friction law inferred from laboratory and theoretical work [Dieterich, 1978, 1979; Ruina, 1983] is the most popular framework to capture slip on a fault [e.g. Marone, 1998; Barbot, 2019]. The response of the fault to stress increase will depend on constitutive parameters determined empirically.

How do we observe this time-dependent three-dimensional motion associated with the seismic cycle in nature? In the following, I describe the current sources of quantitative information on the processes coming into play in the seismic cycle, and latter, in Section 1.2 I provide concrete examples of observations.

1.1.2 Geophysical observables for slip on faults

THE CURRENT BEHAVIOUR of faults extending several kilometres below our feet is only known from measurements at the surface of the Earth. Information passes through mechanical waves and deformation which are recorded with instruments having specific sensitivities and limited spatial and temporal coverage. In this section, I attempt to briefly introduce main techniques of observation for active faults.

SEISMOMETERS have recorded ground shaking due to travelling seismic waves in seismograms since the second-half of the 19th century. The full waveform informs about the location, motion and energy of the source, notably with characteristic features like the arrival time of the first wave, the direction of the first motion and the amplitude and duration of the signal. Seismic waves carry information at rates allowing for rapid source characterisation with automatic algorithms. Information about earthquake source is now compiled routinely on global catalogues such as the Harvard Global Centroid Moment Tensor (GCMT), U.S. Geological Survey (USGS) and International Seismological Center (ISC) catalogs [*Dziewonski et al., 1981; Ekström et al., 2012; ISC, 2020*]; although expert analysis of seismograms often provides better source characterization (e.g. earthquakes of the 2019 Ridgecrest earthquake sequence in Figure 1.3a).

Centroid Moment Tensors encapsulate key characteristics of the source (considered as a point source) including the focal mechanism and scalar seismic moment [*Gilbert, 1971; Strelitz, 1989; Udías et al., 2014*]. The seismic moment, M_o , quantifies the energy release during an earthquake and is equal to [*Aki, 1972*]

$$M_o = \mu A \bar{s} \quad (1.1)$$

where μ is the shear modulus, \bar{s} is the spatial average value of the total slip and A is the area of the ruptured fault surface. Assuming constant stress drop, its value in newton meters can be translated into the logarithmic moment magnitude (M_w) scale with [*Hanks and Kanamori, 1979*]

$$M_w = \frac{2}{3} \log_{10}(M_o) - 6.07 \quad (1.2)$$

This is the most readily used magnitude estimate globally, as it does not saturate for large earthquakes, even though there are other magnitude scales based on the measured amplitude of seismic waves (e.g. like the local magnitude also referred as the "Richter" scale) [*Gutenberg and Richter, 1936, 1956; Scordilis, 2006*]. From global records of seismic magnitudes, *Gutenberg and Richter* [1944] found empirically that the magnitude scales linearly with the decimal logarithm of the frequency of earthquakes below this magnitude. This frequency-magnitude relation works for magnitudes greater than the magnitude of completion of the seismic catalogue and the slope is the b -value (global b -value is

one). Sources of slow slip events cannot be directly characterised with seismometers as they are quiet seismically, although triggered seismic signal may be observed [*Beroza and Ide, 2011*].

FAST AND SLOW SLIP on the fault plane induce surface displacement which can be measured with various methods. The oldest measurements come from repeated triangulation surveys (e.g. Great Trigonometrical Survey of India in the 19th century) with 1-10 m precisions [*Ambraseys and Bilham, 2003a*]. Those surveys may provide precious century-old constraints but the temporal and spatial resolution is low, unlike measurements from satellites.

Measurements from space, includes Global Navigation Satellite System (GNSS)³ and Interferometric Synthetic Aperture Radar (InSAR). GNSS Receivers use the two-way travel time to the GNSS satellites above their horizon to compute their precise location in three-dimensions (longitude, latitude and elevation) [*Enge, 1994; Hofmann-Wellenhof et al., 2012*] either at a high frequency (1 Hz) [*Larson, 2009*] or averaged over each day to gain in precision and accuracy. Thus, GNSS provides precise daily time series of deformation in three-dimensions where receivers are installed (e.g. Figure 1.3e) with an accuracy of the order of the millimetre in the horizontal direction, and a larger uncertainty on the vertical due to geometrical constrains [*Masson et al., 2019*].

³ like the United States' Global Positioning System (GPS), Russia's Global Navigation Satellite System (GLONASS) or Europe's Galileo.

On the other hand, InSAR and optical image correlation allow to quantify relative deformation between two points and two epochs on continental surfaces. InSAR time series retrace the evolution of deformation in the direction of the line of sight (LOS) of the satellite. Their spatial resolution can reach 100 m² and a temporal sampling close to the week, the frequency at which satellites fly back over the same ground [*Massonnet and Feigl, 1998; Simons and Rosen, 2015*]. Principles and limitations of InSAR will be described in greater details in Section 1.3. Optical image correlation has been done in a variety of settings from satellites or airborne photos which can be as old as 1960s (e.g. American reconnaissance satellites, Corona) [e.g. *Michel and Avouac, 2002; Hollingsworth et al., 2012*]. Spatial resolution reaches 50 cm for the very high-resolution satellite missions like Pléiades or WorldView satellite systems and deformation of the order of a few centimetres can be theoretically extracted [*Rosu et al., 2015; Antoine et al., 2021*]. Satellite imagery covers the whole continental surface and does not require ground instrumentation (unlike GNSS), thus informing about remote regions.

LOCALLY, across fault ground measurements provide very precise strain quantifications. In California, across-fault theodolite alignment arrays installed in 1979 measure slow motion of faults when revisited with a precision typically lower than 0.5 mm/yr on a width of 150 m [*Galehouse and Lienkaemper, 2003; McFarland et al., 2017*]. Creepmeters measure fault strain on a narrower zone (within 5-10 meters of the fault trace) with high temporal sampling (about 10 minutes) and a resolu-

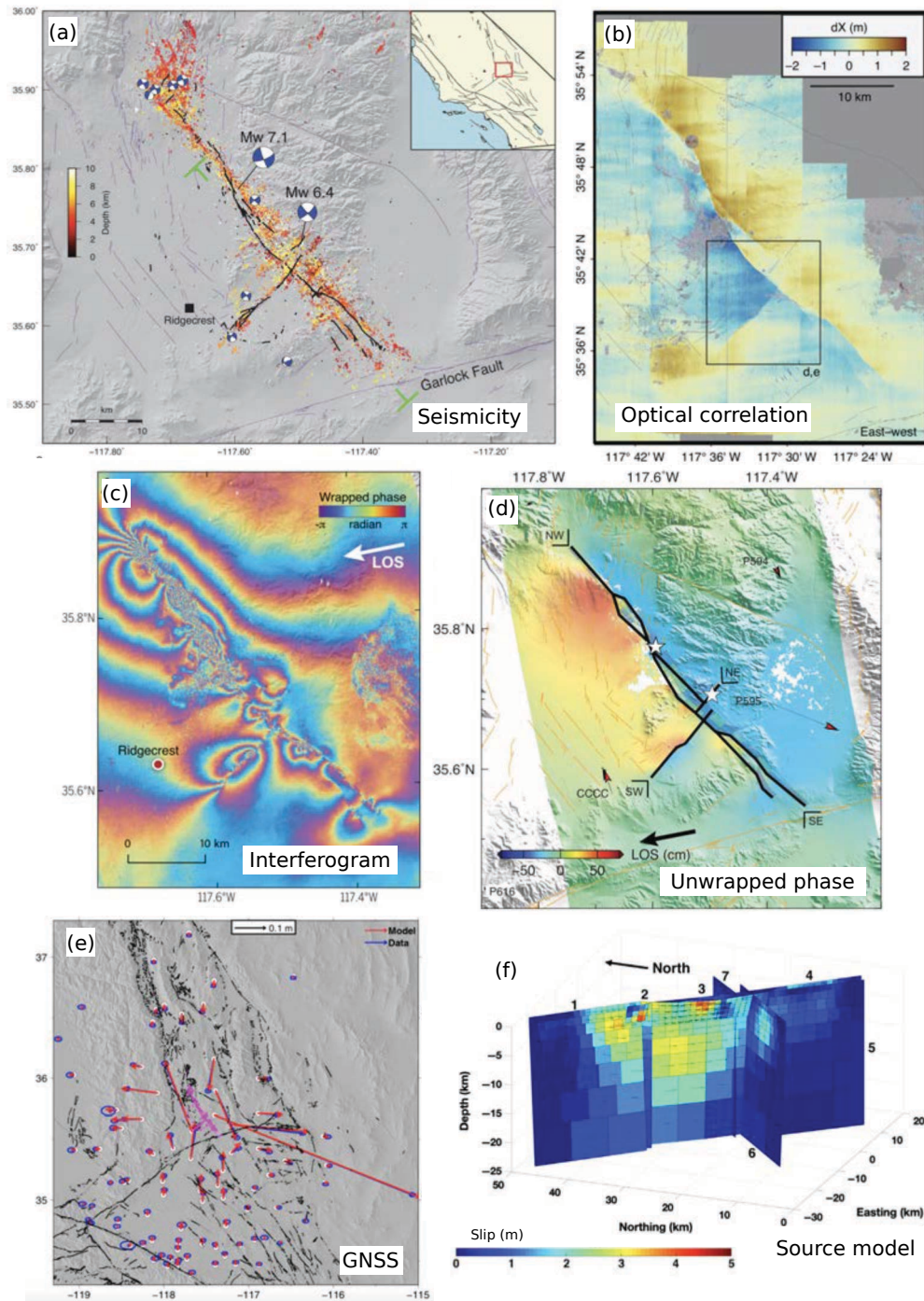


Figure 1.3: Observing earthquakes: the case study of the 2019 Ridgecrest (California, USA) earthquake ($M_w 6.4$ followed by a $M_w 7.1$). (a) Location of earthquake epicenters in the coseismic and postseismic period (many aftershocks). White and blue "beachballs" are graphical representations of the Centroid Moment Tensors for the largest events. The figure (a) is from *Ross et al. [2019]* like (c) and (d). (b) East-west coseismic displacement field computed from optical image correlation from *Barnhart et al. [2020]*. (c) Phase component of the wrapped coseismic interferogram from ALOS-2 SAR images. (d) Unwrapped interferogram providing a continuous displacement field in the line of sight (LOS) of the satellite during the coseismic period. (e) GNSS horizontal velocities represented as arrows with data in blue and model in red computed from the (f) earthquake source model inferred from inversion by *Jin and Fialko [2020]*.

tion which may go down to 10s of micrometers [McGill *et al.*, 1989; Bilham *et al.*, 2019; Victor *et al.*, 2018]. The very fine temporal resolution time series allowed for the identification of fine scale discrete slip events where continuous slip was previously thought to occur [e.g. Bilham *et al.*, 2016]. However, non-tectonic processes like rainfall and seasonal-effects may affect creepmeter data [Roeloffs, 2001].

TO OBSERVE the seismic cycle which frequently extends to several centuries, the short time-span of the instrumental period (about a century) appears as a main limitation. A branch of seismology aims to extend the record in the past compiling geological, archaeological and historical evidences for the description of past earthquakes [Ambraseys, 1971; Bilham, 2004; Marco, 2008].

Another limitation is that geophysical observations are indirect evidences. A model is required to link surface observations (\mathbf{d}) to parameters describing the source at depth (\mathbf{m}), that is $\mathcal{G} : \mathbf{m} \mapsto \mathbf{d}$. How geophysical observations constrain the source of slip?

1.1.3 Inferring the characteristics of the source

THE CHARACTERISATION of an earthquake from surface observation, that is assessing its location, size and energy is an inverse problem, generally ill-posed because surface observations provide an incomplete description of fault slip. Inverse problems find the set of parameters \mathbf{m} (e.g. slip location, amount of slip, slip direction, dip of the fault) that best explains the data \mathbf{d} , assuming a model \mathcal{G} that link observables to parameters. If \mathcal{G} is a linear operator, the direct problems writes as $\mathbf{d} = \mathbf{G}\mathbf{m}$. The inverse solution depends on what is a "better" model, or in other words the choice of the cost or misfit function [Tarantola, 2005]. The most common solution minimizes the square of the residuals $((\mathbf{d} - \mathbf{G}\mathbf{m})^2)$ and is named least-squares [Hartzell and Heaton, 1983]. One of the primary challenge of any inversion is to deal with errors, that is to correctly estimate the uncertainties of the data (with covariances), of the model, and of the prediction ("epistemic error") and propagate those so that estimated parameters with their uncertainties have a meaning (and are not the result of data overfitting) [Lohman and Simons, 2005; Sudhaus and Jónsson, 2009; Duputel *et al.*, 2014; Ragon *et al.*, 2018].

IN fault slip source inversion, parameters have a non-linear dependency on observations and are interdependent (i.e. there are many tradeoffs) so that the solution for a given model and data structure is not unique (e.g. Figure 1.3f). Regularization schemes, such as Laplacian smoothing or positivity constraints, are often used to overcome nonuniqueness and stabilize the solution [Du *et al.*, 1992; Amey *et al.*, 2018]. The choice of an inversion method significantly affect the solution, leading to different rupture model for a same earthquake [Min-

son et al., 2013; Duputel et al., 2014; Lay, 2018]. Moreover, additional assumptions and simplifications of real Earth are made in slip inversion to ease computations and fill knowledge gaps. Layered elastic half-space model ignoring three-dimensionality and topography are most common, even though this may bias the solution [*Gallovič et al., 2015; Langer et al., 2020*]. However, the addition of complexity may go against parsimony and make the output hardly interpretable. Integrating physical constraints and choosing the right level of complexity for the model is a meticulous task.

IN ORDER TO capture the range of possible solutions, it is appropriate to estimate the probability density distribution of parameters using Bayes' theorem [*Bayes, 1973; Tarantola et al., 1982; Minson et al., 2013*]. This Bayesian approach also evidences where observations are not sufficient to constrain model parameters (when *posterior* and *a priori* distributions are equal) [*Dianala et al., 2020*].

Concretely, what is our state of knowledge on earthquake source? In this Section 1.1, I hope that I provided the tools and vocabulary to understand and appreciate key observations and seminal works on active faults. Those are introduced in the following section.

1.2 The observed diversity of slip on continental faults

THIS SECTION is a short literature review focused on observations of the seismic cycle divided into the coseismic, postseismic, interseismic and preseismic periods. I voluntarily focus on the description of surface deformation overlooking most dynamical explanations and models. Nonetheless, I briefly mention physical models explaining postseismic deformation and the nucleation of earthquakes. I also restrain myself to continental faults, excluding subduction zones or volcanic seismic activity. There is no ambition of exhaustiveness.

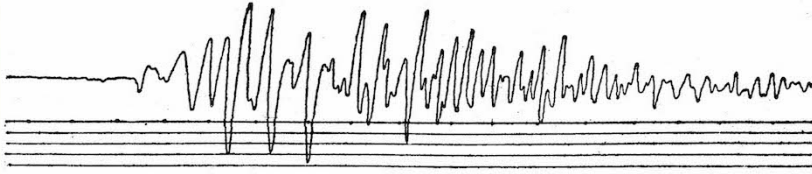
1.2.1 Earthquakes coseismic deformation and structural control

THE QUANTITATIVE OBSERVATION of the 1906 San Francisco (California, western USA) earthquake (Figure 1.4), latter estimated as a $M_w 7.9$, helped H. F. Reid formulate the elastic rebound model [*Reid, 1910, 1911*], the first-order model still in use to describe fault loading and energy release during earthquakes (Section 1.1.1, Figure 1.1). This earthquake belongs to a series of studied strike-slip Californian earthquakes whose observation led to breakthrough in our understanding of earthquakes, probably due to the proximity of precursor scientists and dense instrumentation.

The Parkfield segment of the San Andreas (California) fault hosted repeated $M_w 6$ earthquakes in 1881, 1901, 1922, 1934, and 1966, evidencing the recurrent nature of earthquakes [*Bakun and McEvilly, 1984*].

EARTHQUAKE'S AUTOGRAPH AS IT WROTE IT 3,000 MILES AWAY.

Tracing Made by the Selsmograph Needle in the Office of State Geologist John M. Clarke, State Museum, Albany, Showing How the Earthquake Traveled Across Continent in 19 Minutes.



The drawing represents the vibration of the north and south pendulum of the selsmograph during the time of the most intense activity, beginning in San Francisco at 5:18 A. M., in Albany at 8:32. In Albany the violent agitation ended at 8:48 A. M. The straight lines at the side of the wavy line indicate the normal condition of the record as the recording drum revolves, and this serves to show the contrast between the ordinary progress of the record and that during a disturbance. The spaces between the dots indicate lapses of one minute each. The same violent disturbance was noticeable on the selsmograph at Washington between 8:32 and 8:35 A. M., thus verifying the time of transit across the continent—19 minutes.

Figure 1.4: New York Times article (April 19, 1906, vol. 55 no. 17617) on the seismic wave record of the 1906 San Francisco earthquake in the city of Albany (New York) about 4500 km away.

The latest Parkfield earthquake of 2004 was eagerly awaited, and the anticipated instrumentation led to a record with unprecedented details [Bakun *et al.*, 2005; Barbot *et al.*, 2009, 2012]. Inverted slip on the fault plane evidenced that the 2004 Parkfield coseismic slip is divided into two distinct areas of high slip [Liu *et al.*, 2006].

WHILE INTERFEROGRAMS are now routinely and automatically produced to characterise earthquake coseismic deformation field on land [Monterroso *et al.*, 2020; Lazecký *et al.*, 2020] (Figure 1.3c,d), the first coseismic interferogram was on the 1992 M_w 7.3 Landers (California) earthquake [Massonnet *et al.*, 1993; Peltzer *et al.*, 1994] (Figure 1.5a,b). Interferograms revealed that coseismic rupture can reach a high degree of geometrical complexity. A recent example is the 2016 M_w 7.8 Kaikoura (New Zealand) earthquake during which a complex network of at least 15 faults, both mapped and unmapped, ruptured with a jump of the surface rupture of about 20 km [Hamling *et al.*, 2017; Klinger *et al.*, 2018]. The 2019 M_w 6.4 and M_w 7.1 Ridgecrest earthquakes ruptured an unmapped multiscale network of interlaced orthogonal strike-slip faults [Ross *et al.*, 2019] (Figure 1.3).

ALTHOUGH the San Andreas fault extends beyond the limit of the rupture, Parkfield earthquakes repeatedly nucleate and end at similar locations (implying similar earthquake size and M_w). Another example are the 2008 and 2009 two M_w 6.3 Qaidam earthquakes [Elliott *et al.*, 2011], which also ruptured the same fault segment. This suggests a structural control on the nucleation and size of earthquakes, which can be characterized in terms of lateral segmentation of faults. Fault segments are portion of the fault which tend to rupture at once (i.e. a rupturable unit) and are bounded by fault system geometric complexities like bends, branches, step-overs or fault termination [Wesnousky, 1988, 2006; Manighetti *et al.*, 2009; Klinger, 2010] (Figure 1.5c). Thus, lateral segmentation of mapped active faults is key for seismic hazard analyses. Fault trace geometrical control of rupture propagation is clearer for strike-slip ruptures [Lasserre *et al.*, 2005; Klinger, 2010] than

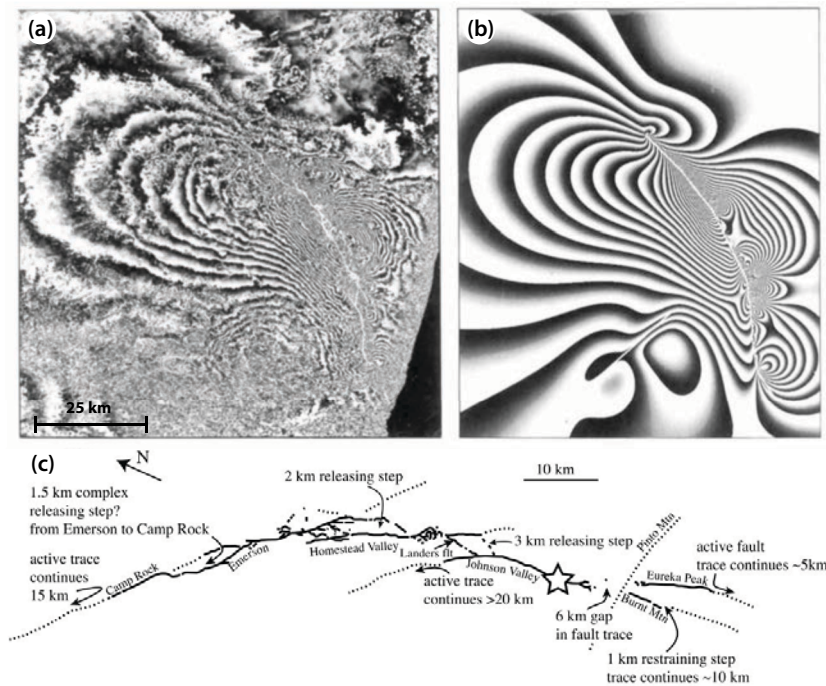


Figure 1.5: Displacement and rupture geometry for the 1992 $M_w7.2$ Landers earthquake. Top: first published coseismic interferogram ever (ERS-1 satellite) (a) and predicted interferogram by an elastic half-space dislocation model (b) from *Massonet et al.* [1993]. One fringe (cycle of gray shading) represents 28 mm of change in line of sight. (c) Sketch of the rupture geometry from *Wesnousky* [2006]. The star locates the epicenter.

for dip-slip ruptures [*Biasi and Wesnousky, 2017*], where structural limit can be in the downdip direction too. For instance, the Nepal ramp of the Main Frontal Thrust limited the dip extend of the 2015 $M_w7.8$ Ghorka earthquake [*Elliott et al., 2016a*]. The geometrical complexity, density of discontinuities and number of segments along a fault is thought to decrease with increasing fault maturity ⁴, a tendency seen for strike-slip faults (in California, Japan, New Zealand China and Turkey) [*Wesnousky, 1988; Stirling et al., 1996*] and normal faults in Afar (Ethiopia) [*Manighetti et al. [2009, 2015]*].

THE GROWING instrumental record of earthquake helped finding empirical scaling relationship between the magnitude, size, and displacement of earthquakes [*Wells and Coppersmith, 1994; Petersen et al., 2011*] which are useful for earthquake hazard quantification. However, the record contains many outliers [*Manighetti et al., 2007; Klinger et al., 2018*] and frequent earthquakes occurring on unmapped fault (e.g. 2019 $M_w7.1$ Ridgecrest earthquake), sometimes at great distances from any plate boundary (e.g. 1988 $M_w6.5$ Tennant Creek (Australia) earthquake or the 2017 $M_w6.5$ Botswana earthquake) [*Bowman, 1992; Gardonio et al., 2018*].

1.2.2 Postseismic signal

COSEISMIC SLIP generates stress perturbations, inducing different dynamical responses on the periphery of the ruptured fault. There are

⁴ According to *Manighetti et al. [2007]* fault maturity increases as the fault accumulates slip throughout time (hundreds of kilometres in millions of years) and is associated with long fault slipping at a few cm/yr.

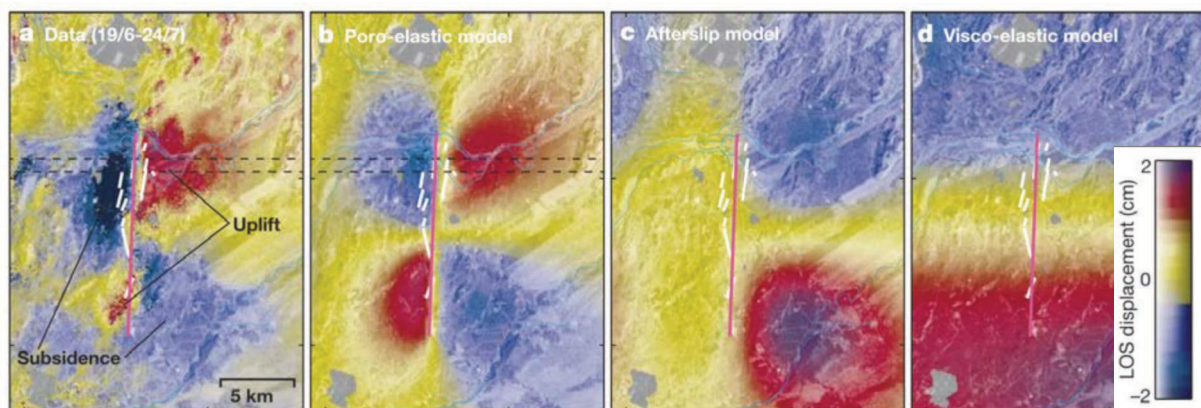


Figure 1.6: Postseismic deformation from InSAR and modelled deformation for the 17 June 2000 M_w 6.5 earthquake in Iceland as presented in Figure 2 of *Jonsson et al.* [2003]. Displacement is in the line of sight (LOS) towards the European radar satellite ERS-2 (more sensitive to vertical motion). The right-lateral earthquake occurred on a near north-south fault. Also shown are simulated post-seismic deformation using poro-elastic (b), right-lateral afterslip (c), and visco-elastic (d) models.

four main physical processes which are listed below.

1. Seismic slip, as a cascade of aftershocks that results from coseismic stress change on nearby fault surfaces with a rate-weakening rheology [Dieterich, 1994]. For instance, moment release following the 2003 M_w 7.2 Altai earthquake is mainly due to aftershocks [Barbot et al., 2008]. The frequency of aftershocks decays with time from the mainshock following a power law [Omori, 1894; Utsu, 1961; Utsu et al., 1995] or a stretched exponential [Mignan, 2015], with a characteristic decay time typically between 7 and 11 years [Parsons, 2002]. Time for rates to return to the background seismicity rate, seems proportional to mainshock recurrence time [Dieterich, 1994].
2. Aseismic slip (i.e. afterslip) on the ruptured fault or its extension evidenced from kinematic inversions of geodetic data [e.g. Savage et al., 1994; Pousse-Beltran et al., 2020] and it may drive postseismic seismicity [Barbot et al., 2009; Jiang et al., 2021]. Mechanically, afterslip is thought of as a relaxation of the coseismic stress perturbation within a rate-strengthening region, and displays a characteristic logarithmic temporal decay (velocity proportional to the inverse of time) [Marone et al., 1991; Perfettini and Avouac, 2004; Zhou et al., 2018; Wang and Bürgmann, 2020]. Rate-strengthening conditions are expected to be met at mid-crustal depth below earthquake maximum coseismic slip (where temperature $> 250^\circ\text{C}$) and close to the surface due to loose sediments or fault gouges. Afterslip at depth dominate after the 1999 Chi-Chi (Taiwan) earthquake [Perfettini and Avouac, 2004; Roussel et al., 2012], the 1999 Izmit (Turkey) earthquakes with a rate of 2 m/yr immediately after the earthquake [Bürgmann et al., 2002], or the 2015 M_w 7.8 Gorkha (Nepal) earthquake with a maximum slip rate of about 50 cm/yr [Sreejith et al., 2016; Wang and Fallico, 2018]. Afterslip near the surface is recorded following the 2016 M_w 6.5 Norcia (Italy) (a few cm/yr in LOS from InSAR) [Pousse-Beltran et al., 2020], or the M_w 7.3 Tabas-e-Golshan (Iran) earthquake

[Zhou *et al.*, 2018], where measured afterslip with InSAR last for 40 years reaching rates down to 2.3 ± 0.6 mm/yr. Marone *et al.* [1991] hypothesises that the need for gouge implies that shallow afterslip is a particularity of old (i.e. mature) faults. In some cases, both updip and downdip afterslip is recorded, like for the 2017 $M_w 7.3$ Zarpol-e-Zahab (Iran) earthquake [Wang and Bürgmann, 2020].

3. Visco-elastic relaxation in the upper mantle or lower crust in response to the deviatoric stresses induced by mainshock [Pollitz, 1997; Deng *et al.*, 1999]. The shape and duration of this relaxation is used to constrain the rheology of the uppermost mantle, which is mostly non-linear (e.g. biviscous Burgers rheology) [Pollitz, 2003; Bürgmann and Dresen, 2008; Zhao *et al.*, 2017]. The relaxation following the $M_w 7.1$ Hector Mine (California) earthquake [Freed and Bürgmann, 2004] is one example. Also, relaxation processes can transfer stress in return to the upper crust and feed long-term (several years) aftershock sequences [Deng *et al.*, 1999].
4. Poro-elastic rebound in the upper crust (above brittle-ductile transition) caused by pore pressure diffusion to the coseismic stress change. It was inferred, for instance, following the 1992 $M_w 7.3$ Landers earthquake combined with deep afterslip [Peltzer *et al.*, 1998; Fialko, 2004] and after two $M_w 6.5$ (2000) earthquakes in Iceland during 1-2 months [Jonsson *et al.*, 2003]. For this earthquake, InSAR displacement field show the characteristic quadrantal pattern opposite in sense to coseismic fault slip and geothermal wells show an associated water level decrease where the ground subsides and increase where there is an uplift (Figure 1.6).

THOSE FOUR PROCESSES are interdependent and are often hard to discriminate from surface deformation only, so that different models can appear equally good [Wright *et al.*, 2013; Ingleby and Wright, 2017; Wang and Bürgmann, 2020]. Frequently, a combination of those processes best explain the complexity of the signal [Rousset *et al.*, 2012; Zhao *et al.*, 2017]. Fault slip in the postseismic period (afterslip and aftershocks) releases moment that is usually a fraction of the coseismic moment. Typically, postseismic moment is 10% to 30% of the coseismic moment, however, there is a high variability in estimates [Zhao *et al.*, 2017; Jiang *et al.*, 2021] and intermediate magnitude earthquakes ($M_w 4-6$) tend to have larger postseismic to coseismic moment ratios [Alwahedi and Hawthorne, 2019].

IN the postseismic period, dynamic triggering of earthquakes and slow slip events may occur on nearby faults. Triggered events are generally not considered as aftershocks or afterslip events if they are large or far away with respect to the coseismic slip size, although processes at play are similar [McGill *et al.*, 1989; Nissen *et al.*, 2016; Victor *et al.*, 2018; Tymofyeyeva *et al.*, 2019].

1.2.3 Interseismic strain

ASSESSING interseismic strain accumulation on continental faults is key for seismic hazard [Wright *et al.*, 2001; Biggs *et al.*, 2007]. Indeed, the differential displacement on each side of the fault at 10s km from the fault trace approximates the rate at which the fault is loaded, and thus is directly related to the shallow slip deficit and expected seismic moment release (Equation 1.1, Figure 1.1) [Molnar, 1979; Bird *et al.*, 2015; Rollins and Avouac, 2019]. Elliott *et al.* [2016a] exhibits the spatial correlation between strain rate, seismic moment release and earthquake rate at the scale of about 20 km for western Turkey and California.

The surface deformation induced by slip on the fault plane can be modelled by a screw dislocation buried in an homogeneous elastic half-space [Savage and Burford, 1973; Okada, 1992]. The corresponding analytical representation links the depth at which the fault slips to the wavelength of the across fault surface deformation. In the interseismic period, this depth is the locking depth (generally between 10-20 km) thought to constrain the maximum earthquake magnitude for long strike-slip faults. The long-term InSAR measurements at fine spatial resolution are ideal to quantify the slow accumulation of slip and assess the wavelength of surface deformation, even though the multiplicity of viewpoints required for three-dimensional description is not easily met. The classical approach consists in using spatially-interpolated GNSS measurements in addition to InSAR with ascending and descending LOS [Wei *et al.*, 2010].

INVERTED subsurface slip rates on a discretized fault plane provide a finer picture of slip at depth during the interseismic period. Slip at depth can be interpreted as a degree of coupling (i.e. the percentage of slip deficit with respect to the long-term (= far-field) strain) in a seismic hazard perspective (Figure 1.1) [Pacheco *et al.*, 1993; Bürgmann *et al.*, 2005; Kaneko *et al.*, 2010; Bletery *et al.*, 2020]. The higher is the coupling (1 for a locked fault), the larger is strain accumulation on the fault plane and, consequently, the larger is the energy to be released through seismic slip. Coupling estimation requires that the far-field loading of the fault is known, which may be tricky for systems of intricate faults (e.g. Chaman plate boundary).

LARGE deforming continental area are now covered, with, for instance, the LiCSAR ambition to process the whole Alpine-Himalayan belt (Figure 1.2) [Lazec̆ky *et al.*, 2020], from Anatolia [Hussain *et al.*, 2016, 2018; Weiss *et al.*, 2020] to Tibet [Wang and Wright, 2012; Wang *et al.*, 2019], through Iran [Watson *et al.*, 2021] using the continuously growing SAR dataset produced by the Sentinel 1 satellites. Slip rates range from plate velocity rates of a few cm/yr down to a few mm/yr. Specifically, the Denali (Alaska) fault accommodates 1 ± 0.5 cm/yr [Biggs *et al.*, 2007]; or the Main Recent fault (Iran) is inferred to slip at 3.0 ± 1 mm/yr below a locking depth of 18 km [Watson *et al.*, 2021]. At the

global scale, *Kreemer et al.* [2014] model strain rate in plate boundary zones with constrains from horizontal GNSS velocities.

STRAIN fields are often converted into maps of the second invariant of the strain rate tensor, thus outlining where horizontal strain focuses [*Wang and Wright, 2012; Kreemer et al., 2012*]. This requires downsampling of InSAR and interpolation of GNSS data as well as additional assumptions [*Bürgmann et al., 2013*]. GNSS data govern the first-order patterns of the inferred second invariant of the strain rate tensor [*Wang et al., 2019; Weiss et al., 2020*] and its irregular spacing implies spatial aliasing. Moreover, the deformation field is inevitably smoothed so that those models do not provide useful information on geodetically constrained fault slip rates [*Bürgmann et al., 2013*]. Spatial resolution of 1 km or less is required to see whether the fault is locked or slipping near the surface.

1.2.4 Creeping faults and slow slip events

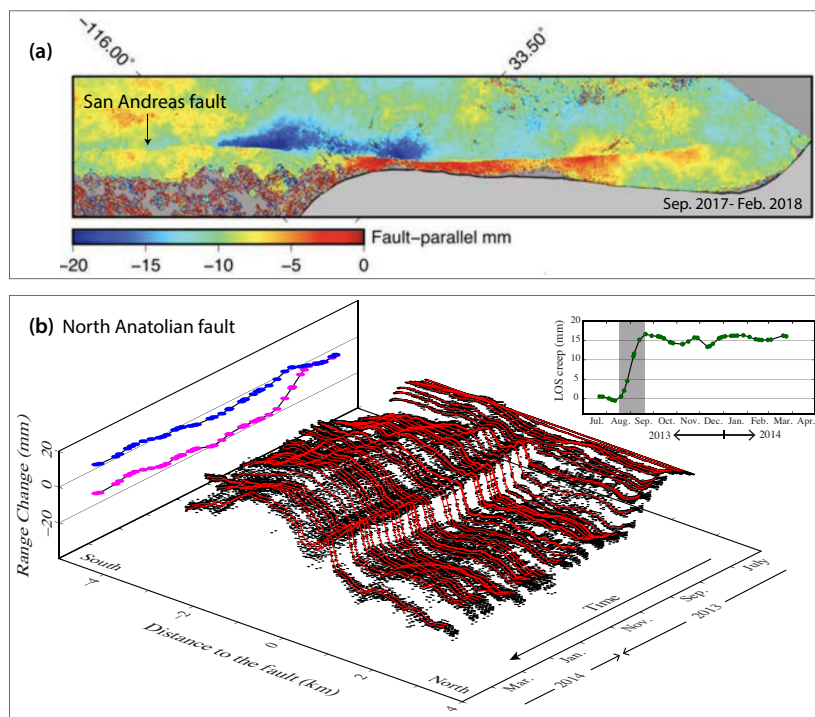


Figure 1.7: Two examples of recorded shallow slow slip transients with InSAR. (a) Inferred fault-parallel displacement from ascending and descending InSAR data over a time period of 6 months following the 2017 Chiapas earthquake [*Tymofeyeva et al., 2019*] (b) Spatio-temporal record of a slow slip event on the North Anatolian fault (Turkey) from InSAR time series by *Rousset et al.* [2016]. The main plot shows the temporal evolution of surface displacement in LOS on a 500 m wide and 8 km long profile centred on the fault. Blue (south) and magenta (north) dots show average range change on each side of the fault, with their difference shown in the top right plot (green dots). The period of transient creep spanning August to September 2013 is highlighted in grey.

THE FIRST MEASUREMENTS of shallow slow slip were based on the offset of masonry and fences crossing the San Andreas fault [*Steinbrugge et al., 1960*] or the North Anatolian fault [*Ambraseys, 1970*]. Soon, ground instrumentation (creepmeters, alignment arrays) and, latter, geodetic measurements allowed to delimit shallow slow slip spatially and temporally, with a critical role of InSAR (Figure 1.7). Recent comprehensive reviews on slow slip are *Bürgmann* [2018] and *Jolivet and Frank* [2020]. Like for afterslip, mechanical conditions for slow slip are

reached on the deepest and shallowest part of the seismogenic fault, due to low effective normal stress near the surface or high temperature at depth. Rate-strengthening minerals, gouge and elevated pore fluid pressure in the fault zone are also thought to favour slow slip [Moore and Rymer, 2007; Bürgmann, 2018; Biemiller et al., 2020]. Subsurface coseismic slip distributions show a systematic shallow slip deficit [Kaneko and Fialko, 2011], which is in favour of ubiquitous shallow creep closing the slip budget. However, part of this deficit arises from fault geometry uncertainties in inversion [Ragon et al., 2018].

THE San Andreas fault is seen to slip quasi-steadily along its 100-km-long central part⁵ with a maximum rate of about 30 mm/yr [Burford and Harsh, 1980; Tong et al., 2013; Maurer and Johnson, 2014; Jolivet et al., 2015a] and along the southernmost 50 km of the fault at 2-6 mm/yr [Lindsey et al., 2014; Tymofyeyeva et al., 2019] (e.g. Figure 1.7a). The North Anatolian fault accommodates a total of 21-25 mm/yr and creeps at about 9 mm/yr in the upper ~6 km of the Ismetpasa segment [Kaneko et al., 2013]. Many other faults exhibit creeping sections, such as the Xianshuihe [Li and Bürgmann, 2021] and Haiyuan [Jolivet et al., 2012, 2013, 2015b] faults in China, the Philippine fault [Duchesnoy et al., 1994; Dianala et al., 2020], the North Qaidam Thrust faults (Tibet) [Daout et al., 2019], the low-angle normal Mai'iu fault (Papua New Guinea) [Biemiller et al., 2020], or, most importantly for this thesis, the Chaman fault (Afghanistan, Pakistan) [Fattahi and Amelung, 2016; Barnhart, 2017]. Creep rates correspond to partial coupling of the fault plane at shallow depth (like in Figure 1.1b) and a reduced seismic hazard with respect to locked fault portions [Michel et al., 2018]. At the end of the spectrum, part of the Philippine fault shows creep rates of 3 cm/yr equivalent to the long-term rate meaning that there is no strain accumulation (coupling of zero) [Dianala et al., 2020].

⁵southeast of the 1906 San Francisco rupture, northwest of the Parkfield segment

USING the fine spatial resolution of InSAR, across-fault strain localization can be quantified (a few meters to several kilometres). Lindsey et al. [2014] found that along-strike changes in creep localization can be explained by Coulomb stress changes due to variations in the local fault strike. However, predicted patterns would favour long-lasting fault bends and even their exaggeration over time in contradiction to the apparent straightness of mature faults [Stirling et al., 1996; Lindsey et al., 2014] (Section 1.2.1). Therefore, there are still uncertainties about how fault geometry and its best-known 1-D intersection with the surface (fault trace) influence tectonic stress concentrations and, thus, the seismogenic potential of a fault.

WHEN OBSERVATIONS have temporal resolution, apparently steady creep often contains discrete slow slip events (phase of slip acceleration). Typically, creepmeters record stair-like time series of surface slip, with discrete hour-to-day-long slow slip events [Schulz et al., 1982; Bilham et al., 2016]. On the San Andreas fault, a slow earthquake se-

quence in 1992 equivalent to a $M_w 4.8$ accompanied by minor seismicity ($M_w \leq 3.7$) was recorded with two strainmeters [Linde *et al.*, 1996]. With additional observations, it seems that slow slip events are frequent and pseudoperiodic in California [Murray and Segall, 2005; Wei *et al.*, 2013; Turner *et al.*, 2015]. Deep-seated bursts of slip near the brittle-ductile transition are also detected in the region [Rousset *et al.*, 2019; Delbridge *et al.*, 2020] through the seismic signals they induce, which takes the form of repeating earthquake sequences⁶ [Nadeau and McEvilly, 2004], earthquake swarms and tectonic tremors [Ito *et al.*, 2007; Beroza and Ide, 2011; Hawthorne and Rubin, 2013; Bürgmann, 2018].

One of the most beautiful observation based on InSAR time series analysis is the spontaneous 15 mm of slip in 1 month along a section of the North Anatolian fault that was previously thought to creep steadily at 8 mm/yr (Figure 1.7b) [Rousset *et al.*, 2016]. Based on 18 years of SAR acquisitions, creep rate acceleration at the decadal-scale of ± 2 mm/yr² is mapped along the central San Andreas fault on 10-km-wide patches and interpreted as the result of changes in pore fluid pressure [Khoshmanesh and Shirzaei, 2018a]. Can we identify more transient slip events? Is the longer geophysical record confirming this picture that continuous creep is the sum of discrete events? Temporal resolution is needed to address this question.

WHAT are the the physical processes governing the initiation and size of slow slip events? In the rate-and-state framework, slow slip is interpreted as an indication of rate-strengthening friction on the fault plane (Section 1.1.1). However, this picture is challenged by evidences that a same asperity may rupture seismically and aseismically [Mele Veedu and Barbot, 2016]. This naturally arises in models with a conditionally stable layer below the surface [Wei *et al.*, 2013]. Then, are slow slip events similar to earthquakes in their statistics and physical relationships? Scaling relationship between seismic moment and characteristic duration for earthquakes and slow slip events have been used to discuss the different nature of those processes [Ide *et al.*, 2007; Michel *et al.*, 2019; Dal Zilio *et al.*, 2020].

1.2.5 Earthquake precursory phase

How a fault switches from an apparently steady interseismic slip regime to a fast (~ 1000 m/s) rupture emitting seismic waves? Physical models predict a stress-sensitive time-dependent nucleation with foreshock rate increase as an inverse power law of time to the mainshock [Dieterich, 1994; Rubin and Ampuero, 2005; Cattania and Segall, 2021]. Thus, foreshock activity has been a primary focus of earthquake hazard studies [Scholz, 1998; Dodge *et al.*, 1995; Bouchon *et al.*, 2013]. The most successful prior warning to a devastating continental earthquake was in 1975, when a 4-day long, extensive foreshock sequence led to the $M_L 7.3$ Haicheng earthquake in north eastern China [Zongjin *et al.*,

⁶ Earthquake are said to be "repeating" when they are recorded with nearly identical waveforms. They are seen as the repeated failure of a small asperity on the fault plane due to aseismic slip on the surrounding fault plane.

1990]. To date, the feat has not been replicated. Extended precursory activity preceding a mainshock continental earthquake is thought to be exceptional, as most significant historical events are not presaged by detectable seismic or geodetic activity [Bouchon *et al.*, 2013; Vidale and Shearer, 2006; Roland and McGuire, 2009].

THE RELATION between foreshock activity and the nucleation process that ultimately culminates in the mainshock remains unclear [Dodge *et al.*, 1995; Ellsworth and Beroza, 1995; Trugman and Ross, 2019]. Some sequences show efficient transfer of static stresses to trigger a mainshock [Helmstetter and Sornette, 2003; Ellsworth and Bulut, 2018] while others require underlying aseismic slow slip to explain seismic recordings [Tape *et al.*, 2018]. For instance, repeating earthquakes preceding the 1999 M_w 7.6 Izmit earthquake [Bouchon *et al.*, 2011]; the spatio-temporal migration of foreshocks and repeating events preceding the M_w 9 Tohoku megathrust earthquake [Kato *et al.*, 2012]; and insufficient stress transfer between foreshocks before the M_w 7.3 Landers earthquake [Dodge *et al.*, 1995] provide indirect evidence of an underlying, slow-slip process preceding these large earthquakes. To date, laboratory friction experiments provide the only direct observations of precursory aseismic fault slip, associated with secondary migrating acoustic emissions [McLaskey, 2019; Marty *et al.*, 2021]. Precursory slow slip and foreshocks are also emerging in rough fault simulations [Cattania and Segall, 2021].

IT IS PRESUMED that, assuming precursory slip is common, it is too deep and/or too small to be geodetically detected [Bouchon *et al.*, 2013]. Can new instrumentation and more thorough data analysis overcome this limitation? I searched for precursory signals of the 2019 Ridgecrest earthquake sequence in four years of InSAR time series and three years of relocated seismicity with Bertrand Rouet-Leduc, Claudia Hulbert, Blandine Gardonio, Daniel T. Trugman, Jorge Jara, Sylvain Michel, Paul A. Johnson and Romain Jolivet. We did not find any convincing precursory signal with our thorough analysis outside of the short foreshock sequence starting 30 minutes before the M_w 6.4 earthquake as published in [Huang *et al.*, 2020].

Human activity may favour earthquake nucleations. Fluid injections is the most studied source of triggered earthquakes [Ellsworth, 2013]. Surface unloading due to quarry extraction may have contributed to the 2019 M_w 4.9 Teil (France) earthquake nucleation [De Novellis *et al.*, 2021].

1.3 InSAR : theory and current issues

AS MORE OBSERVATIONS are acquired and as we diversify the methods of observations it seems that the picture of the seismic cycle becomes more complex with a wide range of strain-releasing processes

happening at different spatial and temporal scales. Interferometric Synthetic Aperture Radar (InSAR) has the potential to measure subtle surface deformation at fine spatial resolution on all continental surfaces from frequent and ongoing satellite acquisitions. Thus, it appears as a powerful tool to answer questions raised in the previous section. However, to assess the extent of the possibilities offered by InSAR and the associated limitations, one has to understand the underlying technology and assumptions used during processing.

1.3.1 How InSAR works

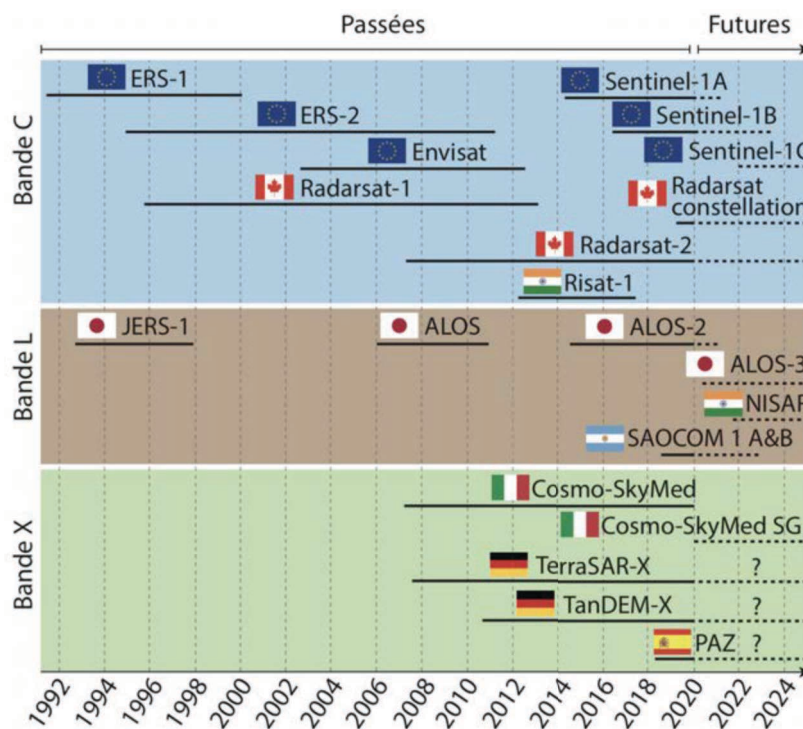


Figure 1.8: Past, current and future SAR satellite missions (unavco.org; *Benoit [2020]*). In this thesis, I principally work with Sentinel 1A and 1B data.

THE FIRST SATELLITE carrying a Synthetic Aperture Radar (SAR) was Seasat launched in 1978 [*Goldstein et al., 1988*], latter followed by ERS-1 (1991), Envisat (2002), ALOS (2006) or Sentinel 1 (2014) to only name a few (Figure 1.8). In this thesis, I work with InSAR using Sentinel 1AB satellites. While the satellite is flying in its azimuth direction, SAR instruments transmit electromagnetic waves sequentially to the ground in the line of sight (LOS) direction and record the backscattered echoes (Figure 1.9). The SAR echo is a complex number with a phase and amplitude. The amplitude informs about the reflectivity of the illuminated ground [e.g. *Massonnet and Feigl, 1998*]. Physical interaction between the radar wave and the ground arises mainly from the roughness, water content (dielectric properties), penetration of waves and slope effect, which in turns depend on the radiated wavelength

(λ) [Massonnet and Souyris, 2008; Scott et al., 2017]. For geophysical applications, C-band (λ of 3.8-7.5 cm) and L-band (λ of 15-30 cm) are the most used, L-band having a lower resolution, but higher penetration through vegetation.

FOR A SINGLE SAR image the backscattered phase appears random spatially with an uniform distribution between 0 and 2π . Patterns arise when looking at the difference in phase between two passes of the satellite over the same ground [e.g. Massonnet and Feigl, 1998] (Figure 1.9). To capture this phase difference, an interferogram is built by computing the complex conjugate product of two SAR images. Thus, the imaginary part of the interferogram is the phase change (or phase delay) Φ_{ij} defined as the difference in phase ϕ_j and ϕ_i acquired at times t_j and t_i , respectively, plus some error arising from InSAR processing ϵ , that is

$$\Phi_{ij} = \phi_j - \phi_i + \epsilon_{ij}. \quad (1.3)$$

The phase change, Φ_{ij} , reflects the variation of the two-way travelled distance (i.e. round-trip propagation path) from the satellite to the ground between both passes of the satellites, known to a fractional wavelength. Therefore, the physical contributions to Φ_{ij} can be decomposed into geometrical variations changing the distance to travel and refractive index variations in the atmosphere affecting the ray path (Snell's law) differently between t_i and t_j [Goldstein, 1995; Tarayre and Massonnet, 1996]. Geometrical contributions to phase change arise from the difference in the exact position of the satellite relative to the ground, orbital and topographic delays Φ_{orb} and Φ_{topo} , [Zebker and Goldstein, 1986] as well as from deformation occurring between t_i and t_j , Φ_{def} . The total phase delay also includes the contribution from spatio-temporal variations in the pressure, temperature and water content of the troposphere, Φ_{tropo} , together with variations in the electronic content of the ionosphere, Φ_{iono} [Wegmuller et al., 2006; Meyer et al., 2006]. This writes as

$$\Phi_{ij} = \Phi_{orb} + \Phi_{topo} + \Phi_{tropo} + \Phi_{iono} + \Phi_{def} + \epsilon_{ij}. \quad (1.4)$$

FOR THE STUDY of the seismic cycle, the challenge is to isolate the phase change due to deformation Φ_{def} from the rest. While orbital and topographic errors can be mitigated through the computation of precise orbits (e.g. accuracy typically below 1 cm for Sentinel 1) and topography (e.g. Shuttle Radar Topography Mission (SRTM) has 1 arc-second (~ 30 m) resolution), tropospheric and ionospheric contributions are harder to deal with. Φ_{tropo} can reach tens of centimetres and often masks subtle deformation signals [Zebker et al., 1997; Delacourt et al., 1998; Daout et al., 2018]. It can be decomposed into a stratified component that correlates with topography and a turbulent part [Jolivet et al., 2014a; Fattahi and Amelung, 2015]. The contribution from the stratified part of the troposphere can be estimated empirically by inferring the linear coefficient between the elevation and the

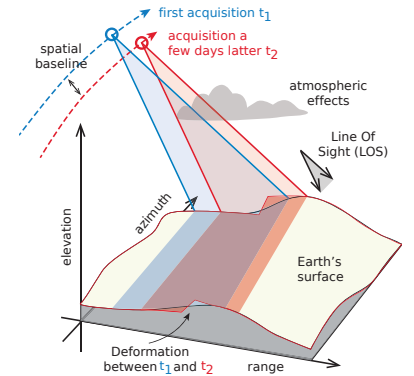


Figure 1.9: Schematics of the acquisition geometry of repeated SAR images for interferometric SAR.

phase change [Cavalié *et al.*, 2008; Elliott *et al.*, 2008; Lin *et al.*, 2010; Welch and Schmidt, 2017]. However, with this approach topography correlated deformation (e.g. volcanic inflation) is in Φ_{tropo} and lateral variations in the stratified atmosphere are neglected [Tarayre and Massonnet, 1996]. Alternatively, the delay from the stratified troposphere is forecast using independent information like *in situ* measurements (e.g. weather stations, multispectral imagery, zenith tropospheric delay of GPS) [Williams *et al.*, 1998; Li *et al.*, 2005] and weather reanalysis of pressure, temperature and water vapour at global scale [Jolivet *et al.*, 2014a; Hu and Mallorqui, 2018; Benoit *et al.*, 2019; Cao *et al.*, 2021] or mesoscale [Puyssegur *et al.*, 2007; Roukounakis *et al.*, 2021].

The turbulent atmosphere is hardly dealt with as it corresponds to rapid small-scale variations in the state of the troposphere associated with convective phenomena, vertical wind shear or rain falls [Tarayre and Massonnet, 1996; Fattahi and Amelung, 2015] (e.g. Figure 1.10a,b). The chaotic nature of the turbulent atmosphere implies that its state decorrelates temporally at scales shorter than a day. Thus turbulent delays in interferograms tend to average out for repeated-enough observations, but this means that temporal resolution is lost or degraded.

Regarding Φ_{iono} it can reach meters, long wavelengths (L-band) and low latitudes being more sensitive [Meyer *et al.*, 2006; Gomba *et al.*, 2016; Liang *et al.*, 2019] (e.g. Figure 1.10c). The spectral width of SAR microwaves can be used to correct ionospheric delays (split-spectrum method) [Gomba *et al.*, 2015, 2016; Liang *et al.*, 2019].

INSAR is theoretically able to measure millimetres of phase change and, thus, deformation at fine spatial scale every week to month. However, uncorrected atmospheric signal and processing errors challenge the extraction of ground deformation. In the following section, I detail how a number of processing steps help mitigating errors and biases in interferograms. Next, I describe InSAR time series analysis.

1.3.2 The challenge of dealing with error and biases

THE CONSTRUCTION of meaningful interferograms for the study of centimetre-scale ground deformation is a challenge with ongoing studies and development. Before building interferograms, both SAR images have to be precisely registered into the same reference frame (coregistration step) in order to maximize interferences and minimize the effect of orbital variations and topography [Michel *et al.*, 1999; Sansosti *et al.*, 2006; Yagüe-Martínez *et al.*, 2016; Fattahi *et al.*, 2017]. Some acquisition modes of SAR images also require to stuck tiles together, like the TOPS (Terrain Observation with Progressive Scans) mode of Sentinel 1 which splits images into bursts and swaths [De Zan and Monti Guarnieri, 2006; Grandin *et al.*, 2016]. The degree of similarity (correlation) between two SAR images and thus the quality of an interferogram is quantified by the interferometric coherence [Zebker and

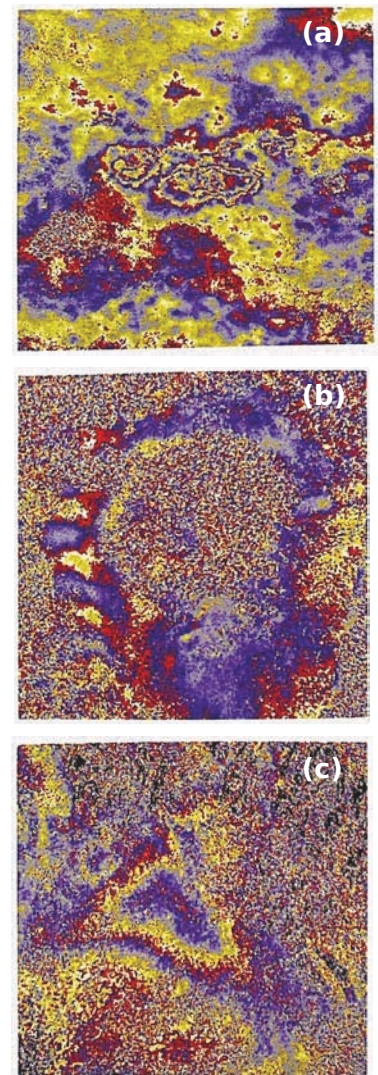


Figure 1.10: Examples of atmospheric artefacts observed in interferograms from [Massonnet and Souyris, 2008]; (a) clouds (cumulus); (b) cloud chains; (c) hole in the ionosphere.

Villasenor, 1992; Hanssen, 2001; Massonnet and Souyris, 2008]. Decorrelation may originate from unprecise coregistration [*Li and Goldstein, 1990*], but it also naturally arises for surface changes in between repeated passes of the satellite with amplitudes on the order of a radar wavelength. Thus, rapidly changing ground cover (e.g. vegetation, snow, water), large deformation and large spatial or temporal base-lines are sources of loss of coherence and decorrelation [*Scott et al., 2017*].

ONCE an interferogram is built, the key is to convert the phase delay in radian on each individual geographical cell (i.e. pixel) to a deformation field. Because of the periodicity of the electromagnetic wave, the phase change on each pixel is ambiguously known modulo 2π . The process of converting phase change in radian (said to be "wrapped")(Figure 1.3c) to continuous length change (Figure 1.3d) is called phase unwrapping [*Goldstein et al., 1988*]. It is needed in order to obtain the phase change between two points. Unwrapping of a single interferogram requires spatial continuity between regions of high coherence in the interferogram. Local unwrapping methods, such as the Branch-Cut algorithm, imply a step by step spatial unwrapping along a path of integration starting at a seed location [*Goldstein et al., 1988; Herszterg et al., 2018*], while global methods such as the Statistical-cost, Network-flow Algorithm for Phase Unwrapping (SNAPHU) [*Chen and Zebker, 2000, 2001*] work on the whole interferogram at the same time [*Pritt, 1996*]. For a set of interferograms, unwrapping in space and time (3-D) also exists [*Hooper, 2010; Hussain et al., 2016*]. Errors during unwrapping generate phase misclosure, ϵ_{ij} , that is proper to each interferogram and, thus, imply that closed triplets of three interferograms are not zero ($\Phi_{12} + \Phi_{23} - \Phi_{13} \neq 0$). Errors are essentially $k2\pi$ (k an integer) offsets in the unwrapped phase (Figure 1.11) and most of them can be automatically corrected [*Yunjun et al., 2019; Benoit et al., 2020*]. Still, any unwrapping method is challenged by regions of low coherence in the interferogram.

TO EASE UNWRAPPING it is common to improve the signal-to-noise ratio of the interferogram through spatial averaging (i.e. multilooking) and filtering [*Massonnet and Feigl, 1998; Goldstein and Werner, 1998*]. While phase preserving filters only affect the sharpness of the signal, multilooking leads to misclosure [*Agram and Simons, 2015; De Zan et al., 2015*]. This misclosure arises from the averaging of complex numbers affected by non-gaussian noise. It is a product of signal decorrelation and, thus, it is related to variations in the scattering and electrical properties of the ground surface induced by, for instance, soil moisture variability or vegetation growth [*Michaelides et al., 2019; Ansari et al., 2020*]. Because of its physical origin (dependant on the nature of the ground), the misclosure from multilooking is spatially correlated, systematic and may have a skewed temporal distribution, thus generating biases in velocity estimates [*De Zan et al., 2015*]. The addi-

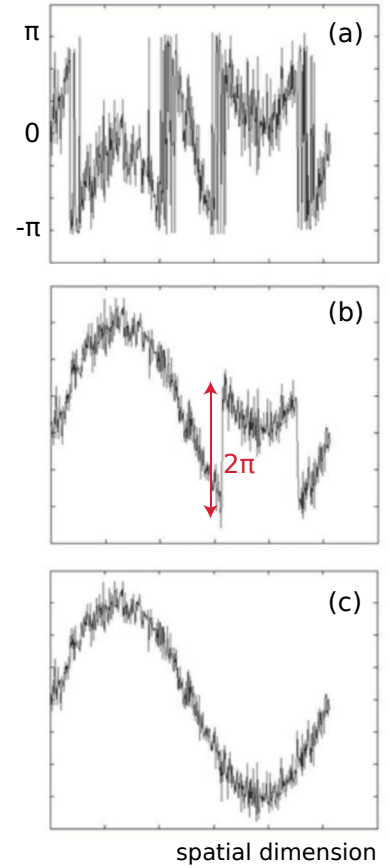


Figure 1.11: Graphical representation of Interferometric phase unwrapping. (a) wrapped phase, (b) unwrapped phase containing an error (2π offset) (c) correctly unwrapped phase. Modified from *Herszterg et al. [2018]*.

tive nature of this systematic error means that the greater is the minimum number of interferograms in the network linking the start and end of the time series (longer path of integration to the reference), the larger is the bias. Therefore, long temporal baseline interferograms help mitigate misclosure error due to multilooking. As a concrete example, a time series of deformation in Sicily (Italy) for a network of short baseline interferograms (maximum 40 days) includes a bias of 6.2 mm/yr with respect to a network of all possible interferometric connections over 4 years [Ansari *et al.*, 2020]. Precise absolute geolocation in three-dimensions (longitude, latitude, elevation) of the imaged point on the ground would free the processing from the need of unwrapping but latest developments still produce locations which are not precise enough [Fattahi *et al.*, 2020].

THEREFORE, although building an interferogram appears numerically simple, the complex interaction of the radar wave with the ground and its sensitivity to slight variations in the acquisition geometry make the process fastidious. Careful step by step processing is necessary followed by critical interpretation of the phase change in terms of deformation. In this thesis, I use the InSAR Scientific Computing Environment (ISCE) software (JPL/Caltech, winsar.unavco.org/software/isce). There are also initiatives of automatic interferogram computations as online services, which facilitate the use of InSAR (e.g. FLATSIM [ForM@Ter, 2020]; COMET-LiCS [Wang and Wright, 2012]; Generic Atmospheric Correction Online Service (GACOS) [Yu *et al.*, 2018]; ARIA Standard Displacement Product and Online processing (aria.jpl.nasa.gov); Hybrid Pluggable Processing Pipeline [Hogenson *et al.*, 2018]).

1.3.3 The evolution of phase change

To COMPUTE the evolution of phase delay over time, a network of interferograms connecting acquisition dates to each other is required. There are two classical ways to build interferometric networks. Persistent Scatterer Interferometry (PSI) works with a subset of pixels which are stable and coherent over the whole time period and requires interferograms to have a date in common (master date) [Ferretti *et al.*, 2000, 2001; Hooper *et al.*, 2007], while the Small Baseline Approach Subset (SBAS) approach includes all pixels and is based on a network of interferograms between acquisitions at nearby dates (small temporal baseline) and on close orbits (small spatial baseline) [Lundgren *et al.*, 2001; Berardino *et al.*, 2002; Schmidt and Bürgmann, 2003].

Both approaches require a temporal reference (a time step considered to show stable ground), but the temporal discontinuity of some pixels in SBAS implies the need for a spatial reference (motionless area) too. For a Persistent Scatterer (PS) the phase delay at a date t_i is uniquely defined by the phase change Φ_{ik} , where t_k is the master date and ϵ in Equation 1.4 is considered null. Indeed, the temporal conti-

nuity of PS implies that unwrapping can be done in time rather than space, so that there is no need for the multilooking processing step which is source of misclosure. On the other hand, SBAS typically contains redundant information with multiple interferograms for a single date, and thus requires to solve an inverse problem minimizing the residual error, called time series analysis (Figure 1.12). Efficient time series analysis and accurate error estimation for large amount of interferograms containing misclosure is a challenge that will be the topic of Chapter 2.

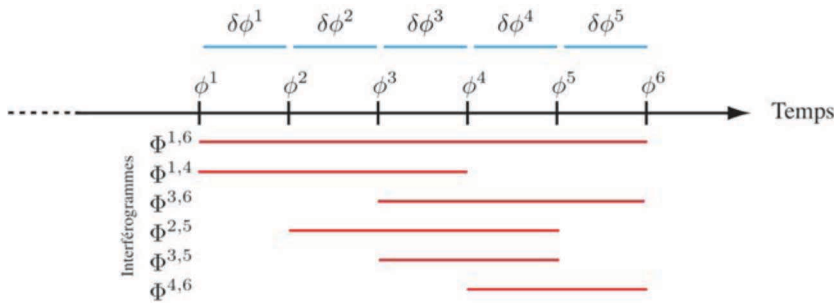


Figure 1.12: Schematics of the problem of time series analysis for a network of small baseline interferograms from *Jolivet [2011]*. Incremental phase delays $\delta\phi^k$, for all k , are inferred from interferograms $\Phi^{i,j}$, so that the evolution of phase ϕ^k over time can be reconstituted.

PERSISTENT SCATTERER are robust to temporal and geometrical decorrelation and are typically characterized by high reflectivity. Man-made structures, boulders, and outcrops can all generate good PS [*Ferretti et al., 2011*]. Thus, if PSI is particularly efficient in urban environments, the scarcity of stable scatterer in natural environment implies limited spatial coverage and the tractability of the method for several-year-long time series remains to be verified. In the aim of imaging faults (mostly in natural environment) and making the most out of the continuously acquired SAR data, I choose to work with SBAS interferometric networks in this thesis. SqueeSAR is an hybrid approach that consists in combining the robust point-wise PS with distributed scatterers (multilooked pixels) using a space adaptive number of looks able to average statistically homogeneous pixels only [*Guarnieri and Tebaldini, 2008; Ferretti et al., 2011*]. Sadly, SqueeSAR is not free.

1.4 Towards systematic InSAR time series : the Chaman plate boundary natural laboratory

1.4.1 Describing active faults and learning from SAR data

THE SEISMIC CYCLE provides a conceptual model of elastic loading and unloading of active faults. However, the complexity of observations summarized in Section 1.2 outlines that fast slip during earthquakes is not the main strain release mechanism on some faults that host slip in the interseismic period adding up to a large fraction of

the far-field displacement. Moreover, stress interactions and feedbacks govern fault dynamics at a variety of scales, from the nucleation phase on a same fault plane, to induced seismic and aseismic slip on nearby portions of the same fault or on distant faults. Mapping detailed stress changes is key in seismic hazard estimate, however, the initial stress state seems hard to obtain as it often results from an unknown history. Fault geometry, which is thought to be related to slip history too, adds an additional level of complexity in the genesis of earthquakes.

Furthermore, the loading of a given fault is often unknown as it belongs to a system of faults accommodating far-field strain together. Strain partitioning between faults is an additional unknown in the slip budget of a single fault, thought to reflect the "deficit" of earthquakes and fault's ability to rupture in a large hazardous earthquake [Billham and Ambraseys, 2005]. Deviations of the local seismicity with respect to the Gutenberg-Richter statistics are also considered as a sign of upcoming earthquakes, but the reliability of this is debated [e.g. Frohlich and Davis, 1993; Wiemer and Wyss, 2002; Michel *et al.*, 2018].

CONTINUOUS geodetic observations, and particularly InSAR, played a key role in unravelling slow, and sometimes subtle (few millimetres on a few kilometres), deformation. Because of the punctual and rare occurrence of earthquakes on a given fault segment, geodetic observations mostly cover the inter-earthquake period (postseismic and interseismic). Nevertheless, while GNSS time series are frequently exploited in details, InSAR measurements are most of the time summarized into a displacement field between two epochs (e.g. coseismic interferograms) or into a velocity field, showing mean rates of deformation. In InSAR time series, the high inter-acquisition noise arising from turbulent atmospheric delays, is the main limitation to the study of short temporal variations (inferior to a month), even though it is possible under some conditions [e.g. Rousset *et al.*, 2016].

The Sentinel 1 satellites (A and B) image the same ground every 6-12 days since the end of 2014, now providing more than 5 years of continuous measurements, and future SAR missions (Figure 1.8) promise many more years of abundant SAR acquisitions. This is a treasure in the quest for transient slip events, providing that time series analysis methods are able to deal with uncertainties arising from non-tectonic processes and to cope with the continuous flow of high-resolution incoming data. Indeed, emerging SAR Big Data raises questions about efficient storage and processing. For instance, currently many SAR satellites discard part of the acquisitions because of the heavy cost of data storage and management (e.g. ALOS, Sentinel observations in area of 12 days return time).

CURRENT time series analysis methods require to reprocess the whole network of interferograms in order to include new data, implying elevated numerical cost and the storage of heavy data (Sentinel 1 wide-swath interferograms contain easily more than 10^7 pixels after multi-

looking). This often means that updates of time series are delayed with respect to the continuous availability of new SAR images. Therefore, as the history of SAR acquisition grows it becomes urgent to design tools able to update pre-existing time-series of surface deformation with minimal numerical cost and reliable tracking of uncertainties and covariances. Sequential near real-time processing is key [Ansari *et al.*, 2017]. A reliable tracking of phase change and a simultaneous interpretation in terms of deformation can be achieved with a data assimilation approach. In Chapter 2, I introduce and test a new algorithm for InSAR time series analysis optimizing knowledge of the interferograms and of the deformation with minimal computational cost. I apply this method to real data along the Chaman plate boundary.

1.4.2 The appeal of the Chaman plate boundary

THE CHAMAN plate boundary in Afghanistan and Pakistan accommodates 25-35 mm/yr of left-lateral motion between the tectonic plates of India and the Afghan block of Eurasia⁷ (Figure 1.13) [DeMets *et al.*, 2010; Yeats, 2012; Altamimi *et al.*, 2017]. It links the Makran subduction zone to the southwest to the Himalayan convergence in the northeast.

THE SEISMICITY of the region and the mapped faults indicate that the deforming plate boundary extends on a width of 100 to 200 km [Bernard *et al.*, 2000; Ambraseys and Bilham, 2003a; Ruleman *et al.*, 2007], corresponding to mountain ranges (Kirthar and Sulaiman ranges) rising above the plains in which the Indus river flows towards the Arabian Sea in the south. Many faults appear in the geology and geomorphology and their current activity is outlined by offset streams and infrastructures (e.g. railways). Hundreds of kilometres long left-lateral faults are, from south to north (Figure 1.13), :

- the Ornach Nal fault, which extends from the coastline of Pakistan along the Arabian Sea in the south to about 28°N, for a total length of about 200 km. At its southern end it is thought to meet the frontier with the Arabian plate in a triple junction.
- the Chaman fault, which is the western border of the Kirthar mountains and Katawaz block extending from 27.5°N to about 35°N (near Kabul, the Afghan capital). The Chaman fault "megatectonic importance", borrowing the words of Auden [1974], is supported by its great length (~ 850 km), and abrupt changes in the geology and structures between both sides.
- the Ghazaband fault is near-parallel to the Chaman fault between 27°N and 31°N.
- the Gardez fault zone branches out of the Chaman fault at 33°N and runs east of Kabul with a strike close to 50° to north.

⁷The Afghan or Helmand block belong to the Cimmerian terranes, which accreted to Eurasia around 200–160 Ma following the closure of the Paleothethys ocean. The collision between India and Eurasia followed the closure of the Neothethys ocean about 40 Ma [Powell, 1979; Seton *et al.*, 2012]. The limit between the Afghan block and Eurasia is the east-west Hari Rud fault system (sometimes named Herat fault) in middle Afghanistan, which shows little to no signs of current activity, with right-lateral slip rate of 0-2 mm/yr [Tapponnier *et al.*, 1981; Wheeler *et al.*, 2005; Boyd *et al.*, 2007].

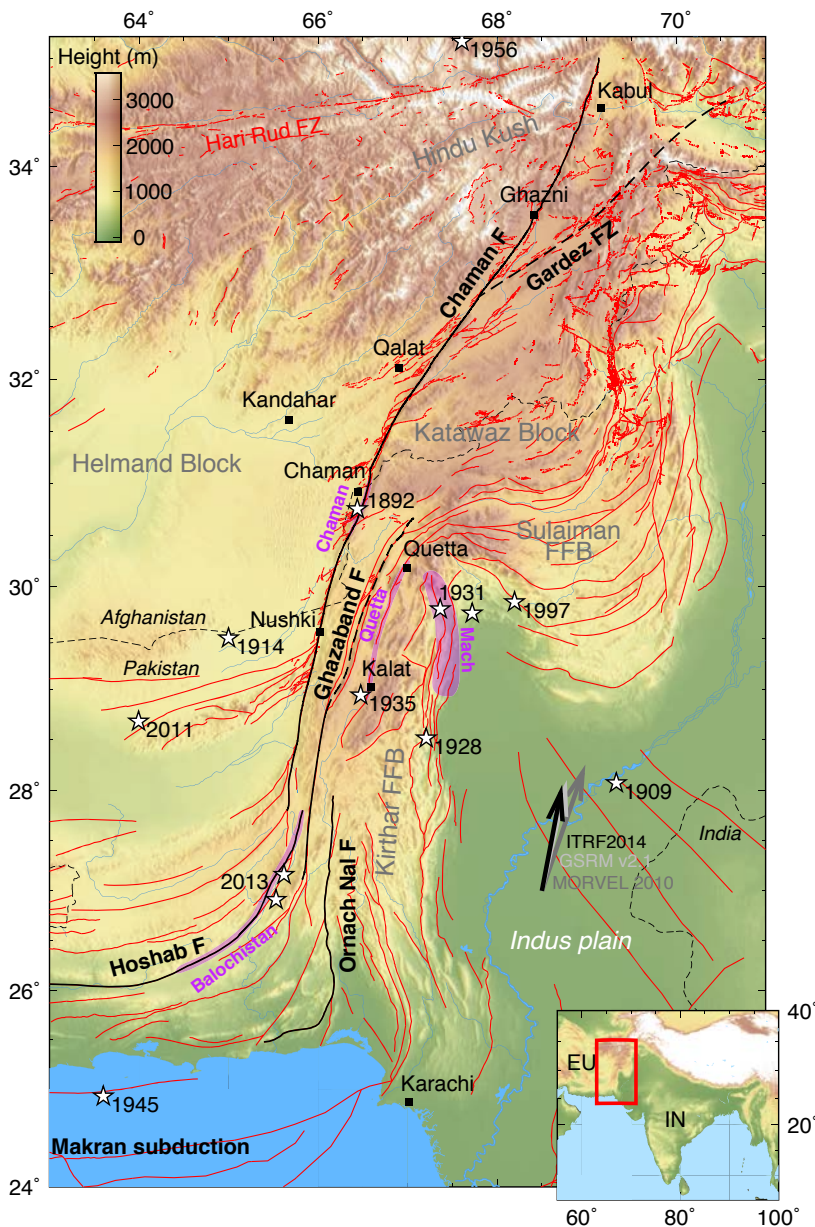


Figure 1.13: Faults and significant earthquakes since the end of the 19th century along the Chaman plate boundary. Red lines are fault traces from [Ruleman et al., 2007], thick black lines outline major named faults (dashed when uncertain). The epicentres of earthquakes with $M_w > 6.5$ (1892-2020) are marked by white stars with their associated dates of occurrence. Rupture extents from [Bilham et al., 2019] and [Jolivet et al., 2014b] are indicated by the purple shaded regions. Arrows show estimated velocities of India with respect to Eurasia at (68.5°W , 27°N) from three global plate models [DeMets et al., 2010; Kreemer et al., 2014; Altamimi et al., 2017]. Black squares are cities, dashed lines are frontiers.

THE only known large ($M_w > 6$) earthquake on the Chaman fault itself is the 1892 $M_w 6.5-6.7$ Chaman earthquake [Bilham et al., 2019]. During the 20th century, other important events in the region occurred east of the Chaman fault, mostly in and along the Kirthar ranges, the largest one being the 1935 $M_w 7.7$ Quetta earthquake which ruptured a still unnamed fault between the cities of Quetta and Kalat [Skirine, 1936; Ambraseys and Bilham, 2003a] (Figure 1.13). Therefore, past large earthquakes evidence distributed deformation.

Long thrust faults are also part of the fault system. Faults of the Makran accretionary prism splay to the southwest of the left-lateral fault system. One of them, the Hoshab fault, hosted the 2013 $M_w 7.7$ Balochistan earthquake, a 200-km-long rupture with essentially left-

lateral slip and a secondary reverse component [Jolivet *et al.*, 2014b; Lauer *et al.*, 2020]. Furthermore, the Kirthar and Sulaiman ranges are fold and thrust belts bounded by active thrust faults to the east. The 1931 M_w 7.3 Mach earthquake was along such thrust fault, probably like seven other M_w >6 earthquake, which occurred between 1908 and 1931 [Bilham *et al.*, 2019]. Consequently, the Chaman plate boundary appears as a transpressional system. What is the relative activity of those numerous faults? Which structure(s) accommodate the relative plate motion?

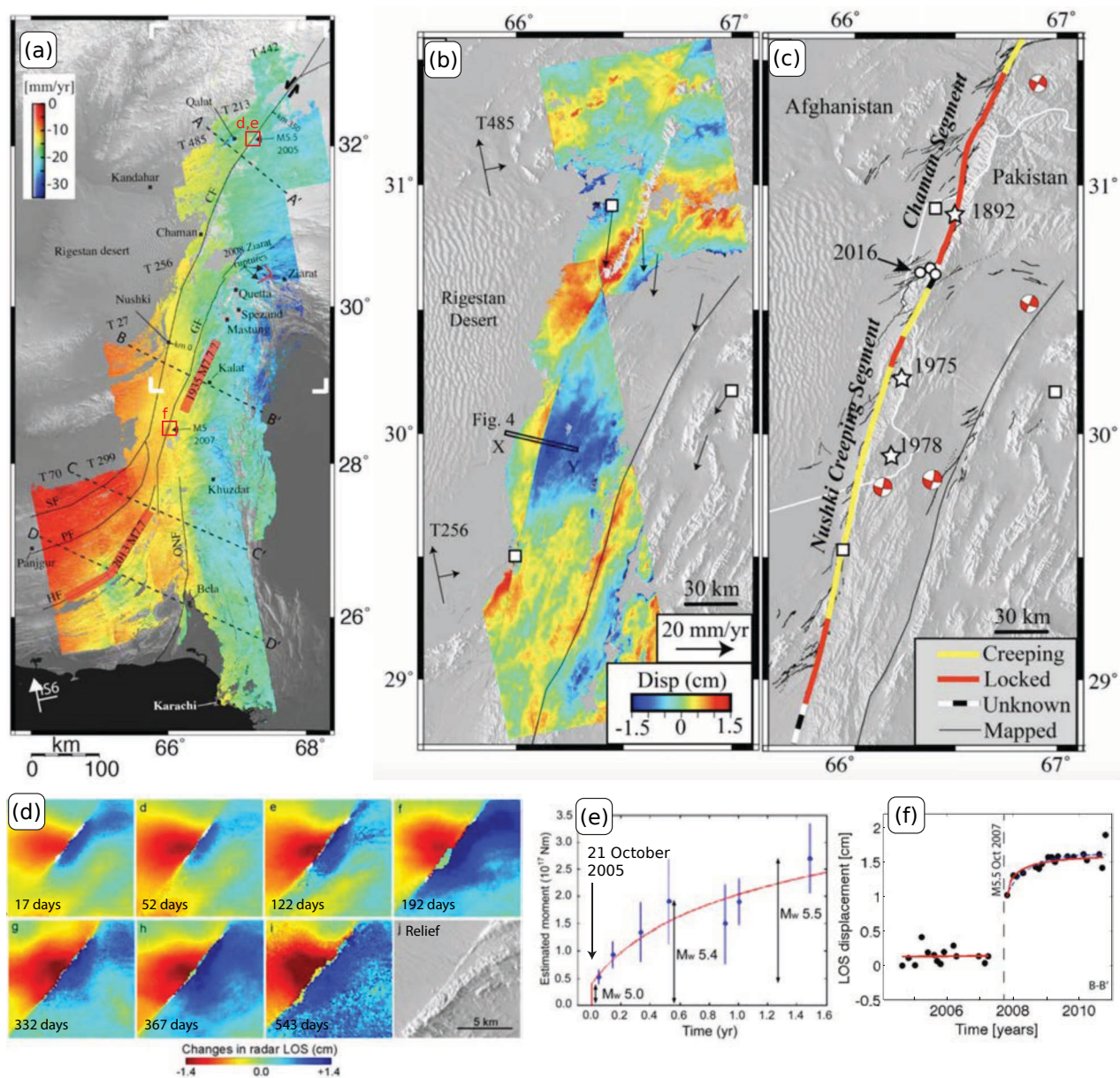


Figure 1.14: Slow slip along the Chaman plate boundary viewed by InSAR. Published line of sight (LOS) velocity maps by *Fattahi and Amelung* [2016] (a) and by *Barnhart* [2017] (b), interpreted segmentation of the Chaman fault by *Barnhart* [2017] (c). Time series of coseismic and postseismic deformation for the 21 October 2005 M_w 5.0 earthquake by [*Furuya and Satyabala*, 2008] (d,e) and for the 19 October 2007 M_w 5.5 earthquake by [*Fattahi et al.*, 2015] (f). Locations of both earthquakes are marked by red squares in (a). In (b), arrows are horizontal GNSS velocities and white squares represent cities (Nushki, Quetta and Chaman in Pakistan).

THE SCARCITY of the recorded seismicity in the past century is another specificity of this plate boundary [Ambraseys and Bilham, 2003a,b; Dewey et al., 2006; Szeliga et al., 2009; Bilham et al., 2019]. That is, the total seismic moment release, and thus slip (Equation 1.1), is small compare to the plate relative plate motion of several centimetres per year. This raises the question of the role of aseismic slip in the release of strain.

Previous geodetic studies estimated that the Chaman fault accommodates 5-15 mm/yr of strain and slips aseismically near the surface [Szeliga et al., 2012; Fattahi and Amelung, 2016; Barnhart, 2017] (Table 1). The most exhaustive studies are based on InSAR velocity maps over 2003-2011 using Envisat and ALOS acquisitions (Figure 1.14a,b). Barnhart [2017] estimates creep rates combining two line of sights and, on this basis, divides the fault length into creeping and locked, earthquake bearing, segments (Figure 1.14c). Furthermore, Furuya and Satyabala [2008] and Fattahi et al. [2015] observe postseismic slip following two earthquakes of M_w 5 and 5.5 in 2005 and 2007, respectively (Figure 1.14d-f). These postseismic, apparently aseismic, slips appear particularly large with respect to coseismic slips [Alwahedi and Hawthorne, 2019]. What is the spatio-temporal slip pattern on the Chaman fault? Is aseismic slip continuous or transient, spontaneous or following earthquakes? Should we expect a future large earthquake or is strain released by aseismic processes?

BECAUSE this region is hardly accessible for scientists, we face short historical records, limited ground instrumentation, little geological or geodetic constraint on slip rates, and uncertain earthquake locations [Bilham et al., 2007]. There is no network of permanent GNSS along this plate boundary. Nonetheless, the low vegetation cover and dry climate make it an ideal region for highly coherent interferograms, even though the broadly north-south orientation of the Chaman fault zone is not optimal for SAR measurements known to be sensitive to east-west displacement (unlike the North Anatolian fault, but like the San Andreas fault). Therefore, InSAR is the most promising tool to characterise this major plate boundary. As already mentioned, there are two published large-scale InSAR studies of the Chaman fault, but none exploit Sentinel 1 data.

1.4.3 Aims and structure of the thesis

IN the four Chapters that follows, I intend to respond to part of the numerous questions formulated in the introduction. The main objectives are to

1. Develop an efficient time series analysis tool for InSAR able to update pre-existing time series (Chapter 2),
2. Describe time-dependent deformations with accurate uncertainty estimates for all parameters at every time steps (Chapter 2, 3),
3. Characterize slip on the Chaman fault at different scales and identify transient slip events (Chapter 3),
4. Detail the fault trace geometry and evaluate its importance in the observed slip distribution (Chapter 3),
5. Evaluate the importance of postseismic slip for local moderate earthquakes (Chapter 3, 5),
6. Assess the amount of strain on other faults in the Chaman plate boundary, notably the Ghazaband fault (Chapter 4),
7. Discuss the resolution limits of InSAR and explicit perspectives for future work (Chapter 5).

CHAPTERS 2 and 3 are self-sufficient published articles, while Chapter 4 is written as a shorter article, soon to be submitted for publication. Finally, Chapter 5 summarizes and discusses main results.

My aim is to use high-resolution InSAR data in an efficient way for the detection and characterisation of slip events (seismic and aseismic) in the Chaman fault zone.

Chapter 2

A KALMAN FILTER TIME SERIES ANALYSIS METHOD FOR INSAR

Une méthode d'analyse en série temporelle reposant sur le filtre de Kalman pour l'InSAR

CE CHAPITRE présente une nouvelle méthode de calcul de séries temporelles de déformation à partir d'interférogrammes déroulés par Romain Jolivet et moi-même. Il a été publié en tant qu'article dans la revue *Journal of Geophysical Research: Solid Earth* en 2020. Cette méthode, nommée KFTS, permet de mettre à jour itérativement une série temporelle pré-existante par la combinaison appropriée des données, du modèle et de leurs incertitudes respectives, au fur et à mesure que les images Radar à Synthèse d'Ouverture (SAR) sont disponibles. KFTS repose sur les équations du filtre de Kalman, une méthode d'assimilation de données qui fonctionne en deux étapes. Dans un premier temps, une prédiction (forecast) de la déformation à un instant donné est faite à partir d'un modèle d'évolution du système préalablement optimisé, avec une incertitude reflétant la justesse du modèle et la connaissance des paramètres. Dans un deuxième temps, cette prédiction est ajustée (ou analysée) tenant compte des observations à l'instant donné (ex. les interférogrammes) et de leurs incertitudes (Figure 2.1). La construction des matrices de covariances (Figure 2.1) est clé pour la combinaison adéquate de ce qui provient du modèle et des données.

KFTS répond au besoin d'analyse rapide à faible coût de calcul des images SAR, acquises en continu sur toutes les surfaces continentales avec des satellites toujours plus nombreux.

KFTS CALCULE les séries temporelles des délais de phase, et optimise les paramètres d'un modèle descriptif de cette évolution (typiquement une vitesse et une oscillation saisonnière) (Figure 2.1). La méthode est d'abord testée sur des données synthétiques, construites pour ressembler à un réseau d'interférogrammes bruités sur une région se déformant. Ceci permet de vérifier qu'à quantité d'information égale, KFTS donne la solution des moindres-carrés (Figure 2.2, 2.4), qui est

celle que donnent les méthodes d'analyse en série temporelle InSAR couramment utilisées. Dans le but de rester le plus proche possible des données, nous déterminons que l'écart-type de l'erreur des données (l'erreur de fermeture du réseau interférométrique, σ_ϵ) doit être une à 10 000 fois plus petite que celle de l'erreur inhérente au modèle (l'erreur de modélisation, σ_γ) (Figure 2.6).

DEUX JEUX de données sont utilisés pour tester KFTS : un réseau d'interférogrammes ENVISAT sur l'Etna (Sicile, Italie) qui a déjà été utilisé pour la validation d'autres études InSAR, et des interférogrammes Sentinel 1 sur la zone de faille de Chaman (Afghanistan, Pakistan). Les stations GPS sur l'Etna enregistrent un signal corrélé avec ce que l'on mesure dans les séries temporelles InSAR (Figure 2.7, 2.8). Sur la zone de Chaman, KFTS estime des délais de phase et des vitesses de déformation très proches de ce que la méthode NSBAS couramment utilisée produit, excepté dans les régions où l'incertitude est grande du fait de données manquantes (Figure 2.9, 2.10). Dans ces régions, l'a priori sur le modèle utilisé pour la première étape de prédiction affecte l'estimation. KFTS a la particularité d'estimer et de propager les incertitudes et covariances temporelles associées, qui ainsi reflètent la durée et la connectivité du réseau interférométrique localement ainsi que l'interdépendance des paramètres.

FINALEMENT, une attention particulière est portée à la paramétrisation de KFTS qui nécessite la définition appropriée (i) des erreurs σ_ϵ et σ_γ , (ii) de la description fonctionnelle de la déformation et (iii) des a priori sur les paramètres de cette description, ainsi que la covariance associée (Figure 2.11). KFTS est implémenté en Python 3 comme un outil libre, flexible et accessible pour la communauté scientifique (Github/KFTS-InSAR).

THIS CHAPTER has been submitted, reviewed and published as a research article in *Journal of Geophysical Research: Solid Earth* in 2020¹. It presents a new processing method named KFTS to compute the evolution of deformation over time from interferograms with a sparing use of computational resources. Since 2020, the algorithm is freely available on an online repository with associated documentation and I regularly update it, adding new options and improving its adaptability and reliability.

¹ **Citation:** Dalaison, M., & Jolivet, R. (2020). A Kalman filter time series analysis method for InSAR. *Journal of Geophysical Research: Solid Earth*, 125(7), e2019JB019150.

Abstract

Earth orbiting satellites, such as Sentinel 1A-B, build up an ever-growing set of synthetic aperture radar images of the ground. This conceptually allows for real-time monitoring of ground displacements using Interferometric Synthetic Aperture Radar (InSAR), notably in tectonically active regions such as fault zones or over volcanoes. We propose a Kalman filter for InSAR time series analysis (KFTS), an efficient method to rapidly update preexisting time series of displacement with data as they are made available, with limited computational cost. KFTS solves together for the evolution of phase change with time and for a parametrized model of ground deformation. Synthetic tests of KFTS reveal exact agreement with the equivalent weighted least squares solution and a convergence of descriptive model parameter after the assimilation of about 1 year of data. We include the impact of sudden deformation events such as earthquakes or slow slip events on the time series of displacement. First tests of KFTS on ENVISAT data over Mt. Etna (Sicily) and Sentinel 1 data around the Chaman fault (Afghanistan, Pakistan) show precise (± 0.05 mm) retrieval of phase change when data are sufficient. Otherwise, the optimized parametrized model is used to forecast phase change. Good agreement is found with classic time series analysis solution and GPS-derived time series. Accurate estimates are conditioned to the proper parametrization of errors so that models and observations can be combined with their respective uncertainties. This new tool is freely available to process ongoing InSAR time series.

2.1 Introduction

SINCE THE 1990s, Interferometric Synthetic Aperture Radar (InSAR) has been used and optimized to measure ground deformation from satellite [e.g. *Griffiths, 1995; Bürgmann et al., 2000; Simons and Rosen, 2015*]. While first studies focused on temporally discrete, large amplitude events, such as earthquakes [e.g. *Massonnet et al., 1993*], recent geophysical applications rely on deriving the temporal evolution of deformation to capture the full spectrum of temporal behaviors, from short episodic deformation events [e.g. *Lindsey et al., 2015; Rousset et al., 2016*] to long-term, decadal trends [e.g. *Grandin et al., 2012; Chaussard et al., 2014a; Jolivet et al., 2015a*]. Examples include continuous monitoring of aquifers [e.g. *Schmidt and Bürgmann, 2003; López-Quiroz et al., 2009; Chaussard et al., 2014b*], volcanoes [e.g. *Pritchard and Simons, 2004; Biggs et al., 2014*] slow moving landslides [e.g. *Hilley et al., 2004; Scheingross et al., 2013; Tong and Schmidt, 2016*] or aseismic slip along active faults [e.g. *Jolivet et al., 2013; Khoshmanesh and Shirzaei, 2018b*].

Capturing the time evolution of ground displacement using InSAR is not direct and requires adequate processing of sets of interfero-

grams [e.g. *Simons and Rosen, 2015*]. An interferogram is the conjugate product of two Synthetic Aperture Radar (SAR) images. The corresponding interferometric phase directly records ground deformation between two passes of the satellite. Reconstructing the temporal evolution of the phase, hence ground deformation, through time should be straightforward. However, this procedure, called time series analysis, remains a challenge as interferograms are often affected by spatial and temporal decorrelation [e.g. *Zebker and Villasenor, 1992; Berardino et al., 2002; Simons and Rosen, 2015*]. Furthermore, the reconstructed phase is the combination of various sources of noise such as atmospheric and ionospheric delays as well as ground displacements. Part of the time series analysis procedure intends to separate these different contributions [e.g. *Bürgmann et al., 2000; Emdarson et al., 2003; Agram and Simons, 2015*].

TWO MAIN APPROACHES have been developed to perform time series analysis. First, Permanent or Persistent Scatterers techniques focus on a subset of reliable pixels with stable backscattering properties over time to perform spatial and temporal unwrapping [e.g. *Ferretti et al., 2000; Hooper et al., 2007*]. Second, Small Baseline Subset (SBAS) techniques rely on the redundancy of the network of interferograms to enhance spatial coverage and resolution [e.g. *Berardino et al., 2002; Hetland et al., 2012*]. In this paper, we focus on SBAS techniques.

Temporal increments of phase change are linked to interferograms by a set of linear equations. As we aim to reconstruct the evolution of phase with time from interferograms, we need to solve an inverse problem, which is usually done using classic least-squares [*Schmidt and Bürgmann, 2003; Usai, 2003; Agram et al., 2013*] or singular value decomposition [*Berardino et al., 2002; López-Quíroz et al., 2009; Jolivet et al., 2012*]. Nowadays, the resolution, frequency and availability of SAR images grow dramatically thanks to recent launches of numerous SAR missions including the Sentinel 1A-1B (European Space Agency) or the ALOS 2 (Japan Aerospace Exploration Agency) missions [*Elliott et al., 2016a*]. Future missions, such as Sentinel 1C-1D and NISAR (NASA, ISRO), will also lead to a growth in the amount of available data, ensuring long temporal coverage of deformation. Existing SBAS techniques will inevitably become overwhelmed by the rapid accumulation of images. These methods require increasing computing power and memory, as the size of the inverse problem to solve grows with the quantity of observations. More importantly, acquisitions at a given time do not inform on the state of deformation at another given time if these epochs are not connected by interferograms. Processing the entire set of interferograms each time a new acquisition is performed is not only computationally expensive, but also not useful.

WE PROPOSE a method to sequentially update pre-existing multi-annual time series of InSAR data considering only the latest observations. We describe how to use data assimilation for the reconstruction of ground

displacements using InSAR, including minimal computing time and little data storage. We derive the formulation of a Kalman filter for time series analysis, hereafter referred as KFTS, an approach analogous to least squares in its assumptions and final solution [Kalman, 1960; Cohn, 1997]. As data assimilation methods require accurate estimation of errors at all steps, our method allows to investigate various sources of errors.

Kalman filtering is already widely used to build Global Navigation Satellite System (GNSS) time series [e.g. Hofmann-Wellenhof *et al.*, 2012], as very frequent acquisition of small amount of data makes such filtering very relevant. Other application in geodesy include modeling of volcanic reservoir properties [e.g. Shirzaei and Walter, 2010; Bato *et al.*, 2018] or of fault slip at depth [e.g. Segall and Matthews, 1997; Bekaert *et al.*, 2016]. Most of these techniques are driven by time series of deformation in order to reconstruct the temporal evolution of a model describing the source of surface deformation. The aforementioned methods require the use of a time series analysis method in order to reconstruct surface displacements beforehand. Furthermore, although uncertainties are fundamental in any assimilation scheme, uncertainties are unfortunately not always correctly estimated [Agram and Simons, 2015; Bekaert *et al.*, 2016]. Here we provide a method to continuously and efficiently build InSAR time series from a stack of SAR interferograms and propagate associated uncertainties.

IN THE FOLLOWING, we detail time series analysis for InSAR and formulate explicitly the corresponding Kalman filter approach. We highlight the efficiency of our approach on two different regions subjected to volcanic and tectonic deformation. We first test our method on a time series of SAR acquisitions by the Envisat satellite between 2003 and 2010 over the Etna volcano, in Sicily, around which several GPS stations enable us to derive local time series of ground deformation. We validate our approach against this independent set of data. We also use GPS data to assess the robustness of the uncertainties derived by our Kalman filter implementation. We then derive a time series of ground deformation using Sentinel 1 data between 2014 and 2018 over western Pakistan and southern Afghanistan. This region is poorly instrumented and no deformation time series are available for comparison with our approach. However, vegetation cover is scarce, hence interferometric coherence is good, and the Sentinel constellation has acquired a large amount of SAR images, allowing us to highlight the efficiency of our time series analysis method.

2.2 A Kalman filter-based approach for times series analysis

2.2.1 Data description and formulation of the problem

THE PHASE of an interferogram is a differential measurement of the spatial and temporal change in the two way travel time of the Radar wave between the satellite and the ground. It is a direct measurement of the change in the apparent distance between the satellite and the ground, hence a function of ground deformation between two dates. Our goal is to reconstruct the evolution of the interferometric phase over time with respect to the first acquisition and to extract ground deformation from this time series. We work on each pixel independently from its neighbors [Berardino *et al.*, 2002; Cavalie *et al.*, 2007]. For a given pixel, the unwrapped phase of the interferogram between two dates at times t_i and t_j is

$$\Phi_{ij} = \phi_j - \phi_i + \epsilon_{ij}, \quad (2.1)$$

where ϕ_j is the unwrapped phase at a time t_j relative to the phase ϕ_0 at time t_0 , and ϵ_{ij} is the error associated with the potentially inaccurate unwrapping of the interferometric phase, with spatial filtering and with multi-looking (i.e. non-coherent phase averaging often used to enhance coherence) [Goldstein *et al.*, 1988; De Zan *et al.*, 2015; Agram and Simons, 2015]. As interferograms connect multiple SAR acquisitions in time, we call a set of interferograms a network and ϵ_{ij} is often referred to as network misclosure [Doin *et al.*, 2011]. Herein, the standard deviation of ϵ_{ij} will be noted σ_ϵ , assuming it is common to all interferograms for simplicity.

Moreover, for a single pixel, the network of interferograms is often incomplete as unwrapping of the phase is not always possible due to spatial and temporal variations of phase coherence. If the fringe rate is too high between neighboring pixels, it is not possible to derive the relative motion of these pixels from one to another, hence phase cannot be unwrapped [Goldstein *et al.*, 1988]. Without connectivity, it is impossible to reconstruct a common phase history between temporally disconnected sets of interferograms. Various methods propose to derive a temporally parametrized model of the phase evolution, either assuming constant velocities between sub-networks [Berardino *et al.*, 2002] or more complex ad hoc models [e.g. López-Quiroz *et al.*, 2009; Jolivet *et al.*, 2012; Hetland *et al.*, 2012; Jolivet and Simons, 2018].

FOLLOWING THE APPROACH of López-Quiroz *et al.* [2009], we consider a parametrized function of time to describe the evolution of the interferometric phase. This function is the linear combination of a set of user-defined functions f_n of time modulated by coefficients a_n , such as the interferometric phase ϕ_i at a time t_i writes

$$\phi_i = \sum_{n=1}^N a_n f_n(t_i) + \gamma_i, \quad (2.2)$$

where γ_i is the error corresponding to mismodeling of the interferometric phase at time t_i , due to limitations of the functional model and decorrelation noise [Agram and Simons, 2015]. Uncorrected atmospheric effects, such as turbulent and ionospheric delays, are the main

contributions to γ_i [e.g. *Doin et al., 2011; Jolivet et al., 2014a*]. In the following, we assume that γ_i is normally distributed with a zero mean and a standard deviation σ_γ , assumed constant with time for simplicity. Functions f_n can be taken for instance as polynomial terms, Heaviside functions or periodic functions describing the time history of the interferometric phase.

OUR GOAL is to solve both Equations 2.1 and 2.2 sequentially, whenever a new acquisition allows to compute new interferograms. We formulate an assimilation framework solving for the interferometric phase ϕ_i at each acquisition time t_i and for the terms of the parametrized function a_k and for the corresponding variances and covariances.

2.2.2 Formulation and set-up

Symbol	Meaning	Structure	Shape
\mathbf{m}_k	state vector	$[a_0, a_1, \dots, a_{L-1}, \phi_0, \dots, \phi_k]$	$(L + k + 1)$
\mathbf{d}_k	measurement vector	$[\Phi_{fk}, \Phi_{gk}, \dots, \Phi_{hk}]$	N
\mathbf{P}_k	state covariance	–	$(L + k + 1) \times (L + k + 1)$
\mathbf{Q}_k	process noise covariance	diagonal matrix* with last element equal to $(\sigma_\gamma)^2$	$(L + k + 1) \times (L + k + 1)$
\mathbf{R}_k	observation noise covariance	diagonal matrix with $(\sigma_\epsilon)^2$ on the diagonal	$N \times N$
\mathbf{A}_k	state-transition matrix	identity matrix with additional row using a_n to forecast ϕ_k	$(L + k + 1) \times (L + k)$
\mathbf{H}_k	observation model	pairs up the phases to build the Φ_{ik} . Contains 0, 1 and -1	$N \times (L + k + 1)$

Table 2.1: Vectors and matrices used in the k^{th} KFTS iteration assimilating N interferograms (Φ_{ik}) constructed with the acquisition at time t_k . At this given step, the filter (re)estimates the $N + 1$ phases $\phi_{i,k}$ and the L parameters a_n of the linear descriptive model. (*) In our applications, diagonal elements of \mathbf{Q}_k are zero except the last one, however, it may be useful to add non-zero systematic error in the first L elements corresponding to a_n . See Appendix A.2 for a detailed example of our KFTS matrices.

A KALMAN FILTER is an iterative procedure that allows to recover the least squares solution of an inverse problem by successively adding data. For a recent and detailed introduction to Kalman filtering, readers can refer to *Evensen [2009]* or *Carrassi et al. [2018]*. Data assimilation procedures propagate and update with newly acquired data the probability density function (PDF) of a given model. In a Kalman filter, the PDF of the model is a Gaussian distribution described by a state vector, \mathbf{m} , containing mean values for model parameters and the associated covariance matrix \mathbf{P} . Each time new data is acquired, a Kalman filter proceeds in two successive steps.

First, at a given time t_k , we forecast the state vector \mathbf{m}_k and its covariance matrix \mathbf{P}_k using the state vector, \mathbf{m}_{k-1} , at step $k - 1$. Second, we update this forecast with the information from data acquired at time t_k in a step called analysis.

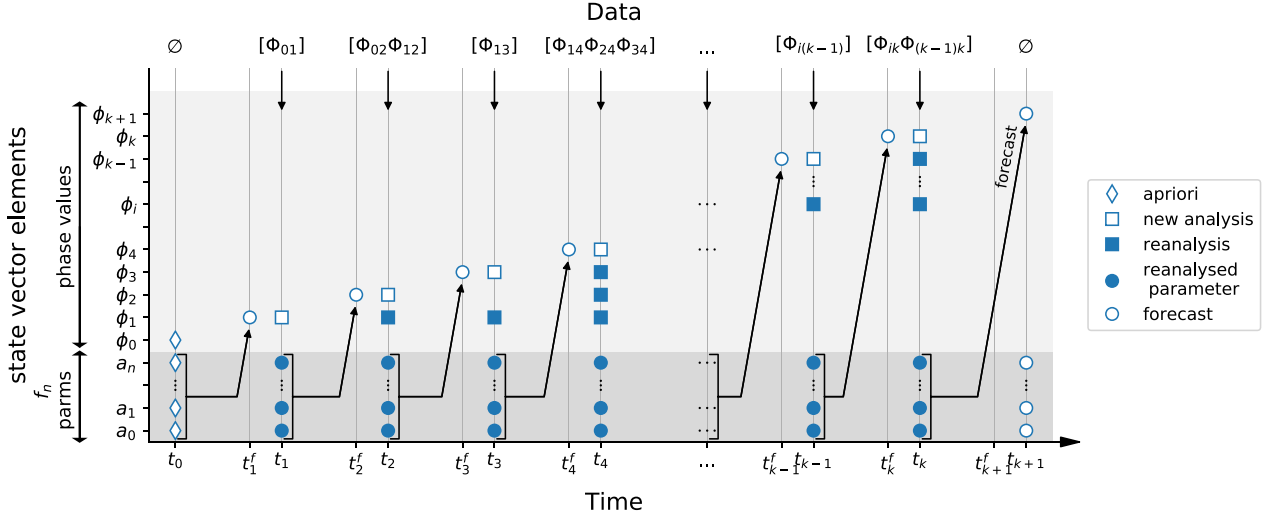


Figure 2.1: Scheme of the temporal evolution of the state vector as a function of assimilation time and available data. Markers highlight elements which are added or modified at a specific time-step. Additional values may be kept and stored for later reanalysis. The last step corresponds to the case when data are not available: the previous state vector is copied and the last phase is forecast using the functional description described by the parameters a_n previously estimated.

IN PRACTICE, at a time t_k , the state vector \mathbf{m}_k includes the reconstructed phase values and the coefficients of the parametrized function of time, a_n (Figure 2.1). We initialize the framework with an *a priori* state vector, \mathbf{m}_0 and associated covariances, \mathbf{P}_0 . This *a priori* reflects our state of knowledge on the different parameters before we input any data. Each time a new SAR image is acquired, we compute the interferograms connecting this last acquisition with previous ones, typically the four previous ones. Then, we use the functional form governed by the terms a_n in the current state vector to forecast the phase at the time of the new acquisition. Afterwards, we analyze the forecast with the information of the incoming data to obtain the updated state vector.

FOLLOWING the marginalization rule, the forecast state vector \mathbf{m}_k^f and its covariance \mathbf{P}_k^f are given by

$$\mathbf{m}_k^f = \mathbf{A}_k \mathbf{m}_{k-1} \quad \text{and} \quad \mathbf{P}_k^f = \mathbf{A}_k \mathbf{P}_{k-1} \mathbf{A}_k^T + \mathbf{Q}_k \quad \forall k \in [1; M] \quad (2.3)$$

where \mathbf{A}_k is the state-transition matrix and \mathbf{Q}_k the process noise covariance (see Table 2.1 for variable description). As illustrated in Figure 2.1, \mathbf{A}_k applied to \mathbf{m}_{k-1} computes the forecast for \mathbf{m}_k based on the latest parametric description of the time series given by a_n at time t_{k-1} (Equation 2.2). \mathbf{A}_k is a matrix representation of the forecast equations. In practice, phase terms of previous acquisitions and functional parameters are kept constant while ϕ_k^f is computed using Equation 2.2. Because \mathbf{A}_k is of rectangular shape, \mathbf{m}_k^f is simply \mathbf{m}_{k-1} augmented with the forecast phase value of the most recent acquisition. The corresponding covariance, \mathbf{P}_k^f , depends on parameter uncertainties and

systematic noise included in \mathbf{Q}_k . Systematic noise in \mathbf{Q}_k represents our level of confidence in an imperfect forecast.

We then update the state and its covariance using the available data \mathbf{d}_k at time t_k applying Bayes' rule, so that

$$\mathbf{m}_k = \mathbf{m}_k^f + \mathbf{P}_k^f \mathbf{H}_k^T \left(\mathbf{R}_k + \mathbf{H}_k \mathbf{P}_k^f \mathbf{H}_k^T \right)^{-1} \left(\mathbf{d}_k - \mathbf{H}_k \mathbf{m}_k^f \right) \quad (2.4)$$

where \mathbf{R}_k is the observation noise covariance, and \mathbf{H}_k the observation model. \mathbf{H}_k is effectively the operator predicting interferograms from the state vector \mathbf{m}_k . \mathbf{R}_k describes our confidence in the observation model, \mathbf{H}_k , for the data \mathbf{d}_k (hence, \mathbf{R}_k describes the statistics of phase misclosure, here assumed normally distributed). The analyzed variance covariance matrix, \mathbf{P}_k , is

$$\mathbf{P}_k = \mathbf{P}_k^f - \mathbf{P}_k^f \mathbf{H}_k^T \left(\mathbf{R}_k + \mathbf{H}_k \mathbf{P}_k^f \mathbf{H}_k^T \right)^{-1} \mathbf{H}_k \mathbf{P}_k^f. \quad (2.5)$$

The term $\mathbf{P}_k^f \mathbf{H}_k^T \left(\mathbf{R}_k + \mathbf{H}_k \mathbf{P}_k^f \mathbf{H}_k^T \right)^{-1}$ is often referred to as the Kalman gain as it quantifies how much the predicted state "has to gain" from the difference between observed and predicted data, $\mathbf{d}_k - \mathbf{H}_k \mathbf{m}_k^f$, called residual or innovation. It also modulates the information transitioning from the covariance in the model space $\mathbf{H}_k \mathbf{P}_k^f$ to the covariance of the analysis. For a practical example of our Kalman filter time series analysis (KF-TS), see the explicit formulation in Appendix A.2. Note that Equation 2.4 is the generalized least squares solution of a linear inverse problem [e.g. *Tarantola, 2005*].

BECAUSE OF OBSERVATIONS equations, there is a need to keep previous estimates of phases in \mathbf{m}_k , whenever they are connected by interferograms used in the analysis step, in order to update phases ϕ_i ($i < k$) for all Φ_{ik} in \mathbf{d}_k (Eqn. 2.1 and Fig. 2.1). For instance, if the data contains interferograms Φ_{ak} , Φ_{bk} and Φ_{ck} we will forecast and analyze ϕ_k and re-analyze ϕ_a , ϕ_b and ϕ_c using past and current observations (Figure 2.1). This is essential to keep improving phase estimates taking advantage of the redundancy of information from all interferograms and, thus, limit the propagation of errors over time. Formally, the re-analysis of past estimates with future data implies that the Kalman filter formulated above is effectively a Kalman smoother [*Cohn et al., 1994; Cosme et al., 2012*].

2.2.3 Configuring parameters

THE ALGORITHM REQUIRES user-based choices for the parametrization of the functional form and for the various covariances on a case-by-case basis. First, we have to choose a parametrization for the functional form used to derive the forecast. This choice is based on our knowledge of deformation and simplicity of the model should be favored over precision to prevent overfitting.

Second, we need to estimate the typical standard deviation of mis-modeling σ_γ for all time steps and of interferometric network mis-closure σ_ϵ for all interferograms. σ_ϵ comes in the construction of \mathbf{R} because it quantifies the error between our data (interferograms) and what we are looking for (the relative phase values). It effectively acts as a regularization term when computing the Kalman gain (Table 2.1 and Equations 2.4,2.5). As underlined by *Doin et al.* [2011], covariance terms in \mathbf{R} are null because ϵ_{ij} is specific to each interferogram Φ_{ij} , independently of the common acquisitions $\phi_{i,j}$. Regarding σ_γ , it depends on both the simplicity of the chosen functional form and on the amplitude of unexpected atmospheric perturbations of the interferometric delay. It is directly fed into the process noise variance-covariance matrix, \mathbf{Q} , since it controls the flexibility given to the process for phase values to be different from those predicted by the chosen functional form. Typically, σ_ϵ should be small with respect to σ_γ because we have greater trust in the interferogram construction (Equation 2.1) than in the functional description of the deformation (Equation 2.2).

Third, we must quantify the *a priori* mean and standard deviation of functional model coefficients a_n within the initial state vector \mathbf{m}_0 and covariance \mathbf{P}_0 . These values directly control the amplitude of the possible values for model coefficients in the analyzed state vector, and, thus, directly affect the quality of the filter's forecast. One needs to chose large enough variances with a realistic *a priori* state vector, so that the natural spread of the variable is within one standard deviation of its mean.

Fourth, we can optionally add some systematic error to the parameters of the functional representation, a_n in the L first elements of the diagonal of \mathbf{Q} in order to slow down their convergence with assimilation steps. Such noise addition introduces some plasticity in the description of deformation (see Appendix A.2). We discuss real case examples below to illustrate the influence of the different parameters and define a quantitative guideline for parametrization in Section 2.4.1.

2.3 Applications of the Kalman filter time series analysis (KFTS)

2.3.1 Synthetic tests

2.3.1.1 Reference case set-up

IN ORDER TO asses how well KFTS retrieves known parameters, we generate a synthetic set of InSAR data combining synthetic signal of tectonic deformation and atmospheric noise. We assess the influence of the choice of parameters and of the design of covariance matrices to validate the approach.

We build a two dimensional, time varying, field of phase change typical of what is expected in a region crossed by a major tectonic

fault. We design a synthetic acquisition planning considering a 3 years observation period with acquisitions every 12 days; similarly to what is expected for recent satellite constellations such as Sentinel 1. For each of these synthetic acquisitions, we compute synthetic unwrapped interferograms with the three preceding acquisitions using Equation 2.1.

WE SIMULATE the contributions of tectonic plate motion and shear due to interseismic loading along a fault (i.e. slow, persistent deformation of a few cm/yr), between blocks moving at 4 cm/yr with respect to each other. We add to the time series the surface displacements due to a typical earthquake (i.e. a discrete, large amplitude deformation event of several cm). The modeled earthquake occurs on day 500 of the time series and induces a maximum of 15 cm of displacement. In addition, we consider the case of a slow transient slip event occurring on the same fault (i.e. episodic, medium amplitude deformation spanning multiple acquisitions in time). This slow slip event has a temporal footprint governed by an integrated spline function of 100-day-width centered on day 210 of the time series, with a maximum cumulative displacement of 10 cm. Epicenters of both events are shown on Figure 2.2. All synthetic displacements are generated considering dislocations embedded in an elastic homogeneous semi-infinite halfspace [Okada, 1992]. Furthermore, we include a constant deformation rate related with interseismic loading on the main fault and seasonal oscillations (i.e. yearly sinusoidal deformation with a phase shift) of the ground everywhere. In the following tests, we aim to recover all terms of deformation described above as well as the resulting phase evolution with KFTS.

CONSEQUENTLY, the chosen parametrized model of the phase, ϕ_k , at a

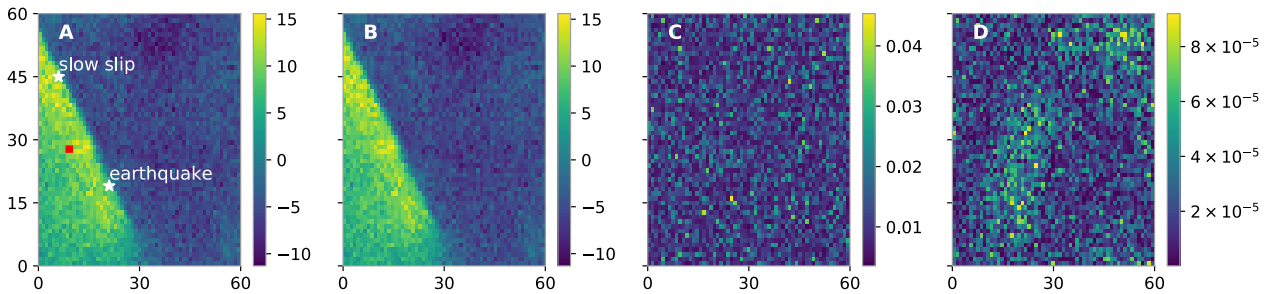


Figure 2.2: Performance of the Kalman filter time series analysis (KFTS) for a two-dimensional synthetic deformation field. The phase evolution with its noise content is retrieved from noisy interferograms (i.e. non-zero network misclosure). *A* : True cumulative phase at the last time-step of the time series including deformation and correlated and uncorrelated noise. *B* : Reconstructed cumulative phase from KFTS. *C* : Root Mean Square error (RMS) of the the retrieved phase (*B*) with respect to the true phase value (*A*). *D* : RMS of the phase retrieved with KFTS (*B*) with respect to the least-squares solution. All scales are in centimeters to ensure the example represents a realistic case study. The location of the pixel of interest for Figure 2.3 is marked by a red square.

time t_k , is

$$\begin{aligned} \phi_k = & a_0 + a_1 t_k + a_2 \sin\left(t_k \frac{2\pi}{T_{year}}\right) + a_3 \cos\left(t_k \frac{2\pi}{T_{year}}\right) \\ & + a_4 S_{sse}(t_k) + a_5 H_{eq}(t_k) + \gamma_k, \quad (2.6) \end{aligned}$$

where $a_n, \forall n \in [1, 5]$, are the parameters to be solved for, T_{year} is a one year period, S_{sse} is an integrated spline function centered on day 210 with a width of 100, H_{eq} is a Heaviside function on day 500 and γ_k is the mismodeling term at time t_k with standard deviation σ_γ .

WE FIRST TEST the performance of the filter on synthetic data without any noise (implying $\gamma_k = 0, \forall k$) and then on data including noise. To do so, we design a composite noise model to mimic real observations. This implies that we have, first, a spatially correlated noise reflecting atmospheric effects on each phase "acquisition" and, secondly, a misclosure error lower by at least an order of magnitude, assuming that we have no contribution from unwrapping errors [Schmidt and Bürgmann, 2003; Lohman and Simons, 2005; Cavalié et al., 2007; López-Quiroz et al., 2009; Agram and Simons, 2015]. We add spatial and temporal deviations to all parameters a_n following a random distribution with a standard deviation equal to 10% of their values, and random noise on interferogram construction equivalent to $\sigma_\epsilon = 0.1$ mm. Moreover, the atmospheric contribution to phase decorrelation is constructed through the convolution of a white noise, with standard deviation of 10 mm, and a decreasing exponential function of inter-pixel distances [Jolivet and Simons, 2018]. The specified values reflect errors observed in processed Sentinel 1 data (see Section 2.3.3). The resulting cumulative phase change after 3 years is shown in Figure 2.2. The temporal evolution of phase change for one pixel is visible in Figure 2.3.

2.3.1.2 Performance with optimal configuration

WE APPLY KFTS with the assumption that the functional form given in Equation 2.6 is known. Results for simpler functional forms applied to the same synthetic data are in Figure A.3 and A.4. *A priori* model parameters in the initial state vector, \mathbf{m}_0 , are set to zero with standard deviations comparable to the expected spread of parameters: 10 mm for a_0 , 0.05 mm/day for a_1 , 5 mm for the *sine* and *cosine* amplitudes and 70 mm for the displacement of slip events. The first phase value for all pixels is set to zero with zero uncertainty. This means that \mathbf{m}_0 is a null vector and \mathbf{P}_0 is a diagonal matrix containing the squared standard deviations listed above. When realistic noise is considered, we chose optimal parameters corresponding to the noise implemented in the synthetic data, that is $\sigma_\gamma = 10$ mm and $\sigma_\epsilon = 0.1$ mm. For comparison, we solve the full problem for all acquisitions using an equivalent least squares inversion with identical model and data covariances [Tarantola, 2005].

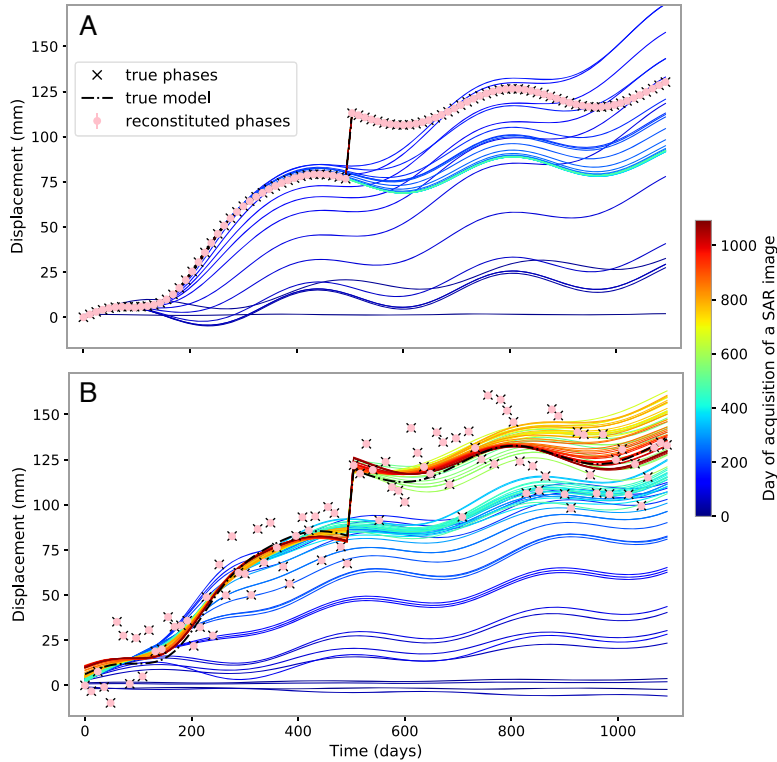


Figure 2.3: Time series for one pixel with temporal evolution of the model on a synthetic set of InSAR data for one pixel. *A* : case without noise in the synthetic data. *B* : same synthetic deformation but with a realistic noise model on top. Pink markers represent reconstituted phases from the Kalman filter, while black crosses are "true" phases. When the phase is well retrieved, markers overlay each other and errorbars are too small to appear. Colored lines are models derived at each assimilation of a new acquisition, which date is indicated by the colorbar. Dashed black line is the true deformation. In *A*, true and reconstituted phases lie on each other and mask the underlying curves, which include the true model and computed models after day 500 (time of the modeled earthquake).

For a model without any noise (except $\sigma_\epsilon = 10^{-5}$ mm to avoid singularity of the gain), phase values are retrieved within σ_ϵ and model parameters converge after the assimilation of ~ 6 months of data (Figure 2.3A). The time required for convergence of the model parameters is justified by the fact that there is an ambiguity between the contribution of the linear and periodic terms to the deformation before reaching half the oscillation period. Regarding the earthquake, the corresponding amplitudes is found within 10^{-5} mm just after it occurred. Similarly, the amplitude of the slow slip event is retrieved once the total cumulative displacement caused by the slow slip event has been fully assimilated.

THE FINAL OUTCOME of KFTS is comparable with basic least squares performance (Figure 2.2 and 2.4). Figure 2.2 shows that the KFTS cumulative displacement root mean square error (RMS) with respect to the true displacement is on the order of σ_ϵ (0.1 mm), while it is of $\sim 10^{-5}$ cm with respect to least squares estimation. Regarding model parameters, the difference between KFTS solution and target value is of ~ 1 mm, whereas it is of $\sim 10^{-3}$ mm between KFTS and least squares solutions. The noticeably large noise in retrieved parameters over areas with target values close to zero (Figure 2.4) is explained by the constant high *a priori* variance applied everywhere. Thus, if the location of the events is known, it is preferable to define a spatially variable *a priori* variance for, at least, slip events.

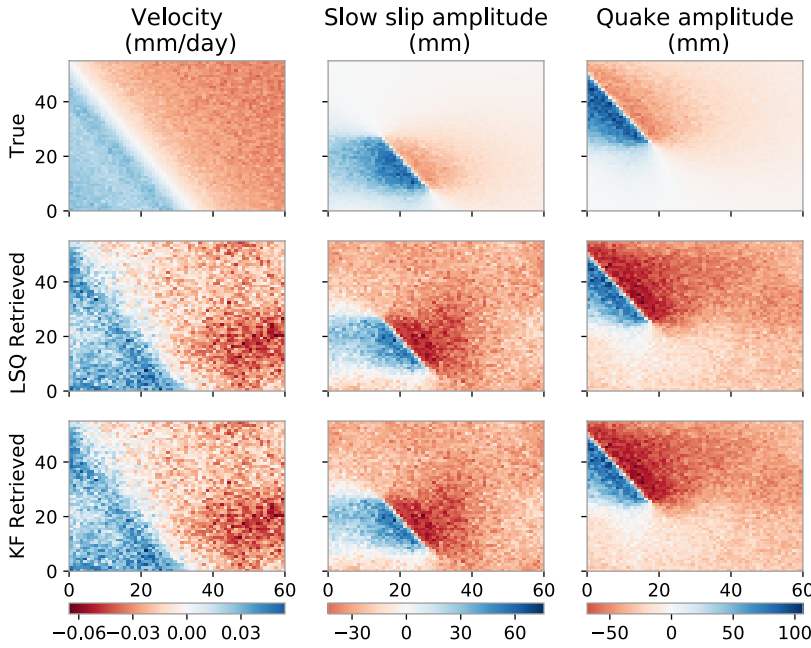


Figure 2.4: Maps of three of the model parameters : velocity, slow slip amplitude and quake amplitude. For comparison the true values (top), the values retrieved through least squares inversion (LSQ) (middle) and the values retrieved through our Kalman filter (bottom) are displayed.

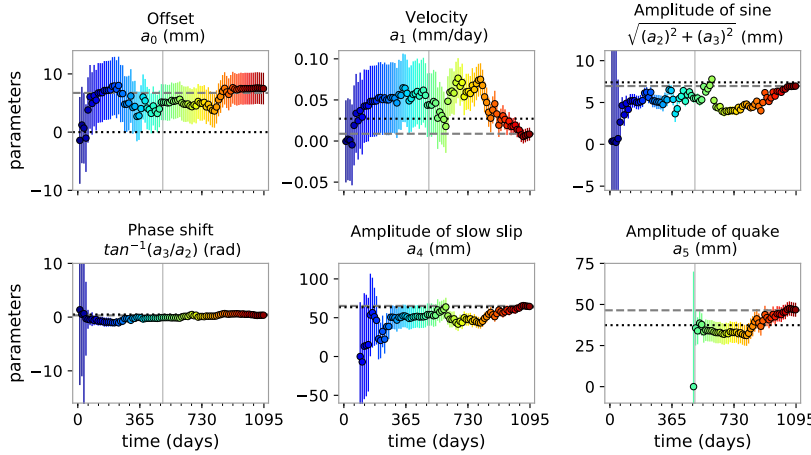


Figure 2.5: Temporal evolution of model functional parameters at each assimilation step for the reference pixel in our synthetic test. Colors refer to time (see colorbar in Figure 2.3). The amplitudes of the slow slip and the quake are added in the parameter space just before they occur. For reference, the dotted black line shows the true parameter value (i.e. target), and the dashed grey line shows the least-squares optimum. The Kalman filter solution tends toward the least-square solution, which itself depends on the interferometric network configuration and the noise in interferograms.

WE DETAIL HERE the behavior of the filter as data is assimilated in time and the requirements for convergence. Figure 2.3B shows the time series of a representative pixel (located on Figure 2.2) and Figure 2.5 the associated evolution of model parameters. The functional model evolves and gains information as data are successively assimilated. Graphically, the dark blue curves combine both the *a priori* null model and the little information brought by the first few points, while the dark red curve uses all available information and closely fits the underlying model. The model progressively converges toward the least squares solution, close to the target model, at a rate that depends on how quickly parameter uncertainties collapse (Figures 2.3B and 2.5), which in turns depends on the Kalman gain (Equation 2.5, Appendix A.2). As shown on Figure 2.5, it takes about 150 days for the offset, a_0 , to be adjusted and around one year for the yearly periodic signal, a_2 and a_3 . However, the inter-dependency of functional param-

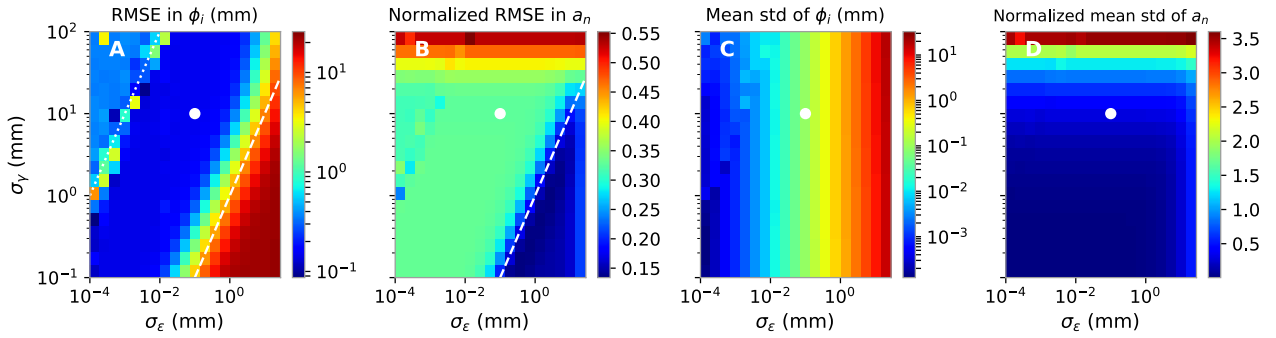


Figure 2.6: Errors in estimated model parameters (a_n) and phases (ϕ_i) from the Kalman filter time series analysis (KFTS) as a function of the standard deviation of the mismodeling noise (σ_γ) and the standard deviation of interferometric network misclosure (σ_ϵ). The true value of the noise injected in the build of the synthetic deformation is marked by the white circle. *A* and *B* reveal variations in the KFTS estimate accuracy by looking at the Root Mean Square Error (RMSE) in ϕ_i (*A*) and in a_n (*B*). *C* and *D* display the mean standard deviation (abbrv. std) of estimates. Values concerning parameters are normalized for homogeneity. The white dashed line corresponds to $\sigma_\gamma/\sigma_\epsilon = 1$ and the dotted line to $\sigma_\gamma/\sigma_\epsilon = 10^4$.

eters clearly appears as variations in the transient event amplitude a_4 induces a change in a_0 by 1-2 mm and the earthquake at $t = 500$ days perturbs almost all parameters, including the velocity which is shifted by ~ 0.01 mm/day. Correlations between parameters appear in the off-diagonal terms of the covariance matrix (Figure A.2).

INTERESTINGLY, we also see that, although the local earthquake amplitude a_5 of 37.4 mm was correctly retrieved after 3 assimilations ± 7 mm, the assimilation steps for $t > 750$ days lead to an overestimate of a_5 and a correlated underestimate of a_1 . As interferograms long after the event do not bring information about its amplitude, the state vector \mathbf{m}_k needs to be modified. That is, to avoid fitting noise and limit trade off between parameters, functional parameters in \mathbf{m}_k can be added or removed from the procedure when relevant. Also, phases which do not appear in latter interferograms can be stored and removed from \mathbf{m}_k . This does not affect final time series and lowers the memory load of the algorithm. Practically, KFTS effectively works with two storage files : one containing time, phases and their uncertainties (from the diagonal of \mathbf{P}_k) and another one containing \mathbf{m}_k , \mathbf{P}_k and other auxiliary information in order to run the next forecast and analysis at time t_{k+1} .

Nevertheless, it is a challenge to optimally parametrized the inversion with real InSAR data, especially because mismodeling and misclosure errors are generally not known [Schmidt and Bürgmann, 2003].

2.3.1.3 Sensitivity analysis to predefined errors

WE STUDY the effect of non-representative σ_γ and σ_ϵ in a sensitivity analysis, for one given pixel (shown in Figure 2.5 and 2.3). We deliberately set poorly chosen values of σ_γ and σ_ϵ in KFTS with respect to the known sources of noise. Subplots of Figure 2.6 display how 4 proxies of the quality of KFTS estimates vary as a function of those two param-

eters. While Figures 2.6A and 2.6B consider the error in the absolute estimates, and thus the accuracy, Figures 2.6C and 2.6D indicate the precision (i.e. standard deviation) associated with those estimates.

The quantity displayed in 2.6A is the Root Mean Square error of phase estimates, and in 2.6C it is the average of the posterior standard deviation of the phase estimates, σ_{ϕ_k} . The exact equations corresponding to fields in 2.6B and 2.6D are

$$\sqrt{\frac{1}{L} \sum_{n=1}^L \left(\frac{a_n - a_n^t}{a_n^t} \right)^2} \quad \text{and} \quad \frac{1}{L} \sum_{n=1}^L \frac{\sigma_{a_n}}{|a_n|}, \quad (2.7)$$

respectively, where the superscript t indicates target value and L is the number of parameters. The first functional model parameters a_0 , a constant offset, is voluntarily excluded because, first, $a_n^t = 0$ and, second, the misfit in a_0 mainly results from the requirement that $\phi_0 = 0$.

AS EXPECTED from governing equations, we see that estimated standard deviations are directly impacted by choices in σ_γ and σ_ϵ . Indeed, phase uncertainties appear sensitive to σ_ϵ and model parameter uncertainties to σ_γ (Figure 2.6C, 2.6D). Another main feature is the improvement of a_n estimates at the expense of the accuracy in ϕ_k when approaching the domain $\sigma_\epsilon \geq \sigma_\gamma$ (Figures 2.6A, 2.6B). This is clearly not desirable, because phase estimate directly derive from interferometric data, while model parameters depend on an *ad hoc* functional description which may have to be improved as new data is assimilated. To the contrary, when too much confidence is given to interferograms with respect to the model (i.e. $\sigma_\epsilon \leq \sigma_\gamma \times 10^{-4}$) the effective misclosure error means that data may be hard to reconcile together and numerical instability arises. Thus, providing $\sigma_\epsilon/\sigma_\gamma$ is in between 10^{-4} and 1 , the quality of ϕ_k and a_n estimates appears robust to several orders of magnitude variations in σ_γ and σ_ϵ . We still observe an upper bound limit of ~ 30 mm and ~ 15 mm for σ_γ and σ_ϵ , respectively, above which estimates are so uncertain that they do not adjust to the data. Time series representative of the overall effect of underestimating or overestimating σ_γ and σ_ϵ are shown in supplementary Figures (A.5-A.8).

In practice, ϵ_{ij} only results from how we construct interferograms and could be directly estimated by quantifying the effect of multilooking and filtering during the processing of each interferogram. Alternatively, it could be measured either before time series analysis by forming triplets of interferograms [De Zan *et al.*, 2015; Benoit *et al.*, 2020] or *a posteriori* by looking at the discrepancy between real and reconstituted interferograms from time series [Cavalié *et al.*, 2007].

IN ADDITION TO uncertainty quantification, another challenge of real InSAR data is that all interferograms do not unwrap everywhere due to local loss of coherence. Consequently, given pixels will potentially show missing links in the interferometric network. In the following

we apply KFTS to two data sets thought to be representative of the challenges brought by real InSAR data.

2.3.2 Application to the Etna Volcano on Envisat Asar images

AS A REAL case example, we first present the assimilation of interferograms over the Etna volcano in Sicily. We have chosen this example as it has been used in the past for multiple validation studies [e.g. *Doin et al., 2011; Jolivet et al., 2014a*] and because several GNSS stations record the relatively large displacements observed over this volcano. We use 63 images from the ENVISAT mission acquired between January 2003 and August 2010 [*Doin et al., 2011*]. Single Look Complex (SLC) images are focused and coregistered to a single master using the Repeat Orbit Interferometry Package [ROIPac, *Rosen et al., 2004*]. Coregistration to a single master image is enhanced using the Digital Elevation Model and all possible interferograms are derived. The 222 interferograms are filtered and unwrapped using a branch cut algorithm [*Goldstein et al., 1988; Goldstein and Werner, 1998*]. We correct interferometric phase delays due to the temporal variations of the stratified troposphere using the output of the ERA-Interim reanalysis of atmospheric data as described in *Jolivet et al. [2011]*. All details about the processing can be found in *Doin et al. [2011]* and in *Jolivet et al. [2014a]*.

We apply KFTS on each pixel of the stack of images that has unwrapped interferometric data. In addition to the precise retrieval of phase evolution, we aim to obtain a mean rate of deformation, including potential transient events and ignoring seasonal contributions. Hence, our parametrized model for the phase evolution includes linear and seasonal terms described by four parameters, a constant term, a rate of phase change, a sine term and a cosine term. This model is very simplified for a volcano which has undergone several eruptive events over 2003-2010. Although this may lower our predictive capabilities, phase estimates of uninterrupted interferometric network should not be affected and more complex model could be applied in a second time (Section 2.3.1). Consequently, we set $\sigma_\gamma = 18$ mm and $\sigma_\epsilon = 0.01$ mm, as a high σ_γ with respect to σ_ϵ limits the confidence in the model-based phase forecast and keeps large uncertainties for model parameters. With the same logic, we chose *a priori* standard deviation equal to 15 mm for the constant term, 5 mm/day for velocity and 10 mm for *sine* and *cosine* terms. We set the initial state vector \mathbf{m}_0 to zeros. Note that, because the constant term reflects the noise in the reference acquisition (ϕ_0) with respect to the model, its standard deviation should be close or superior to σ_γ . The impact of different σ_γ and \mathbf{P}_0 on model parameter estimates is displayed in Figures A.12-A.14.

WE COMPARE local time series of displacement derived from Global Navigation Satellite System (GNSS), often referred to as GPS for sim-

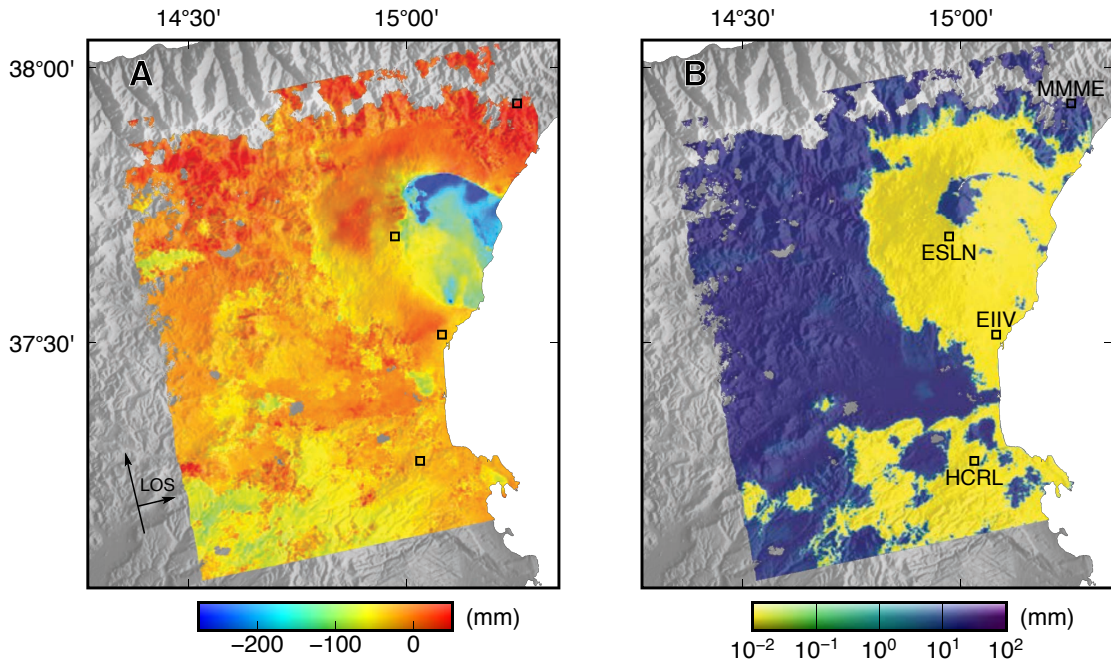


Figure 2.7: *A*: Map of cumulative phase change between 2003 and 2010 over Mt Etna (Sicily, Italy) as inferred from the Kalman filter time series analysis applied on ENVISAT data. *B*: Map of the associated standard deviation. Displacements and associated uncertainties are in the direction of the satellite’s line of sight (LOS). Topography, shown in the background in shades of gray, is from SRTM [Farr *et al.*, 2007]. Holes in the data correspond to pixels excluded from the inversion because less than 20 interferograms were unwrapped at their location. Black squares show a selection of GPS station used for comparison [Blewitt *et al.*, 2018].

plicity, at the stations EIIV, ESLN, HCRL and MMME (Figures 2.7 and 2.8; Blewitt *et al.* [2018]). We consider differential displacements between two GPS stations and the equivalent closest InSAR pixel. Figure 2.7 shows the cumulative phase change and associated uncertainties over 8 years in the direction of the Line Of Sight (LOS) of the satellite as derived by KFTS at t_{61} , 14 July 2010. The displayed penultimate phase ϕ_{61} incorporates most of the studied deformation with limited uncertainty as it is a reanalyse phase, unlike the last phase.

STANDARD DEVIATIONS in Figure 2.7B are marked by a clear spatial dichotomy between the well resolved pixels displaying uncertainties $< 10^{-1}$ mm and other pixels with uncertainties reaching more than 10 mm. Precise estimates are available on the volcano flanks and in the urbanized region to the south, notably around stations ESLN, EIIV and HCRL and, thus, cover the area of geophysical interest. In Figure 2.7A, the displacement field is dominated by aseismic slip along the Pernicana fault extending from the volcano summit to the eastern coast of Sicily [Palano *et al.*, 2006]. Indeed, the fault slipped more than 25 cm locally in the LOS direction over the ~ 8 years covered by the time series. Smaller coherent displacements of a few cm on the volcano flanks are also recovered. In the plains surrounding Mt Etna, cm-scale uncertainties are associated with about ± 2 cm of sharp inter-pixel variations in the displacement field.

Large uncertainties arise in area where more than 50% of interfer-

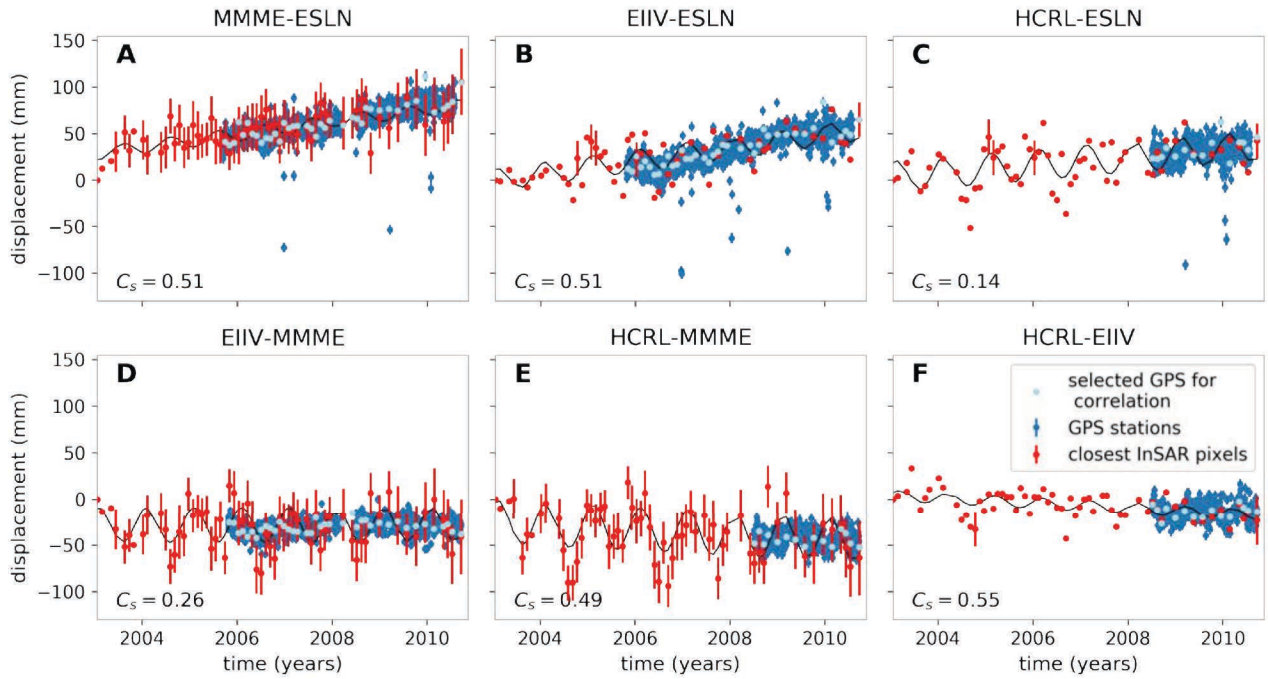


Figure 2.8: Overlay of GPS and InSAR time series of relative deformations. Each subplot includes the complete time series and its uncertainty for InSAR (red dots) and the available GPS time series on the same time period (blue dots). The subplot titles indicate the pair of stations located in Figure 2.7. The GPS data point that are temporally the closest to InSAR measurements are highlighted in light blue. They are used to compute the Spearman correlation coefficient, C_s (Equation 2.8). The black line is the deformation according to the functional model of the Kalman filter on InSAR.

ograms do not unwrap due to significant spatial noise (Figure A.11). When a pixel is not unwrapped, no information is available at this location and the analysis step of the filter cannot be performed. In this configuration, the forecast made from the functional model is taken as the estimate with its large uncertainty (i.e. $\mathbf{m}_k = \mathbf{m}_k^f$ and $\mathbf{P}_k = \mathbf{P}_k^f$). This allows to continue building the time series and to connect different subsets of interferograms which may not be linked by a common phase. However, the error associated with the forecast phase is carried forward in the subsequent solutions, if they are all relative to this one. A solution to lower uncertainties is to re-reference the phases by constructing long-baseline interferograms.

TIME SERIES in Figure 2.8 evidence that the relative InSAR displacement between pixels close to GPS stations is consistent with what is measured independently by GPS. A measure of the monotonicity of this relationship is given by the Spearman's rank correlation coefficient for n pairs of InSAR-GPS observations, defined as

$$C_s = 1 - \frac{6}{n(n^2 - 1)} \sum_{i=1}^n d_i^2 \quad (2.8)$$

where d_i is the difference between the ranks of the i^{th} coeval observations in both sets. This metric was preferred over other correlation coefficients because of its little sensitivity to outliers. For the 6 differ-

ential displacements considered, C_s is always positive indicating that when InSAR measures an increase, so does GPS (Figure 2.8). Moreover, its value close to 0.5 for 4 time series reveals a significant numerical correlation. Nonetheless, the implications of this metric are limited because it is applied to the subset of GPS measurement coincident in time with InSAR acquisitions and both time series are affected by different sources of noise. Independently of the numerical correlation, the overall good match between measured velocities validates our KFTS approach for InSAR time series analysis, even when the quality of data implies that errors are large (Figure 2.8A, 2.8D and 2.8E).

2.3.3 Application to the Chaman fault on Sentinel 1 images

IN THE FOLLOWING section, we illustrate the KFTS performance to reconstruct surface displacements around a tectonic fault imaged by a recent satellite constellation. The satellites of the Sentinel 1 mission launched in 2014 and 2015, are providing SAR images with a better temporal sampling than ever before for C-band satellites. Over the Chaman fault, we construct 364 interferograms with 95 acquisitions spanning November 2014 to May 2019. We use the ISCE package (Gurrola *et al.* [2010]; JPL/Caltech) to build unwrapped interferograms. We coregister SAR images with a network-based enhanced spectral di-

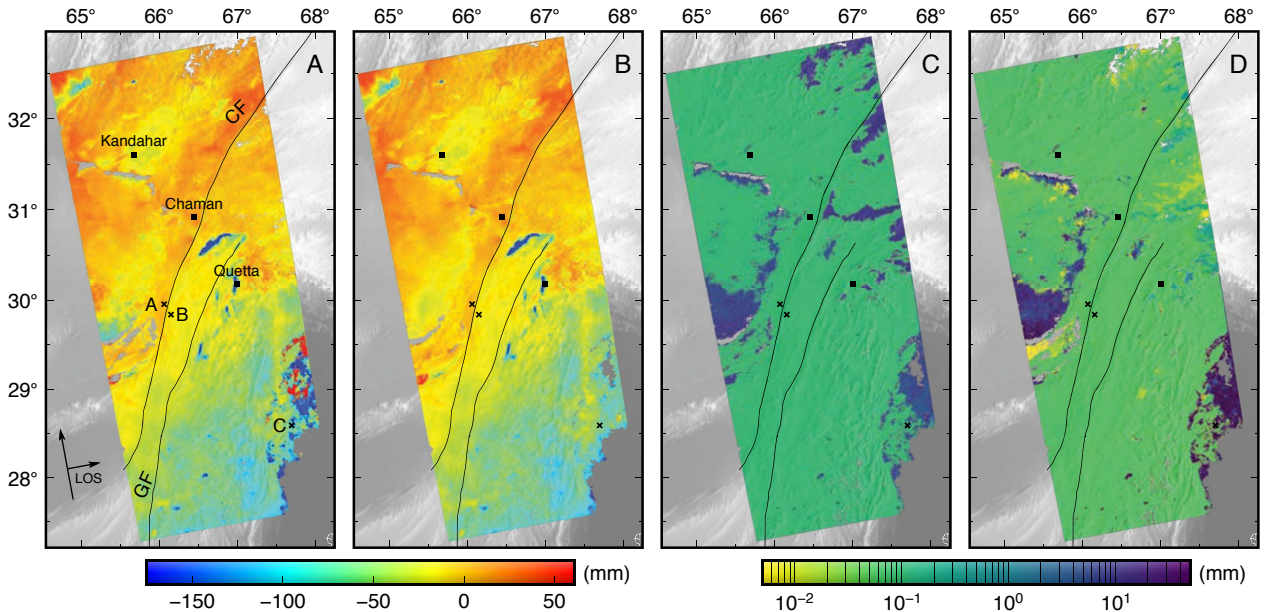


Figure 2.9: Maps of cumulative phase change between late 2014 and early 2019 over western Pakistan and southern Afghanistan from time series analyses applied on Track 42 data of Sentinel 1. *A*: Reference NSBAS solution, with labels of markers appearing in all subplots. *B* and *C*: Corresponding Kalman filter time series (KFTS) solution with its standard deviation. *D*: absolute difference between the NSBAS (*A*) and KFTS (*B*) solutions. Displacements and associated uncertainties are in the direction of the satellite’s line of sight. Two main faults of the region are the Chaman fault (CF) and the Ghazaband fault (GF) [Fattahi and Amelung, 2016]. The topography is shown in the background in shades of gray. Cities are marked by square markers. The three black crosses and letters locate the selected pixels in subplots of Figure 2.10.

versity (NESD) approach [Fattahi *et al.*, 2017] and remove atmospheric perturbations using ECMWF-ERA 5 global reanalysis of atmospheric data (PyAPS software; Jolivet *et al.* [2011, 2014a]). We also multilook and filter interferograms to enhance the signal-to-noise ratio before unwrapping with the branch cut method [Goldstein *et al.*, 1988; Goldstein and Werner, 1998]. The final size of the 2488×7024 pixels is $\sim 80 \times 130$ m. Additionally, we subtract to each interferogram a best fitting ramp (linear function of longitude and latitude) on the subregion north of the fault trace.

FOR COMPARISON, we perform the time series analysis with both the well tested New Small Baseline Subset method, NSBAS [Berardino *et al.*, 2002; Doin *et al.*, 2011] implemented in GIANt [Agram *et al.*, 2013], and KFTS developed here. We chose a simple functional description of deformation with a constant deformation rate and seasonal oscillations. A disadvantage of this model is that it poorly describes deformation for specific areas affected by earthquakes or anthropogenic groundwater pumping. However, because our implementation of NSBAS does not allow for spatial variations of the parametrized model, we prefer not to account for those very local dynamics (i.e. local in comparison with our 600 km long interferograms). Our *a priori* uncertainties are 25 mm for offset, 9 mm/yr for velocity and 8 mm for cosine and sine terms. In agreement with Section 2.3.1.3, we chose $\sigma_\gamma = 10$ mm and $\sigma_\epsilon = 0.05$ mm. Similarly to the previous example, we focus on the reconstructed phases with time rather than on its parametrized description and display maps of the penultimate phase of the time series (Figure 2.9).

FINAL SOLUTIONS from NSBAS and KFTS are very similar (Figure 2.9A and 2.9B). The displacement relative to the first acquisition shows a long-wavelength fault-perpendicular gradient of about 60 mm over ~ 120 km. We also observe strong negative signals with a kilometer scale footprint, such as around the city of Quetta, most likely due to aquifer-related subsidence. Moreover, there is a sharp contrast of displacement across the Chaman fault which reaches up to ~ 3 cm, notably in between labeled pixels A and B or across the northernmost segment, whereas no to little contrast is seen across the Ghazaband fault. This is consistent with Fattahi and Amelung [2016] in depth study of the region.

THE DIFFERENCE in phase reconstruction between both methods is smaller than 0.1 mm after the assimilation of ~ 4 years of data, except in areas where KFTS identified large uncertainty in the output with respect to the ± 0.05 mm precision (equal to σ_ϵ) valid for most pixels (Figure 2.9C and 2.9D). Mismatch between NSBAS and KFTS methods, as well as large uncertainties in phase and model parameters concentrate around the dune desert to the West and the Indus River plain in the South-East corner. There, rapid geomorphological

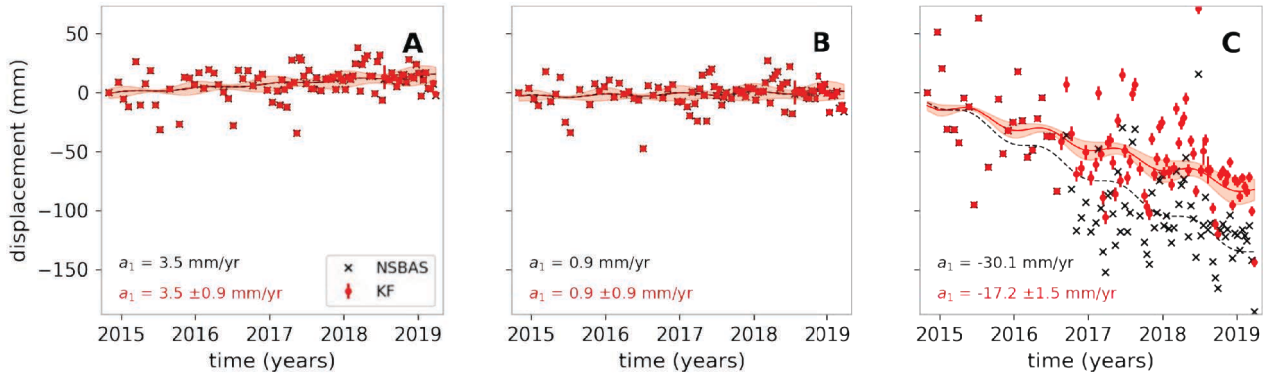


Figure 2.10: Time series for 3 selected pixels (indicated on Figure 2.9). Our Kalman filter time series analysis (KFTS) solution with associated standard deviation (red dots) is shown alongside the solution computed with the NSBAS method [Berardino *et al.*, 2002; Doin *et al.*, 2011]. Most of KFTS phase solutions have standard deviation too small to be visible. The corresponding functional models of deformation are also represented: dashed black curve for NSBAS and red line for KFTS. An idea of the spread of the models within one standard deviation of the KFTS solution is outlined by the red shaded area delimited by the parametrized phase evolution given $a_i \pm \sigma_{a_i}$ (Equation 2.2).

changes, seasonal oscillations and human activity impose a low interferometric coherence and, as a result, many interferograms could not be unwrapped there.

The concordance is also true at all time steps for every parameter of the state vector (displacements and functional model). Figure 2.10 presents three representative time series of deformation on single pixels. The two nearby pixels selected in Figure 2.10A and 2.10B exhibit highly correlated deformation with a spread of ~ 7 cm around the functional model. Phase estimation is precise with ± 0.05 mm and in good agreement with NSBAS estimations. For pixel A, the inferred velocity is found to be 3.5 ± 0.9 mm/yr in the KFTS or 3.5 in the NSBAS solution and, similarly, the seasonal amplitude and phase shift are 0.9 ± 1.2 mm and 0.7 ± 0.1 rad or 0.9 mm and 0.74 rad. Those functional descriptions agree with each other and the uncertainties given by KFTS are precious indicators of the model representativity and, thus, of the confidence in the resulting forecast.

THE TIME SERIES in Figure 2.10C exhibits large error bars of ~ 5 mm from mid-2016 arising from disconnected subsets in the interferogram network. In KFTS, the use of the functional model to forecast a disconnected phase and link subnetworks means that the model error propagates to subsequent phase estimations. The parametrized model of deformation differs sensibly between NSBAS and KFTS methods (Figure 2.10), by opposition to the very good agreement found between KFTS and least-squares for synthetic data (Figure 2.4). A first reason for this is the *a priori* on model parameters in KFTS, which effectively is a form of regularization leading to smaller velocity estimates of $a_1 = -19$ mm/yr instead of the physically unlikely -40 mm/yr for NSBAS. A second reason is that the NSBAS solution does not account for errors in model and data directly and instead attributes a weight to

phase fitting over model adjustment, so that Equation 2.2 only impacts phase values when interferometric connections do not allow an estimate with Equation 2.1 [Doin *et al.*, 2011]. By definition, this weight is similar to the ratio $\sigma_\epsilon/\sigma_\gamma$, and thus was set to 10^{-3} .

Therefore, KFTS can be applied to old, often sparse and incomplete data (ENVISAT) as well as to most recent and memory-consuming data which are collected nowadays (Sentinel 1).

2.4 Discussion

2.4.1 Guideline to choose parameters

EFFICIENT KFTS requires a sensible parametrization of the problem, with the definition of appropriate errors ($\sigma_\epsilon, \sigma_\gamma$), descriptive functional model ($f_n(t_k), \forall n$) and *a priori* knowledge on the model parameters in \mathbf{m}_0 and \mathbf{P}_0 (Section 2.2.3).

For the functional model, it is a good rule of thumb to start with a simple model, which includes a linear polynomial and an annual periodic oscillation. The innovation or residual term is key to assess the relevance of this parametrized model, as it quantifies the difference between the data and the information brought by the forecast (Section 2.2.2). If the model is appropriate the mean innovation at each time step should have a Gaussian distribution around zero on each pixel (e.g. subplots B,C versus D,E in Figure A.4). Thus, during the iterative process, checking the distribution of this mean innovation would help refine the parametrized model. Moreover, some source of deformation are *a priori* known and can be included. For instance, the displacements due to earthquakes affecting the study area can be easily included using a step function, which footprint is constrained by the location and timing of the event in seismic catalogs. To adapt to the diversity of applications of KFTS, other implemented functions include higher degree polynomials, hyperbolic tangent, exponential and logarithmic decay as well as basis spline.

FURTHER ASSUMPTIONS are required on the functional model when evaluating the *a priori* state \mathbf{m}_0 and covariance \mathbf{P}_0 . \mathbf{m}_0 and \mathbf{P}_0 define expected values of the multiplicative coefficients a_n to each functional element f_n . Assuming a_n terms are unknown, \mathbf{m}_0 is set to zero vector with a likely spread in the diagonal of \mathbf{P}_0 . Consequently, small \mathbf{P}_0 dims extrema as it is effectively a regularization term for a_n , while large \mathbf{P}_0 allows parameters to adjust freely to incoming data and stability might be lost (Figure 2.11, A.9, A.10 and A.13). In practice, the order of magnitude of *a priori* errors is determined using our physical knowledge about expected deformation. Higher values will be favored if little smoothing of the model is desired, however, this may lead to unrealistic forecast and very large σ_{a_n} in the first few assimilation steps. The impact of the \mathbf{m}_0 and \mathbf{P}_0 will tend to vanish as more

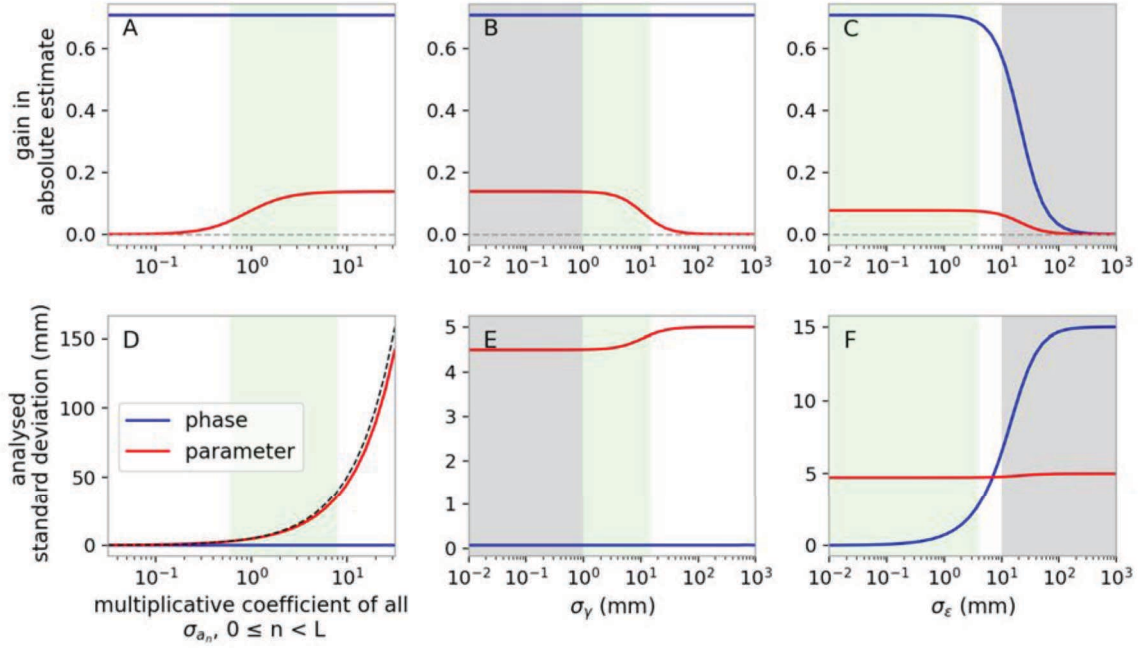


Figure 2.11: Variations of the gain in phase and model parameter estimates (A-C) and of the standard deviation of those estimates (D-F) as a function of the error terms used to initialize KFTS. Quantitative values are derived from Equations 2.3, 2.4 and 2.5 for the parametrization chose in our synthetic example. We look at one assimilation step $k=1$. The blue line is effectively ϕ_1 and the red line a_3 . Similar trends, with different amplitudes are observed for any a_n . We vary successively all σ_{a_n} (in the diagonal of \mathbf{P}_0) (A,D), σ_γ (B,E) and σ_ϵ (C,F). In A,D σ_{a_n} are multiplied by a common coefficient. The dashed grey line indicates zero gain. The black dashed line correspond to the case where σ_{a_3} evaluated at $k=1$ is the *a priori* σ_{a_3} (at $k=0$). The shaded grey area is the domain where $\sigma_\epsilon > \sigma_\gamma$. Green shading highlights the domains where the (i) gain on the phase is maximal, (ii) the gain on model parameter is not null (i.e. the model learns from data), (iii) the uncertainty on phase estimate is small ($\sim 10^{-2}$ mm) and (iv) the uncertainty on parameter estimate is not very large (< 40 mm). Variations in σ_γ or σ_{a_n} do not affect phase estimates. The model parameters are not adjusting to the data when the *a priori* on its standard deviation is too low or when σ_γ is too high.

data is assimilated.

REGARDING the mismodeling noise γ_k and network misclosure ϵ_{ij} (Equations 2.1, 2.2), we assumed that they could be represented by constant standard deviations σ_γ and σ_ϵ , unless variations in acquisition quality (e.g. seasonal noise from snow cover) or in interferogram construction (e.g. varying amount of filtering) are known. Typically, we have $\sigma_\epsilon \ll \sigma_\gamma$ so that phase fitting is strongly favored over parametrized model adjustment (Section 2.3.1.3, Figure 2.11). ϵ_{ij} could be measured by looking at the closure of triplets of interferograms and representative σ_ϵ deduced. σ_γ should reflect the dispersion of the data around the parametrized model, which depends on the chosen model itself and the noise in the data. From previously published studies, σ_ϵ is of the order of the millimeter (assuming no unwrapping error) and σ_γ superior to the centimeter [Schmidt and Bürgmann, 2003; Cavalié et al., 2007; López-Quiroz et al., 2009; Sudhaus and Jónsson, 2009; Agram and Simons, 2015].

2.4.2 Efficiency

A MAIN IMPROVEMENT of KFTS over more conventional method is the data assimilation approach. We have shown that it is capable of accurately solving the same problem than a least-squares method. However, KFTS is designed to solve other problems relevant to our ever-expanding SAR archive. First, it can actualize a pre-existing time-series with new interferograms in a fast and neat way. Secondly, we have built the tool in a modular and flexible manner, so that it can adapt to the evolving knowledge of the deformation as data is assimilated. Below, we discuss and detail those statements.

The iterative procedure allows fundamental discussion about the amount and shape of data necessary to obtain a meaningful description of deformation. Our tests reveal that phases are instantaneously fitted to ± 0.1 mm with later refinement as we gain information from new interferograms. Differently, model parameters require at least one year of data in order to converge, a time that depends on the variability of deformation measured and how precise and accurate is our *a priori* knowledge. Velocity adjusts rather quickly, if no transient event is recorded, compared to the cosine and sine terms which require obviously more than a year. Consequently, forecast within the first year is rarely accurate, which clearly reflects on the uncertainty. Once model parameters have converged toward their final value, the forecast is as good as the model is, independently of the elapsed time of assimilation. The instantaneous innovation reflects the dispersion of the data around the background model.

UPDATING PRE-EXISTING MODEL imply a gain of time, computing power and memory. Quantitative comparisons of computing performance of NSBAS and KFTS methods are not easy because their implementation are different. Indeed, KFTS is implemented for simultaneous processing of pixels in parallel by Message Passing Interface, while NSBAS uses multiple threads with shared memory in its GIANt version [Agram *et al.*, 2013]. However, it is clear that the numerical cost of updating an existing time series with KFTS is much smaller than when retrieving all the phases at once with NSBAS. The time to run a KFTS update incorporates not only the computation time, but also the time necessary to read and write data and models. The latest has been optimized so that, in the example presented in Section 2.3.2, reconstructing phases and parameters for the 62 first dates takes 17 min, whereas updating the time series with the last acquisition takes only 30 sec. As a reference, we use 2 computing nodes with 20 threads per nodes and InfiniBand communication. Concerning memory usage, previously computed interferograms do not need to be stored in order to update existing model, providing that the latest estimates of \mathbf{m}_k and \mathbf{P}_k are available. For the example in Section 2.3.3, this information is stored in a HDF5 file of 6 Go, while all interferograms weigh >25 Go.

ANOTHER ADVANTAGE of KFTS is the systematic and consistent propagation of error through time series analysis. It is a requirement to correctly combine what we know from the data and from the existing model. We have seen that the absolute value of the uncertainty associated with computed phases is a consequence of the *a priori* standard deviation of misclosure (σ_ϵ) (Figure 2.6), which can be measured from interferograms or inferred from the way interferograms are built. Additionally, the standard deviation of mismodeling error (σ_γ) will also come into play in the case of missing data for a time step or disconnection in the interferometric network. This error is a more subjective parameter, as it depends on the functional description chosen, and the dispersion of phases around it. Nevertheless, the relative uncertainty in between pixels and time steps directly results from the data structure, such as the number of interferograms available or how "far" is the temporal reference. Those differences allow us to discriminate pixels and weight estimates for subsequent processing or modeling. This is particularly relevant for long time-series (<1 year). Furthermore, covariance estimation is key to combine different data sets, such as InSAR and GPS [Bekaert *et al.*, 2016; Sudhaus and Jónsson, 2009] or different frames of InSAR acquisitions [Jolivet and Simons, 2018].

2.4.3 Limitation and perspectives

THE PROPAGATION of uncertainty highlights a fundamental limit of time series analysis. The time series being relative to the first date, errors tend to propagate in time. This is a big issue for long time series, such as ones drawn from Sentinel 1 nowadays. Numerous interferograms, especially those with long baselines, are necessary to limit this effect inherent to any classical InSAR time series analysis. Moreover, the similarity with GPS time series evidenced in Section 2.3.2 shows the possibility of a precise re-referencing of the pixel location within the time series. This has been done for vertical displacement [Shirzaei and Bürgmann, 2018]. In addition, our comparison with GPS time series could be improved by correcting interferograms for ionospheric effect [Simons and Rosen, 2015; Liang *et al.*, 2019].

THE PIXEL BY PIXEL approach of KFTS implies that we do not account for spatial covariance [Jolivet and Simons, 2018]. This covariance may take the form of a function of the pixel-to-pixel distance, which empirically models the isotropic part of the InSAR signal not due to ground deformation. Such signal mainly arises from atmospheric effects. In our real case example, we limited the spatial correlation by subtracting a best-fitting ramp to interferograms and by removing the stratified tropospheric delays in each interferogram. Turbulent atmospheric delays remain, however. Nevertheless, because KFTS is built to deal with long time series, the temporally decorrelated contributions of InSAR (e.g. turbulent delays) are reflected by the inter-acquisition dispersion

for a given pixel and is empirically included in the mismodeling error. This contrast with studies looking at few SAR acquisitions to deal with a localized event in time [Lohman and Simons, 2005; Sudhaus and Jónsson, 2009]. Spatial covariances are also implemented to increase spatial continuity [Jolivet and Simons, 2018]. For KFTS, we found that spatial continuity of phase and function parameter naturally arise from the data which only has high inter-pixel noise in regions where coherence is low (e.g. Figure 2.10). In such region, the numerous "holes" in assimilated interferograms ensure low confidence in the KFTS estimates. Spatial constrain would help gain confidence by adding more information in the problem but it would dramatically increase the numerical cost and would require additional parametrization [Agram and Simons, 2015; Jolivet and Simons, 2018]. Additionally, the smoothing of model parameters brought by the *a priori* ensure greater spatial continuity in low coherence area with respect to NSBAS.

WE BUILT KFTS as an accessible tool relevant to many geophysical applications. More specific applications will be implemented in the future, taking advantage of the iterative procedure as well as systematically exploiting outputs of KFTS not detailed in this paper, such as the full temporal covariance matrix or the gain and innovation vectors. For instance, the iterative procedure is ideal to implement automatic detection of transient events, such as slow slip on faults. The quality of the parametrized model could be systematically checked by looking at the instantaneous innovation of phase values but also of model parameters. An automatic detection of non-gaussianity of the innovation distribution over time could send a warning, stop the assimilation and or automatically update the model with predefined functions (e.g. quadratic term, Heaviside function). Another major improvement of our KFTS would be to remove σ_γ from the predefined parameters and include it as a parameter to be recovered during time series analysis.

2.5 Conclusion

WE DEVELOPED a tool to rapidly and efficiently update pre-existing time series of deformation from a set of unwrapped interferograms as they are made available. The Kalman filter (KF) approach is new to InSAR time series analysis and was tested on diverse sets of synthetic and real interferograms in regions affected by tectonic deformations. We show that the filter behaves in agreement with existing methods and GNSS measurements, providing that we correctly estimate errors associated with interferograms as well as with the parametrized description of deformation. We thoroughly studied and described the design and impact of setup parameters. The source code is fully implemented in Python 3 and was built as a flexible and modular tool for the community.

Acknowledgments This article benefited from previous works by Angelique Benoit and discussions with Dr Marie Bocher, Pr Alexandre Fournier, Dr Kristel Chanard, Pr Emmanuel Cosme and Theo Rebert. This work received funding from the European Research Council (ERC) under the European Union's Horizon 2020 research and innovation program (Geo-4D project, grant agreement 758210). Data sets used in this study are freely available online. Synthetic Aperture Radar images are from the PEPs platform (Sentinel 1) and from ESA Earth Online (Envisat). The digital elevation model is from NASA EarthData. ERA-5 global reanalyses of atmospheric data are distributed by the ECMWF. GPS time series come from the Nevada Geodetic Laboratory website. The latest release of the source code is available on Zenodo (KFTS-InSAR; DOI:10.5281/zenodo.3816782).

Chapter 3

THE INTERPLAY BETWEEN SEISMIC AND ASEISMIC SLIP ALONG THE CHAMAN FAULT ILLUMINATED BY INSAR

Les interactions entre glissement sismique et asismique le long de la faille de Chaman éclairées par INSAR

CE CHAPITRE présente et analyse les séries temporelles de déformation calculées avec KFTS (Chapitre 2) le long des 800 km de la faille de Chaman (Afghanistan, Pakistan) entre 2014 et 2019 (Figures 3.1, 3.2). Ces séries temporelles nous renseignent sur le glissement inter-sismique et permettent l'analyse de trois séismes de magnitudes M_w 4,4 à 5,6 et, ainsi, de décrire et quantifier les relations spatio-temporelles entre le glissement sismique et asismique récent. Ce chapitre est soumis en tant qu'article dans la revue *Journal of Geophysical Research - Solid Earth* en 2021 (première soumission en février, révision en juillet) avec les contributions de Romain Jolivet, Elenora van Rijsingen et Sylvain Michel.

NOUS CONSTATONS que la majeure partie du tracé de la faille active glisse de manière asismique et continue (Figure 3.3, 3.4), c'est à dire qu'elle "creep". Du sud au nord, nous identifions trois portions de faille en "creep" : les segments Nushki, Central et Qalat, de longueurs comprises entre 80 et 130 km. Le taux de chargement est de $1,2 \pm 0,3$ cm/an pour les deux portions les plus au sud, tandis qu'il est d'environ $0,7 \pm 0,2$ cm/an pour le segment Qalat (Figure 3.5). Le segment central et les segments "bloqués" voisins ont connu les plus grands séismes historiques recensés sur la faille de Chaman, ainsi que trois séismes de magnitude modérée au cours de notre période d'observation (Figure 3.5e, 3.6). Nous étudions ces trois séismes pour lesquels le glissement modélisé en profondeur (M_w 5 à 5,6) (Figure 3.7) et les séries temporelles de glissement en surface (Figure 3.9) plaident en faveur d'un important glissement asismique induit. Le troisième événement (juin 2018) présente un moment post-sismique plusieurs fois supérieur au moment cosismique (Figure 3.1).

CES OBSERVATIONS sont en accord avec les études basées sur des données InSAR plus anciennes provenant des missions ALOS et Envisat. Ainsi, au cours des deux dernières décennies, le glissement aiséismique continu ou induit domine le long de la faille et peut être colocalisé avec les séismes. Nous observons que les complexités géométriques de la faille délimitent des segments actifs et peuvent être responsables de l'imbrication à l'échelle kilométrique entre les événements sismiques et aiséismiques (Section 3.5.3, Figure 3.5a,f).

THIS CHAPTER has been submitted reviewed and published as a research article in *JGR* special section "Creep on continental faults and subduction zones: Geophysics, geology, and mechanics"¹. In addition to my supervisor, Romain Jolivet, Elenora M. van Rijsingen and Sylvain Michel contributed to this work. Elenora helped me investigate the geometry of the Chaman fault trace and its relationship with slow slip distribution; while Sylvain helped with the comparison of seismic moment release and aseismic slip. We use the Kalman Filter time series analysis for InSAR (Chapter 2) to study the distribution of seismic and aseismic slip on the Chaman fault (the region is introduced in Section 1.4.2). Notes and Figures in the margin are specific to this thesis.

¹ **Citation:** Dalaison, M., R. Jolivet, E. M. van Rijsingen, and S. Michel (2021), The interplay between seismic and aseismic slip along the Chaman fault illuminated by InSAR. *Journal of Geophysical Research: Solid Earth*, 126(12), 2021JB021935.

Abstract

The 700-km-long Chaman fault marks the western edge of the plate boundary between India and Eurasia. Although global plate models predict 2.3-3.6 cm/yr left-lateral motion between both plates, the fault is known to have hosted few earthquakes in historical times. Recent geodetic measurements attested the presence of aseismic slip locally. To detail the interplay between fast and slow slip along the Chaman fault, we build three InSAR time series of ground deformation covering the whole fault length over 5 years (2014-2019). We find that most of the active fault trace slips aseismically and continuously. From south to north, we identify three creeping fault portions: the Nushki, Central and Qalat segments of lengths between 80 and 130 km. The loading rate is 1.2 ± 0.3 cm/yr for the two southernmost portions, while it is about 0.7 ± 0.2 cm/yr for the Qalat segment. The Central segment and the nearby locked segments have hosted the largest known historical earthquakes on the Chaman fault, and three moderate magnitude earthquakes in our observation period. We image these earthquakes for which modeled slip at depth (M_w 5-5.6), time series of surface slip and deformation patterns argue towards large triggered aseismic slip. The June 2018 event displays postseismic moment 3-15 times greater than coseismic moment. Over the two decades covered by geodetic observations, continuous or triggered aseismic slip dominates along most of the fault and co-locates with earthquakes. We observe that fault geometrical complexities delimit active segments and may be responsible for the kilometer-scale intertwining between seismic and aseismic events.

3.1 Introduction

THE POTENTIAL OCCURRENCE of earthquakes depends on the available elastic energy stored in the crust, which in turn depends on external driving forces and fault properties. While some faults are locked most of the time and release energy by rapid (m/s) slip (i.e. earthquakes), some slip slowly (cm/yr) [e.g. *Steinbrugge et al., 1960; Jolivet et al., 2015a; Bürgmann, 2018; Jolivet and Frank, 2020*]. Slow slip is known to influence the budget of slip locally [e.g. *Çakir et al., 2012; Maurer and Johnson, 2014; Jolivet et al., 2015a; Dal Zilio et al., 2020*], hence plays a role in tuning the magnitude [e.g. *Michel et al., 2018, 2019*], as well as the initiation, propagation and arrest of potential earthquakes [e.g. *Kaneko et al., 2010; Avouac, 2015*]. Understanding the interplay between slow slip, shear loading and earthquakes is therefore fundamental for seismic hazard assessment.

BECAUSE SLOW SLIP does not radiate seismic waves, unlike earthquakes, global occurrences of slow slip remain incompletely documented and their ubiquity is an open question. In this study, we focus

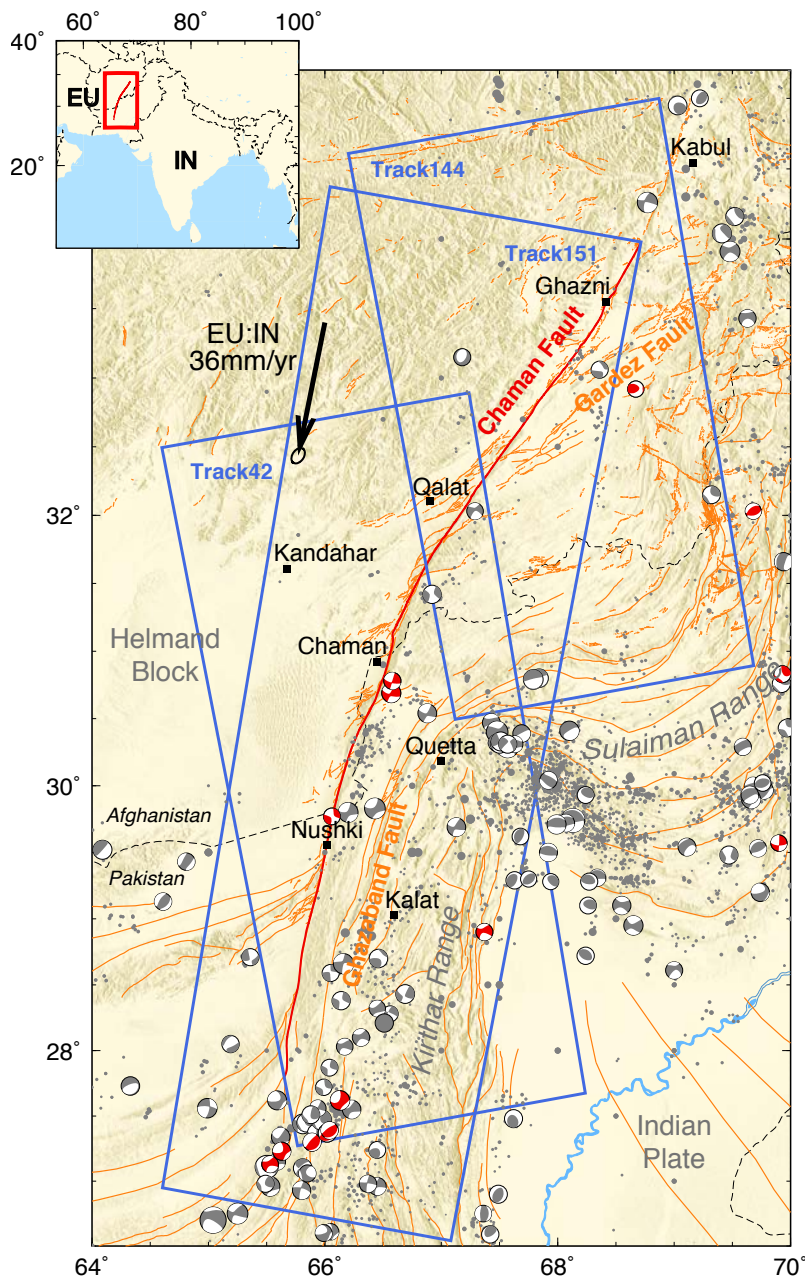


Figure 3.1: Tectonic setting and seismicity of the Chaman fault system. Focal mechanisms are from the GCMT catalogue [Dziewonski *et al.*, 1981; Ekström *et al.*, 2012]. Earthquakes later than 2014 are in red. Gray dots are historical and recent (2000 BC to 2004 AC) seismic events for which magnitude estimates are known (radius is relative magnitudes) [Dewey *et al.*, 2006]. Orange lines are fault traces [Ruleman *et al.*, 2007]. Background shading is elevation gradient from SRTM [Farr *et al.*, 2007].

on the Chaman fault, in Pakistan and Afghanistan, where slow slip has been described [Fattahi and Amelung, 2016; Barnhart, 2017] alongside multiple moderate magnitude earthquakes (moment magnitude, M_w , of ~ 5) [Ambraseys and Bilham, 2003a; Fattahi *et al.*, 2015; Bilham *et al.*, 2019]. This fault belongs to one of the longest continental strike-slip systems extending over a length of 1000 km and accommodates the relative displacement between India and the Helmand Block of the Eurasian Plate [Yeats, 2012] (Figure 3.1). However, a detailed characterization of the spatio-temporal dynamics of slip along the full length of the Chaman fault (CF) is lacking. In the following paragraph, we briefly summarize the current understanding of the kinematics of the

CF and precise the goal of this study.

GLOBAL PLATE MODELS predict that the Chaman fault system, including the CF together with the adjacent fold and fault belts to the east, acts as a transpressional plate boundary and accommodates left-lateral motion ranging from 23 to 36 mm/yr and convergence between 0 and 18 mm/yr [Ruleman *et al.*, 2007; DeMets *et al.*, 2010; Kreemer *et al.*, 2014; Altamimi *et al.*, 2017]. Global Positioning System (GPS) and Interferometric Synthetic-Aperture Radar (InSAR) suggest left-lateral motion is currently accommodated by the CF at about 12 mm/yr with significant along-strike variations [Mohadjer *et al.*, 2010; Szeliga *et al.*, 2012; Crupa *et al.*, 2017; Fattahi and Amelung, 2016; Barnhart, 2017]. Consequently, it is currently accepted that the CF accommodates about 30% of the total relative plate motion between latitudes 27°N and 35°N [Fattahi and Amelung, 2016; Barnhart, 2017]. Remaining relative displacement is probably accommodated by structures east of the CF, such as the Ghazaband fault and the Gardez fault zone [Szeliga *et al.*, 2012; Fattahi and Amelung, 2016; Bilham *et al.*, 2019] (Figure 3.1).

INTERESTINGLY, some observations along this major plate boundary challenge the classic elastic cycle of loading and unloading of a single fault through earthquakes. Indeed, a long-known characteristic of the Chaman fault system is the scarcity of seismicity, which has been reliably documented in the region since the 1880s [Ambraseys and Bilham, 2003a], and, specifically, the very few earthquakes with magnitude greater than 6, which include the M_w 6.6 Chaman (1892) and M_w 7.7 Quetta (1935) earthquakes [Dewey *et al.*, 2006; Ambraseys and Bilham, 2003b,a; Ambraseys and Douglas, 2004; Szeliga *et al.*, 2009; Bilham *et al.*, 2019]. Along the same fault system further north, the city of Kabul was destroyed by an earthquake of magnitude \sim 7.2 in 1505 [Ambraseys and Bilham, 2003a; Yeats, 2012]. So few large magnitude events cannot explain the relative motion accommodated by the CF and even less the whole plate boundary relative motion [Bernard *et al.*, 2000]. Common explanations of the apparent lack of large earthquakes include an important role of (i) aseismic slip and microseismicity below the detection threshold of the local bare seismic network or of (ii) non-rigid deformation within the wide fault system. Distributed deformation on many structures (in support of (ii)) is suggested by detailed fault traces inferred from satellite imagery and current seismicity [Ruleman *et al.*, 2007], both outlining intricate fault patterns with many subsidiary faults and discontinuities over a >80-km-wide region.

HERE, we evaluate the role of aseismic slip and microseismicity on strain release along the CF (hypothesis (i)), focusing on the interplay between seismic and aseismic slip. A 125-km-long creeping segment, called the Nushki creeping segment, has been identified along the CF between latitude 29.28°N and 30.58°N [Fattahi and Amelung, 2016; Barn-

hart, 2017]. Additionally, the inferred shallow locking depth (0-7 km) along the CF is thought to impede the occurrence of large earthquakes [*Szeliga et al., 2012; Barnhart, 2017*]. Moreover, the abnormally large and long (1 year) afterslip following at least two $M_w 5$ earthquakes [*Furuya and Satyabala, 2008; Fattahi et al., 2015*] and the recent creep event presented in *Bilham et al. [2019]* highlight the need to frame observations temporally, and consider the role of transients in long-term behaviour. Detailed time series are needed to untangle the dynamics of the fault system and depict a better image of the fault frictional properties. We therefore propose to examine the distribution of aseismic slip along the whole CF length, using high resolution time series of deformation derived from InSAR. We cover the 2014-2019 period, building on existing geodetic observations for older periods.

WE CONSIDER more than 5 years of Synthetic-Aperture Radar (SAR) acquisitions (2014-2019) on ascending and descending orbits by the Sentinel 1 constellation to characterize spatio-temporal variations of aseismic slip and investigate the recent distribution of seismicity. In the following, we first summarize the structural and geological properties of the CF and detail how we select earthquakes in existing catalogues of seismicity. Then, we detail an innovative systematic data assimilation approach to process InSAR data and deal with five moderate magnitude earthquakes that occurred during our observation period. Next, we carefully extract slip and slip rate along the fault trace from InSAR-derived displacement and velocity maps. Also, through inversion of InSAR-derived earthquake surface deformation, we model slip at depth for three earthquakes affecting the CF and study the spatio-temporal signature of the resulting surface slip. Finally, we describe the intriguing interplay between earthquakes and aseismic slip and discuss a segmentation of the CF, relating slip behaviour with fault geometry.

3.2 Tectonic context and seismicity

3.2.1 Activity and geometry of the fault

IN THE TOPOGRAPHY, the CF sharply delimits the western border of young mountain ranges (Eocene to now) from 28° to 32.5°N : the Kirthar range elongated along a NNE axis and the lobate Sulaiman range north of 30.5°N . With a more subtle topographic and geomorphologic signature, the fault extends north to the Afghan capital, Kabul ($\sim 34.5^\circ\text{N}$) [*Crupa et al., 2017; Wheeler et al., 2005*]. The CF cuts through structural trends and is a major geological boundary between the Miocene-Eocene Khojak flysch unit to the east and the Afghan block essentially made up of meta-igneous, volcanic and plutonic rocks [*Jones et al., 1961; Lawrence and Yeats, 1979; Lawrence et al., 1981*]. The CF is a long-lasting feature that has accommodated several hundred kilometres of

sinistral offset and continues till present time as attested by young stream beds offsets and recent earthquakes [Beun *et al.*, 1979; Tapponnier *et al.*, 1981; Sborshchikov *et al.*, 1981; Lawrence *et al.*, 1992; Wheeler *et al.*, 2005; Ul-Hadi *et al.*, 2013a]. Considering such cumulative offset, the CF reached significant level of structural maturity in the sense of Manighetti *et al.* [2007].

PRECISE FAULT trace mapping for the Chaman fault zone north of 29°N has been done by the U.S. Geological Survey using remote-sensing imagery [Ruleman *et al.*, 2007]. The northeast-trending left-lateral fault zone is associated with smaller-scale thrust faulting indicating transpressional motion (Figure 3.1). From south to north, the main fault trace progressively rotates eastward from 15 to 37° azimuth and displays a 100-km-long restraining and releasing bend in its central portion, close to the city of Chaman (30.9°N). Compressive features mostly focus west of the CF within and north of this restraining bend. East of the CF, the Kirthar and Sulaiman fold and thrust belts host thrust earthquakes and are most likely accommodating a significant part of the 0-18 mm/yr of compression expected from the CF azimuth. The CF geometry at depth is poorly known but according to the parameter exploration by Barnhart [2017] the best hypothesis remains that the fault plane is vertical with negligible fault-normal displacement at least between 29° and 30.6°N.

As reference we draw a unique and continuous CF trace from Ruleman *et al.* [2007]'s mapping, following exact fault coordinates. The assumption of a continuous fault trace is consistent with fault mapping from 28° to 32.5°N, while mapped faults north of 32.5°N tend to be more discontinuous. However, the uniqueness of the fault trace is a challenge as several fault strands are mapped often within 1 km of each other. To get a fine scale quantification of azimuth variation we differentiate the fault trace using Chartrand [2011]'s algorithm. We will discuss fault azimuth variations and their relationship with fault slip at a scale larger than 10 km with specific caution north of 32.5°N in Section 3.5.3.

3.2.2 Seismic record

THE CHAMAN FAULT system seismicity is scarce and distributed over the Kirthar mountain range (Figure 3.1). We explore the seismic record with a double interest: first, we precise their long-term (~100 years) contribution to fault slip along the CF, second, we evaluate their contribution to the observed deformation measured by InSAR over 2014-2019. We compile available seismic events in the Harvard Global Centroid Moment Tensor (GCMT), U.S. Geological Survey (USGS) and International Seismological Center (ISC) catalogues [Dziewonski *et al.*, 1981; Ekström *et al.*, 2012; ISC, 2020]. Because seismic stations are rare and far away, local earthquakes are poorly located with uncer-

tain depths and magnitudes. For instance, the 2005 $M_w 5$ earthquake imaged by *Furuya and Satyabala [2008]* is located about 27 km (ISC) and 30 km (USGS) away from its actual epicentre relocated by InSAR. We take the ISC as a reference for its re-location and compilation of numerous magnitude estimates [*Bondár and Storchak, 2011*]. We use M_w estimates, when available, or transform m_b to M_w using the global linear relation by *Scordilis [2006]*. In order to compare the amount of slip released seismically to aseismic slip on the CF, we collect events since 1900 occurring within 30 km of the CF trace. As a result, our catalogue going back to 1900 includes 139 events of M_w between 3.8 and 6.5.

Among these events, some must affect surface displacements measured by InSAR, hence must be accounted for when inferring surface deformation rates. Therefore, we identify earthquakes in the spatio-temporal frame of the Sentinel 1 acquisitions (blue frames in Figure 3.1) that are likely to influence inferred surface displacements. Identified events must have a focal depth inferior to 25 km, an estimated M_w superior to 5 and have to be distinguishable from each other given the InSAR temporal sampling of 6-12 days. Out of the 16 and 170 events in the GCMT and ISC catalogues, respectively, we identify four events or groups of events corresponding to our criteria with M_w between 5.1 and 5.7 (Table 2). In addition, we consider the earthquake on 27 June 2018 that clearly shows within our data, even though it is not referenced in the GCMT catalogue and the ISC database indicates a m_b between 3.8 and 4.2, depending on sources (Figure A.24).

Therefore, we consider the deformation related to five earthquakes or group of earthquakes during our observation period taking the properties (time, location and magnitude) of the largest earthquake of the group. Each group contains earthquakes within 20 days and 40 km of the largest one, considering uncertainties in location and timing arising from seismic catalogs and from InSAR time series, respectively. Earthquakes sequences will be detailed in Section ???. Among these five events, the two earliest events (3 August 2015 and 21 March 2016) are off the CF towards the southeast, whereas the three most recent events on 13 May 2016, 10 July 2016 and 27 June 2018 occurred close to the CF near the town of Chaman (Figure 3.1).

3.3 Method

IN THIS SECTION, we describe how we use SAR images to obtain a picture of tectonic deformation in the Chaman fault zone, and more specifically along the Chaman fault (CF) itself. First, we detail the way SAR images are combined to produce a network of interferograms (Section 3.3.1). Second, we explain how we derive maps of ground deformation, velocities and associated uncertainties with our innovative and efficient time series analysis method [Chapter 2 that is *Dalaison and Jolivet, 2020*] (Section 3.3.2). Third, we explain how we combine these maps to obtain a 2-D deformation field and to measure surface slip

along the CF (Sections 3.3.3 and 3.3.4). Fourth, we depict the inversion procedure used to get an image of slip at depth for three earthquakes which occurred on the CF during our observation time span (Sections 3.3.5).

3.3.1 Interferometric processing

WE PROCESS all available Sentinel 1A-B wide swath SAR images on two ascending (tracks 42 and 144) and one descending (track 151) tracks until December 31st 2019. The viewing geometry of track 151 makes it nearly insensitive to fault parallel displacement (Figure 3.1) but this second direction of measurement is key to differentiate horizontal from vertical displacement. We use the ISCE package (JPL/Caltech, winsar.unavco.org/isce.html) to corregister SAR images, as well as to compute, multilook, filter and unwrap interferograms [Gurrola *et al.*, 2010]. We build 456, 482 and 424 interferograms out of the 118, 120 and 108 acquisitions over tracks 42, 144 and 151, respectively. Interferograms are built systematically between each acquisition and the next 4 acquisitions. In addition, we build interferograms with longer temporal baselines (several months to years) for track 144 and 151 to tackle the loss of coherence over winter in the northern, mountainous part of the area. Interferometric pairs are shown in Figure A.17. We apply multilooking for a final pixel size of 85 m along the satellite flight direction and of 62 m in the range direction. We apply a phase preserving Gaussian filter [Goldstein and Werner, 1998] on the interferograms and correct the interferometric phase from tropospheric delays using the ERA-5 global atmospheric reanalysis [PyAPS; Jolivet *et al.*, 2011, 2014a]. We unwrap areas with a minimum coherence of 0.6 using a branch cut algorithm [Goldstein *et al.*, 1988] and subsequently correct potential unwrapping errors [CorPhU; Benoit *et al.*, 2020]. To correct for residual orbital errors, we remove a bilinear polynomial ramp from each interferogram. This ramp corresponds to the best fitting ramp of the phase change north of the CF, a region considered as tectonically stable (Figure A.16). The end result of this processing is a network of unwrapped interferograms co-referenced to a small zone of 5 by 5 pixels considered as fixed. Each interferogram is the relative phase change between two dates in line of sight (LOS) converted to millimetres, thus, it contains the effect of ground deformation but also significant residual atmospheric delays.

3.3.2 Iterative time series analysis incorporating coseismic displacements

WE APPLY a Kalman Filter time series analysis (KFTS) [Chapter 2 that is Dalaison and Jolivet, 2020] on each track to reconstruct the evolution of the interferometric phase (ϕ_k) at each time step (t_k) together with

the parameters of a time dependent model and associated uncertainties. Unwrapped interferograms are being ingested sequentially to build the temporal evolution of the phase and refine the parametric model at each time step. The model is used to make a forecast at future time steps, which is then refined by including new interferograms. This data assimilation approach is comparable to the New Small Baseline Subset method as it builds a model of deformation used when data is missing [Berardino *et al.*, 2002; Doin *et al.*, 2011]. However, our method has the benefit of allowing fast and efficient update of pre-existing time-series as new interferograms become available, as well as providing detailed error propagation throughout the process.

The parametric model describes the evolution of deformation with a linear combination of predefined functions of time from which we optimize the L coefficients a_i ($0 \leq i < L$). A well designed model conditions the accuracy of the estimated mean ground velocity [Dalaïson and Jolivet, 2020]. Notably, we must account for instantaneous phase changes caused by earthquakes.

OVER the observation period, we identify five earthquakes (sometimes associated with smaller nearby earthquakes) from the GCMT and ISC catalogues likely to produce significant signal in the time series of phase change (Section 3.2.2). With this *a priori* information, we include a Heaviside step function of time (H_j) centred on the date of each earthquake in our parametrised model. Consequently, our parametrised model of deformation includes a constant term (a_0), a secular rate (velocity a_1), a seasonal oscillation modelled as the sum of a sine and cosine with a period, T_{yr} , of one year, and N Heaviside functions H_j centred at the time of the N earthquakes affecting the area (here $N = 5$). Therefore we optimize a_i for all i in 0 to $N+3$ so that

$$\phi_k = a_0 + a_1 t_k + a_2 \sin\left(t_k \frac{2\pi}{T_{yr}}\right) + a_3 \cos\left(t_k \frac{2\pi}{T_{yr}}\right) + \sum_{j=4}^{3+N} a_j H_j(t_k) + \gamma_k \quad (3.1)$$

where γ_k represents the mismodelling error. The associated *a priori* standard deviations are 25 mm for a_0 , 9 mm/yr for a_1 and 8 mm for a_2 and a_3 . Those values, associated with a null *a priori*, are chosen in such a way that they reflect the expected range of variation [Dalaïson and Jolivet, 2020].

BECAUSE the spatial extent of earthquake related deformation is limited, including a Heaviside function to pixels far from the epicentre might lead to over-fitting. Therefore, to limit the spatial extent of the Heaviside functions, H_j , we force the earthquake amplitude a_j to stay at zero far from the earthquake location by setting a null *a priori* on a_j with zero uncertainty. In practice, we defined the *a priori* variance of a_j for each pixel as a two-dimensional Gaussian function centred on the earthquake location so that the variance decreases smoothly as a

function of the Euclidean distance to the earthquake (Text A.5.1).

As the standard deviation of the null a priori on a_j limits the explored range of values, it should be greater or equal to the order of magnitude expected for a_j [Dalaison and Jolivet, 2020]. In agreement with the amount of displacement and size of the rupture predicted by empirical scaling laws for $M_w \leq 5.6$ [Wells and Coppersmith, 1994; Petersen et al., 2011], we choose to set the maximum a priori standard deviation for a_j to 30 mm and the characteristic width of the spatial Gaussian to 9 km (Text A.5.1 and Figure A.18). This implies that we look for earthquake related displacement within a radius of ~ 40 km, a region much larger than the typical area affected by shallow $M_w \leq 5.6$ earthquakes [Savage and Burford, 1973; Petersen et al., 2011] so that the model does not put too much weight on imperfect earthquake location.

KFTS INCLUDES two additional tunable parameters. First, the standard deviation of the misclosure error, σ_ϵ , measures interferometric misclosure, which originates from interferometric processing, mainly multilooking [De Zan et al., 2015] since unwrapping errors are corrected for. Second, the standard deviation of the mismodelling error, σ_γ , quantifies the difference between phase change evolution and the parametric time dependent model, and, thus, accounts for temporally decorrelated signal in InSAR thought to arise from turbulent tropospheric delays as well as for unmodelled processes. Effectively, it controls the distribution of γ_k in Equation 3.1. Following guidelines in Dalaison and Jolivet [2020] we set σ_ϵ to 0.02 mm and σ_γ to 10 mm. The fact that $\sigma_\epsilon \ll \sigma_\gamma$ guarantees that interferometric phase reconstruction from interferograms is prioritized over fitting the much more uncertain model².

3.3.3 Combining InSAR tracks

FROM the time series analysis on each of the three InSAR tracks we obtain a map of ground velocity in the LOS (i.e. parameter a_1 for each pixel of each track). Where both ascending tracks overlap, the difference in velocity estimates is minimized subtracting a bilinear ramp to the velocity field of track 144. We combine ascending and descending LOS velocities, to get vertical (v_V) and fault-parallel horizontal velocities (v_H), assuming zero fault-perpendicular velocity. The observed velocities $(a_1)_n$ relates to v_H and v_V , for every n^{th} InSAR track imaging the given pixel [e.g. Wright et al., 2004; Tymofjeyeva et al., 2019; Lindsey et al., 2014] as

$$(a_1)_n = \cos(\theta + \beta_n) \sin(\alpha_n) v_H + \cos(\alpha_n) v_V, \quad (3.2)$$

where α_n and β_n represent the varying incidence and azimuth angles of the LOS vector, respectively, and θ the local fault azimuth. We solve this equation minimizing the least-squares criterion. The azimuth of the CF varies between about 0° at 28°N latitude to 40° near

²In particular, postseismic deformation is expected following the earthquakes we account for using Heaviside functions. Therefore, potential logarithmic decay subsequent to these events might affect the time series and, with the mismodelling term, we can afford to not include such functional form in our model and still recover adequate displacement.

Ghazni with significant local variations (Section 3.2.1 and Figure A.19). To determine local fault azimuth, we resample the fault trace with regular spacing (100 m) and smooth its azimuth value with a Gaussian filter of 10 km length.

3.3.4 Measuring fault slip

WE QUANTIFY the amount of slip along the CF, and evaluate the corresponding along-strike and temporal variations. In order to obtain this space and time vision, we work with both the time series of phase-change in LOS and the fault-parallel velocities. Effectively, we extract 500 m-wide fault-perpendicular profiles every 200 m along the fault [Kaneko *et al.*, 2013; Jolivet *et al.*, 2013].

IN A FIRST STEP, we adjust a screw dislocation model in a elastic half-space [Savage and Burford, 1973] to the 30-km-long profiles in fault-parallel velocities, v_H . We combine a shallow dislocation extending from the surface to a given depth, D_C , with a semi-infinite dislocation below a depth, D_S . The model is an approximation of the surface deformation produced by a vertical strike-slip fault creeping near the surface, above the depth D_C , at a constant rate C , and slipping at a constant rate S below the locking depth, D_S . It writes as

$$v_H(x) = -\frac{C}{\pi} \arctan\left(\frac{D_C}{x - X_f}\right) - \frac{S}{\pi} \arctan\left(\frac{x - X_f}{D_S}\right) + Bx + A \quad (3.3)$$

where x is the distance along the profile, A a constant, B a ramp and X_f the fault location [Segall, 2010]. We explore the values of S , D_S , C , D_C , X_f , A and B through Bayesian sampling of the parameter space using a Markov-Chain-Monte-Carlo algorithm [Salvatier *et al.*, 2016]. The A and B terms account for the reference of our velocity map. The *a priori* probability density function of S and C is uniform between 0 and 30 mm/yr (left-lateral slip), while the *a priori* of D_C , D_S and X_f are bounded Gaussians. The fault location is allowed to vary by ± 1.2 km from our mapped continuous fault trace. The creep extent, D_C is within 0 and 8 km with an *a priori* of 1 ± 3 km and it has to be inferior to the locking depth, D_S , which is within 0.01 and 9 km with an *a priori* of 2 ± 5 km (see Text A.5.2 and Table 3 for more details about the parametrisation). We do not allow for greater locking depths as our profiles are short in order to avoid interactions with the nearby Rigestan desert to the west (Figure 3.2)³. Displacement features of wavelength larger than 10 km will be approximated by the additional linear term. As a result, slip below 8 km is not well constrained and we arbitrarily increase the associated uncertainty by 4 mm/yr.

³ The penetrating depth of radar waves into sand is highly sensitive to moisture, complicating the interpretation of the signal in terms of deformation [McCauley *et al.*, 1982]

WE ALSO AIM to measure shallow fault slip without any underlying model. We consider the phase or velocity difference on each side of the fault as a direct measure of the surface expression of slip along the

fault. We measure the phase step across the fault by subtracting the mean values within 500 m and 1.5 km of the fault trace on each side (e.g. profiles in Figure 3.3). We apply this procedure to the phase-change, ϕ_k , at each time step, to the velocity field (a_1 or v_H), and to the associated velocity standard deviations (associated measures are referred to as $d\phi_k$, da_1 , and dv_H , respectively). We carefully computed surface slip rate uncertainties accounting for both the propagation of the previously estimated standard deviations on each velocity estimate and the scattering of velocity values spatially (Text A.5.3). By considering points within 1.5 km of the fault trace, we capture slip at or close to the surface (down to 1.5 km depth) as predicted by Equation 3.3. Measures of surface slip based on points further away from the fault trace (e.g. within 1 and 5 km) show very similar patterns with larger slip amplitudes, but time series estimates are more affected by spatially correlated noise.

3.3.5 Slip inversion for 3 earthquakes

THE THREE most recent earthquakes (M_w 5.6, M_w 5.1 and m_b 4.1) in our time series occurred close to the CF, near the city of Chaman and were imaged by both ascending and descending InSAR data. Corresponding surface displacement fields (Section 3.3.2) are sharply contrasted on each side of the CF trace demonstrating that these events ruptured the CF itself close to or reaching the surface (Figure 3.2). We use these earthquake displacement maps to infer slip at depth along the CF using a constrained least squares inversion [CSI library; Elliott *et al.*, 2016b]. We build a three-dimensional fault plane with triangular elements following the CF trace between latitudes 30.3°N and 31.1°N, dipping vertically down to 10 km (Figure A.20). We assume pure sinistral displacement on a vertical fault, in agreement with focal mechanisms and with Barnhart [2017]. We downsample the reconstructed InSAR map of earthquake displacement ($a_{6,7,8}$ in Equation 3.1) and associated uncertainties using a quadtree algorithm based on model resolution [Lohman and Simons, 2005], with element size between 600 m and 10 km (Figure A.21). We compute the Green's functions relating slip on the fault to surface observations for point sources in a homogeneous elastic half-space with a Poisson ratio of 0.25 [Zhu and Rivera, 2002]. We use data uncertainties obtained from the output of KFTS to build the diagonal data covariance matrix, C_d . The *a priori* model Covariance, C_m , is based on a decreasing exponential of the distance between fault elements [Radiguet *et al.*, 2011]. We adjust defining parameters of C_m , that is, the amplitude of correlation (σ_m) and the characteristic length scale (λ), while we fix the normalizing distance to 1 km (see L-curve in Figure A.22). We find that the combination of $\sigma_m=3$ mm and $\lambda=2$ km results in a model that is both close to the data (i.e., small misfit) and physically sound and smooth (i.e., no large values of parameters for negligible drop in misfit). Additionally, we vary

the value of σ_m from this reference value to regularize the inversion behaviour along fault segments not covered by data. We add 1 mm to σ_m for fault elements below the spatial footprint of data down to the bottom of the fault and remove 1 mm outside (Figure A.23).

3.4 Results: InSAR-derived deformation

3.4.1 Ground velocity

THE INSAR-DERIVED VELOCITY FIELDS display signals with local and regional length scales related to tectonics, hydrology and human activity (Figure 3.2). Earthquake related deformation is treated separately thanks to our parametric decomposition of the signal (Section 3.3.2). The standard deviation on ground velocity in LOS is close to 1 mm/yr for most pixels, except on the edge of the Rigistan Desert, in the Indus plain, above lakes and around the high peaks of the Hindu Kush (north of our study area), where many interferograms could not be unwrapped due to low coherence of the signal. Accounting for earthquakes in our parametric model of deformation increases uncertainties in local velocity estimates to ~ 2 mm/yr due to existing trade-offs between adjusting a ramp and a step function in the time series of interferometric phase change (Figure A.25).

Both velocity fields along ascending tracks show a ~ 100 km wide gradient of deformation perpendicular to the fault of about 20 mm/yr in the LOS direction. This gradient seems larger along two roughly north-northeast-striking regions : the Chaman fault (CF) and the central Kirthar range, west of the CF. We interpret this signal as the accumulation of interseismic strain across a transform plate boundary. In this study, we focus on strain accommodation by the CF only. In addition to the long-wavelength signal (~ 10 km), sharp discontinuities across the CF are visible. In the fault-parallel projection of velocity (Figure 3.3), such contrast is of the order of 1-2 cm/yr, with significant along-strike variations in surface slip rate. Dislocation model adjustment along 30 km-long selected profiles in Figure 3.3 confirms this near-field strain accumulation rate (S from 9 mm/yr in profile C to 20 mm/yr in profile A) and suggest very shallow locking depths along the fault plane (D_S from 1 km in profile D to 5 km in profile A).

Strong local minima in velocity in both ascending and descending tracks are mostly subsidence from anthropogenic water pumping and, to a lesser extent, mining. They are clearly retrieved in the vertical decomposition of the signal with rates close to 15 mm/yr in Kandahar and near Qalat and up to 200 mm/yr in Quetta and Pishin basins, a region known as the "fruit orchard" of Pakistan (Figures A.30 and A.31). Other studies retrieved comparable subsidence rates [Szeliga *et al.*, 2012; Kakar *et al.*, 2016; Ahmad *et al.*, 2017].

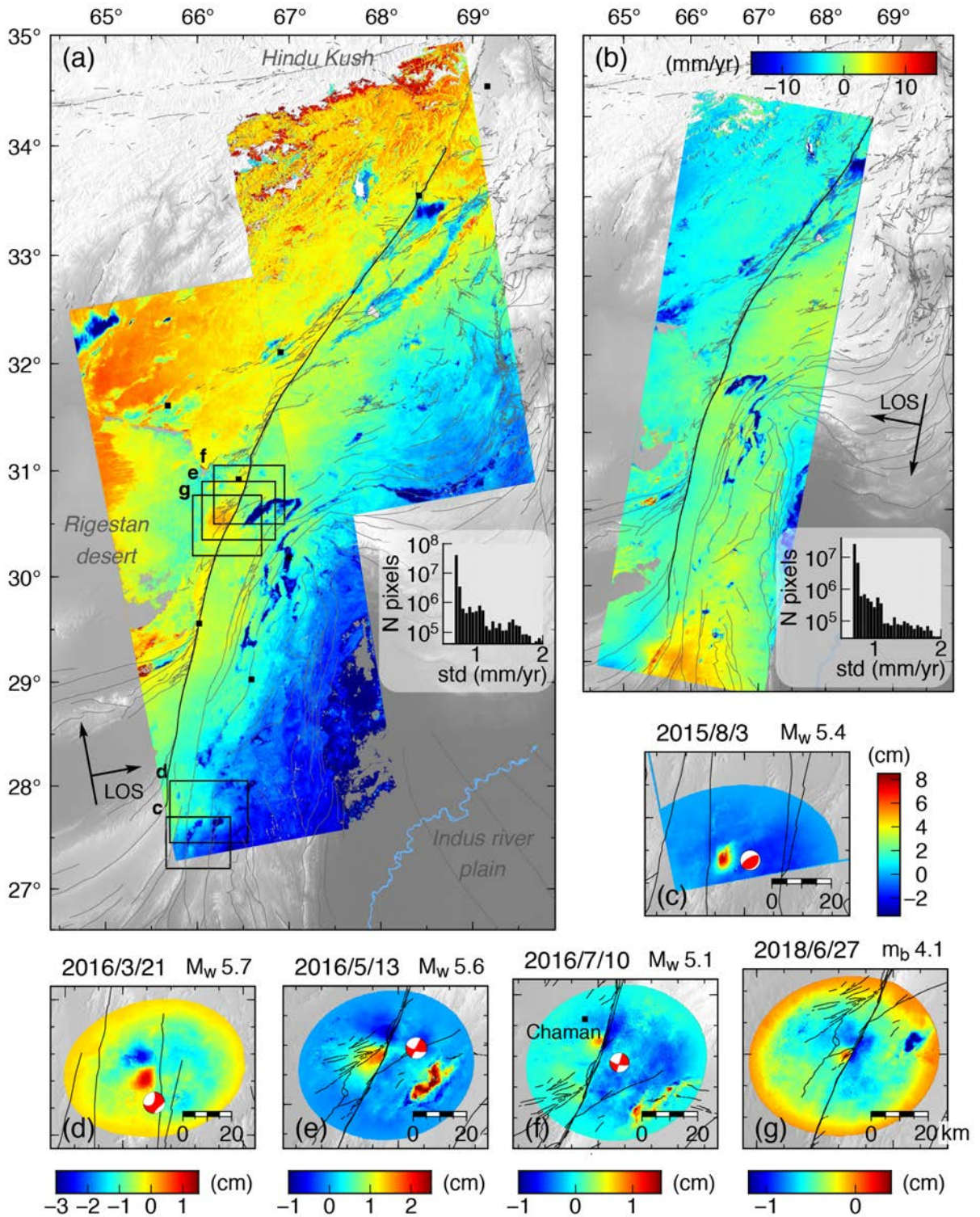


Figure 3.2: Velocity field for ascending tracks (in (a)) and the descending track (in (b)) in the line of sight (LOS) direction with histograms of their associated standard deviations (std). The histogram's vertical axis is the number of pixels in a logarithmic scale (full std map is in Figure A.25). Black line is the continuous trace of the Chaman fault used as reference. Filled black square markers locate cities named in Figure 3.1. Black frames delimit area in subplots (c)-(g) of the estimated coseismic displacement according to the ascending track 42 (see Figure A.26 for descending track and Figure A.27 for coseismic interferograms). Seasonal terms in Equation 3.1 are in Figure A.28 and A.29.

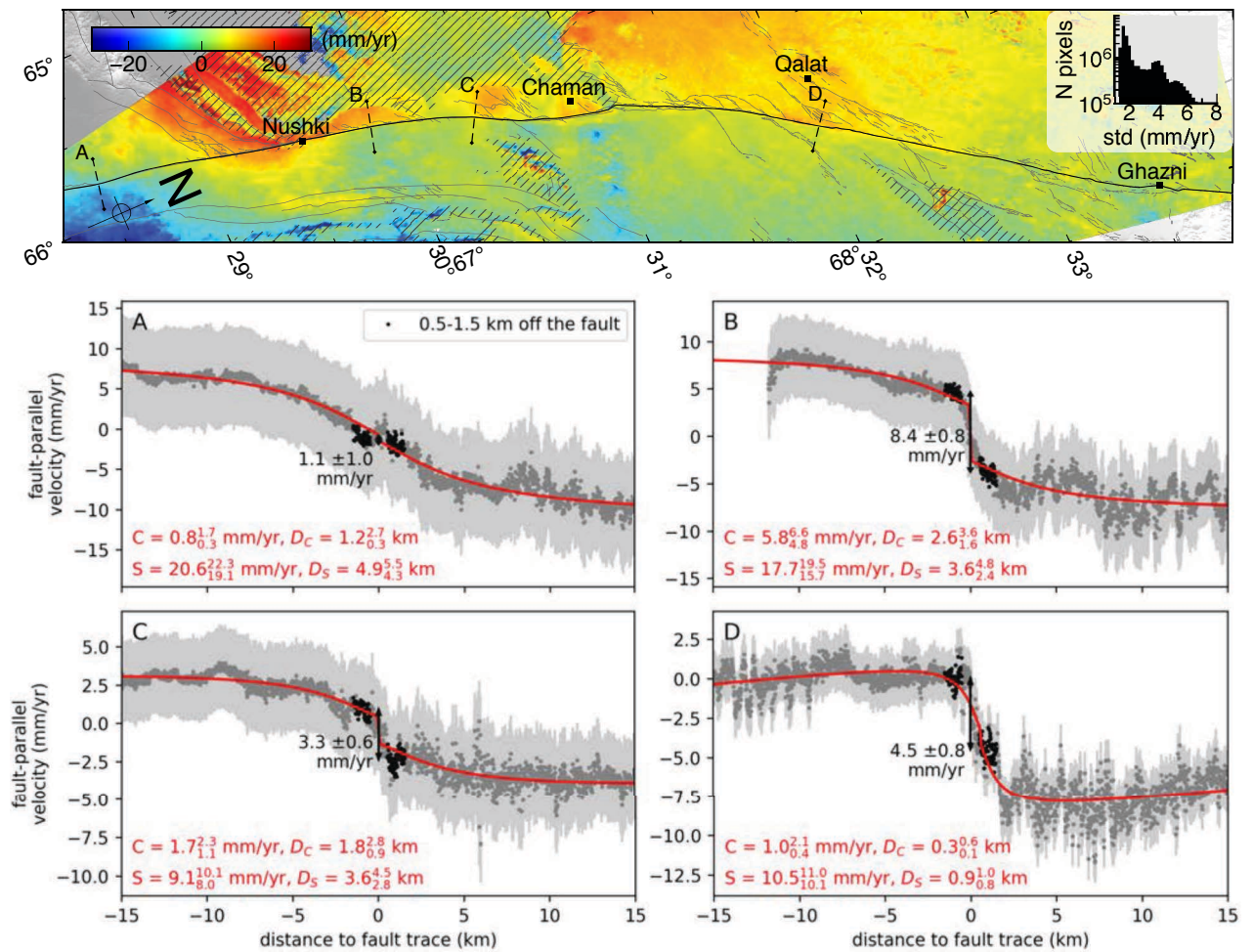


Figure 3.3: Velocity field projected in fault parallel direction (Figure A.19) with histogram of standard deviations (std) and 4 across fault profiles (see Figure A.32 for the full std map and Figure A.33 for a fixed direction of projection). Data with std > 8 mm/yr is not displayed. Note that to the south (left of this plot) the fault azimuth is close to zero implying that projected InSAR velocities are more uncertain (± 6 mm/yr). Velocities where tectonic deformation is known to be secondary compared to anthropogenic activity or geomorphological processes are hatched. Profiles are taken at distances along the fault from Nushki of -120 (A), 40 (B), 100 (C) and 300 (D) km. Measured surface slip from points close to the fault (0.5-1.5 km in black) are outlined by double headed arrows (those values are compiled along the whole fault in Figure 3.5c). Adjusted dislocation model for a vertical left-lateral fault is shown by the red curve with the median estimate and interquartile range of parameters in Equation 3.3 written in red.

3.4.2 Slip along the Chaman fault

FIGURE 3.4 DISPLAYS the spatio-temporal distribution of surface slip in the LOS, da_1 , along the CF with slip accumulating over time. The relative displacement caused by the three earthquakes between 30° and 31° N clearly stands out. Interestingly, these events occurred on fault portions that appear to be slipping beforehand at rates between 1 and 3 mm/yr. It is most obvious for the 2018 event, where ~ 10 mm of LOS surface slip accumulated in the 3.5 years before the earthquake. We refer to this fault portion which creeps and hosted three earthquakes between roughly 30.4° N and 31° N as the Central segment of the CF. Moreover, we see pronounced surface slip on each side of the

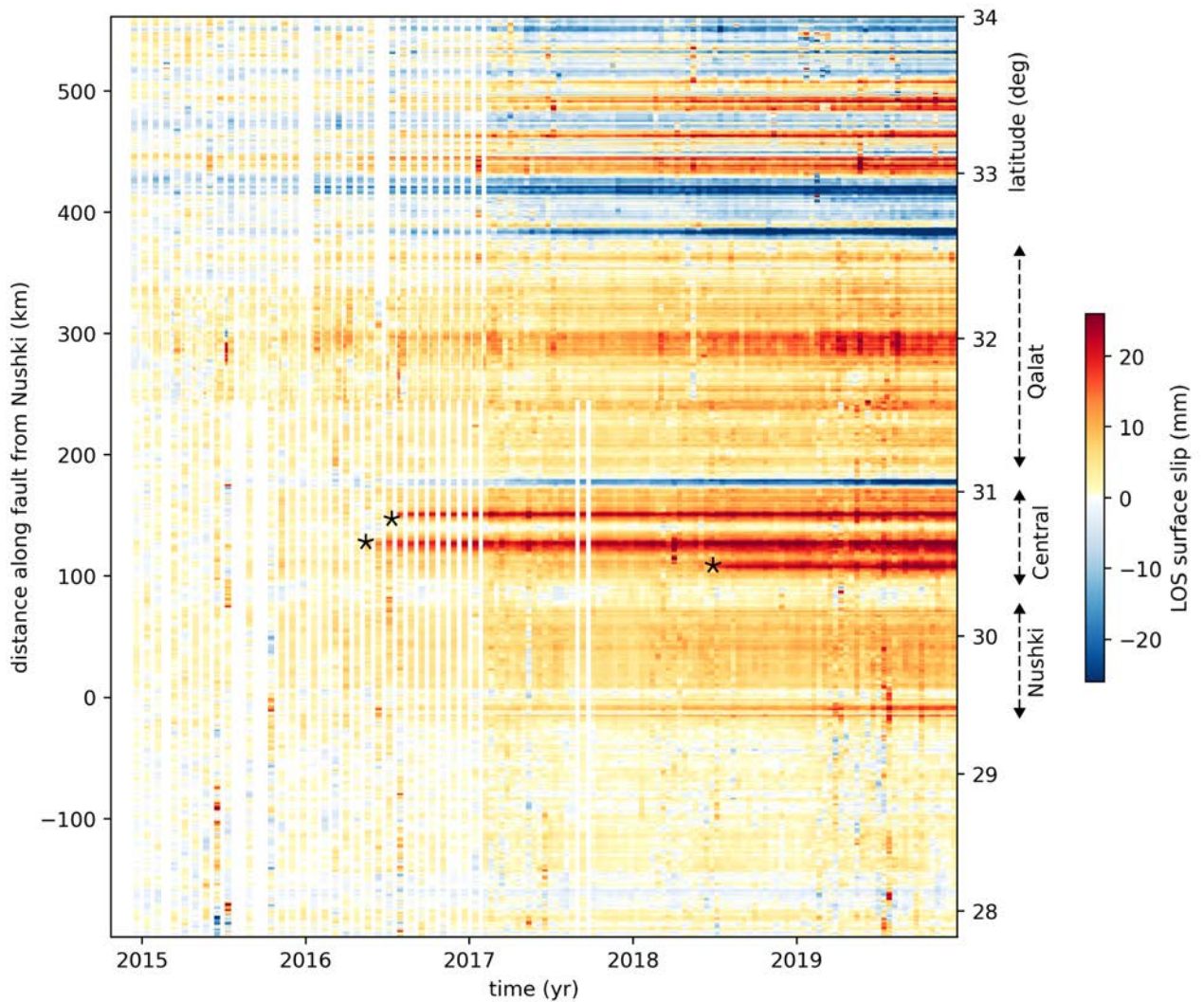


Figure 3.4: Temporal evolution of surface slip along the Chaman fault in line of sight (LOS) for ascending tracks. The color gradient represents cumulative surface slip of seismic and aseismic origin with respect to the first date (see Section 3.3.4 for method). Along most of the fault, positive slip indicates a left-lateral sense of slip (depending on the angle between fault azimuth and LOS). The timing and location of the 3 identified earthquakes are marked by black stars. Named portion of the fault with their approximate extent are indicated by labelled dashed arrows. The spatial reference (i.e., zero of the vertical axis on the left) is the latitude of the city of Nushki (29.556°N), Pakistan. For a variant see Figure A.34.

Central segment. In the south, we recognize the Nushki creeping segment [Barnhart, 2017] between about 0 and 80 km north of the city of Nushki, Pakistan, with a surface slip rate of about 1.4 ± 0.5 mm/yr in LOS. Another portion of the fault between 200 and 350 km north of Nushki slips with a maximum rate of 3.4 ± 0.8 mm/yr in LOS (Figure 3.5b). We refer to this fault portion as the Qalat segment. On both portions, the temporal evolution of slip is linear and continuous at the temporal scale of SAR acquisitions (several days). We do not identify any obvious transient slip events apart from post-seismic transients (see Section 3.5.2).

LEFT-LATERAL SLIP RATE close to the surface in Figure 3.5c is quanti-

fied either measuring the offsets in velocity on each side of the fault, dv_H , or using the median of the modelled creep rate C (Equation 3.3). Slip rate at depth (or loading rate) in Figure 3.5d is modelled slip rate, S , below the locking depth D_S . These measures are inferred from the horizontal, fault-parallel velocity (v_H in Equation 3.2). In the following, we detail along-strike variations in slip rates using the distance from the city of Nushki as reference. A strong negative slip rate (i.e. apparent right-lateral slip) estimate around 180 km comes from a 10-km-wide region of low velocity anomaly west of the fault. This region is collocated with the sharp releasing bend of the CF (Figure 3.5a) suggesting local extension and subsidence. Additional subsidence may originate from irrigation and human settlements clustering around the Dori river (Figure A.35).

Highest surface left-lateral (i.e. positive) slip rates ($dv_H \sim 8$ mm/yr) are measured south of 180 km, on three fault segments separated by null surface slip rate within uncertainty: the 80-km-long Nushki creeping segment, a 30-km-long segment around 120 km and a 20-km-long segment around 165 km. Measures of surface slip rates north of 180 km are lower but still positive with a notable peak at 5.6 ± 1.7 mm/yr between 275 and 300 km. Variations of C and dv_H are close, however, C tends to reach lower slip rates because of the larger uncertainty arising from the use of a model [e.g. Duputel *et al.*, 2014] and because of the existing trade-off between C and S when D_C and D_S estimates are close to each other such as along the Nushki segment (Figure 3.5d, Figure A.41). North of 380 km, measured surface slip rate is null within 1.7 mm/yr, an uncertainty arising from high near-fault variability in velocity measures. South of Nushki, low and slightly positive dv_H is recorded with an uncertainty of 0.5 mm/yr while the mean interquartile range of C is 0.5-2 mm/yr; indicating no certain surface slip.

PREVIOUSLY identified creeping segments have locking depths, D_S , of 4 ± 2 km and a locked depth range, $D_S - D_C$ of 2 ± 2 km suggesting that the whole width of the fault plane slips with a change in rate at about D_S . The 20-km-long portion between the Nushki and Central segments displays a $D_S - D_C$ of 3.5 ± 1.3 km while in between 190 km and the Qalat segments $D_S - D_C$ is 4 ± 2 km. Moreover, positive locked depth range is also modelled around 140 km (3.4 ± 1.1 km, $D_S \sim 4$ km), within the Central segment, and between 310 and 325 km (5 ± 2 km) in what we named the Qalat segment (Figure 3.5d, Figure A.39). Modelled slip rates at depth, S , are consistently non-zero along the fault portion between -140 and 380 km with limited along-fault variations. Between -80 and 165 km S are 12 ± 3 mm/yr, while it is 7 ± 2 mm/yr between 190 and 380 km. Therefore, the change in fault azimuth around 180 km appears as a discontinuity in the CF loading rate. North of 380 km, the median model is 1 mm/yr of slip (0.6-2 mm/yr interquartile range) below 5.6 ± 2 km depth with large uncertainties, suggesting that there is no significant loading of the fault at high latitude, in agreement with the absence of across fault gradient in velocity maps

(Figure 3.2a,b and 3.3). Lateral variability in modelled slip north of 380 km probably arises from poor fault location and numerous basins along the hypothetically continuous fault trace. South of the city of Nushki, we obtain significant amount of slip at depth, especially between -130 and -90 km where it is in average 21 ± 4 mm/yr below 6 ± 2 km (e.g. Profile A in Figure 3.3). This corresponds to a strong across fault gradient in projected velocities (Figure 3.3). However, the near north-south orientation of the fault trace on this portion implies that uncertainties associated with fault-parallel velocities are larger than 5 mm/yr. Therefore, we conclude that the fault is locked at the surface south of Nushki down to at least 5 km, but the amount of strain accommodated is uncertain (probably 5-20 mm/yr).

AS A SUMMARY, we delimit the ~ 400 km-long shallow slipping CF between the latitude of the city of Nushki, 29.5°N , and about 32.6°N (~ 380 km). This length includes creeping segments that slip continuously at 4-9 mm/yr over 2015-2020 from the surface to about 4 ± 2 km, a depth below which higher slip rates are expected (roughly 7-12 mm/yr). Creeping segments are separated by 5 40-km-long segments locked down to at least 3-6 km depth. The releasing bend of the fault 180 km north of Nushki ($\sim 31.1^\circ\text{N}$) marks the frontier between two fault portions of similar length, the southern portion slipping faster than the northern portion by about 3 mm/yr. North of 32.6°N , the CF seems inactive at our scale of observation, whereas the fault appears to slip below roughly 6 km south of the city of Nushki. In the following section, we further explore the slip behaviour of the central CF between the creeping Nushki and Qalat segments where earthquakes have been identified.

3.4.3 Seismic events

3.4.3.1 Surface displacement fields

FIGURE 3.2C-G DISPLAYS earthquake related displacement fields imaged by ascending track 42 (see Figure A.26 for descending track). Our time dependent model simplifies this displacement as a Heaviside function of time without specifically accounting for postseismic deformation but allows to extract surface deformation for quite small earthquakes [Liu *et al.*, 2021]. Postseismic slip rate is typically the largest immediately after the earthquake and then decays rapidly with time [e.g. Perfettini and Avouac, 2004]. As a result, most of the postseismic deformation is included in the computed amplitude of the Heaviside function of time, implying that coseismic and postseismic slip are not distinguishable using our parametric description of interferometric phase change alone.

The earliest (August 2015) earthquake of our time series is a $M_w 5.4$ thrust event on the Ghazaband fault, with maximum uplift close to 8.5 cm in LOS and a rupture length of about 10 km. According to GCMT,

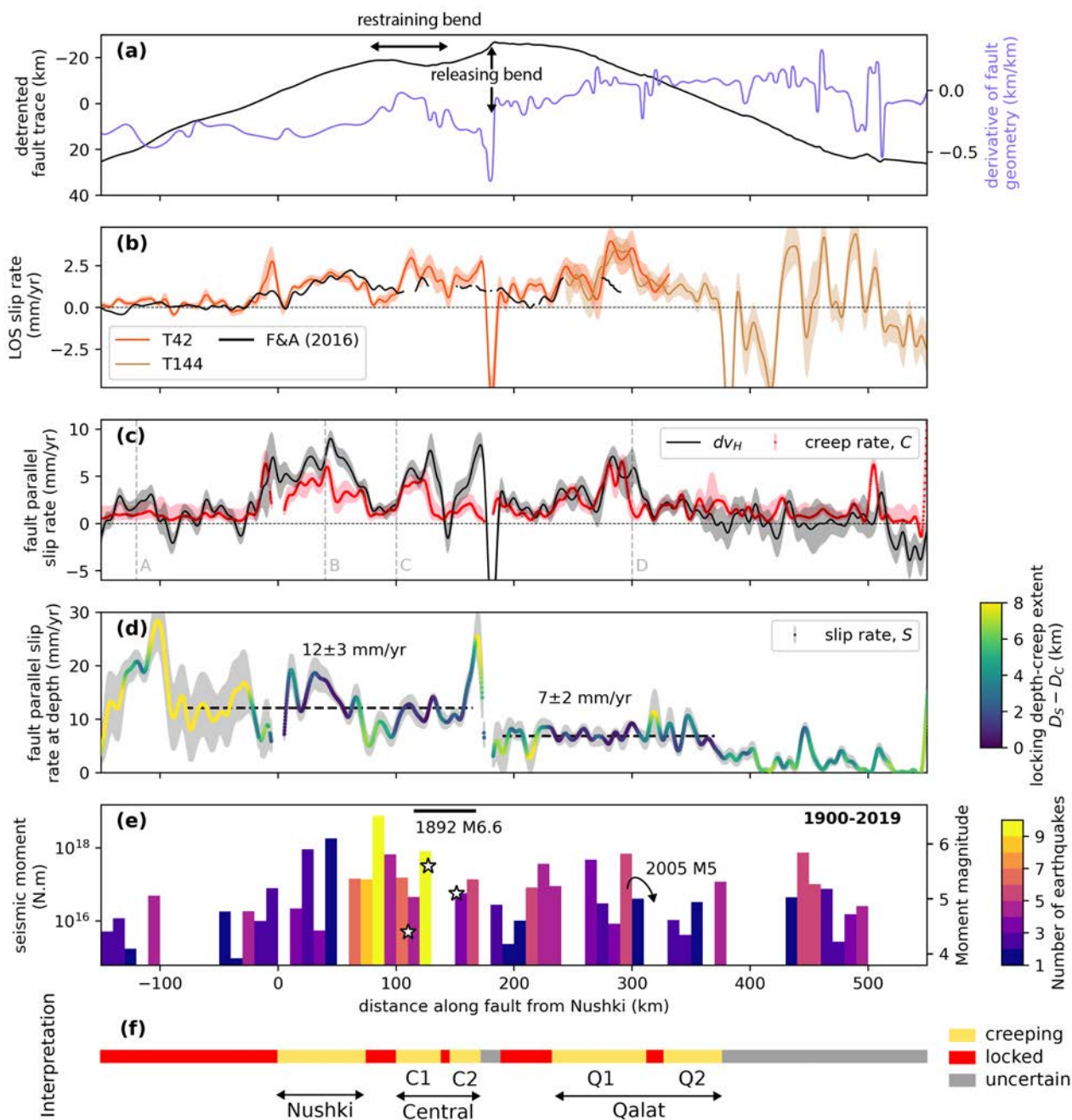


Figure 3.5: Geometry, measured slip rates and seismicity along the Chaman fault. (a) Fault trace and its first derivative, quantifying the variation in fault azimuth along its length in radian. (b) Surface slip rate according to the across fault velocity offset, da_1 , in the direction of the line of sight (LOS) for our two ascending tracks (T42 and T144) as well as from *Fattahi and Amelung* [2016] study (F&A 2016). Notice that the LOS varies from pixel to pixel for Sentinel, and that F&A 2016 data are acquired with Envisat in another (but close) geometry. (c) Surface slip rate projected in fault-parallel direction (Section 3.3.3) according to the velocity offset on each side of the fault, dv_H , or the median of the modelled creep rate, C (Section 3.3.4). (d) Mean of the modelled slip rate S below the locking depth, D_S , colored as a function of the locked depth range (difference of the median depths, $D_S - D_C$). While shading of da_1 , dv_H and S are the one-standard deviation range, shading around C is the interquartile range reflecting the asymmetry of estimated creep rate distributions. Slip rates in (b), (c) and (d) are low-pass filtered, to remove frequency higher than $1/10 \text{ km}^{-1}$ (Figures A.37-A.39). (e) Histogram of seismic moment releases from 1900 to 2019 in 10 km wide bins along the CF (Section 3.2.2). Bar colors indicate the number of events summed per bin. Equivalent M_w are on the right axis (Figure A.40 for other seismic catalogues). Our understanding of the fault segmentation based on aseismic slip rate lateral variations is sketched in (f).

it was preceded by a $M_w 5.3$ earthquake 19 days before and followed by a $m_b 4.4$ two days later at distances within expected location uncertainties (see Figure A.24 for a compilation of magnitude estimates). Surface motions associated with those smaller earthquakes may be included in our InSAR-derived deformation. These earthquakes are close to the northern termination of the 2013 Balochistan earthquake sequence and may relate to the induced stress change [e.g. *Jolivet et al., 2014b; Avouac et al., 2014*]. All other studied earthquakes are essentially left-lateral strike-slip events. The $M_w 5.7$ earthquake that occurred on 21 March 2016 (Figure 3.2d) is located on the northern termination of the Ornach Nal fault and displays up to 4 cm relative displacement in LOS along a 20-km-long fault segment. It is in the spatio-temporal vicinity of nine other earthquakes of smaller magnitudes for a total moment equivalent to a single $M_w 5.73$. Because the August 2015 and March 2016 sequences are off the CF, we will not study them further.

OUR IMAGES of surface displacement produced by the last three earthquakes clearly show that they occurred on the CF itself. The horizontal displacement fields from the combination of the two LOS (Equation 3.2) in Figure 3.6 are essentially made up of two lobes along the fault trace, a positive one west of the fault and a negative one to the east indicating left-lateral motion. The symmetry and shape of the deformation lobes are close to the expected shape of the quadrants of compression for an idealized strike-slip earthquake in a homogeneous medium. Deformation within the extensive quadrants is not retrieved due to the geometry of the ascending and descending LOS with respect to the fault orientation. The May 2016 ($M_w 5.6$) earthquake resulted in a maximum of 8 cm of relative horizontal displacement at the surface and is located right at the junction of a thrust structure to the west (i.e. the Spinatizha fault) and the CF main strand. Two months later, a smaller ($M_w 5.1$) earthquake occurred north of it with similar amplitude of displacement on a shorter fault segment. Note that ~ 5 mm of what looks like postseismic slip of the May 2016 event is included in the displacement field of the July 2016 event (Figure 3.6) due to their spatio-temporal proximity. In June 2018, a strike slip event produced about 2 cm of surface displacement along a 10 km long fault portion.

WHILE the $M_w 5.1$ July 2016 earthquake is isolated, the other two individualized events seem to correspond to groups of earthquakes. The 13 May 2016, three earthquakes in three minutes occurred with $m_b 4.9$ - 5.3 , $m_b 4.7$ - 4.8 and $M_w 5.6$ for a total seismic moment equivalent to about $M_w 5.7$ (Figure A.24). The 27 June 2018, a second earthquake occurred two hours after the $m_b 3.8$ - 4.2 , but with $m_b 3.6$ so that it appears negligible with respect to the main earthquake. Therefore, out of the three events on the CF, the May 2016 event only is treated as a sequence of earthquakes (with total $M_w 5.7$). We now examine the results of the source inversion for these three events.

3.4.3.2 Results of the slip inversion

INVERTED SLIP at depth reaches the surface for all events with a maximum slip of ~ 10 , 8 and 4 cm for the May 2016, July 2016 and June 2018 earthquakes, respectively (Figure 3.7). We observe a chronological decrease in area and amount of slip, consistent with the estimated magnitude from seismic station records (Table 1). The moment magnitude (M_w) of the May 2016 and July 2016 events are 5.7 and 5.1, respectively. For the 2018 event, the National Earthquake Information Center (NEIC) estimates a m_b of 4.1, equivalent to $M_w = 4.4 \pm 0.2$ [Scordilis, 2006]. Our modelled slip on the fault, converted to M_w , yields moment magnitudes of 5.6, 5.3 and 5.0 for the three earthquakes in chronological order, respectively.

THE SOURCE of the May 2016 earthquake is a roughly circular patch centred at about 5 km depth. To first-order, slip of the July 2016 is also best represented by a roughly circular patch at shallow depth (0-5 km depth) where most of the surface deformation is imaged (around 30.65°N). 20 km to the south, a subtle slip signal is interpreted as post-seismic slip remaining from the May 2016 event, while no slip is observed in between above 5 km depth (Figures 3.6 and 3.7). This presumably postseismic signal reaches amplitudes of 1 cm on the fault plane and affects a large area. To improve our estimated M_w of the May and July 2016 earthquakes, we isolate the sub-source moment induced by fault-slip between 30.6 and 30.8°N (dashed lines in Figure

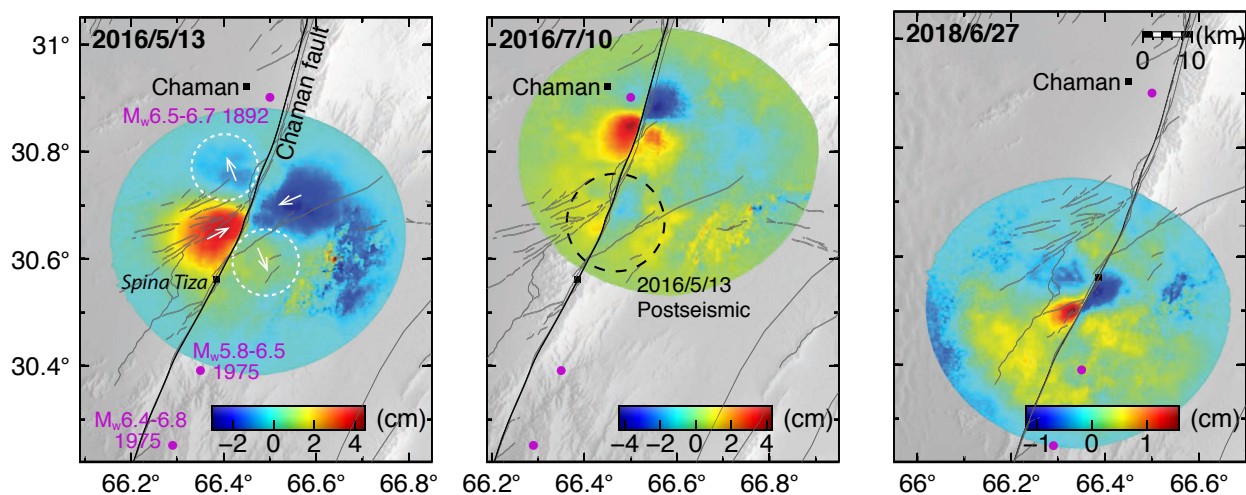


Figure 3.6: Surface horizontal displacement induced by each of the three earthquakes close to the town of Chaman during their coseismic and postseismic periods combining ascending and descending InSAR observations (Equation 3.2). Fault azimuths are assumed constant and equal to 26.7° , 17° and 29° for each event respectively, from left to right. Interpreted direction of horizontal motion for the May 2016 earthquake are shown by white arrows and expected extensive quadrants are circled with white dashed lines. The geometry of the InSAR line of sights (LOS), imply a poor sensitivity to the motion in those extensive quadrants, likely to be as large as recorded motion in the compressive quadrants. This is also true for the July 2016 and June 2018 events. The epicentre of large historical earthquakes attributed to the Chaman fault are located by purple circles with the associated range of moment magnitude (M_w) estimates and year of occurrence labelled in the left plot [Ambraseys and Bilham, 2003a]. Spina Tiza is a frontier post of Pakistan.

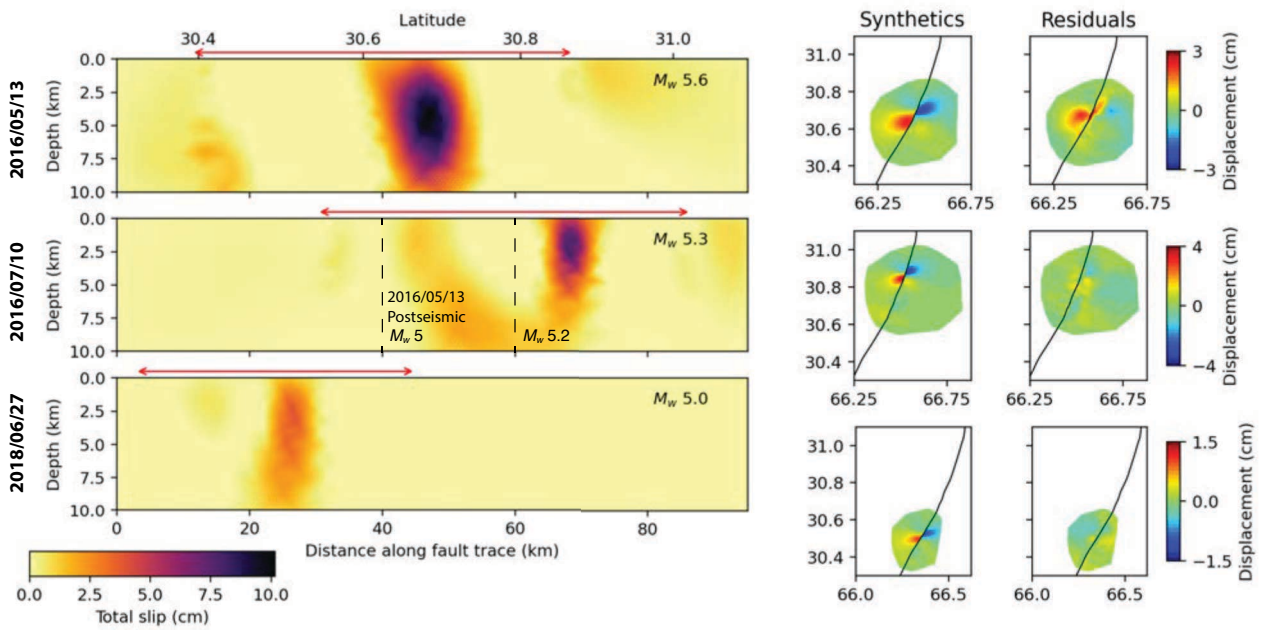


Figure 3.7: Modelled earthquakes slip on the fault plane and associated surface displacement fields for the earthquakes that occurred on 13 May 2016 (top), 10 July 2016 (middle) and 27 June 2018 (bottom). *Left*: Inferred moment magnitudes (M_w) from modelled slip distributions are specified. Red arrows show the fault extent covered by the available deformation field for each earthquake and, thus, under which part of the fault, slip is constrained. The vertical exaggeration is 2. *Right*: Synthetics horizontal surface deformation fields comparable to observations in Figure 3.6 and residuals. The black line is the continuous Chaman fault trace used for inversion.

3.7) and find a corresponding M_w of 5.0. Re-attributing the postseismic moment to the May 2016 event would not change our M_w estimate of 5.6, whereas the July 2016 M_w , ignoring slip between 30.6 and 30.8°N, becomes 5.2.

The residuals between observed and modelled surface displacement are one order of magnitude smaller than the modelled earthquake-related displacement for the July 2016 and 2018 events (Figures 3.7 and A.42). Regarding the May 2016 event, residuals are large (+2 cm in horizontal) with a spatial distribution indicating (i) unmodelled deformation in the south-west lobe and (ii) the difficulty to model the fact that the north-east lobe is offset to the east with respect to the fault trace. This complex spatial pattern may be the consequence of a multi-fault rupture by the three earthquakes involved. Therefore, we only model a fraction of the energy released during the coseismic and postseismic phase, implying M_w estimates from modelled slip of the May 2016 may be underestimated.

3.5 Discussion

3.5.1 A decadal perspective on Chaman fault slip

FAULT SLIP along the 700-km-long Chaman fault (CF) is shown in Figure 3.5 together with a description of the continuous fault trace and the compilation of the seismicity recorded since the beginning of the

20th century. In our interpretation, we divide the CF into creeping, locked and uncertain (probably inactive) segments combining the vision given by fault parallel surface slip rates, modelled slip rates and locking depths only (Figure 3.5f). Because we do not *a priori* consider the fault trace geometry or the seismicity, our segmentation is purely based on the description of aseismic slip and does not pretend to provide units that may rupture in a single earthquake. In this section, we compare our slip rates and segmentation with the seismic record and past slip estimates. We identify two 80-km-long continuously slipping segments: the Nushki segment and the southern part of the Qalat segment (Q1), with mean surface slip rate of 6 ± 1 and 4 ± 2 mm/yr, respectively, measured within 3 km of the fault trace (Figure 3.5c). Three shorter creeping segments are also outlined, two in the Central segment with slip rates comparable to the Nushki segment and separated by a ~ 5 -km-long locked portion, which significance is unclear, and one 50-km-long segment in the Qalat segment (Q2), with less clear evidence : a locking depth of 3.5 ± 0.5 km and a slip rate at the surface of 2 ± 0.8 mm/yr. These creeping segments are separated by "locked" segments with null or uncertain near-fault slip rate, a locking depth exceeding 4 km and a non-zero modelled slip rate at depth. The fault portions north of the Qalat segment as well as between 165 and 190 km are labelled "uncertain" as we cannot identify left-lateral strain on the the fault with our data.

OUR OBSERVED distribution of surface slip along the CF shows good agreement with previous studies and independent data sets. With the method described in Section 3.3.4, we extract slip rate estimates along the CF between 2004 and 2011 from Envisat velocities [Fattahi and Amelung, 2016]. The mean slip rates in 2004-2011 and the previously described slip rates over 2014-2019 exhibit very similar along-strike variations as shown in Figure 3.5b. Additionally, our conversion from LOS to left-lateral slip rate using both viewing direction of Sentinel 1 satellites matches values derived by Barnhart [2017] from previous SAR missions (Envisat and ALOS) with peak creep rate around 10 mm/yr (Figure 3.5c). Barnhart [2017] 's locking depth routinely shallower than 500 m along the Nushki segment cannot be directly compared to our value as the fault model is different. Therefore, we have robust observations representative of the aseismic surface slip rate along the CF which seems constant over at least the past 15 years, between $\sim 28^\circ\text{N}$ and $\sim 31^\circ\text{N}$. In general, shallow aseismic slip (C or dv_H) is significantly lower than the apparent loading rate (or slip rate, S) suggesting stress increases despite the occurrence of aseismic slip.

WE COMPARE this seemingly continuous aseismic slip rate with local slip from earthquakes. We consider the past-century seismic record (1900-2019) and assume that earthquakes within 30 km of the CF occurred on the fault itself (more details in Section 3.2.2). We observe a total seismic moment release of 1.8×10^{19} N.m along the ~ 700 km

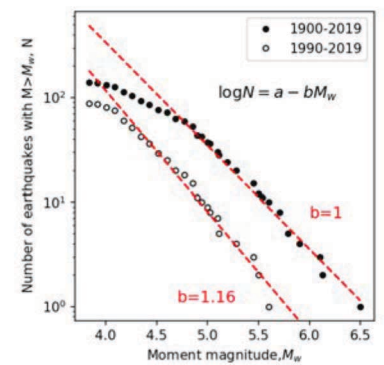


Figure 3.8: Frequency magnitude plot for all earthquakes along the Chaman fault according to the International Seismological Center (ISC) catalogue. The Gutenberg-Richter law is adjusted to two samples of the catalogue covering 1900-2019 (filled circles), and 1990-2019 (outlined circles), 2019 included, and the b -value deduced (red text and dashed lines).

of fault in 120 years (Figure 3.5e, Table 4). The frequency-magnitude relation [Gutenberg and Richter, 1944] indicates that the record of earthquakes with $M_w < 4.5$ on the CF is incomplete, and leads to an estimated b -value of one (Figure 3.8). On this basis, the cumulative moment released associated with unrecorded $M_w 0.1$ to 4.5 over the same period of time is equal to 7.3×10^{18} N.m. The combination of recorded seismicity and extrapolated microseismicity reaches then 2.5×10^{19} N.m, a value equivalent to the moment released by a $M_w 6.8$ earthquake. Based on this estimate, assuming a shear modulus of 30 GPa and a locking depth of 3-6 km, the seismic moment released over 100 years corresponds to slip rates from 3.5 to 1.5 mm/yr, respectively. This suggests that seismicity along the CF contributes to less than 15% of the relative plate motion (about 30 mm/yr) over the last century. Over this time period, the recorded $M_w 5.6$ in May 2016 appears to be exceptional, as were the nearby $M_w \sim 6.6$ of 1975 and 1892 [Bilham *et al.*, 2019]. Nonetheless, in the region, large historical earthquakes ($M_w \geq 7$) were recorded east of the CF within the fold and fault belt (e.g. 1931 $M_w 7.3$ Mach and 1935 $M_w 7.7$ Quetta earthquakes) [Ambraseys and Bilham, 2003a; Dewey *et al.*, 2006]. Hence, assessing the partitioning of deformation between the CF and structures in the fold and fault belt is necessary to assess the seismic hazard of the region, and the CF specifically, but this is out of the scope of this study.

ALTHOUGH the total moment released by earthquakes is small, the along-strike distribution of seismicity and moment is key to assess the relationship between earthquakes and continuous aseismic slip. Historical records attest that earthquakes occurred on both the Nushki and Qalat creeping segments (Figure 3.5e). A seismic crisis between 1975 and 1978 struck the fault 30-100 km north of the city of Nushki with at least four $M_w > 5.5$ earthquakes [Lawrence and Yeats, 1979; Ambraseys and Bilham, 2003a]. Nonetheless, the largest event ($M_w 6.4-6.8$ Spina Teza (also spelled Spin Tezha) earthquake) dating back to October 1975 falls on the locked segment at the northern limit of the Nushki segment with its epicentre at about 85 km. This segment hosted the epicentre of about 15 events since 1900 and, according to our model, accumulates elastic strain. The adjacent creeping segment to the north appears to be particularly seismically-active too and hosted the largest aftershock of the Spina Teza earthquake (with estimated M_w between 5.8 and 6.5), the May 2016 $M_w 5.6$ and the June 2018 event. Those two segments focusing most of the recorded seismicity are along the ~ 100 -km-long restraining bend in the central CF (Figure 3.5a,e). Moreover, a nearby creepmeter (157 km north of Nushki) recorded a slow slip event starting on the 1st of March 2019, and accommodating 4.5 mm of left-lateral slip in 40 days [USGS; Bilham *et al.*, 2019]. This suggests that what we imaged as continuous aseismic slip may include discrete transient slip accelerations. Further north, the only individual earthquake studied, a $M_w 5$ in 2005 relocated with InSAR [Furuya and Satyabala, 2008; Fattahi and Amelung, 2016], occurred on the 20 km-long

locked segment between Q1 and Q2. Considering that our compilation of seismic event generously includes events within 30 km of the fault trace, we have no direct evidence of any earthquake on the Qalat creeping segment itself. The peak of seismicity more than 420 km north of Nushki ($\sim 33^\circ\text{N}$) is on a portion of the CF on which we are not able to identify tectonic strain accumulation (labelled as "uncertain"). Looking at earthquakes in map view (Figure 3.1), the corresponding events are located around subsiding area southeast of the CF (south of the city of Ghazni and along the Gardez fault zone) with negative signal in LOS and deemed fault parallel motion (Figures 3.2a,b and 3.3).

To SUMMARIZE, we measure surface slip and its lateral variations due to aseismic processes stable on a decadal scale, while recorded earthquakes have induced very limited displacement over the past century. We divide the fault into 5 creeping segments separated by locked segments according to the measured slip and locking depth. We find that the central restraining bend is the most seismically active section of the fault and hosts in close spatio-temporal relationship seismic and aseismic slip. In the following, we investigate the importance of postseismic signal for the three recent earthquakes imaged for the accommodation of tectonic stress before discussing mechanical implications.

3.5.2 Postseismic signal characteristics in comparison with coseismic deformation

Date	Latitude	LOS slip rate [†] (mm/yr)	seismic M_w	InSAR M_w	post/coseismic moment	post/coseismic slip [‡]
13 May 2016	30.63	1.2 ± 0.5	$\sim 5.7^*$	≥ 5.6	> 0.09	1.3
10 July 2016	30.78	1.1 ± 0.5	5.1	5.2	0.4	0.4
27 June 2018	30.50	2.4 ± 0.1	$4.4 \pm 0.2^{**}$	5.0	3-15	0.8

Table 3.1: Properties of the three earthquakes imaged on the Chaman fault. InSAR M_w are computed from modeled slip at depth. * This magnitude is equivalent to the sum of the seismic moment from the three earthquakes included in the event. ** This magnitude is a conversion using *Scordilis [2006]*'s relationship from a body-wave magnitude (m_b). [†] Ascending line of sight (LOS) slip rate before the earthquake occurrence looking at a distance to the fault of 0.1-1 km. [‡] This is a lower bound estimate.

Two studied $M_w 5$ (21 October 2005) and 5.5 (19 October 2007) earthquakes within the Chaman fault zone display abnormally large and long postseismic signal with respect to what is usually measured for large ($M_w > 6$) earthquakes [*Furuya and Satyabala, 2008; Fattahi et al., 2015; Alwahedi and Hawthorne, 2019*]. Postseismic slip lasted for more than a year with postseismic to coseismic moment ratio estimates of 0.7 ± 0.1 [*Fattahi et al., 2015*], and 1.1 [*Furuya and Satyabala, 2008*], while it is typically less than 0.3 for large earthquakes (in California) [*Alwahedi and Hawthorne, 2019*]. We further analyze the spatio-temporal footprint of our three earthquakes on the CF to explore potential mechanical characteristics of the fault zone.

We first look back at the moment magnitude (M_w) estimates from the modelled slip on the fault plane (Section 3.4.3.2). Because the reconstructed surface displacement includes coseismic and postseismic slip, we can assess postseismic moment by subtracting the moment computed from seismic waves to our modelled moment. This postseismic moment would also include preseismic transient slip, if any. For the May 2016 event, the estimated M_w of 5.6 is smaller than the total seismic M_w equal to about 5.7. Nonetheless, residuals indicate that our model does not explain a large part of the observed deformation signal, suggesting that the M_w from the model underestimates the InSAR M_w (Section 3.4.3.2). Moreover, we identify a fraction of the May 2016 postseismic slip equivalent to a M_w 5 and, thus, the postseismic to coseismic moment ratio is at least 0.09. Regarding the July 2016 event, we estimate a M_w 5.2, while seismological catalogues indicate a seismic M_w 5.1, which converts into a postseismic to coseismic moment ratio of 0.4. The last recorded event of June 2018 is associated with a seismic M_w of 4.4 ± 0.2 much smaller than the M_w 5 we estimate, leading to a postseismic to coseismic moment ratio between 3 and 15 (Table 1). Therefore, the 2018 event appears mostly as an aseismic event, an idea further supported by the time series of surface slip at this location (Figure 3.9e), in which the step across the fault results from a month-long transient event rather than a clear cut in between two acquisitions.

WE NOW CONSIDER the relationship between coseismic and postseismic deformation using time-series in LOS. From InSAR time-series, the closest measure of coseismic displacement is given by the relative phase change between 6 days framing the time of the earthquake and, thus, it also includes a few days of postseismic slip. We divide the subsequent fault slip into what we name an early postseismic phase lasting 2-3 months and a long-term postseismic in the 300-500 days after the early postseismic phase (pink and blue shadings in Figure 3.9a,c,e). Corresponding across-fault profiles for each period are in Figure 3.9b,d,f. Time series of fault displacement on each side of the fault, averaged between distances of 0.1-1 km of the fault trace, display characteristics logarithmic decay of slip in the months to years following the earthquakes which we interpret as afterslip (Figure 3.9a,c,e; method in Section 3.3.4) [Perfettini and Avouac, 2004; Thomas et al., 2017].

PROFILES in Figure 3.9 allow to compare the amount of slip and its spatial wavelength for the coseismic, early and postseismic phase. The spatial wavelength of deformation qualitatively locates slip at depth, as predicted by Equation 3.3 (i.e. the wavelength of surface deformation roughly equals the depth of slip). First, the almost identical shape of the coseismic and early-postseismic profiles for the event in May 2016 (Figure 3.9b) argues towards an overlap of co- and postseismic slip with comparable amplitudes. Second, the steep across fault gradient of the July 2016 coseismic and early postseismic, indicates that fault slip reached the surface during the earthquake and during the early

postseismic phase. However, postseismic signal is about three time smaller than co-seismic for this event. Third, coseismic displacement related to the 2018 event contrasts with the sharp postseismic signals lasting over a few months indicating the earthquake did not reach the surface and triggered postseismic afterslip near the surface. Taking the specific profiles in Figure 3.9b,d,f and their highlighted optima, we measure peak-to-peak postseismic to coseismic surface slip ratios considering together what we named "early" and "long-term" postseismic and subtracting the preseismic slip rate on our period of postseismic observations (Table 5 compiles all values). We find slip ratios of 1.3, 0.4 and 0.8 for the May 2016, July 2016 and 2018 events, respectively (Table 1). Because our InSAR coseismic images include the first few days of postseismic expected to have the highest slip rates according to logarithmic decay predictions, our postseismic to coseismic surface slip ratios are lower bounds.

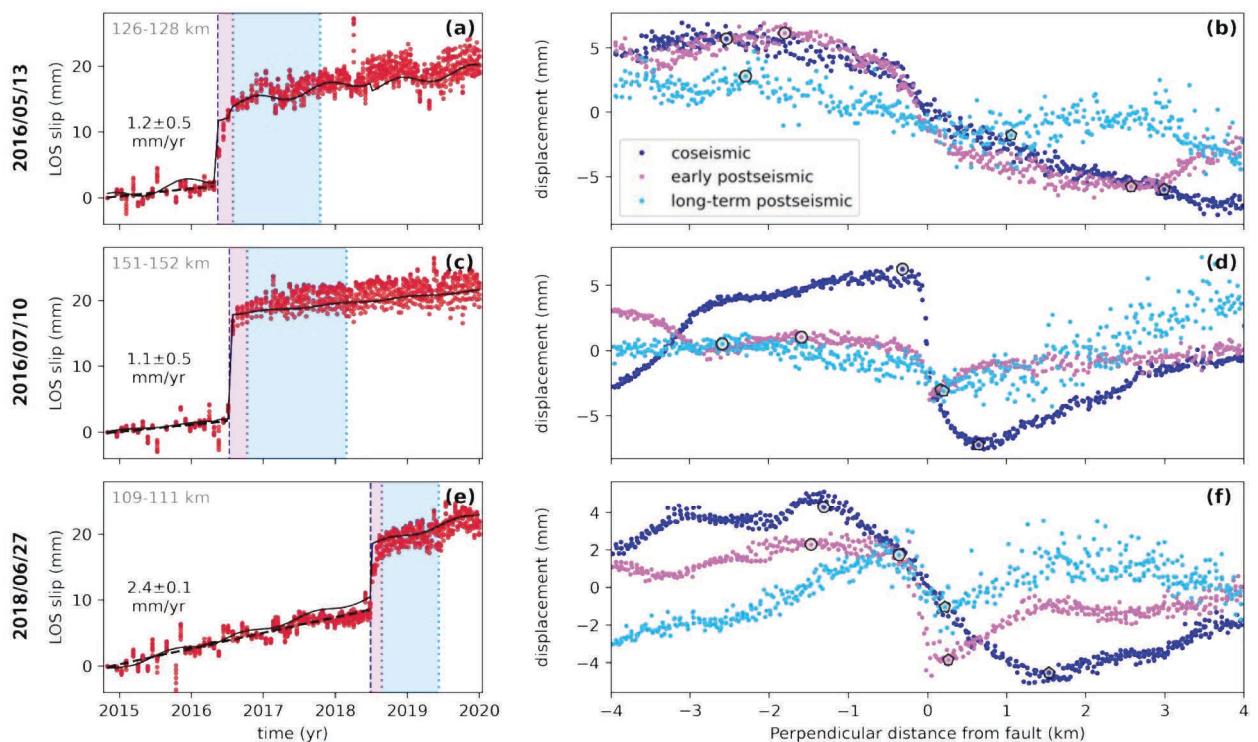


Figure 3.9: Temporal and spatial footprint of coseismic and postseismic deformation according to track 42 for earthquakes on the Chaman fault. **Left**: time series of differential displacement across the fault in LOS at the earthquake location on a 1-2 km long fault segment. The distance in the upper left corner refers to the distance along the fault to Nushki (Figure 3.4). Displayed velocities refer to the best-fitting slip rate before the earthquake. The differential parametrised model from KFTS on each side of the fault is the black line. The dark blue vertical dashed line indicates the timing of the earthquake and shaded regions corresponds to the periods over which the displacement in the plots on the right are measured. **Right**: Profiles of displacement in LOS reflecting the spatial distribution of slip during the coseismic phase as well as during the immediate and longer postseismic phases. Coseismic deformation is taken as the displacement recorded between the two SAR acquisitions framing the earthquake occurrence (dark blue). The local extrema used to compute peak-to-peak displacement are marked by white symbols outlined in black (pentagones for minima, circles for maxima). Profiles cover contiguous but mutually exclusive periods.

OUR DATA for the May 2016 sequence and June 2018 earthquake show

that transient postseismic slip may accommodate as much slip as coseismic slip along the CF and, thus, is key in tectonic strain accommodation. In particular, the June 2018 event imaged with InSAR appears as predominantly aseismic with its postseismic moment being 3-15 times larger than the M_w estimated from seismic waves. Our computation of a postseismic to "coseismic" slip ratio of 0.8 only, indicates that our InSAR coseismic computed using an acquisition on the 7th of July, 10 days after the earthquake occurrence, includes most of the aseismic slip. The significance of the aseismic slip following the May 2016 event is supported by the postseismic to coseismic surface slip ratio of 1.3 for this earthquake. On the other hand, the July 2016 earthquake appears to scale like classical earthquakes, with post- to coseismic ratios in moment and slip equal to 0.4.

FINALLY, these three events are close to the rupture of the 1892 M_w 6.5-6.7 Chaman earthquake [Bilham *et al.*, 2019] and the 1975 Spina Teza earthquake sequence (with a mainshock of M_w 6.4-6.8) [Ambraseys and Bilham, 2003a; ISC, 2020]. The extent of the 1975 Spina Teza surface rupture is not precisely known, but it likely terminated close to the southern termination of the 1892 rupture where the May 2016 earthquake locates (Figure 3.6). This is consistent with either a complex fault structure that would have stopped the rupture [Wesnowsky, 2006] or with local stress concentration left in the wake of the largest events recognized on the CF. The spatio-temporal proximity of the July 2016 earthquake and its inverted slip pattern on the fault plane connected to the May 2016 event (Figure 3.7) indicate that this second event could have been triggered by the first one. Regarding the June 2018 event, the high postseismic to coseismic ratio could lead us to consider this transient deformation event either as a classic co- and postseismic sequence, or as a slow slip event triggered by a small earthquake (with m_b estimates between 3.8 and 4.2). We therefore consider as a follow-up question whether other triggered or spontaneous events can be found along this fault segment, like the one recorded by a creepmeter in 2019 [Bilham *et al.*, 2019].

3.5.3 Variations in slip behaviour, implications for rheology and fault system orientation

WE OBSERVE a spatial segmentation in slip behaviours along the fault with complex interactions between seismic and aseismic slip. What appears as continuous aseismic slip includes the collocated occurrence of earthquakes or slow slip events, and our identified long-lasting Nushki creeping segment has hosted earthquakes in the 1970s. Therefore, the traditional divide between seismically-active locked segments and creeping segments does not fully apply here.

FAULT SLIP is the frictional response of a fault to stress loading. Clas-

sically, considering a rate-and-state formalism, aseismic slip is promoted by rate-strengthening materials, such as serpentine or various clay minerals [Dieterich, 1979; Marone, 1998]. Lawrence and Yeats [1979] mapped serpentinite bodies in the Chaman fault zone at least between 30.55°N and 30.9°N , which hints at velocity strengthening regime along the fault section that, paradoxically, hosted the May and July 2016 earthquakes as well as the $M_w 6.5-6.7$ 1892 earthquake. Hence, the fault plane along this section must also have rate-weakening patches to allow earthquakes to nucleate. However, evidence of spatially overlapping coseismic and postseismic slip challenges this vision. First, we infer shallow continuous slip in the first few kilometres below the surface before the three earthquakes, which are also seen to have reached the surface. Second, the May 2016 postseismic slip probably locates on the coseismically ruptured circular patch at 5 km depth. Evidence comprise the postseismic slip identified in the inversion of the July 2016 event in Figure 3.7 and the comparable coseismic and early-postseismic profiles in Figure 3.9b. Actually, in a rate-weakening regime, geometrical complexities alone promote a variety of slip rates in a continuous spectrum, from earthquakes to very slow events on the same fault segment [Romanet et al., 2018]. Furthermore, low effective normal stress from high pore fluid pressure could favor aseismic slip [Scholz, 1998]. We therefore argue that the coexistence of aseismic and seismic slip along the CF could be explained by a rate-weakening regime within a geometrically complex fault zone including complex fluid circulations. Such hypothesis now remains to be tested against numerical models.

FAULT GEOMETRY and local topography are intrinsically related to local fault activity. The CF geometry is only known through its fault trace (Figure 3.5a, Section 3.2.1). The Nushki segment appears particularly straight compared to the rest of the fault, and can also be recognized by its low mountain front sinuosity [Crupa et al., 2017]. Together with other geomorphological indexes, this low roughness of the fault trace is interpreted as a sign of a tectonically more active fault segment by Ul-Hadi et al. [2013a] and Crupa et al. [2017], an idea confirmed by the elevated surface slip rate along the Nushki segment. At smaller scale, the two peaks in surface slip (and seismic moment release) within the central bend segment are along rather straight fault portions (i.e. the derivative of the fault trace is flat) between 100-130 km and 147-170 km (Figure 3.5). Furthermore, sharp azimuth variations at about 95, 135 and 310 km north of Nushki coincide with three of the observed locked segments (zero surface slip and greater locking depth) separating the creeping segments. This is compatible with the idea that fault trace variations act as barriers to slip propagation [e.g. Wesnousky, 2006; Manighetti et al., 2015; Jolivet et al., 2015b; Van Rijsingen et al., 2019] or that they are the locations of significant off fault deformation [e.g. Okubo et al., 2019]. Actually, numerous subsidiary faults concentrate at bends in the fault system [Ruleman et al., 2007]. Those

are mainly thrust faults, and seem to densify north of 31.3°N where the misorientation of the CF is accentuated by the eastward tilt of the fault.

IN SECTION 3.4.2, we outlined the difference in slip regime south and north of the releasing bend at 180 km. Compared to the Nushki segment, the Qalat segment appears as geometrically more complex and more oblique to plate motion. This obliqueness of about 30° implies that the differential plate displacement projected in fault normal direction rises from 0 ± 2 mm/yr south of 30°N to 15 ± 2 mm/yr on the Qalat segment, according to *DeMets et al.* [2010] and *Altamimi et al.* [2017] (Figure A.43). Thus, the zero fault normal displacement is likely to be a big approximation in this zone where both rigid plate rotation and geomorphological feature of non-rigid deformation evidence non-negligible fault normal motion with respect to the ~ 30 mm/yr fault-parallel motion.

3.6 Conclusion

WE PRECISELY describe slip patterns along the Chaman fault from InSAR time series covering 2015 to 2019. By integrating observations in space and time we outline five continuously creeping segments with maximum left-lateral slip rate in the shallow fault portion (< 2 km) reaching 5-10 mm/yr. This segmentation includes two prominent 80-km-long segments, notably the Nushki creeping segment which locates just south of the Central fault portion, also about 80-km-long, that hosted the most and largest earthquakes in the past-century. This description agrees with previous InSAR measurements from ALOS and Envisat. We estimate an upper bound for the seismic slip contribution to strain accommodation of about 3 mm/yr on average over 120 years. In our observation period, we observe the surface displacement induced by five slip events, and model the source at depth for the three events located on the Central Chaman fault. Significant aseismic slip is found in close proximity to those three earthquakes as pre-seismic slip and large afterslip, for a total induced aseismic strain release close to the one resulting from the earthquakes itself. For the M_w 5.6 May 2016 earthquake, part of the afterslip overlaps with the co-seismic rupture.

Finally, we relate the variations in slip behaviour along the Chaman fault at regional scale with the corresponding length-scales expressed in the fault geometry. The most striking feature is the correlation between the change in fault azimuth north of the Central portion and the change in left-lateral loading rate at depth from 12 ± 3 mm/yr south to 7 ± 2 mm/yr north. As a whole, the Chaman fault accommodates about one third of the differential plate motion. In order to assess long-term seismic hazard, the next step is to quantify the distribution of loading between the Chaman fault and nearby active faults of the plate boundary.

Acknowledgements This work received funding from the European Research Council (ERC) under the European Union's Horizon 2020 research and innovation program (Geo-4D project, grant agreement 758210). Dr Angelique Benoit provided codes and methods at the foundation of this work. Dr Heresh Fattahi shared ENVISAT velocity maps and uncertainties used in *Fattahi and Amelung [2016]*. Raw data used in this study are freely available online. Synthetic Aperture Radar images are from the PEPS platform (scihub.copernicus.eu). The digital elevation model is from NASA EarthData. ERA-5 global re-analyses of atmospheric data are distributed by the ECMWF. Processed data represented in figures are archived on Zenodo (DOI:10.5281/zenodo.5221208). We thank both reviewers, the associate editor and the editor in chief for the extensive and complete reviews which greatly helped improving the initial manuscript. Many figures were created using Generic Mapping Tools [*Wessel and Smith, 1998*].

Chapter 4

PARTITIONING ALONG THE CHAMAN PLATE BOUNDARY: OBSERVATIONS TOWARDS A MIGRATING TRANSFORM PLATE BOUNDARY

Partitionnement du glissement le long de la frontière de plaques de Chaman : observations en faveur d'une migration vers l'est de cette frontière

LA FRONTIÈRE de plaque de Chaman est une large ceinture de failles et de plissements abritant une sismicité distribuée et délimitée à l'ouest par la faille Chaman. Actuellement, le glissement le long de la faille de Chaman ne dépasse pas 12 mm/an (Chapitre 3), alors que le déplacement relatif entre les deux plaques tectoniques est proche de 30 mm/an. Les grands séismes enregistrés au cours du dernier siècle nous indiquent qu'une partie significative de la déformation est prise par des failles à l'est de la faille de Chaman, avec notamment le séisme de Mach en 1931 ($M_w 7,3$), celui de Quetta en 1935 ($M_w 7,7$) et celui, au sud, du Baloutchistan en 2013 ($M_w 7,7$). Nous cherchons à localiser la déformation distribuée, de manière à identifier les structures actives susceptibles de rompre lors de grands séismes.

NOUS UTILISONS les vitesses du sol calculées à partir de séries temporelles InSAR sur 6 ans en ligne de visée ascendante et descendante pour cartographier les gradients de déformation dans la chaîne de Kirthar (Figure 4.1). Les données InSAR ascendantes révèlent un gradient de vitesse est-sud-est qui s'étend sur une centaine de kilomètres de la faille de Chaman au bord de la chaîne de montagne (Figure 4.2). Le saut de vitesse de part et d'autre de la faille de Chaman est abrupt alors que le gradient à l'est apparaît plus diffus, atteignant des amplitudes supérieures à 10 mm/an.

Nous modélisons ces gradients comme l'expression en surface du glissement décrochant sénestre sur trois ou quatre failles verticales : la faille de Chaman, la faille subparallèle de Ghazaband, la faille de Hoshab et une faille inconnue à l'est. L'exploration des paramètres du

modèle souligne que la majeure partie de la déformation actuelle de la limite de plaque se concentre à l'est des failles de Chaman et de Ghazaband, dans le prolongement de la faille d'Ornach Nal au sud et le long de la faille de Quetta-Kalat qui aurait été le siège du séisme de Quetta en 1935 (Figure 4.3, 4.4). Trois portions discrètes de la faille de Ghazaband glissent à des vitesses proches de 10 mm/an.

NOTRE DESCRIPTION du partitionnement est en accord avec les ruptures sismiques connues, et a du sens dans une perspective géodynamique et géologique (Figure 4.6). Nous proposons un modèle tectonique d'évolution de la frontière de plaques avec une migration de la déformation vers l'est (Figure 4.7).

WHILE Chapter 3 focuses on the Chaman fault proper, in the following sections I investigate the role of subparallel strike-slip faults within the Kirthar ranges in the accommodation of differential plate motion. The Sulaiman ranges is not considered because of its more complex geometry and greater compressional component of motion compare to the Kirthar ranges. The present Chapter has been written in prevision of a future paper with Romain Jolivet.

Abstract

The Chaman plate boundary is a wide faulted region hosting distributed seismicity delimited by the Chaman fault along its western edge. The Chaman fault currently accommodates no more than 12 mm/yr, while the differential left-lateral motion between both tectonic plates is close to 30 mm/yr. In the past century, significant earthquakes have ruptured structures east of the Chaman fault, including the 1931 Mach earthquake and 1935 Quetta earthquake with magnitudes greater than 7. We aim to identify where strain focuses so that active structures likely to rupture in large earthquakes are outlined. We use ground velocities computed from 6 years-long InSAR time series in ascending and descending line of sights to map gradients of deformation in the Kirthar ranges. InSAR data reveals that most of the current plate boundary strain focuses east of the Chaman and Ghazaband fault in the central axis of the ranges. We model velocities along profiles across the plate boundary as the surface expression of left-lateral slip on three to four vertical faults: the Chaman fault, the subparallel Ghazaband fault, the Hoshab fault and an unknown fault to the east. We localise strain in the continuation of the Ornach Nal in the south and along the Quetta-Kalat fault which is thought to have hosted the 1935 Quetta earthquake ($M_w 7.7$). Three discrete portions of the Ghazaband fault slip with rates close to 10 mm/yr. Our description of partitioning matches known seismic ruptures, and makes sense in a geodynamical and geological perspective. We propose a tectonic model of the plate boundary evolution with an eastward migration of strain.

4.1 Introduction

THE ONGOING COLLISION between India and Eurasia produces a wide actively deforming margin part of the Alpine-Himalayan belt [Molnar and Tapponnier, 1975; Yeats, 2012; Kreemer et al., 2014]. The western margin of the Indian plate is a 1000 km long strike-slip system in Afghanistan and Pakistan connecting the Himalayan front to the Makran subduction zone [Auden, 1974]. The fault zone reaches widths of 200 km with a complex network of active strike-slip and compressive features along and within the orogenic belt [Bernard et al., 2000; Ruleman et al., 2007]. The seismic record supports this picture, exhibiting distributed seismicity across the range [Quittmeyer et al., 1979; Ambraseys and Bilham, 2003a]. The largest earthquakes (magnitudes, M_w , greater than 7) occurred along the central axis and east margin of the fault system, as well as on the Hoshab fault, splaying west in the Makran prism (Figure 4.1).

THE FAR-FIELD DISPLACEMENT rate is 28-36 mm/yr between India and Eurasia according to global rigid plate rotation model [DeMets

et al., 2010; *Altamimi et al.*, 2017]. This displacement is likely partitioned between several major structures striking roughly north-northeast [*Szeliga et al.*, 2012; *Fattahi and Amelung*, 2016; *Billham et al.*, 2019], including the Chaman fault (CF) at the western end of the fault system between latitudes 27°N and 35°N, the Ornach Nal fault (ONF) in the south (between 25°N and 28°N), the Ghazaband fault subparallel to the CF and the Gardez fault which branches out of the CF around 33°N (Figure 4.1). With respect to those fault's azimuth, the relative motion is essentially in the left-lateral direction (22-36 mm/yr) with a slight compressional component (0-15 mm/yr). Geological estimates of left-lateral slip over the past ~25-20 Myr find 19-24 mm/yr across the whole fault system [*Yeats*, 2012; *Lawrence et al.*, 1992], which is consistent with plate models and with more localized estimates by *Beun et al.* [1979] despite their large uncertainties. Measurements of strain accumulation and aseismic slip rates along the CF are in average no greater than 12 ± 3 mm/yr from Interferometric Synthetic Aperture Radar (InSAR) [*Fattahi and Amelung*, 2016; *Barnhart*, 2017; *Dalaison et al.*, 2021] and Global Navigation Satellite System (GNSS) [*Szeliga et al.*, 2012; *Crupa et al.*, 2017]. This demonstrates that the CF currently accommodates no more than 40% of the total relative plate motion. Where is the rest of the relative plate motion accommodated? This question is directly linked to the identification of active structures likely to produce future large earthquakes and is not straightforward to answer with the current state of knowledge (e.g. very uncertain active quaternary fault in the central Kirthar foldbelt [*Mohadjer et al.*, 2016; *Danciu et al.*, 2017]). Therefore, it is key to measure where strain localizes over this >100 km-wide plate boundary.

WE FOCUS on the 80-120 km wide plate boundary in and along the Kirthar mountain range, from 27°N to the latitude of the city of Chaman (in Pakistan, about 31°N). We map relative ground velocities across the region using InSAR in two lines of sight (LOS) over October 2014 to the end of 2020. Assuming that strain gradients are the surface expression of left-lateral slip, we locate active faults and quantify the amount and depth of slip through Bayesian parameter exploration. We compare the geodetically measured partitioning of strain with the long-term tectonic evolution of this margin.

4.2 Current understanding of the plate boundary

ALTHOUGH there is no consensus, the active Northwest edge of the Indian subcontinent is generally thought to follow from south to north the Ornach Nal fault (ONF), Chaman fault (CF) and Gardez fault zone (GFZ) [*Auden*, 1974; *Powell*, 1979]. However, there is a 50 km offset to the west between the northern end of the Ornach Nal fault and the southern extremity of the Chaman fault. The Ornach Nal fault is considered as the southern en echelon extension of the Chaman

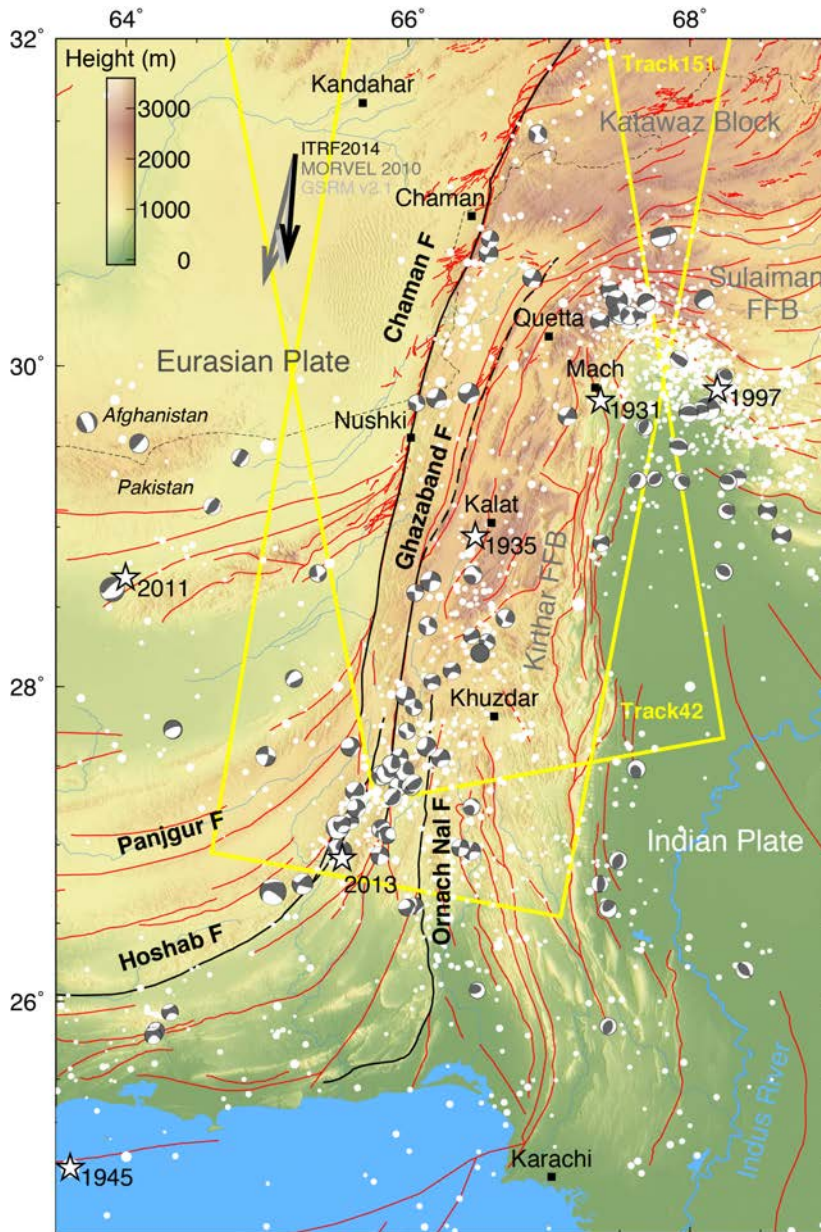


Figure 4.1: Tectonic setting and current seismicity along the southern Chaman fault system. Focal mechanism are from the Centroid Moment Tensor catalogue (starting in 1976) [Dziewonski *et al.*, 1981; Ekström *et al.*, 2012]. Earthquake epicentres in the International Seismological Center (ISC) catalogue from the beginning of the 20th century are indicated by white dots, which sizes are scaled with magnitudes. Epicentres of earthquakes with magnitude estimate greater than 7 are marked by white stars with their year of occurrence. Fault traces are from the USGS report by *Ruleman et al.* [2007]. Arrows show estimated velocities of Europe with respect to Eurasia from three global plate models [DeMets *et al.*, 2010; Kreemer *et al.*, 2014; Altamimi *et al.*, 2017]. Footprints of InSAR tracks are outlined in yellow. Cities of reference are located by black squares. Digital Elevation Model is from SRTM [Farr *et al.*, 2007]. F for Fault. FFB for Fold and Fault Belt.

fault as both faults mark the most significant truncation of structural and stratigraphic trends in Afghanistan and Pakistan [Powell, 1979; Quittmeyer *et al.*, 1979]. Nonetheless, while the CF separates the Central Afghan block to the west and the Miocene to Eocene Khojak flysh belt to the east, the Ornach Nal fault separates the Khojak flysh from Mesozoic sediments further east like the Ghazaband fault [Gansser, 1979; Lawrence *et al.*, 1981; Maldonado *et al.*, 2011]. Thus a similar role in regional tectonic evolution can be associated to the Ornach Nal fault and the Ghazaband fault, although the transition between 27.5 and 28.5°N is unclear. This is probably where the Arabian, Indian and Afghan plates met in a triple junction in the late Mesozoic, early Cenozoic after the closure of the Neothetys Ocean about 40 Ma [Jacob and Quittmeyer, 1979; Seton *et al.*, 2012; Siehl, 2017].

Ophiolites (i.e. fragments of oceanic crust and subjacent mantle) are found east of the Ornach Nal fault (Bela ophiolites) and south of the Katawaz Block (Muslim Bagh ophiolites) locating the suture between the Eurasian plate and the Indian subcontinent East of Ghazaband fault [Asrarullah *et al.*, 1979; Bannert and Raza, 1992]. However, geological studies suggest that those ophiolites have moved relative to the underlying basement and have probably been thrust onto the subcontinent in a thin-skinned fashion during the Paleocene or earliest Eocene [Powell, 1979; Gansser, 1979; Allemann, 1979; Tapponnier *et al.*, 1981; Gnos *et al.*, 1997; Khan *et al.*, 2007]. How does this long-term geological picture fit with historical records of seismicity?

ALONG the plate boundary, the largest recorded earthquakes ($M_w > 7$) since the end of the 19th century are the 1935 $M_w 7.7$ Quetta earthquake, which ruptured an unnamed fault between the city of Quetta and Kalat, the 2013 $M_w 7.7$ Balochistan earthquake on the Hoshab fault in the Makran accretionary prism, the 1931 $M_w 7.3$ Mach earthquake accompanied by two $M_w 7.1$ along the eastern edge of the Kirthar fault and fold belt where the topographic gradient is steep, and, lastly, the 1997 $M_w 7.1$ in the Sulaiman fault and fold belt [Skirine, 1936; Ambraseys and Bilham, 2003a; Aouac *et al.*, 2014; Jolivet *et al.*, 2014b; Nissen *et al.*, 2016]. While the Quetta and Balochistan earthquakes were essentially strike-slip, the Mach and 1997 earthquakes ruptured with a thrust motion. The largest event on the Chaman fault itself is the 1892 $M_w 6.5-6.7$ [Bilham *et al.*, 2019].

Considering all recorded magnitudes, past century seismicity is distributed over broad zones of Cenozoic deformation but it tends to focus (1) at the hinge between the Kirthar and Sulaiman Fold and Fault Belts (FFB), around the Sibi re-entrant; (2) along the Chaman fault north of the town of Nushki and (3) in the central Kirthar FFB between the epicenter of the 2013 Balochistan earthquake and the town of Kalat (Figure 4.1). While (1) contains mainly thrust events, the other two are broad strike-slip deforming regions aligned with the plate boundary (north-northeast) [Quittmeyer *et al.*, 1979; Reynolds *et al.*, 2015]. From the seismic record only, it is unclear whether (3) corresponds to a fault, or many faults and mapped faults tend to end in this region. We aim to clarify the transfer of deformation from south to north between the Ornach Nal fault and the Chaman fault through mapping of current strain using InSAR.

4.3 Materials and method

4.3.1 Obtaining velocities from InSAR

WE BASE this work on InSAR velocities obtained from time series analysis. Two time series covering 2015-2020 were built along ascending (Track 42) and descending (Track 151) passes of the Sentinel 1A-B

satellites (scihub.copernicus.eu). The data and method is the same as in Chapter 3 extended in time to December 2020. Our time series analysis method (KFTS; Chapter 2) computes the evolution of ground deformation over time with its uncertainty based on unwrapped interferograms and a simple parametrised model describing deformation. Interferograms are constructed using the ISCE package (JPL/Caltech, winsar.unavco.org/isce.html) and corrected from atmospheric delays with ECMWF-ERA 5 global atmospheric model (PyAPS software; *Jolivet et al. [2011, 2014a]*). Areas with a minimum coherence of 0.6 are unwrapped using a branch cut algorithm [*Goldstein and Werner, 1998*] and potential unwrapping errors are corrected based on local misclosure (PhaCo software; Benoit et al. 2020). The best-fitting two dimensional linear ramp north of the Chaman fault is subtracted to each individual interferogram to remove long-wavelength biases. The parametrised model of deformation corresponds to a linear combination of functions of time from which, among others, the mean ground velocity in the Line of Sight (LOS) direction is obtained (see Section 3.3.2 for more details).

4.3.2 Defining an appropriate model for InSAR velocities

OUR STUDY AREA benefits from a land cover and a dry climate particularly suitable for InSAR study implying high coherence and small uncertainties. Indeed LOS velocities are known to precisions inferior to 1 mm/yr on most pixels (Figure 4.2). Ascending velocities display a east-southeast gradient spreading from the edge of the Ridgestan desert to the Indus plain consistent with along-fault left-lateral motion. On the opposite, the near-fault-parallel orientation of the descending track implies that the LOS velocity field has a very poor sensitivity to left-lateral motion. Still, to the north, where the Chaman fault (CF) has a greater azimuth, localised across-fault velocity gradient is identifiable along the descending track. Furthermore, a prominent positive velocity anomaly is imaged along and east of the Hoshab fault, which we associate with postseismic motion of the 2013 $M_w7.7$ Balochistan earthquake. A negative gradient across the eastern edge of the Kirthar ranges in both viewing directions indicate vertical motion, with the Kirthar ranges going up with respect to the valley.

WE WOULD LIKE to assess if the computed InSAR velocities in the ascending and descending direction can be the result of localized left-lateral slip on a number of faults. We draw 160-km-long profiles in the velocity maps every 2 km along the Ghazaband fault, centred on the fault and perpendicular to it. The Ghazaband fault is chosen as a reference as it lies in the center of our region of interest in the axis of the plate boundary (NNE) (Figure A.44). Data covering towns, cultivated areas and mines are ignored because of the potential effect of human activities on measured ground velocities (mainly subsidence as

a consequence of groundwater withdrawal). Remaining surface velocity gradients in profiles are considered to be of tectonic origin.

FAULT GEOMETRIES and slipping directions in the central axial belt are very uncertain. While the Chaman fault trace is precisely known, other fault traces are roughly mapped from limited field work (1960s Colombo plan) and aerial and space images [Jones *et al.*, 1961; Auden, 1974; Ruleman *et al.*, 2007]. Focal mechanisms south of Kalat (Figure 4.1) indicate a dominating sinistral strike-slip motion in the central axial belt (Global Centroid Moment Tensor catalog, Ambraseys and Bilham [2003a]). Thrust earthquakes, reverse faults and vertical motion in our InSAR velocities are identified along the eastern border of the ranges, but this region is not covered by our profiles. With this state of knowledge, the best model corresponds to slip on several strike-slip faults, assumed to be vertical for simplicity.

4.3.3 Modelling parallel strike-slip faults

SURFACE DISPLACEMENT due to a strike-slip fault is modelled by the displacement field around a screw dislocation embedded in an elastic half space model [Savage and Burford, 1973]. We include four faults

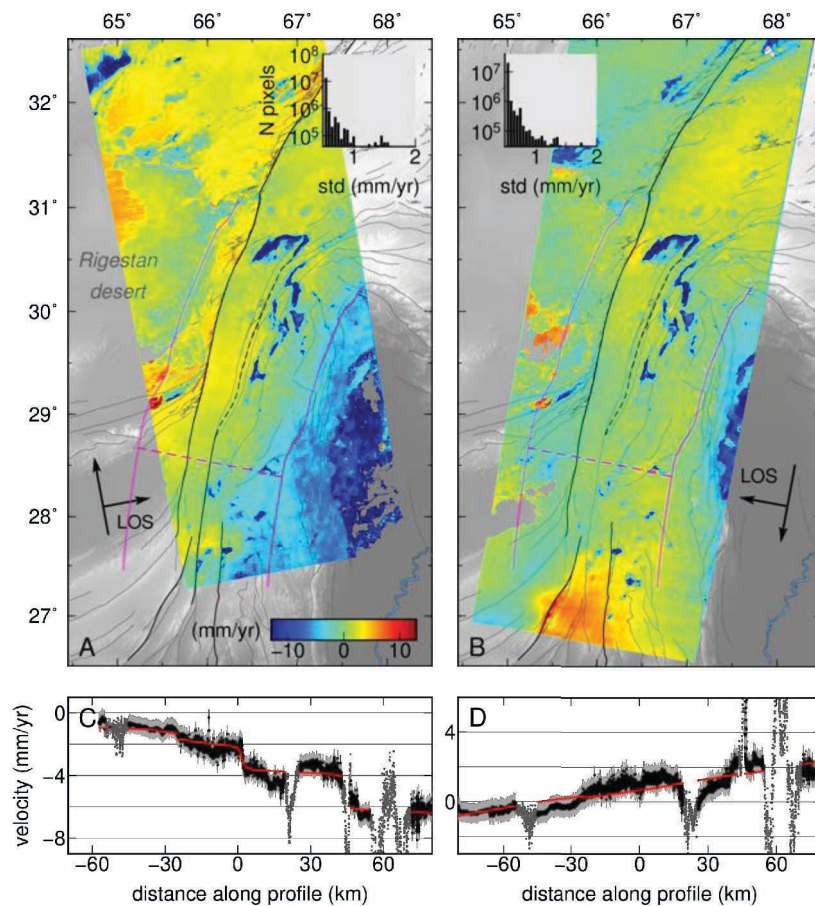


Figure 4.2: Velocity in ascending (A, C) and descending (B, D) directions computed with InSAR. A and B show velocity fields overlaid on topography, while C and D are velocities from a profile located in maps by the dashed magenta lines. This profile is an example of the 193 profiles centred on the Ghazaband fault, which endpoints are located by magenta markers in A and B. Histograms of velocity standard deviations (abbreviated std) are in A and B. Profiles in C and D include data kept for the model in black with light grey error bars, masked data in grey and the predicted velocities in red from the median of our posterior model. LOS: line of sight.

which are, from west to east, the Chaman fault (CF), the Hoshab fault (HF), the Ghazaband fault (GF) and an unnamed fault to the East, thereafter named "Eastern fault" (EF). We assume vertical faults and impose fault parallel displacement consistent with sinistral sense. The assumptions of 90° dip and zero rake were already used by *Fattahi and Amelung [2016]* and tested by *Barnhart [2017]* for the case of the CF.

EACH FAULT accommodates strain below a locking depth. Geodetic observations and frictional laws show that many faults also "creep" (i.e. slip slowly) near the surface, producing an across-fault step in measured surface velocities. Such aseismic slip is attested on the Chaman fault (Chapter 3) and probable along the Hoshab fault as a result of post-seismic of the 2013 Balochistan earthquake [*Peterson and Barnhart, 2017; Wang and Fialko, 2017*]. Sharp velocity changes around the Ghazaband fault or to the east are not evidenced by our InSAR velocity field. To limit the number of parameters to explore we assume no shallow aseismic slip for those two easternmost faults.

Therefore, surface displacement in LOS, f , for ascending and descending tracks (a, d superscripts) as a function of the distance, x , along the profile is modelled as :

$$f(x)^{a,d} = \frac{-1}{\pi} \left(\sum_{i=1}^4 \mathbf{L}(x)^{a,d} \mathbf{G}_i S_i \tan^{-1} \left(\frac{x - C_i}{D_i} \right) + \sum_{i=1}^2 \mathbf{L}(x)^{a,d} \mathbf{G}_i A_i \tan^{-1} \left(\frac{E_i}{x - C_i} \right) \right) + Y^{a,d} + V^{a,d} x \quad (4.1)$$

With $\mathbf{L}(x)$ the varying LOS vector of Sentinel 1 wide swath images, \mathbf{G}_i the vector of fault orientation depending on the local fault azimuth α_i ($\mathbf{G}_i = [\sin(\alpha_i), \cos(\alpha_i), 0]$), S_i the amount of slip below a locking depth D_i on a fault located at C_i with respect to $x = 0$. Subscripts i are for each of the 4 faults from west to east (1, 2, 3, 4 for CF, HF, GF, EF respectively). Creep rate and extent for CF and HF are A_i and E_i . Lastly, Y is a constant offset of the profile and V a slope along the whole profile length.

INTERDEPENDENT PARAMETERS S_i, C_i, D_i (i in [1,2,3,4]) A_i, E_i (i in [1,2]) Y and V are explored with a Metropolis-Hastings sampling ¹ [*Metropolis and Ulam, 1949; Metropolis et al., 1953; Salvatier et al., 2016*]. While parameters characterizing the fault are common to the two viewing directions, parameters Y and V are proper to each viewing direction. When a fault does not cross a given profile, then it is excluded from the inversion. This is true for CF in the south, or HF in most profiles except in the south. For a profile crossing all 4 faults there are 20 parameters to adjust.

¹ 5×10^4 samples of the parameter space to infer probability density functions plus 1×10^4 discarded samples used for initial tuning

4.3.4 A priori knowledge on parameters

WE ADD a systematic prediction error of 2 mm/yr to the data to account for errors induced by the imperfect functional description in Equation 4.1 [e.g. *Tarantola, 2005; Duputel et al., 2014*]. Parameters are explored within a likely spread of natural values, incorporating physical and tectonic knowledge of the region. This limits the realm of possibilities maximizing the chance to find meaningful optima. *A priori* distributions are truncated Gaussian functions except for the amount of slip S_i and the offset Y for which a uniform law is preferred in order to minimize the role of the *a priori* in the final slip estimate (see Table 6 for a complete description of *a priori* distributions). Maximum locking depth is set to 15 km. The Chaman and Hoshab faults have been precisely mapped [*Ruleman et al., 2007; Jolivet et al., 2014b*], whereas the mapped Ghazaband fault has several strands and the location of the Eastern fault is completely uncertain. Hence, the standard deviation of the distribution of C_1 and C_2 is 250 m, while it is 1 km for C_3 and 4 km for C_4 .

FOR physical consistency, we set that the creep extent on a given fault has to be inferior to the locking depth (i.e. $E_i < D_i$ for $i = 1, 2$). Moreover, to incorporate what we know from global geodetic models we add the condition that the sum of slips on all faults, except the Hoshab fault ($S_1 + S_3 + S_4$) should be 30 ± 3 mm/yr. This tectonic constrain on total slip limits the ambiguity between slip depth and amount of slip. Indeed, large deep slip may seem equivalent to smaller and shallower slip as seen in the joint distributions of S_i and D_i (e.g. Figure A.45). Furthermore, the maximum locking depth of the Ghazaband fault, D_3 , is limited by the proximity of the Hoshab fault in the south so that the strong postseismic signal does not leak into the Ghazaband fault slip estimate. The maximum locking depth is then two third of the *a priori* along-profile distance between both faults.

4.4 Results

FIGURE 4.3 displays the inferred fault location, slip and locking depths for each profile. The mean behaviour per fault is in Figure 4.4. Because of the positivity constraint on slip and locking depth, their *posterior* probability distributions are skewed (Figure 4.4). Therefore, we chose the median and interquartile range as reference statistics. Results of our inversion confirm the previous idea that slip is shallow on the CF, especially along the segment north of Nushki, with slip rates close to 10 mm/year. More specifically, on the Nushki segment of the CF (0-80 km) the difference between creep extents and locking depths is 1.2 (0.9-2) km (Figure 4.5), while south of Nushki there is no significant creep and a locking depth of 7.2 (4-9.5) km. The interquartile range of slip along the studied CF is 5.7-11.2 mm/yr.

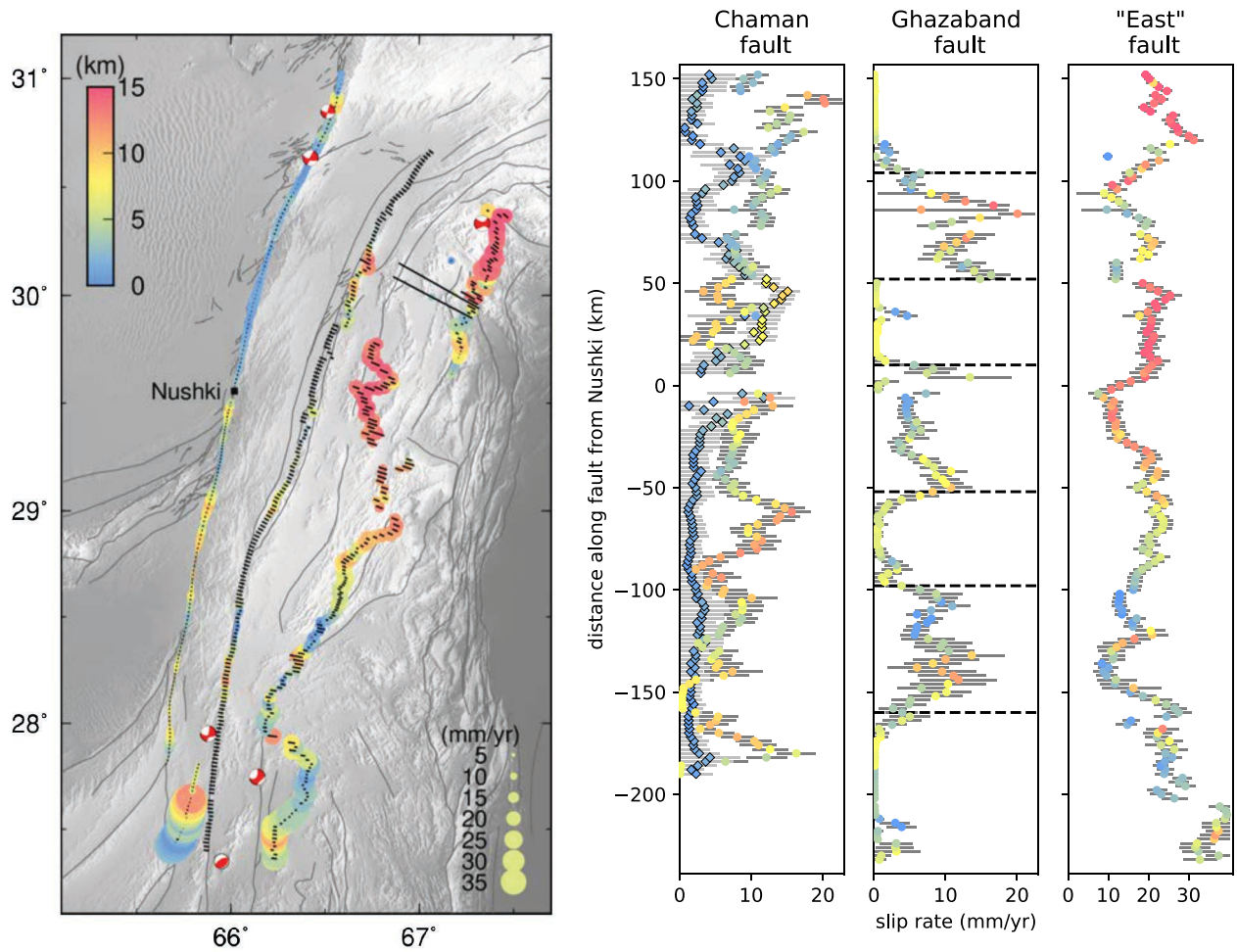


Figure 4.3: Inferred velocities, fault locations and locking depths from the adjustment of Equation 4.1 to InSAR velocities (Figure 4.2). On the left is a map with fault location indicated by round markers, which sizes are scaled with slip and colour depends on locking depth (minus creep extent for the CF and HF), overlaid on topography. Median estimates are taken as reference and the spread of likely fault locations is shown by black bars. Uncertainties associated with slip are on the right plot for the three faults of interest. Creep on the Chaman fault corresponds to outlined diamond marker and lighter grey error bars. Marker colours have the same scale as the left plot and refer to locking depth or creep extent. What we identify as strained segments of the Ghazaband fault are delimited by black dashed lines.

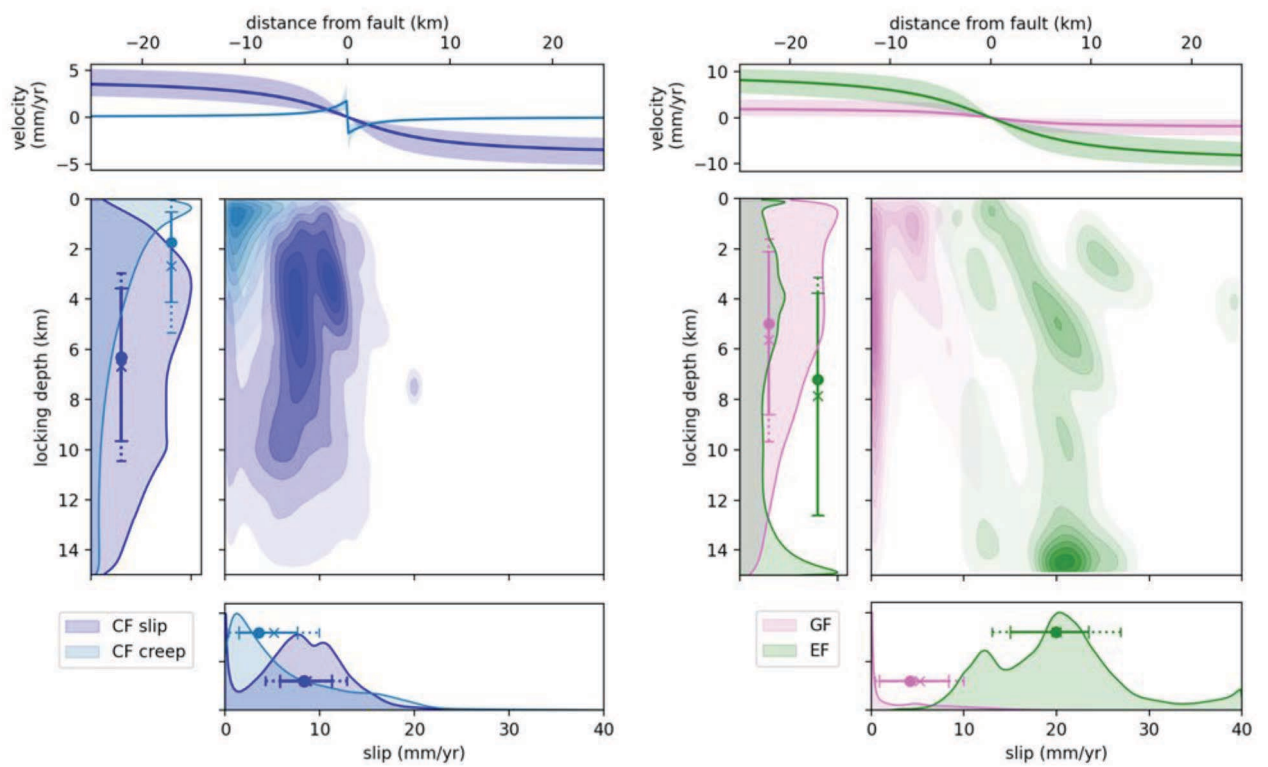


Figure 4.4: Slip and locking depth statistics per fault: Chaman fault (CF) on the left, Ghazaband fault (GF) and East fault (EF) on the right. Median and interquartile range are shown by the round marker and plain bars, while mean and standard deviations are crosses and dashed bars. The across fault surface velocity produced by the median model is on the top plot. This outlines that we measure little strain along the Ghazaband fault, that the Eastern fault consistently accommodates about 20 mm of slip per year along most of its length, and that the Chaman fault has shallow locking depth.

IT SEEMS that the Ghazaband fault (GF) can be divided into portions of roughly 50 km in length which alternatively host measurable strain or not (Figure 4.3). The southernmost slipping section is located just north of a segment that ruptured in August 2020 (M_w 5.7 from GCMT) and slips at rates between 4 and 14 mm/yr with locking depth that reaches small values (<1 km) at the location of the 2007 M_w 5.5 earthquake described in *Fattahi et al. [2015]* (located in Figure 4.6), indicating sharp across-fault velocity gradients. The middle slipping section of the GF is south of Nushki and displays similar characteristics, while the northern section seems to host more slip (reaching 20 mm/yr) but with large uncertainty. The inferred location of those slipping portions outline that the active fault trace of the GF is the eastern strand along the mountain ridge.

OUR MODEL'S most striking output is the large amount of strain focusing 25-60 km east of the GF. On the hypothetical Eastern fault (EF), the median slip rate (i.e. S_4) is 20 (15-23) mm/yr. Inferred EF location suggest that different physical faults are modelled with this unknown fault, which has lots of freedom in its likely parameter values. Indeed, lateral jumps between successive profiles (2 km away) reach about 40 km like around 0 km on our along-fault distance scale with respect to the profile passing through the city of Nushki (Figure 4.3). Around 28°N , the EF location fall exactly in the continuation of the mapped Ornach Nal fault (ONF) and the locking depth inferior to 10 km indicate a narrow gradient, that is also visible in raw data (Figure 4.2). Our EF is in the continuation of the ONF up to the latitude of Kalat, further north the EF is shifted west along the Kalat-Quetta axis and then back east near the town of Mach. Nonetheless, north of the town of Kalat the locking depth is most of the time greater than 12 km, suggesting a spread-out gradient of deformation in this region and, consequently, the fault origin of the displacement is more uncertain. The northernmost profiles may be affected by thrust motion that we are unable to model especially near the town of Mach, where the 1931 M_w 7.3 thrust earthquake occurred. Additional uncertainty near Quetta arises because of the high population density in this zone which resulted in large area of the data being masked (Figure A.44).

Velocity estimates in the south are disturbed by three contemporary earthquakes in 2015, 2016 and 2020 whose co-seismic displacements are estimated during time-series analysis. The 2016 M_w 5.7 earthquake on the northern end of the Ornach Nal fault lies in the continuity of the EF further north and its postseismic deformation may produce the nearby eastern shift of the EF (Figure 4.3). Indeed, at those latitudes the EF location seems to follow the edge of a 30-km wide lobe surrounding the epicentre (Figure 4.2).

REGARDING the Hoshab fault (HF), large slip rates are inferred but

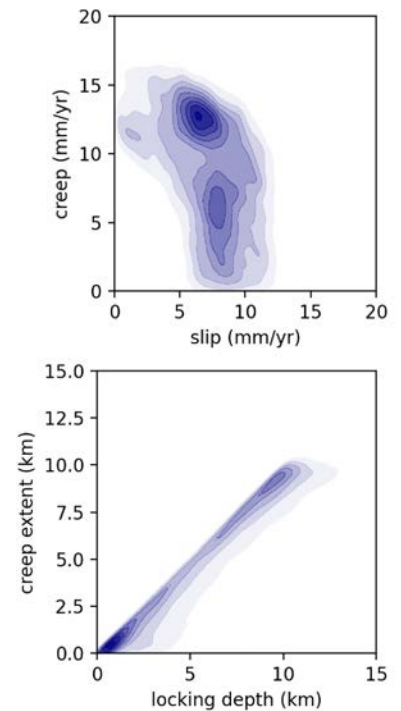


Figure 4.5: Statistics for the Nushki segment of the Chaman fault (between 0 and 80 km). The joint distribution of creep A_1 and slip S_1 (top) and of locking depth D_1 and creep extent E_1 (bottom) are from thousand samples drawn randomly in the posterior distribution for each profile crossing the Nushki segment.

values are poorly constrained as the ascending data on the western side of the fault is missing. Moreover, the deformation pattern seems to spread on more than 100 km (Figure 4.2) suggesting postseismic viscous relaxation which spatial signature is not properly modelled with our oversimplified dislocation model. Therefore, the modelled slip on the HF is hardly interpretable and we will not study it further. In the following, we confront our numerical description of strain distribution with the understanding of the plate boundary arising from seismology, geology and geodynamics.

4.5 Discussion

4.5.1 Partitioning of slip and mapped earthquake ruptures

EARTHQUAKES provide the most robust evidence of current strain partitioning in the plate boundary independently of what we learn from InSAR velocities, since there are very limited Global Navigation Satellite Systems (GNSS) stations [*Khan et al., 2008; Szeliga et al., 2009; Mohadjer et al., 2010; Szeliga et al., 2012*].

Identified slipping portion of the Ghazaband fault (GF) in the south are in agreement with contemporary seismicity ($M_w 5.5$ in 2007 and $M_w 5.7$ in 2020). Along our central slipping GF portion (29-29.5°N), with a similar approach to ours [*Fattahi and Amelung, 2016*] identified 16 ± 2 mm/yr of slip below a locking depth of 11 ± 2 km. We measure no strain along the northernmost terminus of the fault. InSAR velocities from Envisat and ALOS (2003-2011) [*Barnhart, 2017*] like GNSS velocities over 2007-2011 [*Szeliga et al. [2012]*] do not show any gradient associated with the GF at the latitude of Quetta either. However, the 1993 rupture ($M_w 5.6$) in the continuations of the GF at the latitude of Chaman suggests a favourable stress for rupture on the GF at high latitudes too.

THE DRAMATIC 1935 Quetta earthquake has been attributed to the GF [*Lawrence et al., 1992; Yeats et al., 1997; Szeliga et al., 2012; Fattahi et al., 2015*]. However, a review of observations made at that time [*West, 1935; Skrine, 1936; Ambraseys and Bilham, 2003a*] suggest that slip was on a subparallel fault extending from Kalat to Quetta (about 20 km east of GF) [*Dewey et al., 2006; Bilham et al., 2019*]. Two observations suggest that this active Quetta-Kalat fault (QKF), also named "Chiltan-Takhatu fault" or "Quetta fault", may continue north of Quetta : a 1.6 km-long (one mile) surface fracture has been observed following the 1955 Quetta earthquake along the fault [*Kazmi, 1979*] and one of the rupture in the 2008 Ziarat earthquake sequence [*Pinel-Puysségur et al., 2014*] is aligned with the QKF (Figure 4.6). At those latitudes our model of strain distribution is particularly uncertain due to extensive groundwater withdrawal for agriculture, which overwrites tectonic signal in InSAR (up to 20 cm/yr of subsidence; Figure A.31).

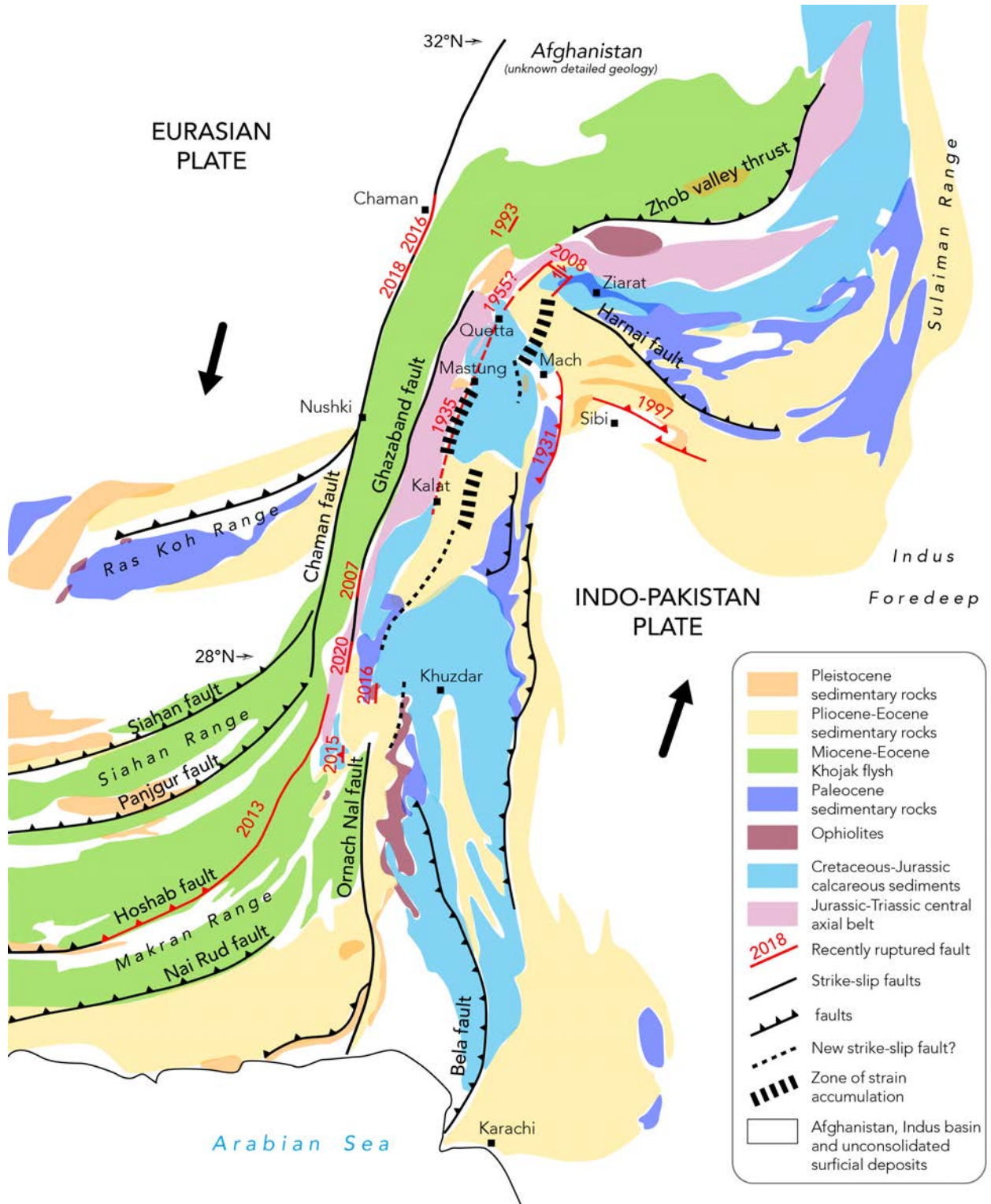


Figure 4.6: Plate boundary geology and faults. Geology is essentially from *Bakr and Jackson [1964]; Maldonado et al. [2011]*. Main faults only are included. Strike-slip faults with no direction of motion specified are left-lateral. Rupture extent in red are from *Kazmi [1979] (1955), Ambraseys and Bilham [2003a] (1931), Szeliga [2010] (1993), Jolivet et al. [2014b] (2013), Pinel-Puysségur et al. [2014] (2008), Fattahi et al. [2015] (2007), Nissen et al. [2016] (1997), Bilham et al. [2019] (1931,1935), Dalaison et al. [2021] (2015, March 2016 on the ONF, May 2016 on the CF, 2018) and this study (2020)*.

Identified strain is localized further east, just west of Mach, where the "Johan fault" is mapped [Kazmi, 1979; Kazmi and Rana, 1982]. Along the same axis, the deeper and broader deformation zone north of 30°N is more uncertain and is aligned with another rupture of the 2008 Ziarat earthquake sequence [Pinel-Puysségur *et al.*, 2014; Usman and Furuya, 2015].

The multiple rupture of conjugate and parallel faults involved in the Ziarat earthquake sequence and post-seismic phase outline complex faulting and partitioning, at least in the Quetta syntaxis (the hinge between the Kirthar and Sulaiman FFB along an axis between the cities of Sibi and Chaman). This pattern of parallel left-lateral faults is interpreted by Szeliga [2010] as an evidence of Bookshelf tectonics at the 100-km-scale ("en echelon" faults), producing a long-term clockwise rotation of the system, which induces right-lateral shear along the Sibi-Chaman axis (Northwest-southeast). According to Khan *et al.* [2008], right-lateral shear occurs in the underlying basement at about 8 mm/yr and relates to the co-located bend in the Chaman fault.

SUBPARALLEL RUPTURES with similar spacing of about 30 km is also seen around 28°N, to which we can extrapolate the Quetta syntaxis deformation model. The March 2016 rupture (M_w 5.7) on the Ornach Nal fault (ONF), like the nearby 2015 and 2020 ruptures may be related to subsequent stress transfer related to the 2013 Balochistan earthquake and its aftershocks [Avouac *et al.*, 2014; Jolivet *et al.*, 2014b]. In turns, the 2016 may also contribute to the loading of nearby faults: the GF, and perhaps an unknown structure to the East where we measure significant and sharp strain (20-40 mm/yr).

REGARDING the Chaman fault (CF), our measured slip rates (about 10 mm/yr) and shallow locking depth (80% <5 km) are in agreement with previous observations and models [Furuya and Satyabala, 2008; Szeliga *et al.*, 2012; Barnhart, 2017; Fattahi and Amelung, 2016]. Along the Nushki segment, data corroborate the idea that the fault slips from the surface down to the brittle ductile transition as previously outlined in Barnhart [2017] and Chapter 3.

Therefore, our observations combined with mapped earthquake ruptures highlight the distributed character of deformation occurring in continuous and transient events within a broader left-lateral shear zone.

4.5.2 Inset from Geology

AS OUTLINED in Section 4.2, the CF and GF are the most prominent discontinuities in the geology and structures (Figure 4.6). Nevertheless, the other active faults that we map lie along geological boundaries. The QKF falls on the contact between Jurassic and Triassic sedimentary rocks of the Shirinab formation (pink in Figure 4.6) and more

recent units to the west [Szeliga *et al.*, 2009]. The ONF northern continuation is subparallel to the structural trends but our inferred fault trace cuts through the Kalat plateau of Eocene sedimentary rocks (yellow in Figure 4.6). This plateau, bounded by a thrust to the East, is known to be faulted in its central part by the "Pandran fault" [Bakr and Jackson, 1964; Kazmi and Rana, 1982; Bannert and Raza, 1992; Ruleman *et al.*, 2007] (Figure 4.1). According to Arshad *et al.* [2011] surface faults in the Kalat plateau are thrusts with a left-lateral root below 5 km-depth, which is consistent with our locking depth estimates in this region (Figure 4.3). Our inferred fault just east of the March 2016 rupture (north of the Bela fault) lies along the Bela Ophiolites.

Only the diffuse zone of strain accumulation north of Mach has little geological meaning, outside of the fact that the Quetta syntaxis zone is highly deformed along several directions which our model do not capture because EF is assumed parallel to the GF (perpendicular to profiles) and purely left-lateral.

THEREFORE, observations seem consistent with localized slip on several faults within a lithosphere deforming as a rigid plate, as previously inferred on the rest of the India-Eurasia margin (the greater Tibetan plateau region) where GNSS measurements provide a stronger constraint on two-dimensional horizontal velocities than InSAR [Peltzer and Tapponnier, 1988; Avouac and Tapponnier, 1993; Tapponnier *et al.*, 2001; Thatcher, 2007; Loveless and Meade, 2011; Zheng *et al.*, 2017]. Our model of partitioning implies that there is a deficit of shallow slip east of the GF and, thus, that the northern ONF may have accumulated enough strain for a large earthquake.

ESTIMATED SLIP DEFICIT and the chance of a large earthquake on our EF is lowered if part of the deformation is continuous deformation from ductile processes. The geology contains many folds and features of ductile deformation [Ruleman *et al.*, 2007]. Creep is seen on the CF, but no comparably sharp velocity contrast are seen east of the GF (Figure 4.2). If subsurface creep occurs in the central axial belt it does not reach the surface. The width and topography of the Kirthar and Sulaiman FFB are compatible with the action of a weak low-angle detachment fault, decoupling the sedimentary sequence from the underlying basement [Sarwar and DeJong, 1979; Davis and Engelder, 1985; Jadoon, 1991]. Seismic reflection profiles and geology suggest that pelitic rocks or fine carbonates may lubricate an effective zone of decoupling in the Sulaiman range below a depth of more than 10-15 km [Davis and Lillie, 1994; Humayon *et al.*, 1991; Jadoon, 1991] in a similar fashion than layers of precambrian evaporite in the Trans-Indus Salt Range [Jones *et al.*, 1961; Lillie *et al.*, 1987], north of our study region.

Slip on decollement would be driven either by a rearward push or by spread under the topography gravitational potential [Powell, 1979; Copley, 2012]. Nevertheless, gravitational flow would be in the direction of the Indus foredeep (eastward) [Reynolds *et al.*, 2015], while the

weak velocity gradient measured along the descending track implies that the gradient in the ascending direction cannot originate from eastward displacement. Moreover, whether gravitationally driven deformation within the Kirthar ranges would induce deformation rates sufficient to be measured with InSAR remain to be proven. Left-lateral motion on the decollement plane at 5-10 km depth would be hardly distinguishable from the dislocation signal we model from surface deformation only [Jolivet *et al.*, 2008], however, earthquake focal mechanisms suggest that elastic strain accumulation on a vertical fault is at least responsible for part of the deformation.

What are the implications of our mapped deformation gradients for long-term regional tectonics?

4.5.3 Long-term evolution of the plate boundary

THE TRANSPRESSIVE Chaman plate boundary has progressively widened as the result of the convergence between India and Eurasia since about 40 Ma [Seton *et al.*, 2012]. As India moves North, sedimentary rocks from the Neo-Tethys pile up and are overthrust onto the Indian

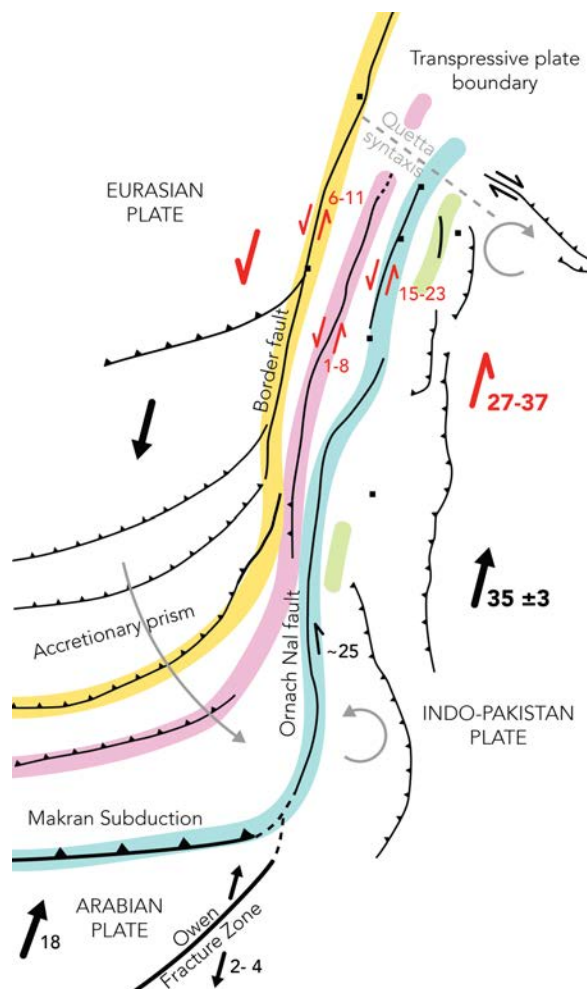


Figure 4.7: Schematic interpretation of the plate boundary cinematic and long-term evolution. Interquartile range of fault slip rates from our inversion in millimetres per year are in red. Geometry and rates of the India-Arabia-Eurasia triple junction are from Minshull *et al.* [1992]; Khan *et al.* [2008]; Fournier *et al.* [2008]; Rodriguez *et al.* [2014].

plate [Qayyum *et al.*, 1996]. They formed the current fold and fault belts (FFB) through progressive accretion on the eastern side, half of the current FFB surface dating from the most recent orogenic period (Pliocene to Quaternary) [Pubellier *et al.*, 2008]. At geological time-scale, the eastward age progression also applies to faults and fractures in the FFB, which are currently long enough to rupture in $M_w 7.5$ earthquakes (e.g. in 1935) (Figure 4.6). We claim that current strain measurements on the comparably very short-term of a few years reflect this long-term evolution. The most obvious evidence is that most of the current left-lateral surface strain seems to be accommodated east of the CF (Figure 4.7).

THE CF is not to be dismissed from its status as the western boundary of the Indian plate, because it evidences significant slip and hosts moderate earthquakes, in addition to being the oldest [Lawrence *et al.*, 1992; Pubellier *et al.*, 2008] and longest fault in the region. Across-fault contrasts in crustal thickness evidenced by Bouguer gravity anomalies indicate that crustal shear is deeply rooted [McGinnis, 1971; Jadoon and Khurshid, 1996]. Hundred kilometres south of Nushki, the CF seems less active and left-lateral strain seem transferred to the southern GF particularly active since 2013. The nearby termination of the Balochistan rupture on the Hoshab fault is partly responsible for this, but not only [Bernard *et al.*, 2000], outlining the connection between the strike-slip system and the Makran thrust faults which splay to the west. Furthermore, the gradual azimuth change of the Makran faults and the mixed thrust and strike-slip mechanism of the Balochistan aftershocks ruptures [Jolivet *et al.*, 2014b] mapped at the surface indicate a gentle transition between strike-slip and thrust mechanisms (Figure 4.7). The continuity between faults and their direction of slip fit into the long-term picture. Indeed, the relative plate motion implies an elongation of the strike-slip zone over time and the relative migration of the active subduction and accretionary wedge. Probable structural evolution involve the abandon of past thrust in the accretionary prism, like the Usman fault in the Ras Koh range [Lawrence and Yeats, 1979], or the progressive alignment of thrusts with strike-slip structures and change of slip direction due to stress rotation. The anticlockwise rotation of the Khuzdar-Karachi block in the south has been previously outlined [Sarwar and DeJong, 1979; Arshad *et al.*, 2011]. Moreover, the clockwise rotation in the Quetta syntaxis suggests that the Sulaiman range may be a mature version of the lobe forming near Karachi.

Acknowledgements This work benefited from rich and constructive discussions with Pr L. Le Pourhiet and Dr N. Chamot-Rooke. We thank A. Janin for his comments. Several figures were created using Generic Mapping Tools [Wessel and Smith, 1998].

4.6 Conclusion

BASED on six years of ground velocities measured by InSAR over the Kirthar ranges in Pakistan and Afghanistan, we localise strain deformation and estimate partitioning along a 350 km-long portion of the plate boundary between India and Eurasia. We confirm previous observation of continuous slip on the Chaman fault reaching the surface with rates no greater than 15 mm/yr. For the first time we show the key role of the central axial belt in the accommodation of the differential plate motion in agreement with seismological evidences. We precisely locate actively loading faults, which seem to fit the picture of subparallel en-echelon faults spaced by 20-40 km connected with known faults further south. We notably exhibit that the Ornach Nal fault extends 100 km further north than previously mapped with slip rates close to 20 mm/yr. Further north, still in the eastern part of the ranges, inferred slip rates reach 25 mm/yr below >10 km with greater uncertainty and may be connected to deep shear, simpler than the apparent complex thin-skinned tectonics. The Ghazaband fault evidence strain accommodation on discrete segments.

Large strain on the central and east Kirthar range fits in the long-term picture and may indicate an eastward shift of the plate boundary to younger structures, associated with the relative southward migration of the active Makran compressional wedge. This allows us to close the local plate boundary slip budget which stayed an enigma for several decades. Our interpretation has a geological meaning.

Chapter 5

OPEN QUESTIONS, REMARKS AND PERSPECTIVES

Questions ouvertes, remarques et perspectives

EN GUISE de conclusion, ce dernier chapitre synthétise et rassemble les questions et réserves associées aux résultats présentés précédemment et suggère quelques futurs axes de recherche pour y répondre.

J'APPORTE une nouvelle interprétation de l'outil de calcul de séries temporelles InSAR, KFTS, au regard des essais et applications ultérieures et énonce de possibles directions d'amélioration. Par exemple, l'estimation systématique des déformations co-sismiques au fur et à mesure nécessiterait une stricte sélection automatique des séismes à modéliser, pour ne garder que ceux qui déforment effectivement la surface (Figure 5.1 versus Figure 5.2) et limiter les incertitudes induites par les autres. L'approche itérative du filtre de Kalman favorise l'évaluation constante du modèle et sa réactualisation.

Néanmoins, la traçabilité des covariances au cours du temps dans KFTS n'est pas évidente du fait de leur grand nombre. Elles sont pourtant importantes pour la juste incorporation des interférogrammes à longue ligne de base (c'est à dire reliant des acquisitions éloignées dans le temps) qui augmentent la fiabilité du réseau interférométrique. Une construction systématique des interférogrammes permettrait de garder sélectivement en mémoire les covariances qui serviront lors des futures étapes de mise à jour des séries temporelles.

LES LIMITES géométriques et atmosphériques liées à la détection de la déformation par InSAR sont soulignées. En effet, les géométries des acquisitions par satellite font que la méthode est beaucoup moins sensible aux déplacements nord-sud qu'est-ouest (Figure 5.3), un élément clef pour l'interprétation de nos observations le long de la faille de Chaman qui a un azimuth d'environ 10 à 30°N. Les implications pour nos images du déplacement horizontal produit par les séismes au Chapitre 3 sont illustrées (Figure 5.4).

LES ACCELERATIONS de l'ordre du millimètre sur quelques kilomètres contenues dans les séries temporelles de glissement ont-elles un sens

physique ? Sommes-nous capables de détecter de si petits changements ? La comparaison avec un événement de glissement enregistré par un 'creepmeter'¹ nous suggère que c'est effectivement possible (Figures 5.6, 5.5).

Les méthodes permettant de retirer le bruit dans l'InSAR promettent d'augmenter significativement la capacité de détection de cet outil. Je mentionne l'exemple de l'extraction automatique de déformations millimétriques à l'aide d'apprentissage profond, que Bertrand Rouet-Leduc présente dans une étude à laquelle j'ai contribué (Figures 5.7, 5.8).

POUR FINIR, je résume les propriétés générales de la frontière de plaques de Chaman qui, bien qu'hébergeant une part importante de glissement asismique sous la forme de glissement continu et de glissement post-sismique (et donc induit), ne semble pas présenter de glissement asismique spontané. Le long de la faille de Chaman, les séismes étudiés présentent un rapport du glissement post-sismique sur co-sismique important (>0.4) qui n'est pas retrouvé dans les deux séismes plus à l'est ($M_w 5.3$ et 5.4).

L'aléa sismique le long de la frontière de plaques est discuté de manière qualitative et relative. La faille de Chaman en soit ne semble pas pouvoir héberger des séismes de magnitude supérieure à 7, excepté au sud de la ville de Nushki où les résultats de cette thèse seuls ne permettent pas de trancher, l'observation indiquant une accumulation importante de contraintes dans une direction où les mesures ont une sensibilité moindre. Le risque semble plus important au sud-est de la faille de Chaman, dans la prolongation de la faille de Ornach Nal jusqu'à la latitude (29°N) de la ville de Kalat. La syntaxe de Quetta est une autre zone de forte activité sismique où un séisme dévastateur a été enregistré le 6 octobre 2021, 15 jours avant le rendu de cette thèse, soulignant la vulnérabilité des populations aux séismes de taille modérée ($M_w 5.9$) tel ceux que j'ai étudiés.

DANS CETTE THÈSE, avec l'aide de mon superviseur, Romain Jolivet, j'ai montré comment l'InSAR à haute-résolution peut être utilisé de manière efficace pour construire et régulièrement mettre à jour des séries temporelles de déformation de surface avec leurs incertitudes. L'application sur la frontière de plaques de Chaman nous apporte une bien meilleure compréhension de cette zone de faille énigmatique qui s'étend sur un millier de kilomètres.

IN THIS FINAL CHAPTER, I would like to discuss the implications of the results presented in the preceding Chapters and raise considerations on the limits of InSAR to answer research questions enunciated in the Introduction. The following discussion is open and extends to fields beyond my expertise. It aims to gather ideas in their infancy.

¹ un instrument installé à la surface, en travers de la faille, qui mesure la déformation de très courte longueur d'onde (quelques mètres)

5.1 How time series analysis can be further improved for the study of tectonic deformation?

IN CHAPTER 2, I present a Kalman filter-based time series analysis method for InSAR, referred as KFTS, a method which was continuously improved during my thesis. For instance, in Chapter 3, I outline how earthquakes can be dealt with, making the most out of the *a priori* model parameters. On one hand, the need for *a priori* parameters appears as a weakness of KFTS because it raises the weight of the user decision on the final solution; on the other hand, it is a way to physically constrain the inversion and define spatially-dependent parameters.

THE KFTS algorithm allowed me to regularly extend my time series on the Chaman plate boundary and image new recent earthquakes (e.g. M_w 5.7, the 12 August 2020 in Figure 5.1). However, other processing steps delay the update of the pre-existing time series with respect to real-time. Quality-assured ERA-5 needed to correct interferograms from the stratified atmosphere are published with a delay of 2 to 3 months. A delay of 2 weeks is also required to obtain high precision orbits of the Sentinel 1 satellites.

MOREOVER, systematic description of coseismic deformation is not straightforward because of the uncertainties, often unknown, in *a priori* locations and magnitudes taken from global earthquake catalogues [Monterroso *et al.*, 2020; Lazecký *et al.*, 2020]. The study of the Chaman plate boundary, whose seismicity is characterized from sparse and distant seismometers, taught me that there are significant discrepancies in magnitude estimates of moderate size earthquakes (Figure A.24).

One could add an Heaviside function to the parametrised description of deformation (Equation 3.1) for any event above M_w 4 within the study area. However, existing trade-off between parameters implies that each additional Heaviside function results in more uncertain ground velocity locally (Section 3.4.1, Figure A.25). This is also an argument to minimize the spatial footprint of the Heaviside amplitude parameter. Earthquake epicentre depth should be the most discriminating criterion to decipher if a moderate size earthquake will produce measurable surface deformation or not. However, it seems that depths of the source are practically unknown in the Chaman fault zone. For instance the 21 March 2016 earthquake (M_w 5.3) located at 17 km-depth in the GCMT catalogue appears to have ruptured the surface according to InSAR recorded displacement (Figure 3.2), while the 14 November 2020 earthquake (M_w 5.6) estimated at 19 km-depth is associated with a surface deformation signal in InSAR that is not clearly distinguishable from noise (Figure 5.2).

Therefore, to improve the systematic account of earthquake-related deformation and minimize biases in velocity estimates, a future project

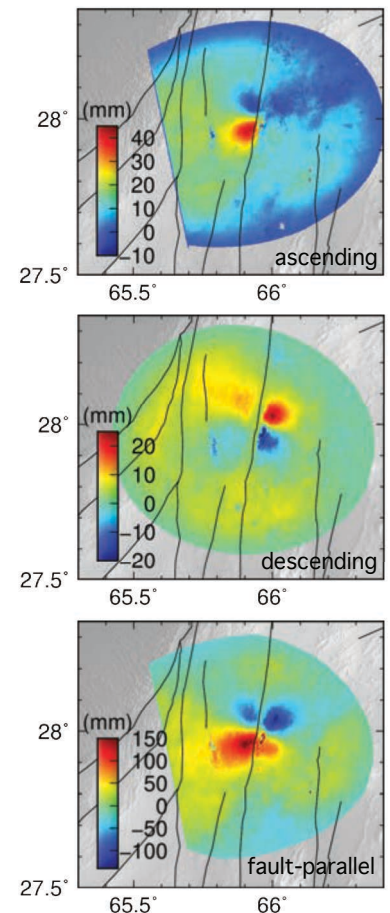


Figure 5.1: Coseismic deformation for the 12 August 2020 earthquake (M_w 5.7) on the Ghazaband fault from the adjustment of the amplitude of an Heaviside function in time with KFTS on the ascending (track 42) and descending (track 151) Sentinel 1 data. Combined and projected deformation in fault parallel direction (12° N) is the bottom plot.

could be to build an algorithm that automatically identifies that the spatial pattern in Figure 5.1 is more likely to originate from slip on a fault plane than in Figure 5.2. The number of parameters in KFTS can be updated consequently: an earthquake which produces surface deformation too close to noise could be removed from the parametrised description and other model parameters could be re-analysed. The iterative nature of a Kalman filter facilitates continuous assessment of outputs.

THE TIME SERIES description of earthquakes allows to average out sources of noise which are random in time (e.g. part of the turbulent atmospheric delays), and thus results in a clearer picture of earthquake-related deformation than coseismic interferograms only. This approach is particularly relevant for moderate-size earthquakes [Fattahi *et al.*, 2015; Liu *et al.*, 2021]. It also has the obvious advantage to frame the earthquake in between a pre-seismic and post-seismic regime of deformation. With similar objectives, the Diapason LiCSBAS tools provide automatic interferograms for most continental earthquake with $M_w > 5.5$ [Lazecký *et al.*, 2020; Morishita *et al.*, 2020].

IN THE INTRODUCTION, I outlined the need for long temporal-baseline interferograms to mitigate biases in InSAR time series (Section 1.3.2). Those are a challenge for KFTS, which is designed to work on a window of a few acquisitions moving in time. Specifically, the off-diagonal elements of the state covariance matrix, P_k , are only kept for the n th last acquisitions, otherwise storage files easily grow to intractable size (hundreds of Gigabytes). It seems that the off-diagonal terms in P_k are not easily predictable, so at the moment when a long-baseline interferogram is in the data (Φ_{km} , t_m being a few years before t_k), the previously estimated phase and standard deviation (ϕ_m and σ_{ϕ_m}) are retrieved and inter-phase covariance are supposed null, the best assumption for most pixels.

A systematic structure of the interferometric network such as, for instance, long-baseline interferograms always connecting the first two acquisitions of June, would help keep selectively in memory informations that will be used in future updates. Alternatively, data reduction method could be used, like the Principal Component Analysis method implemented for the sequential estimator of Ansari *et al.* [2017].

LAST BUT NOT LEAST, the forecast step of KFTS is made from a purely descriptive model. A physically informed model would allow to learn from data the physics of the system, and may lead to a greater prediction power. For instance, Bato *et al.* [2018] presented an Ensemble Kalman filter applied to volcanic eruption forecasting. Nevertheless, physical models for fault slip include non-linear dependencies between parameters, preventing the use of the inherently linear Kalman filter. Alternatively, a particle filter is a data-assimilation algorithm with minimal assumptions, which, therefore, work with non-linear

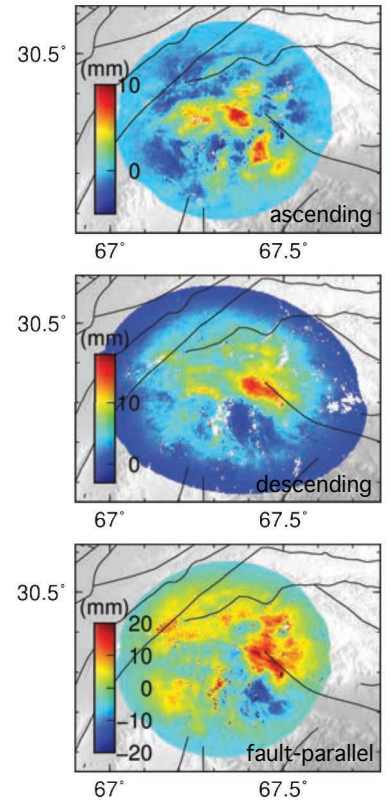


Figure 5.2: Same as Figure 5.1 for the coseismic deformation of the 14 November 2020 earthquake ($M_w 5.6$). The fault parallel direction is 330°N . The mapped deformation may not be earthquake related. The earthquake is likely too deep to produce clear surface displacement but this is hard to know *a priori*.

models and non-Gaussian probability density functions. Post-seismic afterslip may be the simplest process to model in terms of stress [Perfettini and Avouac, 2004; Thomas et al., 2017].

CONSIDERING state-of-the-art InSAR time series analysis, how large has to be the surface deformation in order to be recognisable? Considering the amplitude of noise, many deformation signal may be hidden inside it. Then, what are the new clever way to denoise InSAR and thus improve its readability?

5.2 What is the detection limit of InSAR?

TO EXTRACT ground deformation we face three main types of limitations related to InSAR:

- technical; processing is time-consuming and numerically heavy. This topic was already discussed (Section 2.4).
- geometrical; the two line of sights of most satellite missions (ascending and descending) provide an incomplete view of the three-dimensional deformation.
- atmospheric; the sensitivity of InSAR is very high, but deciphering between coloured atmospheric delays (reaching easily a few centimeters in an interferogram) and deformation signal is not straightforward.

In the following, I discuss geometrical and atmospheric limitations.

5.2.1 Geometry of acquisition and sensitivity

MANY studies claim that InSAR line of sights (LOS) are 'insensitive' to displacement in the north-south direction [e.g. Weiss et al., 2020]. This argument is conveniently used to convert LOS to east-west and vertical components of deformation. The near-polar orbits of SAR satellites result in a reduced sensitivity in this direction but, thankfully for the study of the Chaman fault (striking $\sim 10^\circ$ - 30° N), ascending and descending tracks are not completely parallel and there is some sensitivity to displacement in this direction [Chang et al., 2018; Brouwer and Hanssen, 2021]. Typically, horizontal north-south motion along Sentinel 1 LOS appears an order of magnitude smaller (Figure 5.3). When combining ascending and descending views, a 10° angle to north means that LOS is six times smaller than ground motion, and four times when this angle is raised to 20° . The low angle to vertical (LOS incidence of 29° - 46° for Sentinel 1 wide swath mode) implies that InSAR is most sensitive to vertical motion.

In any case, combining ascending and descending observations (two LOS) always requires an assumption to reduce the number of unknowns to two and thus provides a partial description of three-dimensional

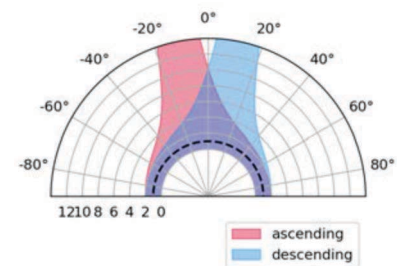


Figure 5.3: Multiplicative coefficients between Sentinel 1 LOS and horizontal ground motion with different azimuthal directions (in degrees to north). Mean LOS geometry is taken with an incidence, α , of 31° and an azimuth of $\pm 79^\circ$ N. The dashed black line is a coefficient of one. At best, that is for pure east-west motion, the motion in LOS is half of the ground motion ($\cos(\pi/2 - \alpha) \sim \cos(60)$ which is about 0.5).

deformation which biases the projection (e.g. Equation 3.2 assumes a null fault-perpendicular motion). For instance, the modelled surface motion of the 13 May 2016 earthquake is always inaccurately represented by projection even when considering other assumptions (null vertical instead of null fault perpendicular motion) as shown in Figure 5.4.

USING the varying LOS angle of Sentinel 1 Terrain Observation by Progressive Scan (TOPS) acquisition mode [De Zan *et al.*, 2014; González *et al.*, 2015], horizontal north-south motion can be extracted on region of burst overlap, where the squint angle is about 1° , with an accuracy of about 5 cm for a single interferogram or about 2 cm/yr for a stack of interferograms [Grandin *et al.*, 2016; Hooper and Spaans, 2016; Vajedian and Motagh, 2018; Hooper *et al.*, 2021].

FOR CLASSICAL LOS measurements, phase change is very precisely known (down to a fraction of millimetres) but its interpretation in terms of deformation is attached to a subjective and uncertain interpretation. In time series, a reference quantity is the LOS velocity. Along the Chaman plate boundary, where InSAR coherence is maintained over the six-year-long time series, uncertainties are as low as

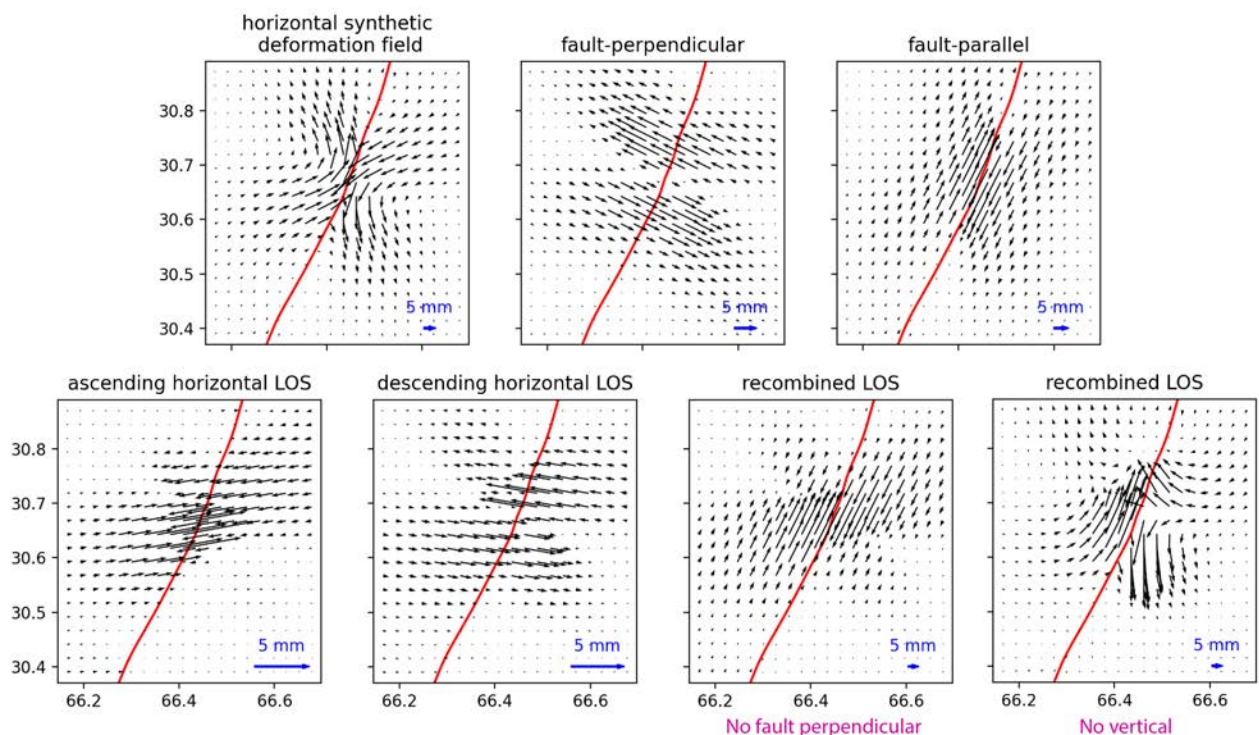


Figure 5.4: Synthetic horizontal surface deformation field as predicted by the solution of the 13 May 2016 earthquake represented in Figure 3.7 (top left). The true fault-perpendicular and fault-parallel motions are represented in the central and right top plot. The three-dimensional deformation is projected along the true line of sights (LOS) of the Sentinel 1 ascending (track 42) and descending (track 151) wide swath acquisitions. LOS displacements are re-combined through a least-square inversion into fault-parallel and vertical (3rd plot on 2nd row) like in Figure 3.6 and into fault-parallel and fault-perpendicular (4th plot of 2nd row). Working from synthetics clarify that the limitations are geometrical and not related to resolution.

1 mm/yr (thus, theoretically a north-south deformation rate greater than 1 cm/yr is detectable) (Figure A.25). This compares well with, for instance, the 2.3 ± 0.6 mm/yr of creep measured from a 3-year-long Sentinel 1 time series in Zhou *et al.* [2018], or the 2 mm/yr of sediment compaction in Daout *et al.* [2019]. With such precision can we push further our interpretation of the time series of surface slip on the Chaman fault ?

5.2.2 Flirting with the limits: comparison with creepmeter data

A CREEPMETER installed on the Chaman fault in Amir Khan (Pakistan, 157 km north of Nushki) recorded a slip event starting on the 1st of March 2019 [Billham *et al.*, 2019]. The record attests that a total of 4.5 mm of left-lateral slip occurred in 40 days, including 3.2 mm within the first day of the slow slip event (Figure 5.5). Is this signal detectable in InSAR time series? The challenge is not only the small amplitude of the signal, but also its spatial footprint which may not extend beyond the creepmeter length-scale of a few meters, while InSAR pixel size is close to 80 m.

Figure 5.6a suggest an acceleration in InSAR-derived surface slip on a ~800 m-long fault segment corresponding spatially and temporally to the slow slip event recorded by the creepmeter. Profiles across the fault confirm that the measured offset increases by 1.3 mm within 48 days (27 January to 16 March 2019), an amount equivalent to the total slip accumulated during the whole preceding year (Figure 5.6b).

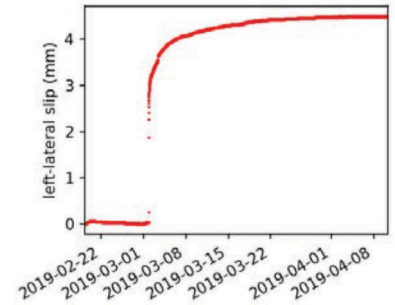


Figure 5.5: Creepmeter time series in Amir Khan (Chaman fault) published in Billham *et al.* [2019] and available from unavco.org.

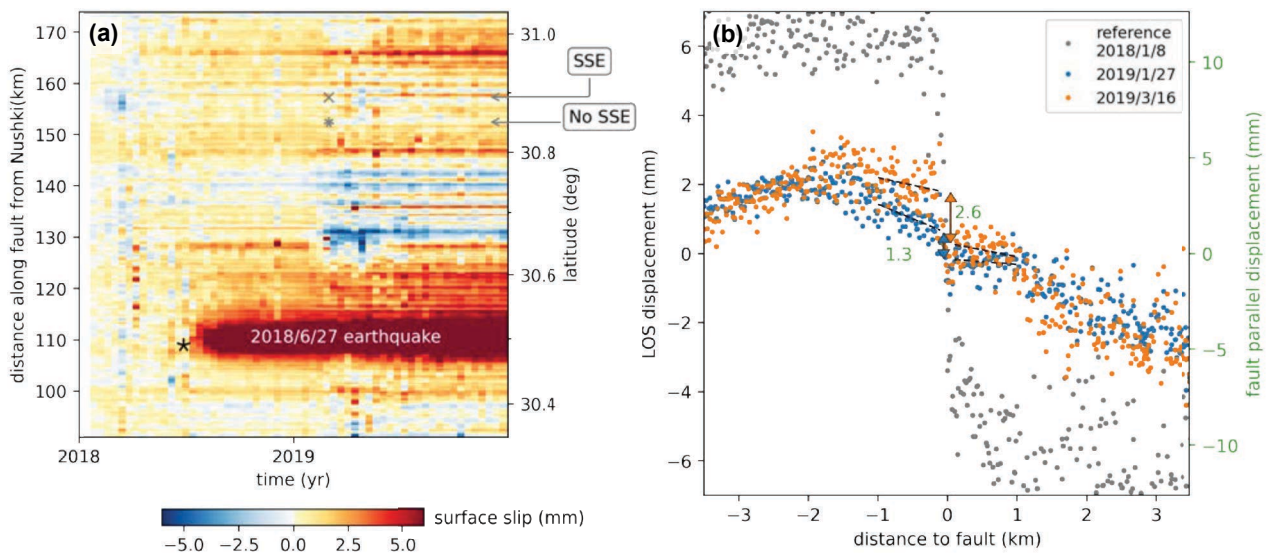


Figure 5.6: (a) Closer view of the evolution of surface slip on the central fault segment with respect to early 2018 (8th of January). It is the same data as in Figure 3.4, but re-referenced. The two gray arrows locate the creepmeters mentioned in Billham *et al.* [2019] and indicate whether a slow slip event (SSE) was recorded or not according to the same article. Timing of the SSE is marked by the gray cross. What appears as red horizontal lines outlines creeping portions. (b) Selected across-fault profile of displacement at the location of the northern creepmeter at different dates. In gray is the reference profile showing fault offset resulting from the July 2016 earthquake, while orange and blue points are displacements relative to this gray profile at two dates framing the SSE. Green numbers refer to slip values in fault parallel projection ($LOS \times 1.8$ locally).

Thus, assuming that those very small variations are actual slip, slip rate would have been multiplied by 8 during Jan-March 2019.

The match between what is seen from this creepmeter and from our measured slip, is further supported by the lack of surface slip recorded by a second creepmeter [Bilham *et al.*, 2019] 152 km north of Nushki where our measured slip is null too. Multiple signals similar to what is seen at 157 km are recorded along the fault (e.g. at latitude 30.8 in Figure 5.6a). Therefore, it seems that such very shallow micro-slip events are affecting numerous segments of the Chaman fault. However, the discrete nature of those millimeter scale events is hard to capture with InSAR because of (i) the rate of SAR acquisitions (several days), (ii) spatial averaging on hundreds of meters and (iii) temporally decorrelated noise mostly arising from turbulent atmosphere. Consequently, what appears to be continuous surface slip may be the result of successive discrete slip events silent to the installed seismic stations. Algorithms targeted to denoising InSAR time series is a hope for the fine scale mapping of slip.

5.2.3 Automatic denoising of time series

UNDESIRED delays captured in interferograms (mainly from the atmosphere) reach amplitudes of several centimetres and, thus, potentially hide deformation signal [Lohman and Simons, 2005; Agram and Simons, 2015]. Numerical signal decomposition may help filter out noise, for instance, using Principal Component Analysis (PCA) [Fornaro *et al.*, 2014; Maubant *et al.*, 2020] or Eigendecomposition [Ansari *et al.*, 2018]. Alternatively, deep-learning-based denoising and image enhancing techniques [Mao *et al.*, 2016; Zhang *et al.*, 2017] seem suited to learn the complex structure of noise in InSAR.

I CONTRIBUTED with Romain Jolivet, Paul A. Johnson and Claudia

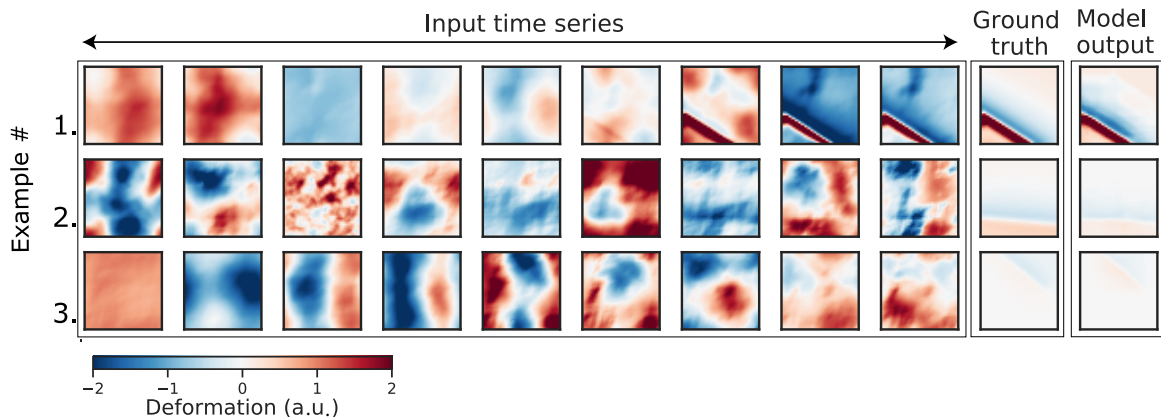


Figure 5.7: Example of the performance of the autonomous denoising algorithm for InSAR time series. Three sample synthetic time series (not in the training set) constructed with different ratios of signal-to-noise, which are 0.7 (top), 0.02 (middle) and 0.004 (bottom). Those time series are fed into the algorithm as is (with topography) and the denoised output is shown on the right. Even with very high level of noise, model output resemble ground truth. Modified from Figure 2 of Rouet-Leduc *et al.* [2021].

Hulbert to the study by Bertrand Rouet-Leduc entitled "Autonomous Extraction of Millimeter-scale Deformation in InSAR Time Series Using Deep Learning", accepted at *Nature Communication* in 2021. This paper presents a convolutional auto-encoder specifically designed to remove noise in InSAR time series. The convolutional neural network is trained on synthetic cumulative evolution of phase change, containing deformation due either to a slipping fault [Okada, 1992] or to an inflating or deflating point source [Mogi, 1958] overlaid with different noise signals, which mimic turbulent and stratified atmospheric delays, incoherent pixels and unwrapping errors. The final trained model outperforms the eye, recovering with reasonable fidelity the cumulative deformation signals occurring in time series with signal-to-noise ratios down to a few percents (Figure 5.7). In real case examples, the auto-encoder isolates the surface deformation due to a slow slip event on the North Anatolian fault (Turkey) with no prior knowledge of the fault location (Figure 5.8) and it extracts the few millimetres of subsidence signal (in LOS) between April and November 2016 due to geothermal activity in Coso (California) [Rouet-Leduc et al., 2021]. Therefore, this algorithm is able to disentangle actual ground deformation from atmospheric noise at short time scales, with a resolution of a few millimetres, significantly lowering detection threshold for InSAR.

Other unsupervised machine learning tools are able to detect transient deformation, especially volcanic unrest, [Schwegmann et al., 2017; Anantrasirichai et al., 2018, 2019, 2020; Shakeel et al., 2021] but they generally require large signal-to-noise ratios, notably because they work on single interferograms.

5.3 How peculiar is the Chaman slip distribution ?

EVEN THOUGH I analysed time series of fault slip with a lot of care for details, I cannot assert that there are spontaneous slow slip events on the Chaman fault (CF), like what has been identified on other faults with InSAR [e.g. Jolivet et al., 2015a; Rousset et al., 2016; Khoshmanesh and Shirzaei, 2018a; Jolivet and Frank, 2020] (Section 1.2.4). A doubt concerns the occurrence of very small-scale slip accelerations of a few millimetres per month affecting fault portions of length no greater than 1 km (Section 5.2.2).

Still, slow slip seems pervasive along the CF under the form of slow continuous creep or aseismic slip triggered by earthquakes. Triggered slip reaches large fraction of the estimated coseismic slip (Chapter 3). The 27 June 2018 event was followed by an acceleration of slip on fault portions that were already creeping before the triggering event, including the ruptured and adjacent portions (Figure 5.6a).

IN CHAPTER 3, I compare coseismic and postseismic energy release for three earthquakes on the CF (13 May 2016 (M_w 5.6), 10 July 2016

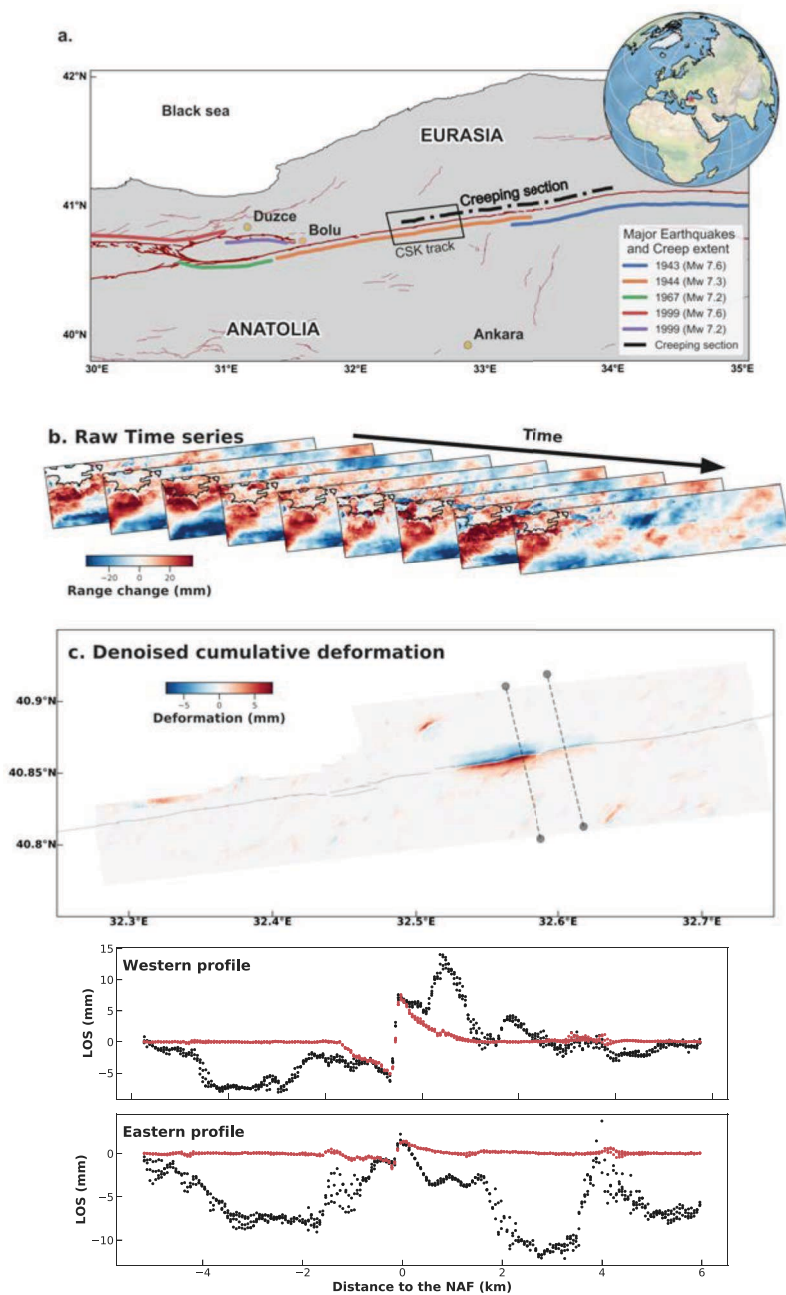


Figure 5.8: Application of the autonomous denoising algorithm on an InSAR time series built from COSMO-SkyMed observation in northern Turkey over Aug-Sept 2013 [Rousset *et al.*, 2016]. The auto-encoder outputs ground deformation (c and red dots in bottom profiles), which contains a strong signal of surface slip reaching 1.5 cm (in LOS) right on the North Anatolian fault, without prior knowledge of its location. Taken from Figures 3 and 4 of Rouet-Leduc *et al.* [2021].

($M_w 5.1$) and 27 June 2018 ($M_b 4.2$); Table 3.1). All of them, in agreement with two previously observed earthquakes in the region [Furuya and Satyabala, 2008; Fattahi *et al.*, 2015], support the idea that moderate magnitude earthquakes have large postseismic signal with respect to their coseismic formulated by Alwahedi and Hawthorne [2019]. Nonetheless, the three ruptures exhibit diverse time series of strain release and the description of more earthquakes is required to determine whether or not the CF has a peculiar behaviour compare to other strike-slip faults. At the end of the spectrum, the June 2018 event with its estimated magnitude, M_b , of 4.2 seems to have been followed by a postseismic 3-15 times greater than the inferred coseismic, and thus may

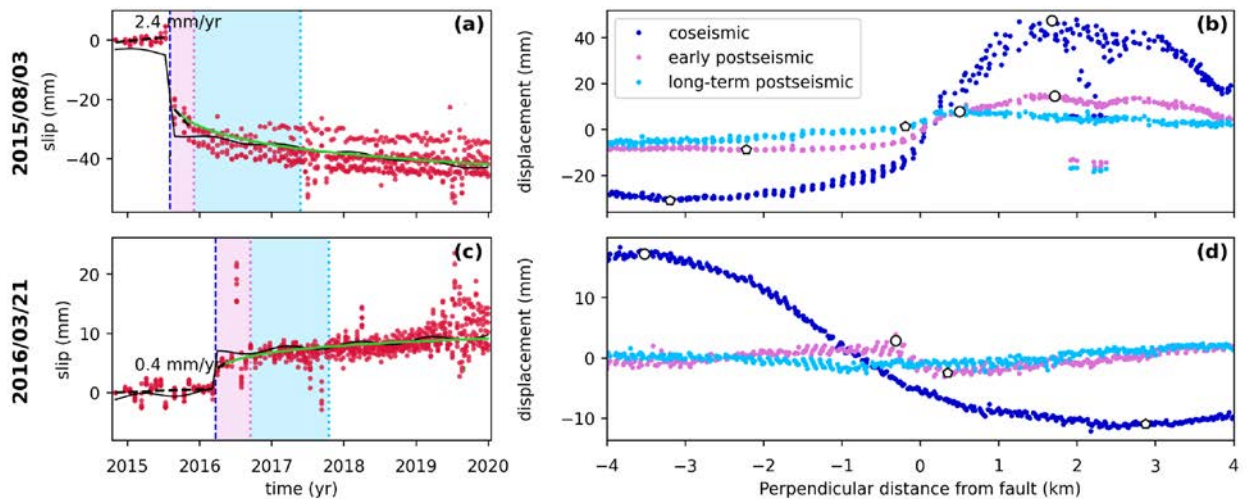


Figure 5.9: Time series of surface slip in LOS (track 42) at earthquake locations (a,c) and associated profiles of deformation (b,d). This Figure is the same as Figure 3.9 for the two earliest earthquakes south east of the Chaman fault (Figure 3.2).

be reclassified as a triggered slow slip event. The intricate behaviour of fault slip argues towards a simplified terminology.

I also image two other earthquakes (3 August 2015, 21 March 2016) south-east of the CF; a thrust (M_w 5.4) and a strike-slip (M_w 5.3) earthquake. Both events display moderate postseismic deformation with respect to coseismic displacement (Figure 5.9). This is clearer in the spatial profiles across the rupture zone (Figure 5.9b,d) where the peak-to-peak postseismic (including what I named "early" and "long-term") to coseismic surface slip ratio is roughly 0.4 and 0.2 in chronological order. Hence, is important postseismic specific to the CF, the only obviously creeping fault along this plate boundary? The time series of deformation for the 12 August 2020 (M_w 5.7) earthquake on the Ghazaband fault (Figure 5.1) may help decipher.

THE SPATIAL DISTRIBUTION of surface slip along the Nushki and C1 creeping segments has a quasi-elliptical shape (Figure 3.5c), which resembles what is predicted for an elastic crack [Pollard and Segall, 1987; Scholz, 2002], unlike the triangular distribution sometimes associated with faults [Manighetti et al., 2001; Davis et al., 2005] and dynamic ruptures [Manighetti et al., 2009]. This distribution implies steep along-strike gradients of slip near the tip of the creeping segments, which may be dissipated through non-elastic deformation and earthquakes. The pronounced seismicity north of the Nushki creeping segment and around the Central segment, as well as the geometrical complexities at the tip of our segments are in agreement with this picture.

5.4 Seismic hazard along the Chaman plate boundary

ON THE 6TH OF OCTOBER 2021, 15 days before finishing this manuscript, a M_w 5.9 earthquake struck close to Harnai (90 km east of Quetta) in Pakistan causing fatalities, injuries and numerous damages. This earthquake located in the Sulaiman fault and fold belt near the Quetta syntaxis, outlines the vulnerability of local population, even to moderate magnitude earthquakes in this densely populated region of the world. Quetta has more than a million inhabitants, Kalat 412 000, Nushki 178 000 and Chaman 123 000 (2017 census by [Pakistan Bureau of Statistics](#)). Thus, assessing seismic hazard along the Chaman plate boundary is critical.

THIS RECENT EVENT is in agreement with the fault system depicted in Chapter 4 of a transpressive plate boundary with strain partitioning. Along the Kirthar range, the distribution of strain outlines the critical role of the eastern faults about 80 km east of the Chaman fault (CF) and significant slip deficit near the surface in the continuation of the Ornach Nal fault, south of the city of Kalat. Moreover the Quetta-Kalat fault, which ruptured in a M_w 7.7 in 1935, seems to still represent a major hazard with ongoing strain accumulation. This may help refine the coarse seismic hazard map of Pakistan [[Waseem et al., 2020](#)].

THE CF ITSELF is generally considered as the greatest threat and is associated with a constant high probability of ground shaking in seismic hazard maps [[Boyd et al., 2007](#); [Ruleman et al., 2007](#)], including the area of Kabul, the Afghan capital. From Chapter 3, it seems that the CF north of 32.7°N is not a major structure and that the plate boundary is located further East (along the Gardez fault zone or on the eastern side of the Katawaz block), an idea supported by the seismic record. Thus, seismic hazard for Kabul does not emanate from the CF itself (which does not mean hazard is low).

Further south, the CF is associated with measurable strain of the order of 1 cm/yr. The significant aseismic strain release due to continuous aseismic slip and after-slip following M_w 4-5 earthquakes limits the available stress and may explain the scarcity of large earthquakes historically. However, this does not exclude the occurrence of destructive events such as the M_w 6.5-6.7 in 1892 which occurred on a segment that is still showing elevated seismicity with respect to the rest of the fault. Did the 1892 earthquake durably perturb the local stress with effects lasting more than a century? Or is the elevated seismicity a structural property of what I coined the Central CF arising from its rheology and geometry?

South of Nushki, a 100-km-long portion of the CF appears locked (Figures 3.5, 4.3). Observations tell us that it accommodates about 8-12 mm/yr of strain below a depth of 8 to 10 km. Therefore, this segment seems the most likely to host a large earthquake along the CF. However, the orientation of this fault portion is not optimal for INSAR (Section 5.2.1) and additional ground instrumentation like GNSS stations would be key to confirm this inference.

ALONG the Chaman plate boundary, studies outlined the high rate of M_w5 earthquakes [Szeliga *et al.*, 2012], which seems to agree with the discussed earthquakes in this Thesis. However, this may only be the result of the magnitude of completion close to 4.5 for the region, which furthermore follows the Gutenberg Richter statistics (Figure 3.8). Additional and closer seismic stations would provide a finer picture of seismic hazard by recording more and smaller earthquakes with better localisation, for an accurate characterisation of their spatio-temporal relationships.

5.5 Final Conclusion

IN THIS THESIS, with the great help and support of my supervisor, Romain Jolivet, I demonstrated how high-resolution InSAR can be used in an efficient way to build long and regularly updated time series of surface deformation on actively deforming regions like the Etna volcano or the Chaman plate boundary. I focused on the description of slip and surface strain distribution along the Chaman plate boundary, with great care to keep a methodology as general and systematic as possible so that it can be applied on other regions of the world.

THE CHAMAN transpressive boundary between the Indian and Eurasian plates is intriguing because of its wide deforming region, scarce seismicity which includes some large historical earthquakes and the few published studies about the region, which kept many questions open, notably, about current fault activity and associated seismic hazard. I compiled and summarized previous observations of the plate boundary and integrated those with newly computed InSAR time series of deformation along ascending and descending passes of Sentinel 1A-B satellites.

I describe along-strike slip distribution and locking depths along the Chaman fault using systematic profiling every 2 km and define a new segmentation which nicely relates to the fault trace geometry. The Chaman fault seismicity in the last century seems to focus on the central part of the fault, in the main restraining bend. The fault accommodates a maximum strain rate of about 15 mm/yr, with a northward decrease which goes with the greater obliquity of the fault at the latitude of the Sulaiman fold and fault. Therefore, the Chaman fault accommodates only a fraction of the 25-35 mm/yr differential motion between India and Eurasia.

THE PLATE BOUNDARY host significant seismicity east of the Chaman fault, within the 100-km-wide fold and fault belt notably at two hinge zone of rotating strain, that is, first, at the latitude where the thrust fault of the Makran prism splay to the west and, second, around the Quetta syntaxis where the southeast thrusts and right-lateral faults meet the north-northeast left-lateral faults. With a simple dislocation

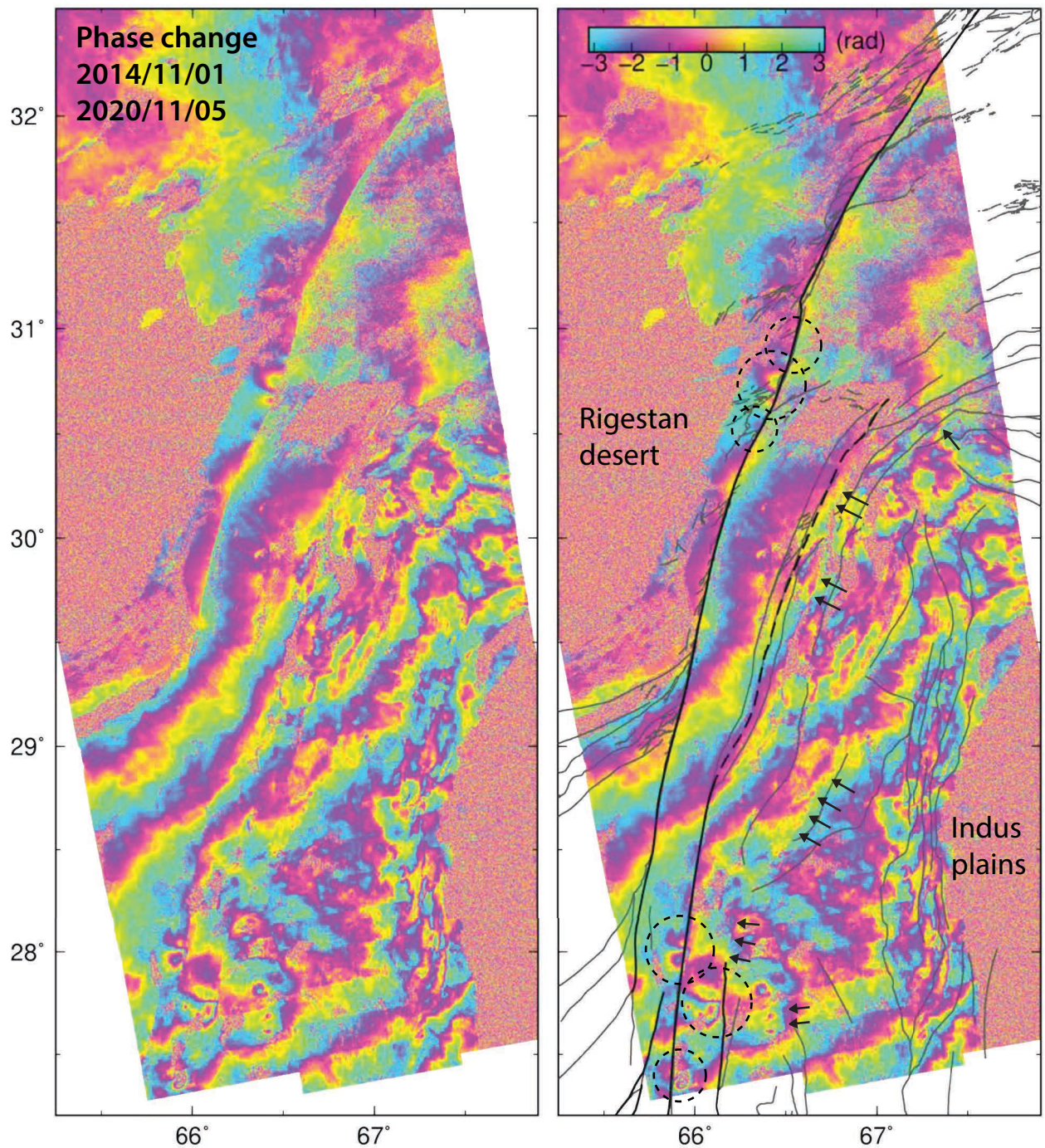


Figure 5.10: Interferogram connecting acquisitions six years apart (November 2014 to November 2020) on ascending track 42 of Sentinel 1. The phase change (between $-\pi, \pi$) contains information about the deformation that occurred during this period of time. Both figures display the same interferogram, the right one being overlaid by elements of interpretation: fault traces, arrows pointing at fault-related offsets, and dashed circles surrounding identified earthquake-related deformation. This interferogram, like the entirety of those processed and used in this thesis, is corrected from stratified atmospheric delays and slightly filtered. The long temporal baseline implies that phases decorrelate over many regions (e.g. the Rigestan desert, the Quetta-Pishin basin or the Indus plains), and that the method to reconstruct the full image from bursts (Network-based Enhanced Spectral Diversity approach) is less efficient. Thus, offsets parallel to the track boundary particularly obvious in the south are processing errors, which motivate the exclusion of such interferogram in time series analyses. Subsets of this interferogram decorate the title page.

model I blindly map left-lateral strain on an unknown structure east of the previously described Chaman and Ghazaband faults. The Ornach Nal fault thought to be the main structure of the plate boundary near the triple junction with Arabia in the south, is seen to have associated strain extending further north than previously mapped.

THE CUMULATED ground deformation captured in a six-year-long interferogram (Figure 5.10) nicely images the different processes discussed in this thesis; as it exhibits sharp and more diffused across fault gradients including some across newly identified active faults east of the Chaman fault, as well as earthquake-related deformations. It also provides a simple way to qualitatively validate results which were drawn from multi-step processing required to individualize each process, quantify associated displacement in two-dimensions, estimate uncertainties and gain in temporal resolution.

APPENDICES

A.1 Review of published slip rates along the Chaman plate boundary

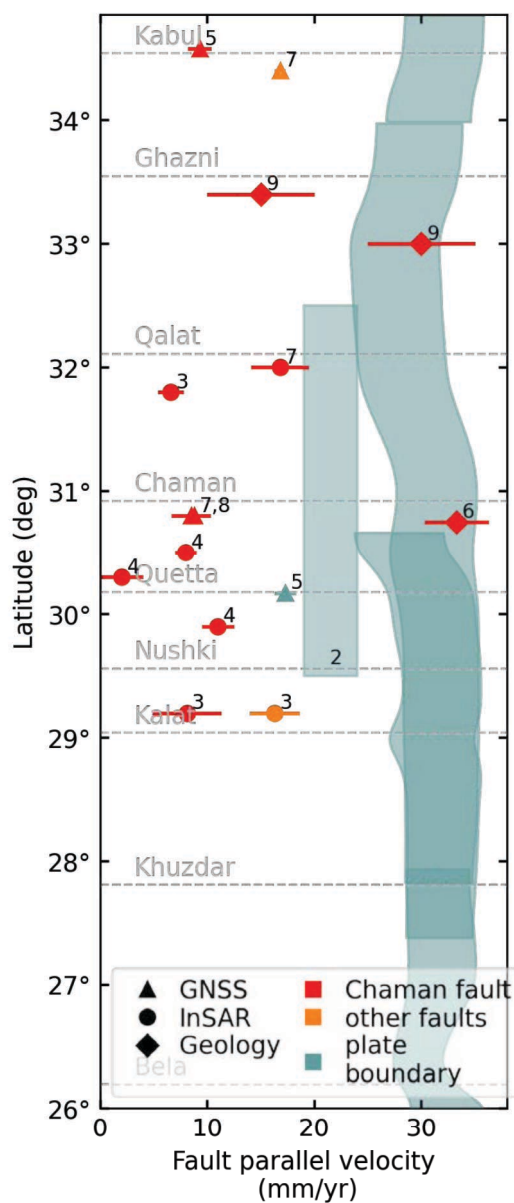


Figure A.1: Summary of published strike-slip velocity estimates along the Chaman fault plate boundary (details in Table 1). Blue symbols are estimates of the motion of India with respect to Eurasia. Red markers are slip rate estimates along the Chaman fault (CF). Orange markers refer to other sub-parallel faults (Ghazaband fault to the South, Gardez fault to the North). Shaded blue curves are the range of relative plate motion predicted by MORVEL and ITRF14 [DeMets et al., 2010; Altamimi et al., 2017] along the trace of the CF, Ornach Nal fault and Ghazaband fault, in the fault-parallel direction. The blue box corresponds to the range of velocities estimated by (2) Lawrence et al. [1992]. The shape of markers indicates the type of observations (InSAR, GNSS or geological features). Representative values out of continuous velocity fields have been selected from (3) Fattahi and Amelung [2016] and (4) Barnhart [2017]. Other sources are: (5) Mohadjer et al. [2010] (6) Ul-Hadi et al. [2013b] (7) Szeliga et al. [2012] (8) Crupa et al. [2017] (9) Beun et al. [1979].

sinistral rate [convergence rate] (mm/yr)	Location name	Latitude (°N)	Which fault?	Tool	observation period	Details on method	Source
8.1 ± 3.2	South of Nushki	29.2	CF	InSAR	2004-2011	Dislocation model	<i>Fattahi and Amelung [2016]</i>
16.3 ± 2.3	South of Nushki	29.2	Ghazaband F	InSAR	2004-2011	Dislocation model	<i>Fattahi and Amelung [2016]</i>
11 +1/-2	Nushki segment	29.9	CF	InSAR	2003-2011	Use different viewing geometry	<i>Barnhart [2017]</i>
< 2.0	Nushki segment	30.3	CF	InSAR	2003-2011	Use different viewing geometry, $D_L = < 3$ km	<i>Barnhart [2017]</i>
17.3 ± 1 [7.7 ± 1]	Quetta	30.166	All west of Quetta	GPS	2006-2008	Eurasia-fixed reference	<i>Mohadjer et al. [2010]</i>
7-9	Nushki segment	30.5	CF	InSAR	2003-2011	Use different viewing geometry	<i>Barnhart [2017]</i>
33.3 ± 3	Bostankaul	30.75	CF	Geology	35 kyr	Datation of sediments	<i>Ul-Hadi et al. [2013b]</i>
8.5 +1.8/-1.7	Near Chaman	~30.8	CF	GPS	2007-2012	Dislocation model, $D_L = 3.4$ km	<i>Szeliga et al. [2012]</i>
8.8	Near Chaman	~30.8	CF	GPS	2012-2016	Rough fit	<i>Crupa et al. [2017]</i>
6.6 ± 1.2	Near Qalat	31.8	CF	InSAR	2004-2011	Dislocation model	<i>Fattahi and Amelung [2016]</i>
16.8 ± 2.7	Near Qalat	~32	CF	InSAR	2004-2008	Dislocation model, $D_L = 5.4 ± 2.4$ km	<i>Szeliga et al. [2012]</i>
19-24	Whole central CF	29.5-32.5	Chaman FZ	Geology	~25-20 Myr	Based on >100s km offsets of a fault and geological units	<i>Lawrence et al. [1992]; Yeats [2012]</i>
25-35	Muqur to Qara Bagh	~33	Chaman FZ (30 km)	Geology	~2 Myr	Offset of volcanic structures	<i>Beun et al. [1979]</i>
10-20	17 km south of Ghazni	~33.4	CF	Geology	50-100 kyr	Offset and erosion of an ash pile	<i>Carbonnel and Blondeau [1977]; Beun et al. [1979]</i>
16.8 ± 0.5 [9.2 ± 0.4]	Kabul	~34.4	Gardez FZ	GPS	2006 and 2008	Displacement between Kabul and Peshawar	<i>Szeliga et al. [2012]</i>
9.3 ± 1.1 [3.7 ± 1.1]	Kabul	34.574	All west of Kabul	GPS	2006 and 2008	Eurasia-fixed reference	<i>Mohadjer et al. [2010]</i>

Table 1: Review of previous slip estimates along the Chaman plate boundary. D_L : locking depth. CF: Chaman Fault. F: Fault. FZ: fault zone

A.2 Explicit formulation of an example for KFTS

To explicitly present our Kalman filter time series analysis (KFTS; Equations 2.3, 2.4 and 2.5) and the design of each matrix for InSAR data (Table 2.1), we describe an example below. We consider the case of KFTS at the 2nd assimilation of data ($k = 2$) for a linear phase model, with an offset and a velocity $\phi_i = a_0 + a_1 t_i$. The state vector, then, writes as $\mathbf{m}_1 = (a_0, a_1, \phi_0, \phi_1)$. After assimilation of data at time t_1 , we have the covariance \mathbf{P}_1 , the measurement \mathbf{A}_2 and the noise \mathbf{Q}_2 as

$$\mathbf{P}_1 = \begin{pmatrix} \sigma_{a_0}^2 & & & \\ & \sigma_{a_1}^2 & & \\ & & \sigma_{\phi_0}^2 & \\ & & & \sigma_{\phi_1}^2 \end{pmatrix}, \quad \mathbf{A}_2 = \begin{pmatrix} 1 & & & \\ & 1 & & \\ & & 1 & \\ 1 & t_2 & 0 & 0 \end{pmatrix} \quad \text{and} \quad \mathbf{Q}_2 = \begin{pmatrix} q_0 & & & \\ & q_1 & & \\ & & 0 & \\ & & & 0 \\ & & & & \sigma_\gamma^2 \end{pmatrix}. \quad (1)$$

Because we want to exactly reconstruct phases with respect to a fixed null starting phase, ϕ_0 , then σ_{ϕ_0} must be set to zero. The parameters q_0 and q_1 are non-zero if there is a need to add systematic noise for functional parameters $a_{0,1}$. This would relax the weight of the previous estimate of $a_{0,1}$ on each forecast.

We consider two interferograms, $\phi_2 - \phi_0$ and $\phi_2 - \phi_1$, from 3 acquisitions at times t_0, t_1 and t_2 . Thus the data, observation model \mathbf{H}_2 and covariance \mathbf{R}_2 are given as

$$\mathbf{d}_2 = (\Phi_{02}, \Phi_{12}), \quad \mathbf{H}_2 = \begin{pmatrix} 0 & 0 & 0 & 0 & 1 \\ 0 & 0 & 0 & -1 & 1 \end{pmatrix} \quad \text{and} \quad \mathbf{R}_2 = \begin{pmatrix} \sigma_\epsilon^2 & 0 \\ 0 & \sigma_\epsilon^2 \end{pmatrix} \quad (2)$$

Applying Equations 2.3,

$$\sigma_{\phi_2}^f = \sqrt{\sigma_{a_0}^2 + \sigma_{a_1}^2 t_2^2 + \sigma_\gamma^2} \quad \text{and} \quad \phi_2^f = a_0 + a_1 t_2 \quad (3)$$

Note that, if data is sufficient, the phase ϕ_1 would have been reconstructed at the previous step with little uncertainty, so that $\sigma_{\phi_1} \rightarrow 0$. Following this assumption and using the data in d_2 , we update the forecast with Equations 2.4 and 2.5. As an example, we have

$$(\sigma_{\phi_2})_{k=2} = \sqrt{(\sigma_{\phi_2}^f)^2 - 2\kappa(\sigma_{\phi_2}^f)^4} \quad \text{and} \quad (\phi_2)_{k=2} = \phi_2^f + \rho\kappa(\sigma_{\phi_2}^f)^2 \quad (4)$$

$$(\sigma_{a_1})_{k=2} = \sqrt{\sigma_{a_1}^2 - 2\kappa\sigma_{a_1}^4 t_2^2 + q_0} \quad \text{and} \quad (a_1)_{k=2} = a_1 + \rho\kappa\sigma_{a_1}^2 t_2 \quad (5)$$

with κ the common part of the gain to all analyzed parameters and ρ the residual expressed as

$$\kappa = \frac{1}{\sigma_\epsilon^2 + 2(\sigma_{\phi_2}^f)^2} \quad \text{and} \quad \rho = \Phi_{02} + \Phi_{12} + (\phi_1)_{k=1} - 2\phi_2^f \quad (6)$$

The subscript $k = 2$ outlines that the values are those evaluated at the second assimilation step. The velocity a_1 will be re-analyzed at each assimilation step and the phase ϕ_2 may be re-analyzed if interferogram(s) Φ_{2k} for any k are assimilated over the course of subsequent assimilation steps. If noise associated with interferogram construction is small (i.e. $\sigma_\epsilon \rightarrow 0$), then Equation 4 tells us that the phase at time t_2 is perfectly reconstructed with zero uncertainty. In a more general sens, Equations 4 and 5 evidence the dependency of any phase and model parameter estimate to error terms arising from governing Equations 2.3, 2.4 and 2.5 (see Figures 2.11).

A.3 Illustration of KFTS parametrization tests for Chapter 2

The following additional Figures provide a graphical appreciation of the effect of parametrization on the behavior of the Kalman filter. Hence, most Figures are variants of Figures in the main text. Figures A.2 to A.10 are the results of the Kalman filter applied to the synthetic case (Section 2.3.1), whereas Figures A.11 to A.15 refer to the application on ENVISAT data over Mt Etna. The effect of ‘wrong’ parametrization is highlighted by deliberately imposing unrealistic values with respect to recommendations given in Section 2.3.1.3 and 2.4.1. We chose to detail the example on Mt Etna rather than on the Chaman fault as it forms a finite length dataset (while Sentinel data are continuously acquired) and it includes fewer pixels.

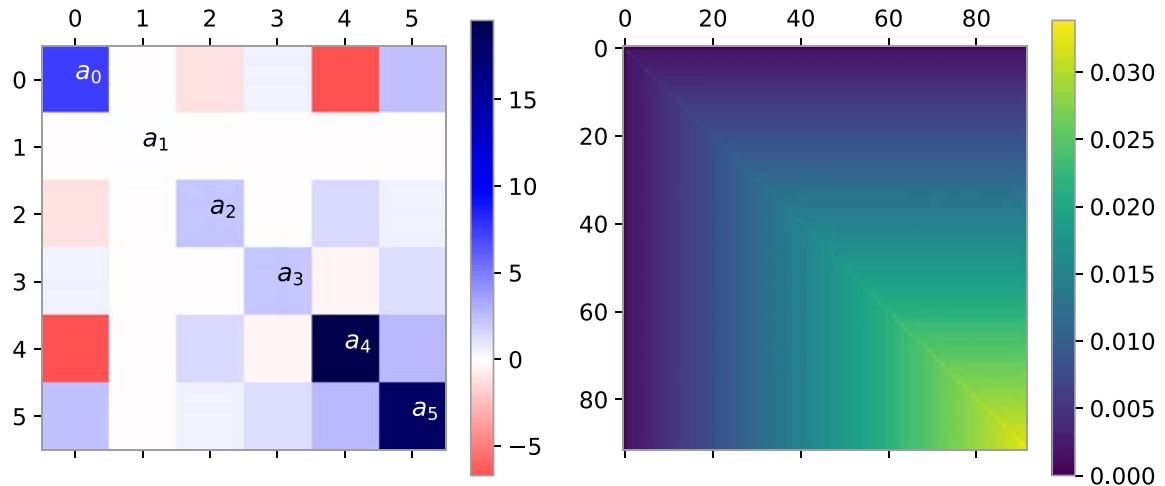


Figure A.2: Graphical representation of the final Covariance matrix (P_{91}) in the reference synthetic test (Section 2.3.1) for the same selected pixel than in Figure 2.3 and 2.5. Elements characterizing the variance-covariance of model parameters, a_n , (left) are represented separately from the variance-covariance of phase estimates, ϕ_k , (right). A striking feature on the left subplot, is how well the velocity a_1 is constrained with this optimally parametrized inversion. For other parameters, inter-dependency is strong, especially with the initial offset a_0 . This is why we recommend to store out of the state vector parameters that have already converged (i.e. those for which new data is not informative). Notice the very small uncertainty and significant temporal correlation of phase estimates.

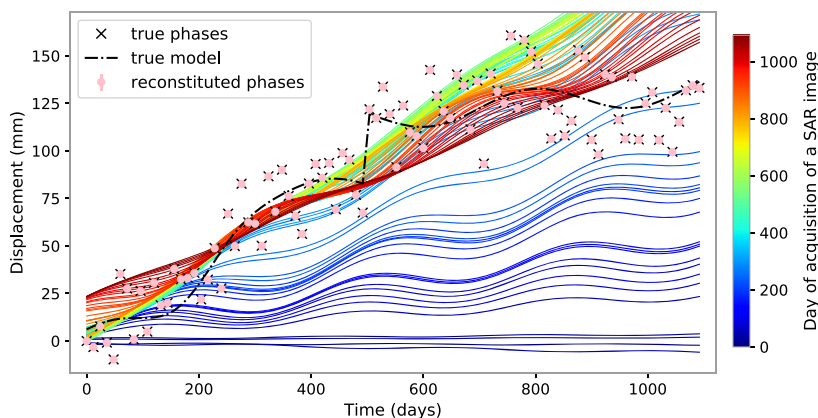


Figure A.3: Same as Figure 2.3B for a parametrized model with missing step and spline components (i.e. a_4 and a_5 are excluded from the inverse problem). We can see that phase values are well retrieved even though model parameters are wrong with respect to the true value. Providing the same functional form is used, the match with least-squares solution is still true. Note that the correct retrieval of phases in the case of a “wrong” model is possible providing the network of interferograms connects all dates to the initial and reference date.

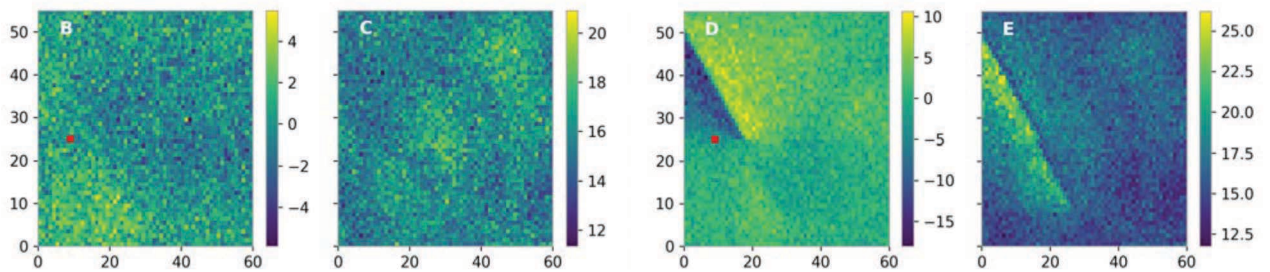


Figure A.4: Median (*B,D*) and standard deviation (*C,E*) per pixel of the time series of mean innovation in the case of optimal parametrization (presented in Section 2.3.1.2) (*B,C*) and in the case of missing step and spline components in the description of deformation (*D,E*) (like in Figure A.3). In real cases, the statistical **distribution of innovation** per pixel allows to clearly identify areas with "wrong" model description, here those next to the simulated active fault. In this region, innovation is not normally distributed and the center of the distribution is not zero, which literally means that the forecast based on the parametrized model does not appropriately describe the phase evolution. In such case the model should be updated, and this can be done in between assimilation steps.

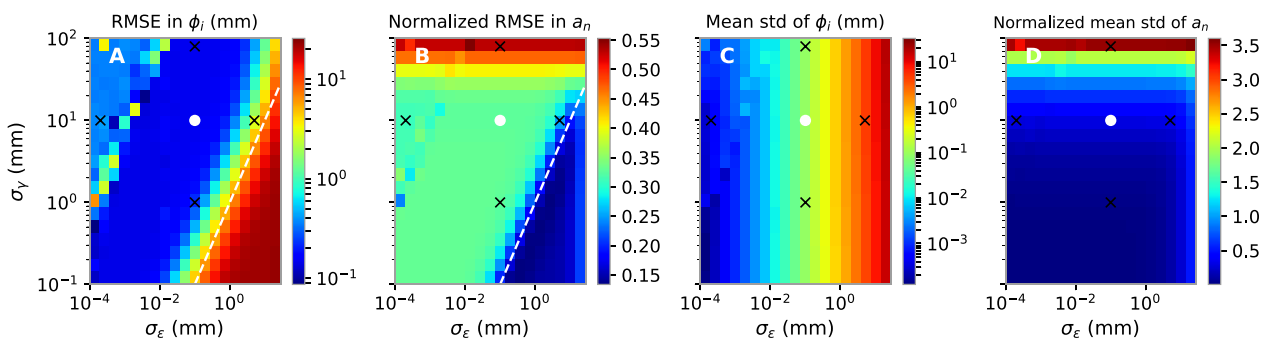


Figure A.5: Same as Figure 2.6 with four additional crosses locating the $(\sigma_\gamma, \sigma_\epsilon)$ configuration of the cases presented in the 3 subsequent Supplementary Figures (A.6 - A.8). Those examples are representative of the overall effect of reducing or increasing σ_γ or σ_ϵ .

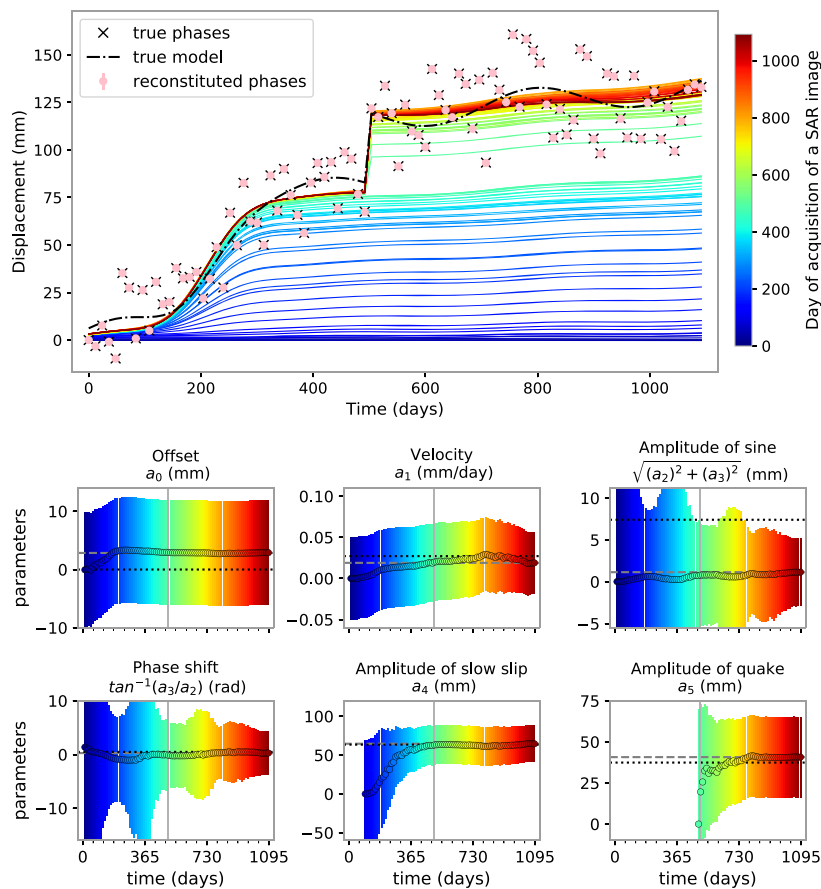


Figure A.6: Same as Figure 2.3B and 2.5 for a large *a priori* standard deviation of the mismodeling error (σ_γ of 80 mm). This implies that we have little trust in the ability of the functional model to describe the phase evolution. Thus, model parameter uncertainties are very large, and more assimilation steps (and thus data over time) are needed for convergence of the functional description. Consequently, small seasonal oscillations are hardly adjusted for and the state vector remains close to its *a priori* value, \mathbf{m}_0 , until enough data is assimilated.

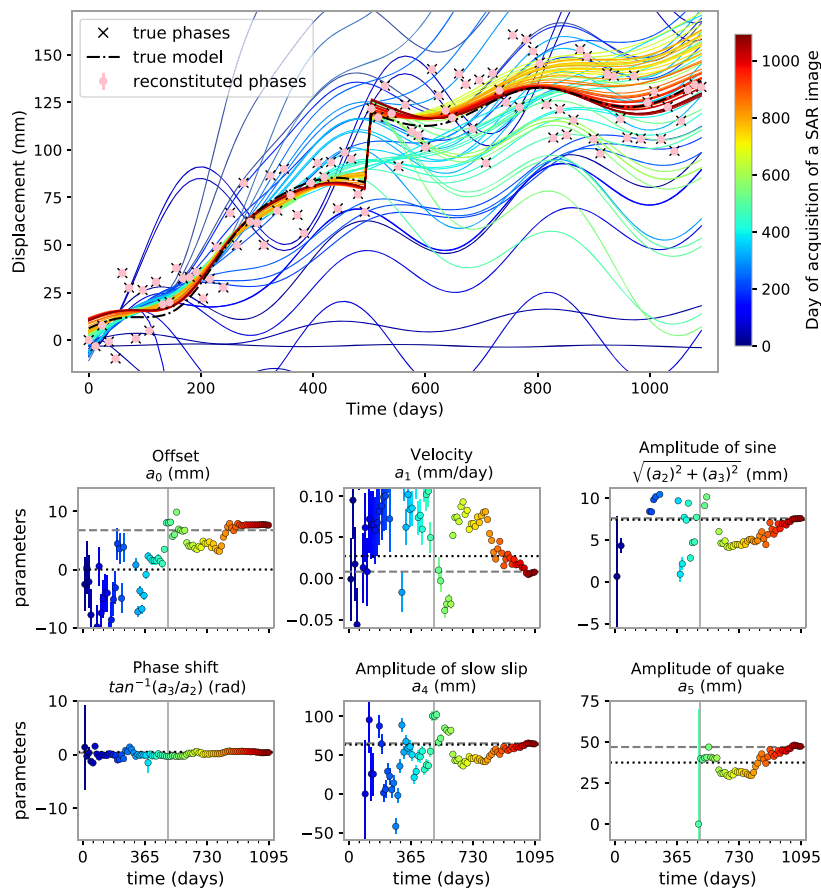


Figure A.7: Same as Figure 2.3B and 2.5 for a low *a priori* standard deviation of the mismodeling error (σ_γ of 1 mm). This implies that we trust too much the ability of the functional model to describe the phase evolution. Thus, model parameter uncertainties drop quickly and the model is very sensitive to new data and tries to adjust at each new assimilation step. This is particularly marked when little data has been assimilated. The final estimation is not too biased but parameter uncertainties σ_{a_n} are clearly underestimated.

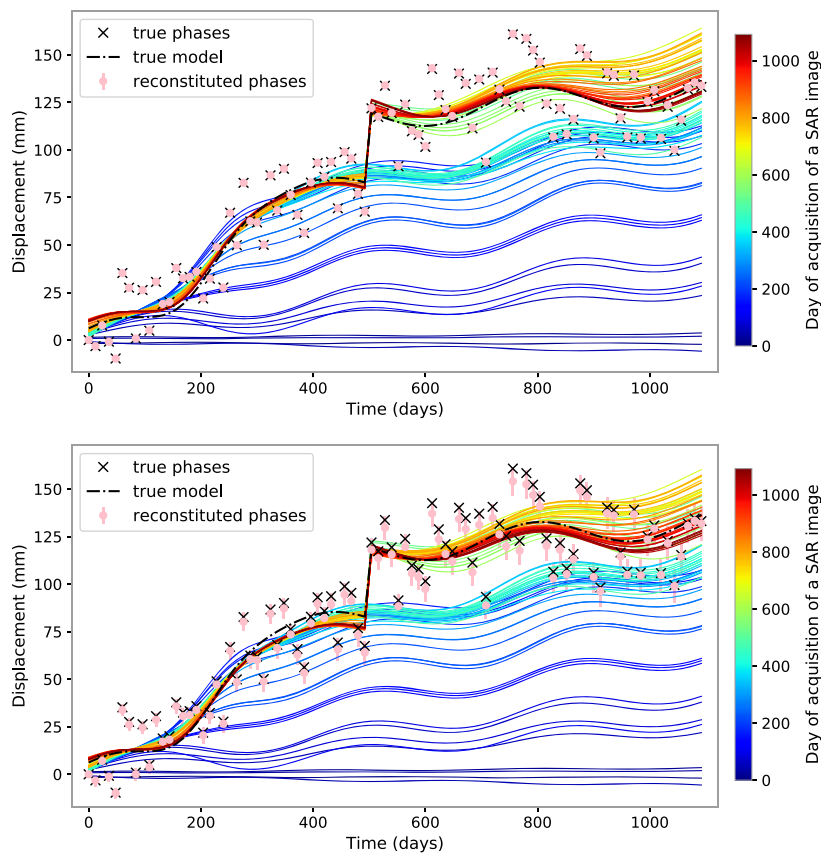


Figure A.8: Same as Figure 2.3B for a very low (top) and high (bottom) *a priori* standard deviation of the misclosure error (σ_ϵ of 2×10^{-4} mm and 5 mm). Lowering σ_ϵ induces a subtle shift in phase estimate with respect to true value. This bias increases over time. On the other hand, increasing σ_ϵ lowers the confidence in the phase estimate. However, we have to underestimate σ_ϵ by 3 orders of magnitude, or multiply the value by 50 (and, thus, get close to σ_γ) to notice a change in the graphical representation of the time series, which is consistent with the small sensitivity to this parameter.

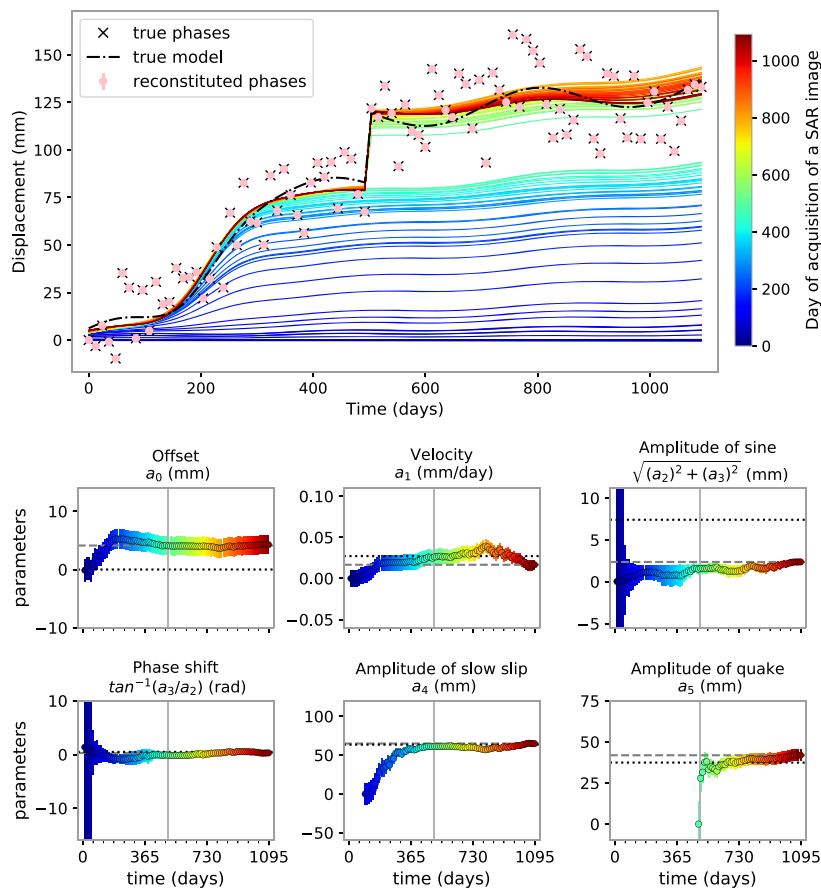


Figure A.9: Same as Figure 2.3B and 2.5 for a very low *a priori* error on model parameters (all reference standard deviation σ_{a_n} , $0 \leq n < L$ in Section 2.3.1.2 have been divided by 5). As a consequence, there is great confidence in the initial null model and smoother solution is found. The role of σ_{a_n} as a regulation term is clearly outlined.

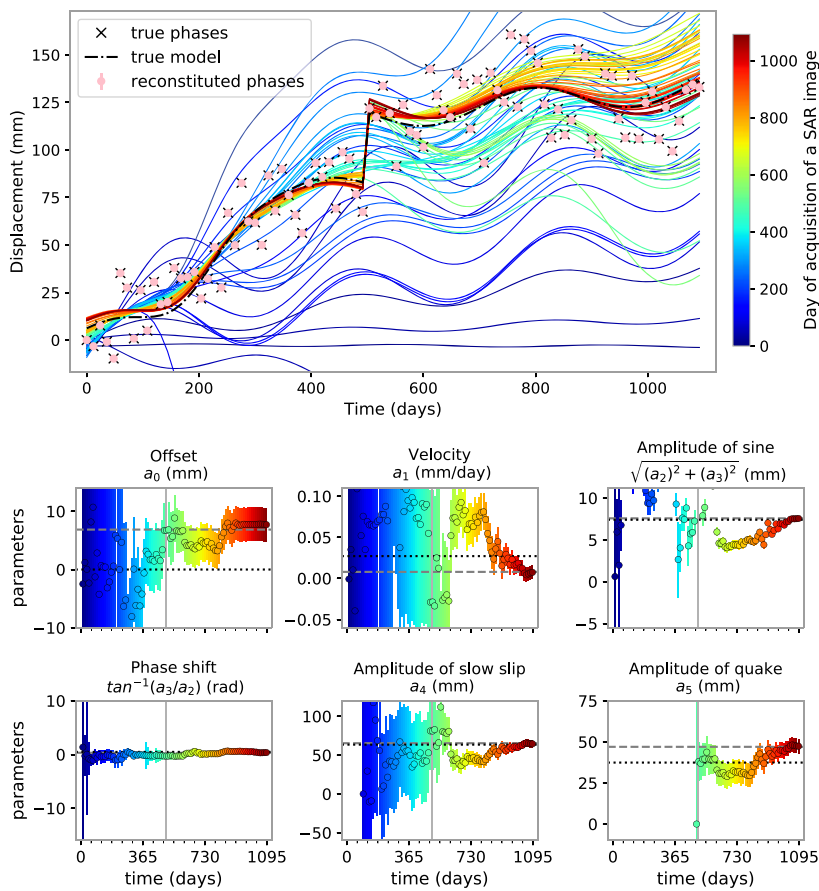


Figure A.10: Same as Figure 2.3B and 2.5 for a very high *a priori* error on model parameters (all reference standard deviation σ_{a_n} , $0 \leq n < L$ in Section 2.3.1.2 have been multiplied by 5). As a consequence, the model parameters computed in the first assimilation steps is a lot more uncertain and is very sensitive to the new data assimilated. From Figures A.7 and A.8, it seems that the diagonal of \mathbf{P}_0 has the inverse effect than σ_γ on model parameter value (Figures A.4, A.5). However, the effect on parameters uncertainty differs. Notice that the model progressively recovers, as data is assimilated, from "bad" *a priori*.

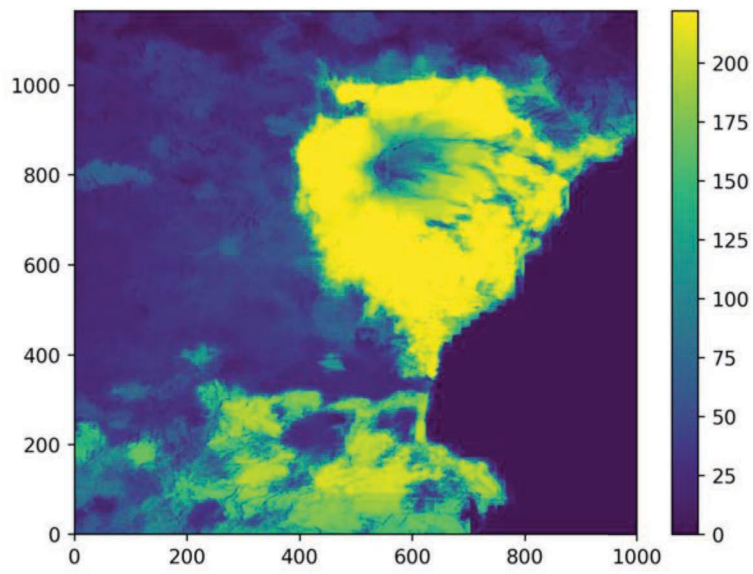


Figure A.11: Number of interferograms available per pixel, which directly affects the phases (and parameters) variances (Figure 2.7B and A.12).

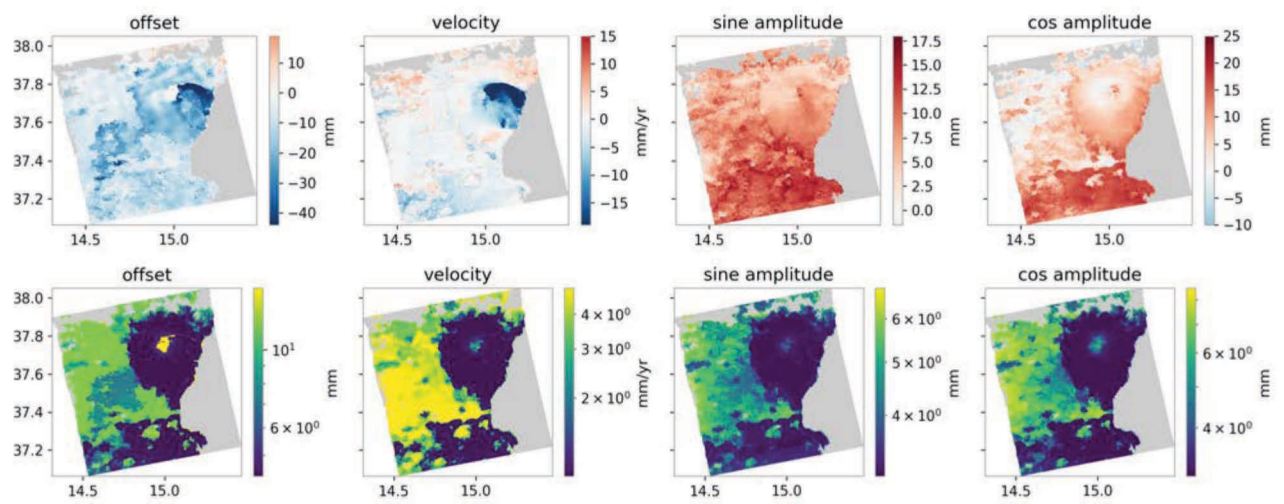


Figure A.12: Model parameters, a_n , reconstructed for Mt Etna (top) and their standard deviation (bottom).

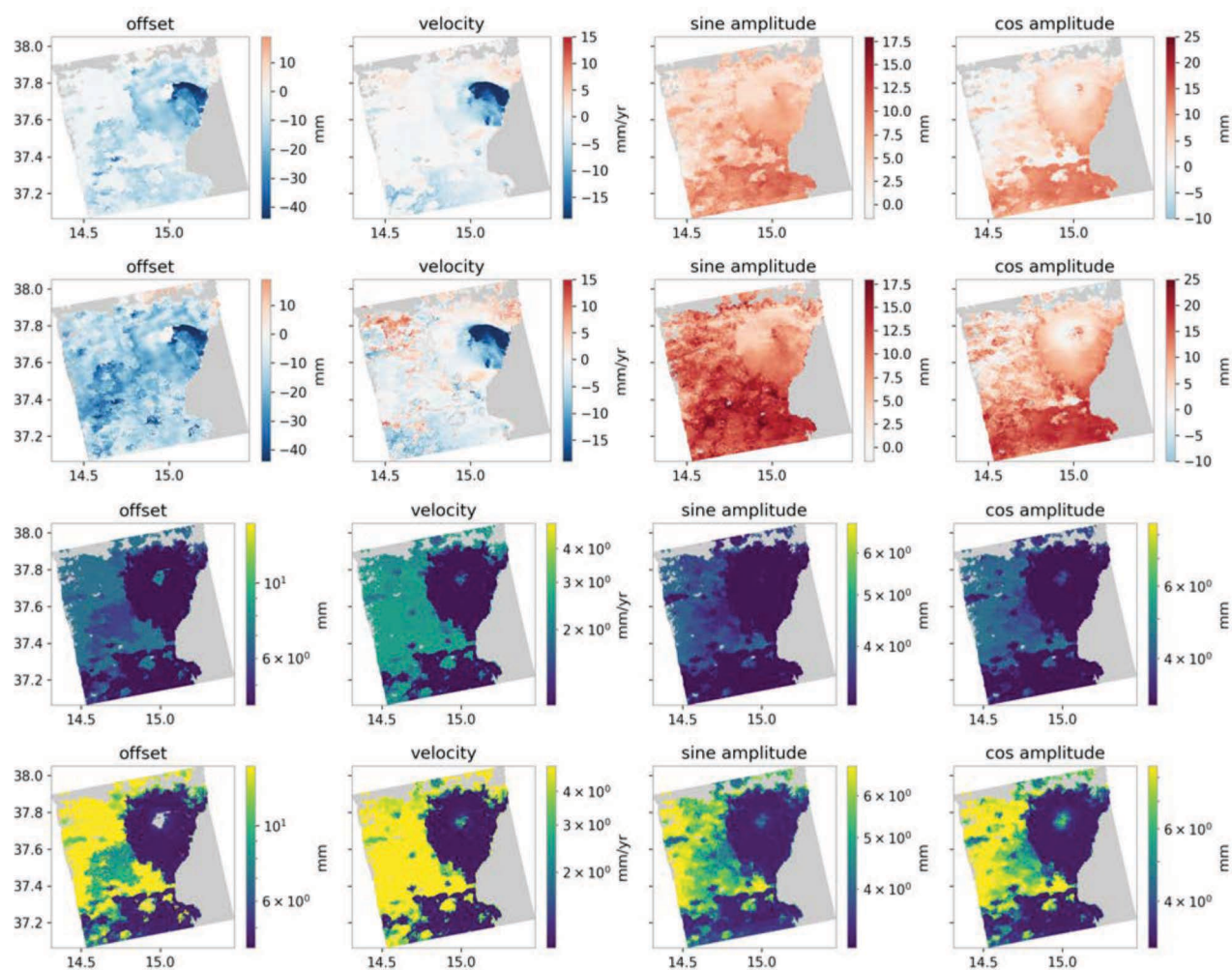


Figure A.13: Same as Figure A.12 for a Kalman filter for which P_0 was changed. The standard deviation of *a priori* model parameters was either divided by 2 or multiplied by 2 with respect to reference case. Colorbars are bounded using the reference case in Figure A.12 for easy comparison. Row by row from top to bottom: parameters for low P_0 , parameters for high P_0 , standard deviations associated with each parameter for low P_0 and, below, for high P_0 . Notice the persistence of the dominant patterns on the volcanic edifice. Most of the differences concentrate in the plains surrounding the volcano with fewer data, hence a greater influence of the forecast.

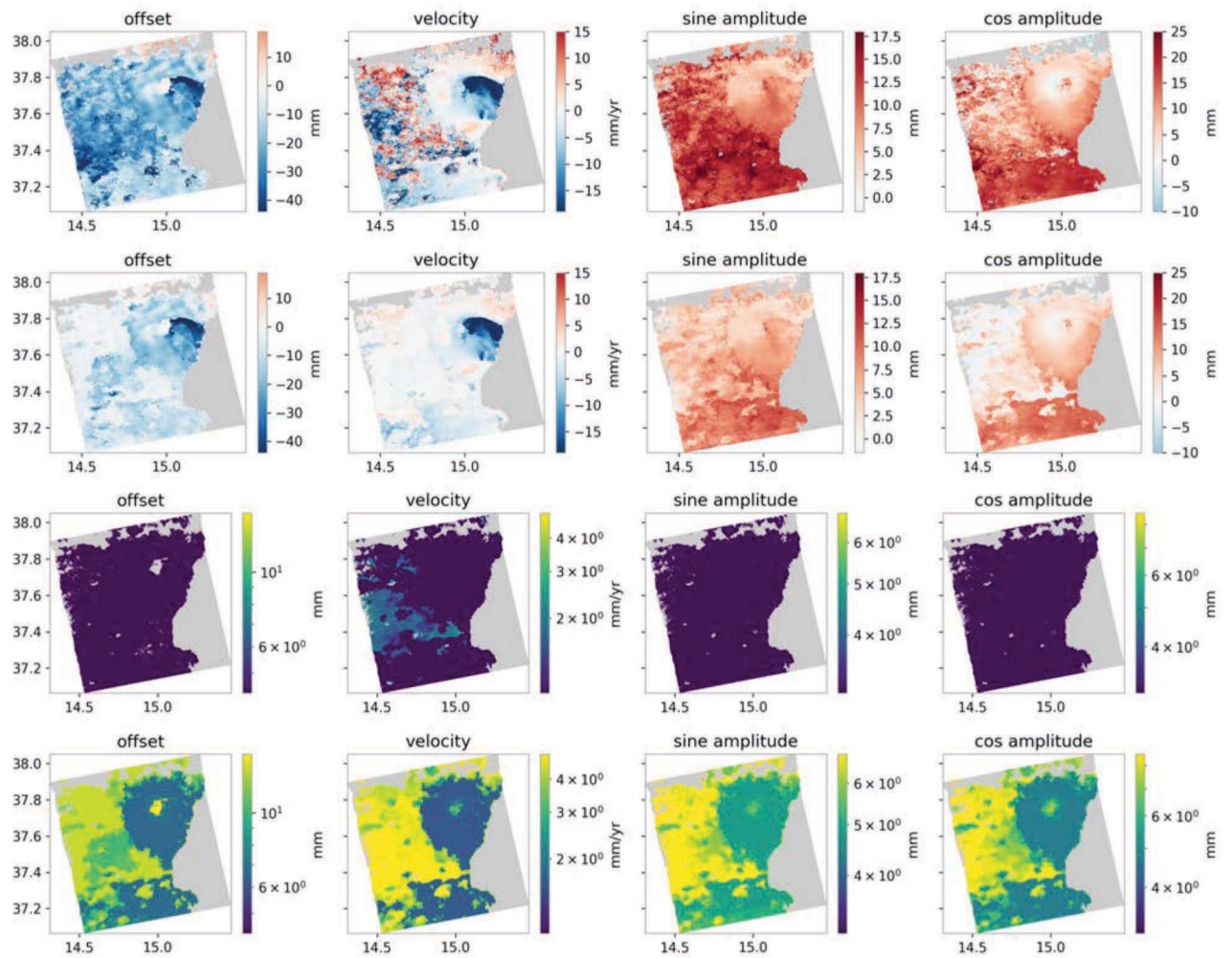


Figure A.14: Same as Figure A.12 for a Kalman filter for which σ_γ was changed to 1 mm or to 30 mm. Colorbars are bounded using the reference case in Figure A.12 for easy comparison. Row by row from top to bottom: parameters for low σ_γ , parameters for high σ_γ , standard deviations associated with each parameter for low σ_γ and, below, for high σ_γ .

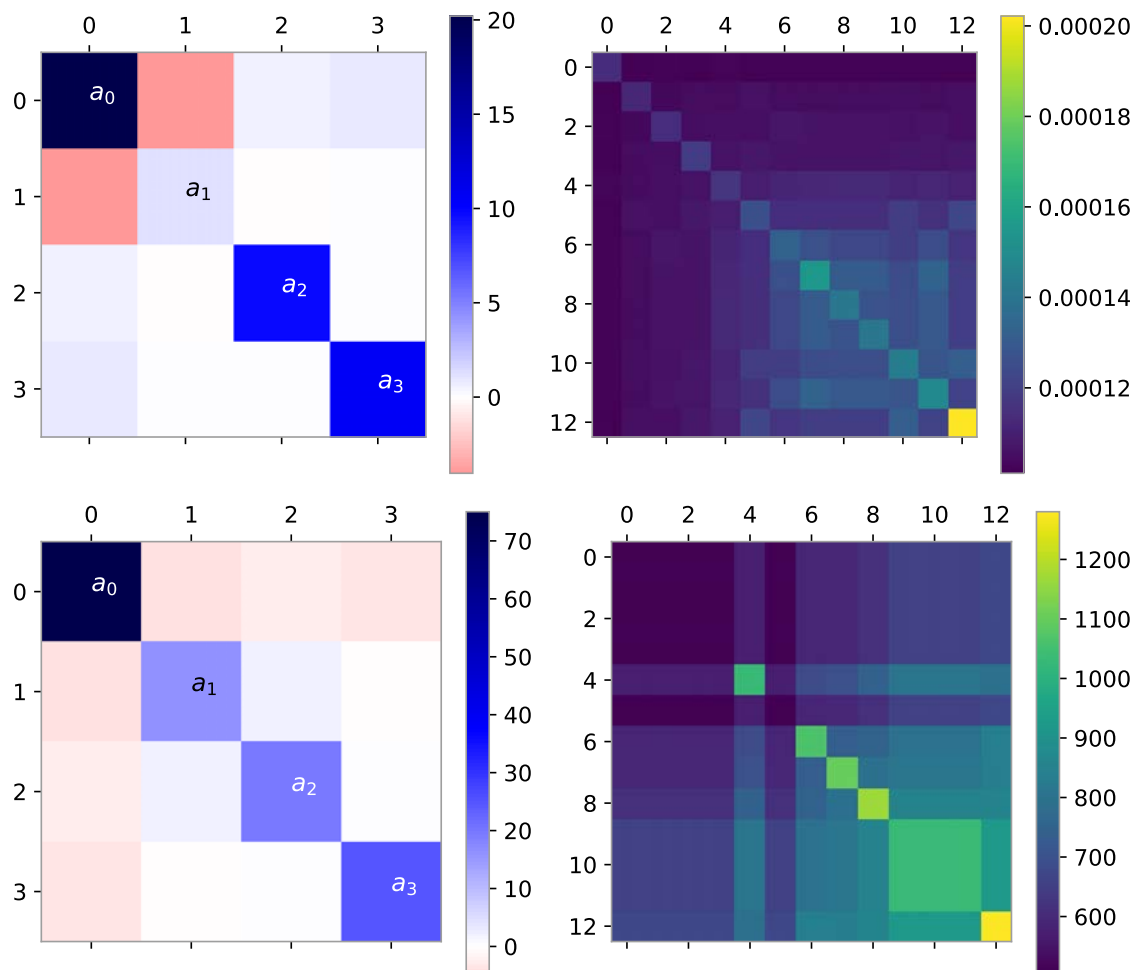


Figure A.15: Same as Figure A.2 for the application of the KF on Mt Etna (Section 2.3.2). We see the final Covariance matrix (\mathbf{P}_{62}) for the pixels in the KF solution at the location of GPS stations ESLN (top) and MMME (bottom).

A.4 Structure of interferometric networks

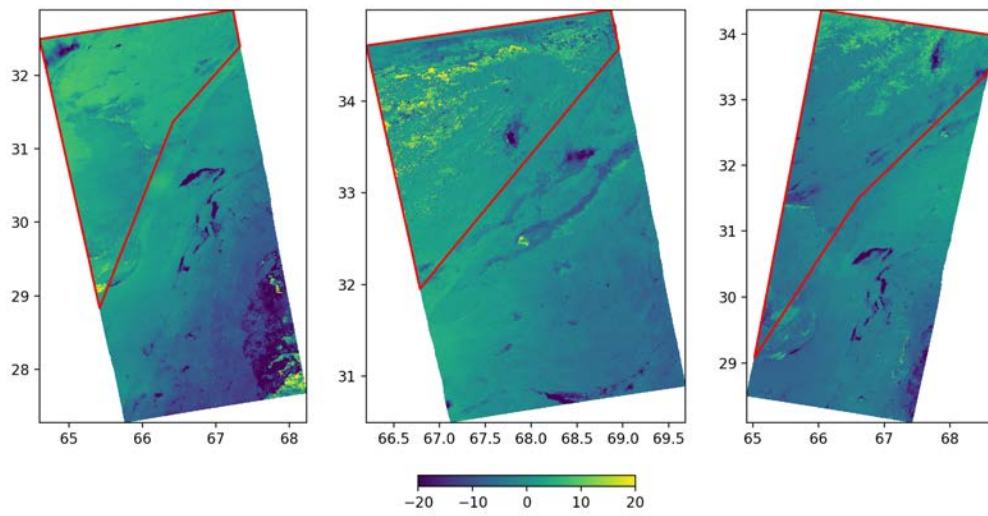


Figure A.16: Red line delimits the reference zone used for deramping interferograms on tracks 42 (Left), 144 (Middle) and 151 (Right). The average velocity field is in the background for easier spatial reference (in mm/yr).

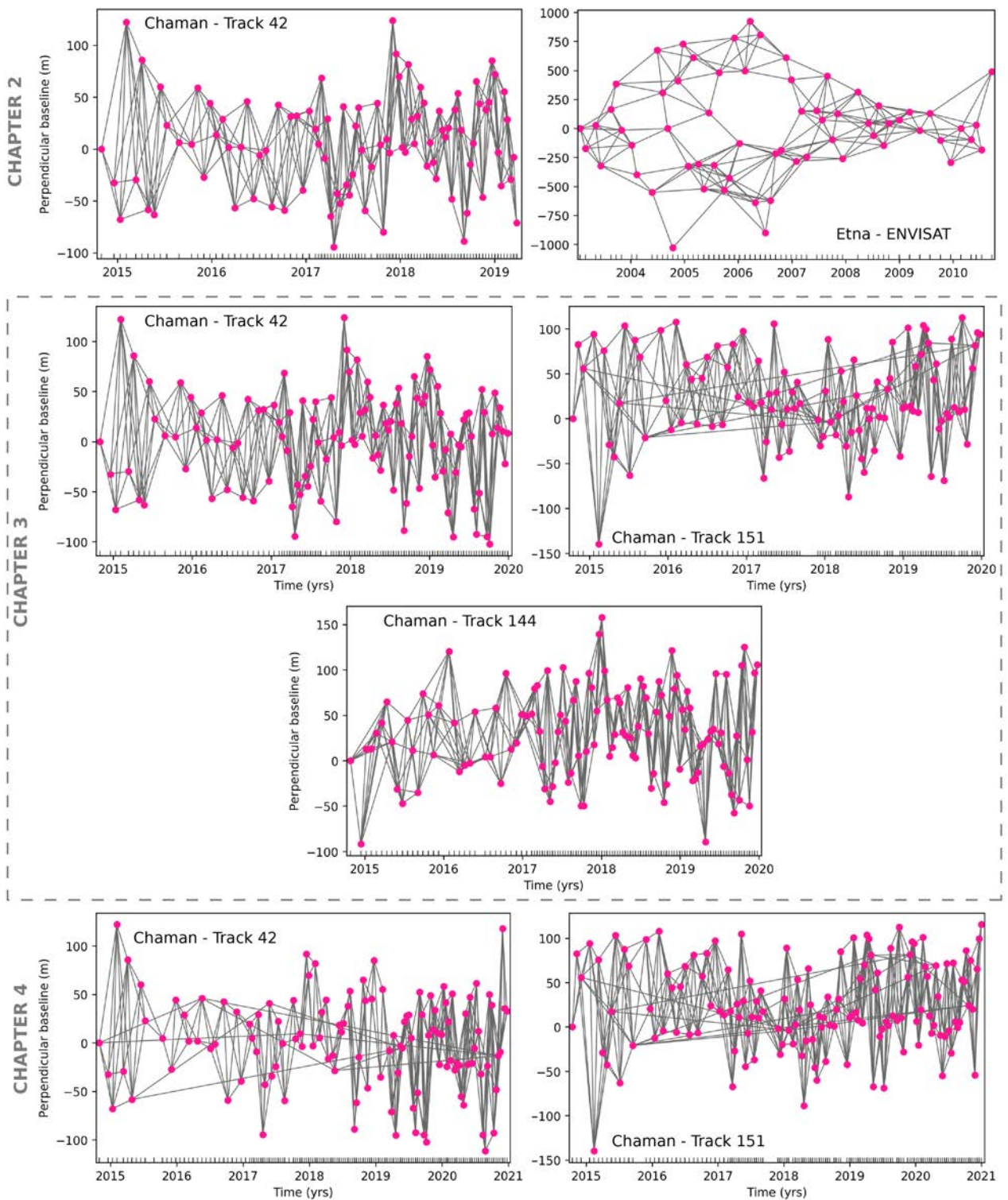


Figure A.17: Perpendicular baseline versus date of acquisitions for the all interferometric networks discussed in this Thesis. Each dot is a SAR acquisition and connecting lines are interferograms. Perpendicular baseline refers to orbital configuration during acquisitions. Networks are grouped by Chapter and are all built from Sentinel 1A-B data except the earliest ENVISAT data on Mount Etna presented in Chapter 2 (upper right baseline plot). Track 42 and 144 are ascending while track 151 is descending. The same network has been extended between chapters to incorporate the latest acquisitions at the time of processing.

A.5 Additional details on Chapter 3 methodology

A.5.1 On the earthquake step amplitude *a priori*

Date (UTC)	Longitude	Latitude	Depth (km)	M_w	Numb. of events	Total M_w
2015/08/03 13h16	66.020	27.370	12	5.4	3	5.57
2016/03/21 14h48	66.140	27.747	14.9	5.7	10	5.73
2016/05/13 6h59	66.472	30.633	12.6	5.6	3	5.74
2016/07/10 21h33	66.580	30.780	15	5.1	1	5.1
2018/06/27 16h53	66.334	30.495	12	4.1*	2	4.52

Table 2: Detailed information of the earthquakes modeled by our Kalman filter from the Global Centroid-Moment-Tensor (GCMT) Project and the International Seismological Center (ISC) Bulletin (see Section 3.2.2) [Dziwowski et al., 1981; Ekström et al., 2012; ISC, 2020; Bondár and Storchak, 2011]. (*) The last magnitude is a body-wave magnitude (M_b)

THE *a priori* range of a_j , the amplitudes of the Heaviside functions H_j , for each pixel depends on the Euclidean distance, d_j , to the earthquake epicenter. For a given pixel (superscript p), a_j are initially set to zero with a *a priori* variance given by a two-dimensional Gaussian function centered on the earthquake epicenter with a maximum amplitude, b_j^2 , and a characteristic width, w_j , that is

$$(\sigma_{a_j}^p)^2 = b_j^2 e^{-\frac{1}{2} \left(\frac{d_j^p}{w_j} \right)^2}. \quad (7)$$

CONSEQUENTLY, the *a priori* standard deviation, $\sigma_{a_j}^p$, is also a two-dimensional Gaussian with a characteristic width equal to $\sqrt{2}w_j$ and a maximum amplitude of b_j (Figure A.18). For all earthquakes, we choose to set the maximum standard deviation, b_j , to 30 mm and the width, w_j , to 9 km. This means that, for instance, $\sigma_{a_j}^p$ is 15 mm about 25 km away from the predicted earthquake location. Below a threshold of $\sigma_{a_j}^p = 1$, we set $\sigma_{a_j}^p$ to zero to avoid having small but non-zero covariance extending faraway from the earthquake and, thus, simplify the problem mathematically. With $w_j = 9$ km this threshold is reached at a distance of about 40 km from the earthquake location.

In addition to potential over-fitting of the data, another reason to limit the spatial extent of the modeled earthquake step is the impact of this additional parameter on velocity estimates. Indeed, there is an interdependency which arises mathematically between the earthquake step amplitude and velocity, which results in larger uncertainties (see map of velocity uncertainties in Figure A.25).

A.5.2 On the parameterization of the dislocation screw inversion

WE MODEL interseismic slip at depth on the Chaman fault (CF) using a dislocation screw model, an equation relating ground velocity as a function of the perpendicular distance to the fault to the amount of slip S below a locking depth D_S , and the amount of creep C above the creep extent D_C (Section 3.3.4) [Savage and Burford, 1973]. We adjust this model to 3556 profiles across the CF independently, allowing for an offset in the fault location X_f , a constant shift of velocities A and a ramp B . We invert for those 5 parameters using a Markov-Chain-Monte-Carlo implemented in the python package PyMC3 [Salvatier et al., 2016]. The description of the prior distribution of all parameters is in Table 3.

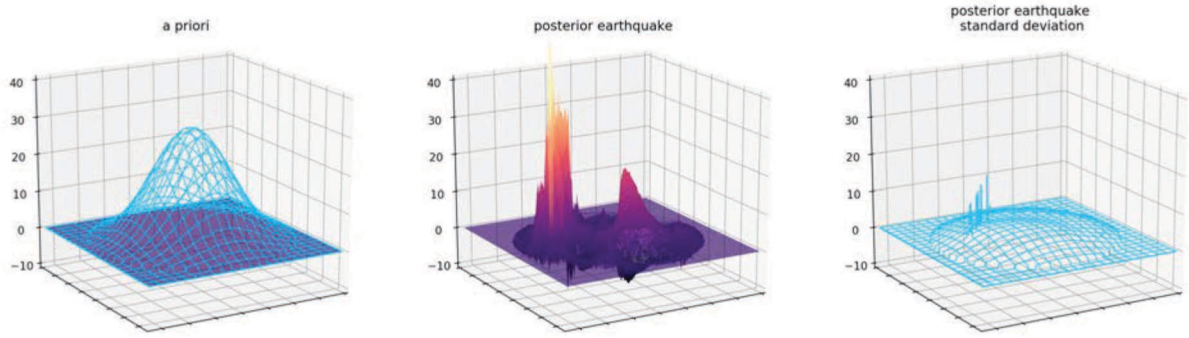


Figure A.18: Representation of the *a priori* for the parameter corresponding to earthquake amplitudes (left) and the example of the final estimate for the 13th May 2016 earthquake (center and right). Horizontal axes are spatial directions, while the vertical axis shows the earthquake amplitude and uncertainties in millimeters. Colored surfaces are earthquakes amplitudes and blue meshes are the associated standard deviations. The center plot contain the same data as Figure 3.2e in a 3-D projection.

OUR PARAMETERIZATION does not allow locking depth larger than 9 km because of the difficulty to distinguish the corresponding surface strain rates from a linear ramp on 30 km-long profiles. Longer profiles in the fault-related deformation are impossible to extract because of the proximity of the Rigestan desert west of the CF. We consider velocity estimates and their associated uncertainties. Moreover, we add a prediction error of 2 mm/yr to all velocities, to account for the fact that the design of the model is source of additional uncertainties [Duputel *et al.*, 2014]. The posterior probability density function, product of the prior probability density functions, and of a Gaussian likelihood function, is sampled with a Metropolis-Hastings algorithm through 4 independent chains of 10000 samples each; the 5000 first samples are burned.

Name	Bounds	Mean	Std	Unit
Constant A	-10, 10	-	-	mm/yr
Ramp, B	-0.5, 0.5	0	0.05	(mm/yr)/km
Creep, C	0, 30	-	-	mm/yr
Creep extent, D_C	0, 8	1	3	km
Slip, S	0, 30	-	-	mm/yr
Locking depth, D_S	0.01, 9	2	5	km
Fault location, X_f	-1.2, 1.2	0	0.25	km

Table 3: Descriptive parameters for the prior distributions used in our dislocation model inversion for slip on the Chaman fault during the interseismic period. The three parameters with no mean or standard deviation (std) specified have uniform distributions.

A.5.3 On the uncertainty propagation from interferograms to surface fault slip

OUR time series analysis method (KFTS) estimate covariances for all parameters including interferometric phases at each time step and velocities [Dalaison and Jolivet, 2020]. Resulting standard deviations take into account predefined errors from phase misclosure and mismodelling (including temporally decorrelated noise like tropospheric delays), uncertainty coming from the structure of the interferometric network on a given pixel and trade-offs between describing parameters. Interferometric phase estimates are very precisely known. However, the interpretation of this phase in terms of deformation is associated with significant, hardly quantifiable uncertainty that is thought to be of the order of magnitude of the mismodelling error ± 10 mm [Dalaison and Jolivet, 2020].

PARAMETERS of the time dependent model, like velocity, have non-negligible uncertainties (e.g. Figure A.25). To get surface slip rates, we draw profiles in the velocity map (a_1 in Equation 3.1 or v_H in Equation

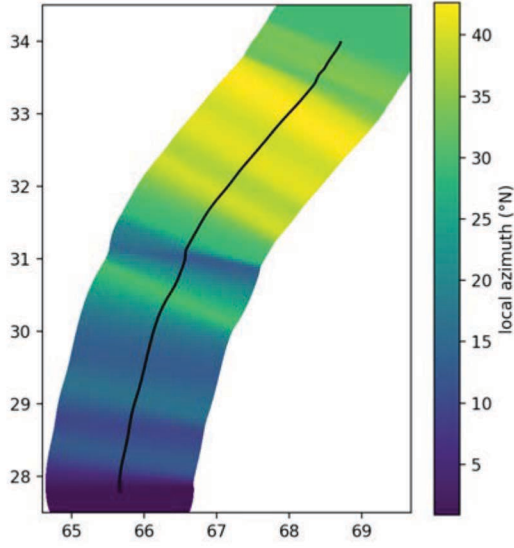


Figure A.19: Fault azimuth map used as projection angle in Figure 3.3.

3.2) and in the map of the associated standard deviation, so that each measure of velocity, $v(x_i)$, at distance x_i from the fault along the profile has associated uncertainty, $\sigma_v(x_i)$ (Section 3.3.4). We compute the weighted mean velocity, \bar{v} , within 500 m and 1.5 km on each side of the fault. For instance, the formula for N points satisfying $0.5 \text{ km} < x_i < 1.5 \text{ km}$ is

$$\bar{v}^{\text{right}} = \sum_{i=1}^N \frac{v(x_i)}{\sigma_v(x_i)^2} \times \left(\sum_{i=1}^N (\sigma_v(x_i)^2)^{-1} \right)^{-1}. \quad (8)$$

There are two ways to compute the error associated to the mean value: we can either propagate the known uncertainties $\sigma_v(x_i)$ (i in $[1, N]$) assuming uncorrelated measures or compute the standard deviation of the N averaged $v(x_i)$. While the first definition takes into account observational error, the second quantifies the amount of spatial scattering in velocity estimates. For each \bar{v} , we choose the definition leading to the largest error $\sigma_{\bar{v}}$. Numerically, it writes as

$$\sigma_{\bar{v}} = \text{MAX} \left[\sqrt{\left(\sum_{i=1}^N (\sigma_v(x_i)^2)^{-1} \right)^{-1}}, \sqrt{\frac{\sum_{i=1}^N (v(x_i) - \bar{v})^2}{N}} \right]. \quad (9)$$

Consequently, the surface slip rate standard deviation, σ_{dv} , is

$$\sigma_{dv} = \sqrt{(\sigma_{\bar{v}}^{\text{left}})^2 + (\sigma_{\bar{v}}^{\text{right}})^2}. \quad (10)$$

AS A RESULT of this two-folded definition, we obtain a conservative estimate of across fault slip uncertainty for da_1 and dv_H (Figure 3.5c,d), meaning that the uncertainty is likely smaller than what we estimate. This outlines the robustness of our slip measures.

A.5.4 On earthquake slip inversion

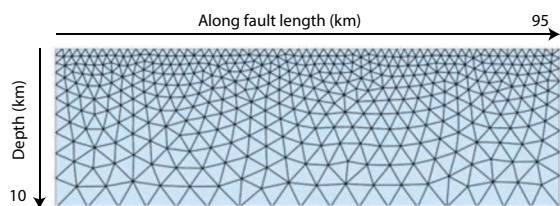


Figure A.20: Mesh of the fault for source modeling of the three Chaman fault earthquakes.

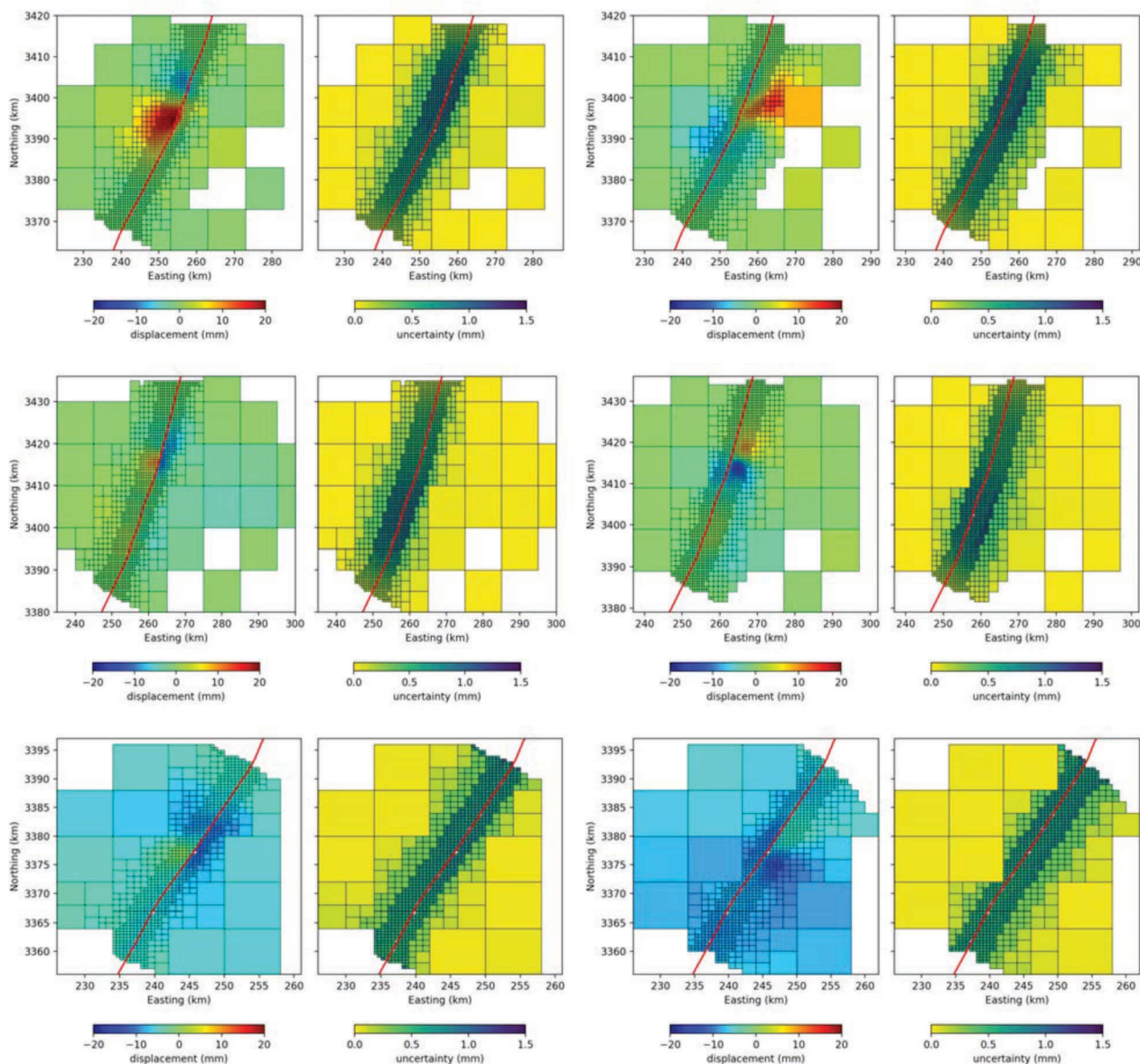


Figure A.21: Downsampled coseismic displacement and associated uncertainties using a quadtree scheme. Observations along ascending (left column) and descending (right column) tracks are shown for each earthquake: 13 May 2016, 10 July 2016, 27 June 2018 (from top to bottom).

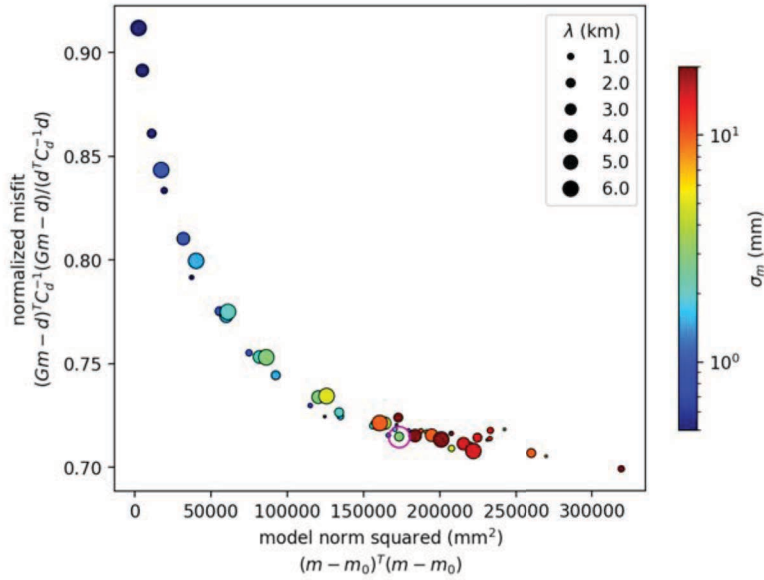


Figure A.22: L-curve to optimize parameters of the *a priori* model covariance: the characteristic length (λ) and model standard deviation (σ_m) [Radiguet et al., 2011]. In violet is surrounded the chosen parameter $\lambda=2$ km $\sigma_m=3$ mm. This is for the first earthquake only, taken as a representative example for the three events.

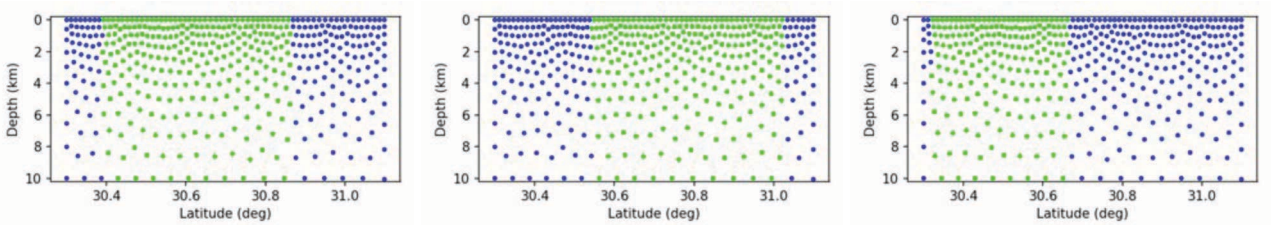


Figure A.23: Variations in σ_m and thus of the diagonal of the model covariance matrix C_m as a function of the localization of the fault patch center for our three inverted earthquakes : May 2016 (left), July 2016 (center), June 2018 (right). Light green nodes are for $\sigma_m=2$ mm and blue nodes for $\sigma_m=1$ mm (outside of data footprint).

A.6 Additional results for Chapter 3

Source	Number of earthquakes	Minimum M_w	Maximum M_w	1900-2019 M_o (Nm)	1990-2019 M_o (Nm)
GCMT	8	4.9	5.9	1.69×10^{18} *	7.29×10^{17}
USGS	85	3.6	6.7	2.38×10^{19}	8.89×10^{17}
ISC	139	3.8	6.5	1.79×10^{19}	1.57×10^{18}

Table 4: Statistics of the seismicity within 30 km of the Chaman fault. *GCMT catalog starts in 1976.

Date (UTC)	Pre-seismic (mm/yr)	Coseismic (mm)	Early postseismic (mm)	long-term postseismic (mm)	postseismic period (days)	postseismic to coseismic
2016/05/13	1.2	11.7	11.9	4.6	521	1.3
2016/07/10	1.1	13.5	4.0	3.6	595	0.4
2018/06/27	2.4	8.8	6.1	2.8	346	0.8

Table 5: Peak-to-peak surface slip in profiles of Figure 8 across earthquake-related displacement as considered in Section 5.2. Those values are indicative and used to compute postseismic to coseismic slip ratios only, defined as : [early postseismic + long-term postseismic – preseismic slip \times postseismic period/365] / coseismic.

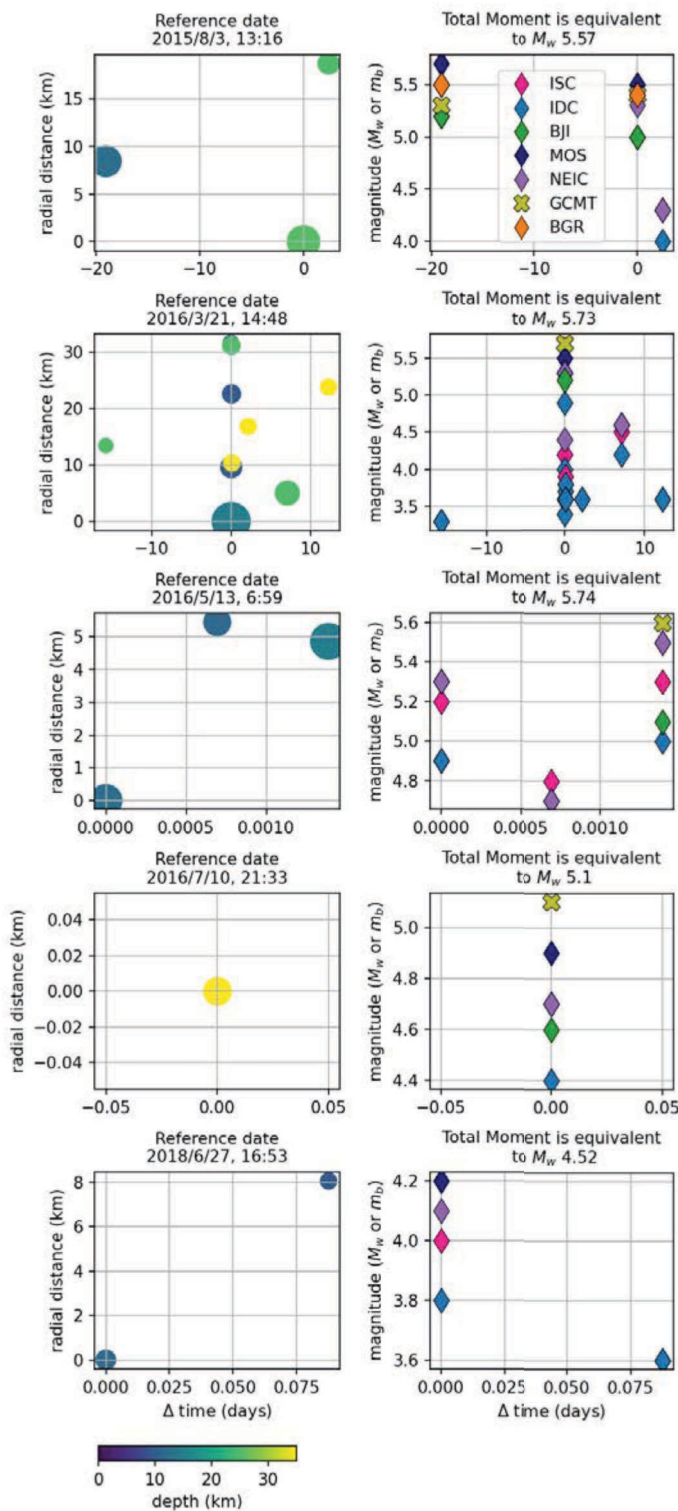


Figure A.24: Timing and magnitude estimates from the International Seismological Center (ISC) Bulletin [consulted in August 2019] of earthquakes in spatio-temporal proximity to the studied events (Table ??). The left column displays the spatio-temporal relationship of events within 20 days and 40 km radius around each of the five studied earthquakes. The size of the marker is scaled with its magnitude and its color reflects the estimated depth. The right column shows the range of magnitude estimates from different sources (seismological institutes). The color of the marker depends on the source (legend in top right plot): ISC, International Data Centre (IDC), China Earthquake Networks Center (BJI), Geophysical Survey of Russian Academy of Sciences (MOS), National Earthquake Information Center (NEIC), Global CMT Project (GCMT), Bundesanstalt für Geowissenschaften und Rohstoffe (BGR). Two types of magnitude estimates are shown: crosses are M_w (only from GCMT), while diamonds are m_b . The total moment is computed using the M_w when available or the mean m_b value converted to M_w using Scordilis [2006]'s relationship.

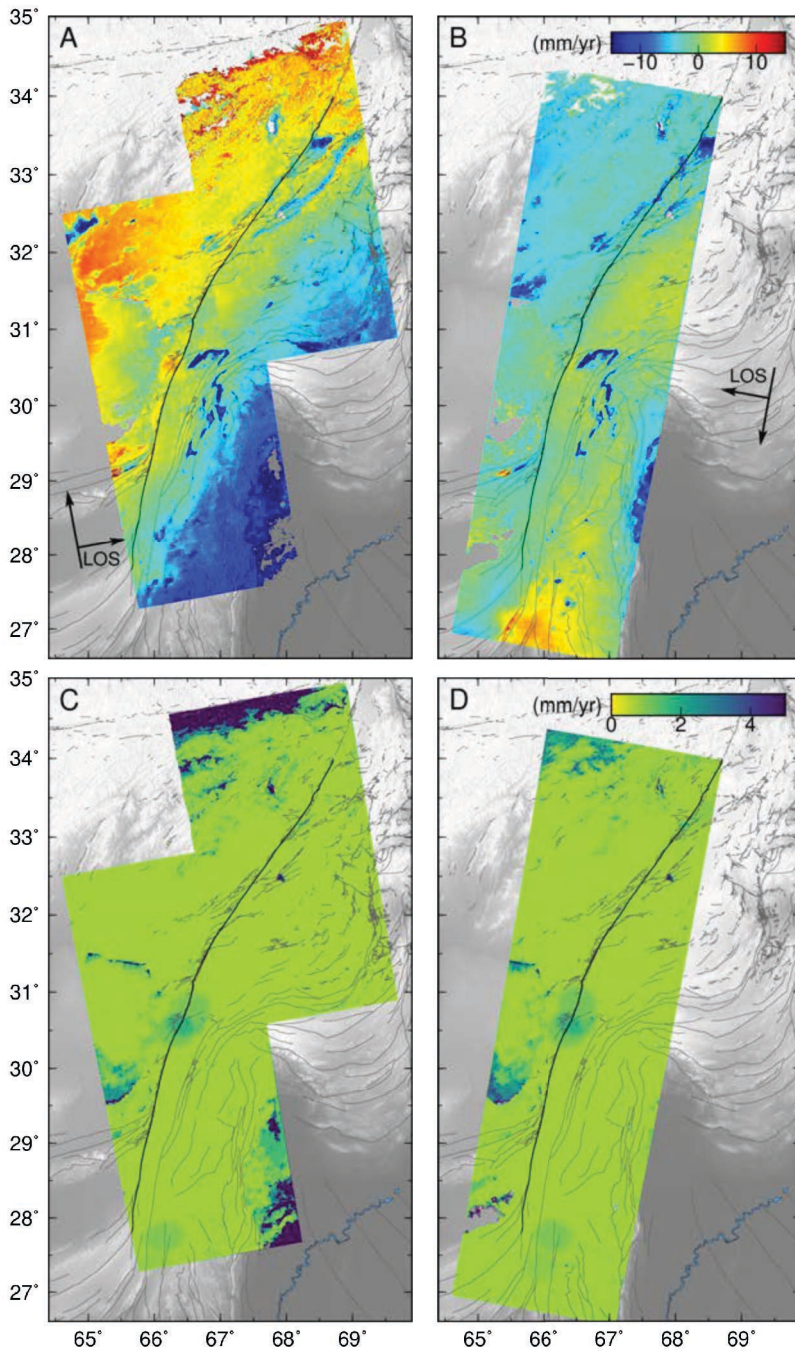


Figure A.25: Velocity field for ascending tracks (A) and the descending track (B) in the Line Of Sight (LOS) direction with the associated standard deviations (C and E).

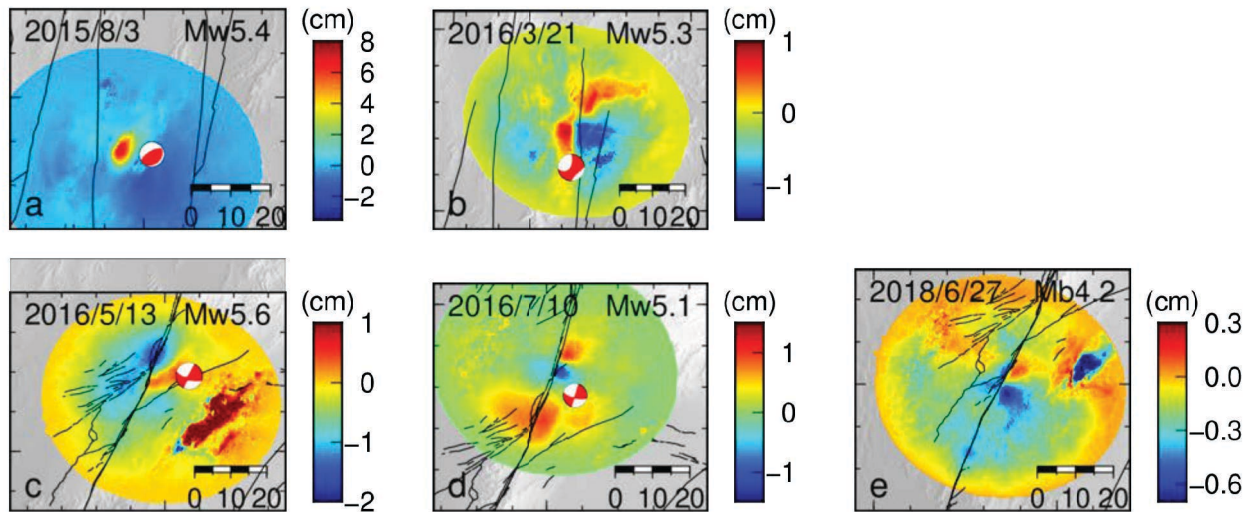


Figure A.26: Estimated coseismic displacement according to our parameterized model of deformation for the descending track (T151). The same observations for the ascending track (T42) is in Figure 3.2c-g with the location of frames in Figure 3.2a.

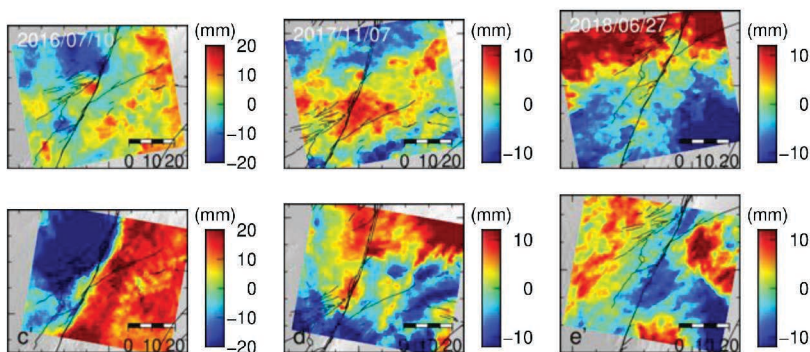


Figure A.27: View of the coseismic earthquake displacement measured as the difference between acquisitions right before and after each event for the three events close to the city of Chaman. Because each pattern is the phase difference between acquisitions before and after each event, it includes turbulent atmospheric delays. Those undesired atmospheric delays are temporally decorrelated and, thus, tend to average out when looking at the time series as a whole, justifying our preference for the parametric model solution to characterize earthquake induced deformation, although it does include some post-seismic signal. Ascending (top row) and descending (bottom row) data are displayed.

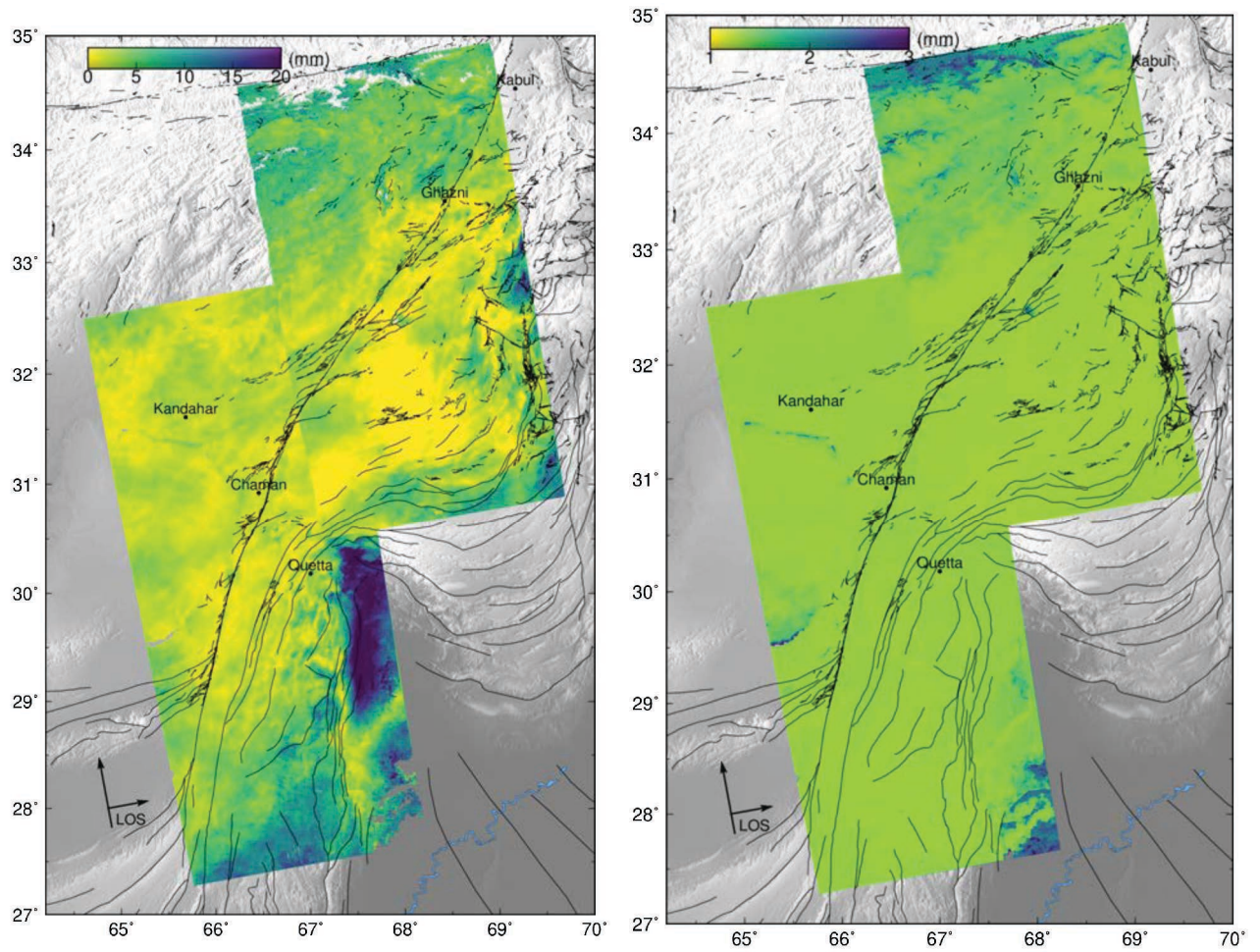


Figure A.28: Map of the amplitude of seasonal signal (left) and the associated uncertainty (right). It resembles the amplitude of the annual zenith wet delay from NASA's Moderate Resolution Imaging Spectrometer (MODIS) observations (shown for the same region in Figure S5.5 of [Fattahi, 2015]).

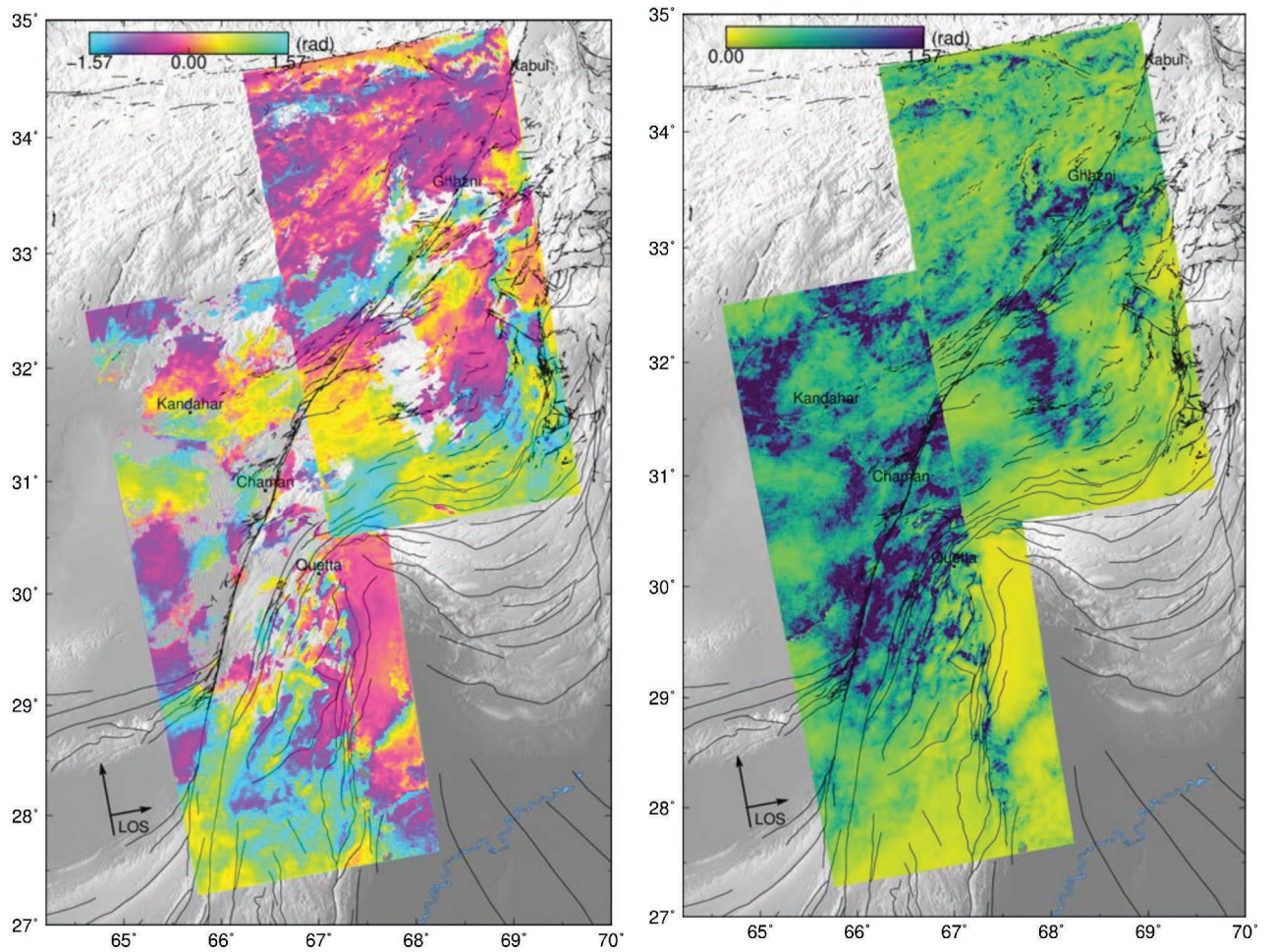


Figure A.29: Map of the phase shift of seasonal signal with respect to the first date of track 144 (earliest date of ascending time series) and associated uncertainty (right). Masked area correspond to area with no or little seasonal signal meaning that phase shift cannot be determined.

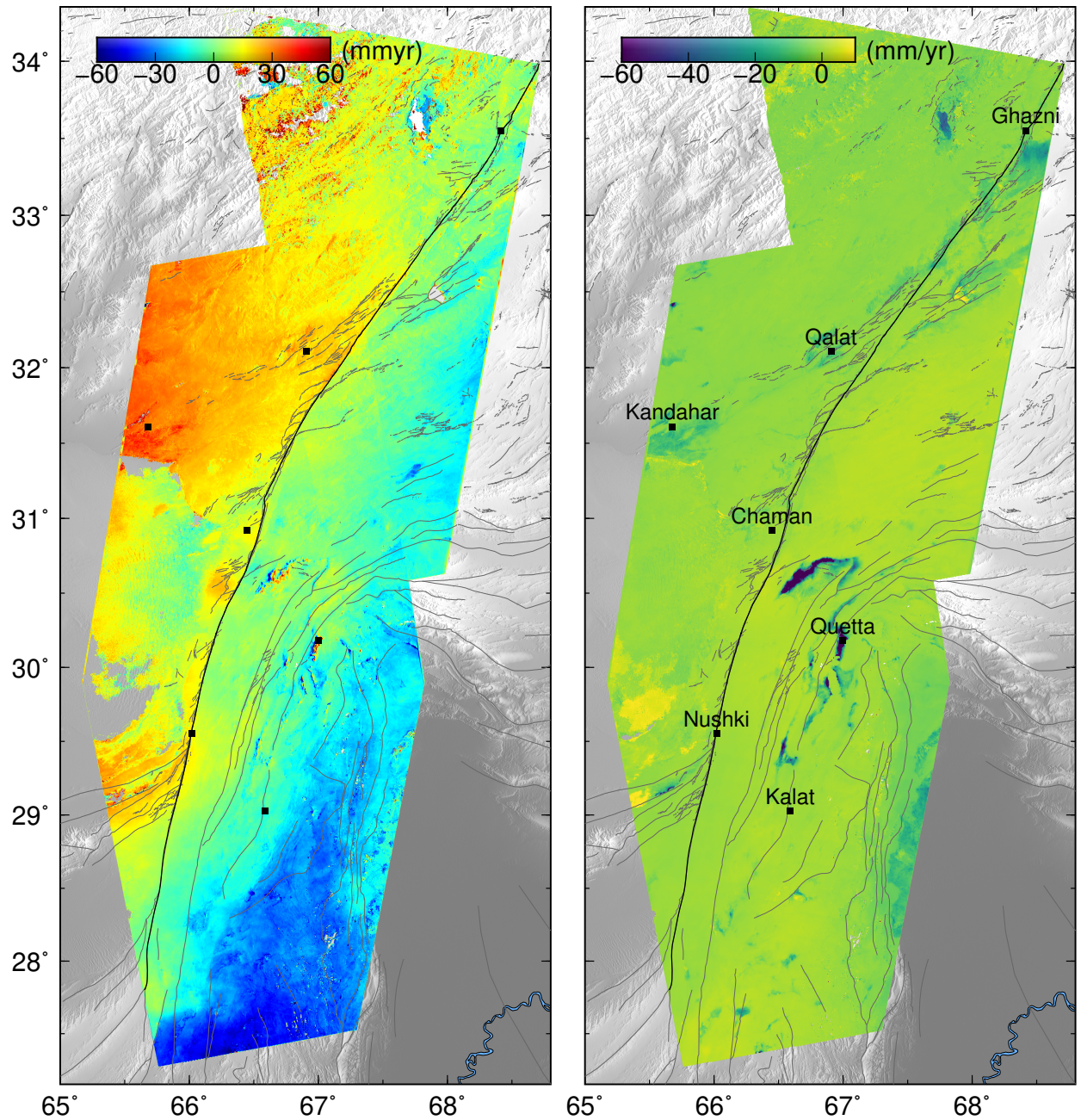


Figure A.30: Velocity field when projected in the 15° North direction (close to IN-EU plate motion, left) and associated vertical velocities (right). Data with standard deviation >6 mm/yr is masked. Maximum subsidence rate exceeds the colorbar limit (see Figure A.31).

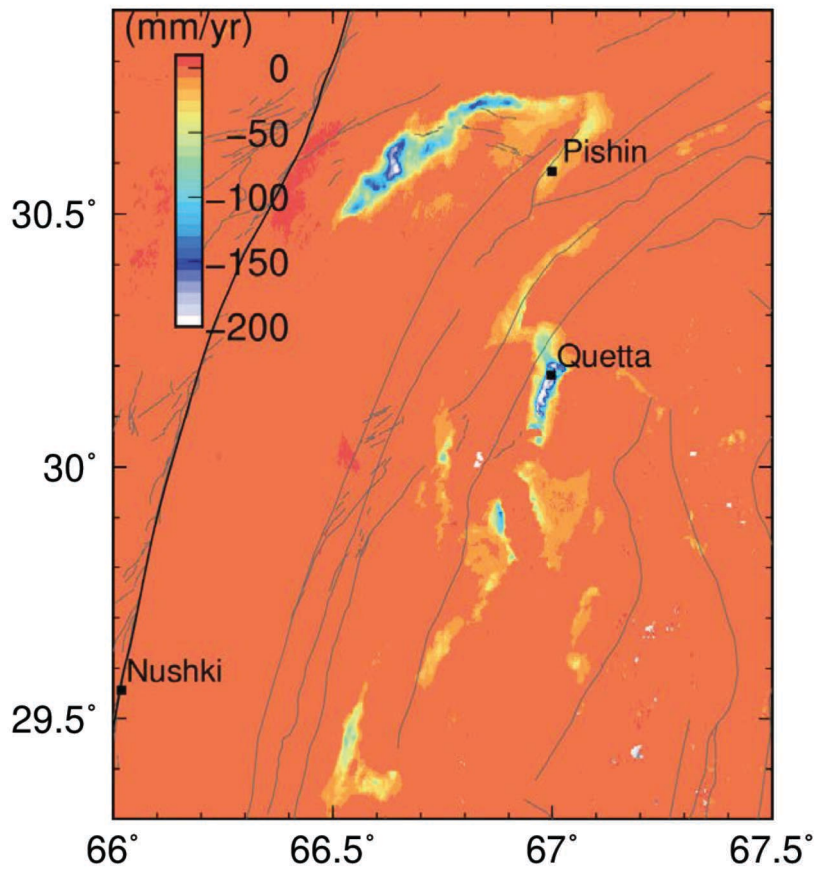


Figure A.31: Zoom on the subsidence rate according to our vertical decomposition of the signal. Same data as previous figure (right subplot) but with a color scale more adapted to see localized extrema within regions of dense human occupation (Pishin basin, Quetta...). The subsidence originates from the massive groundwater decline recorded in Quetta (up to 5-15 m/yr locally), a resources under great stress from recent climatic and demographic trends: more drought and a dramatic growth of Quetta valley population and cultivated area in the past 30 years [Kakar *et al.*, 2016].

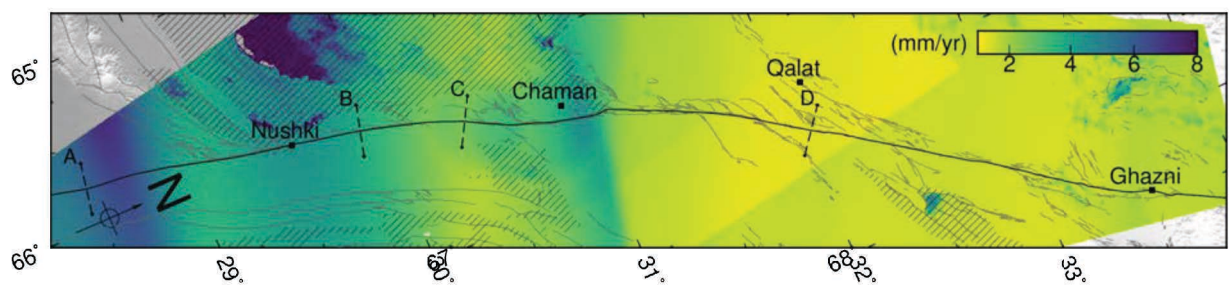


Figure A.32: Map of the standard deviations of the velocity field projected in fault parallel direction shown in Figure 3.3.

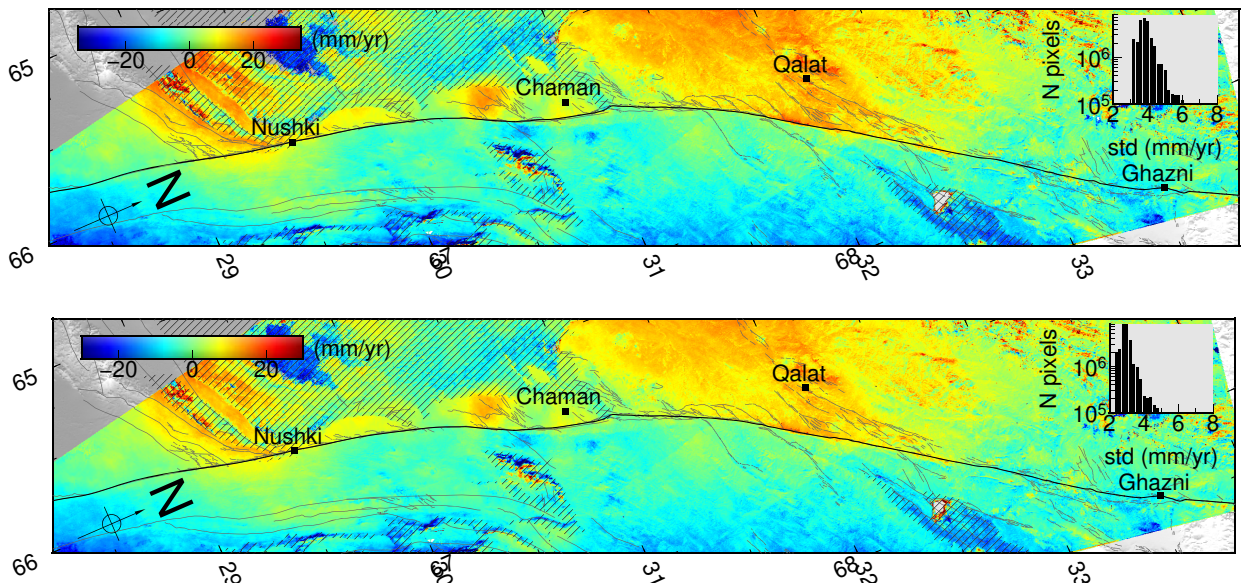


Figure A.33: Same as the map in Figure 3.3 for different angles of projection. Velocity field when projected in the 15° North (top) and 20° North (bottom) directions (close to IN-EU plate motion) with associated histograms of standard deviations (std).

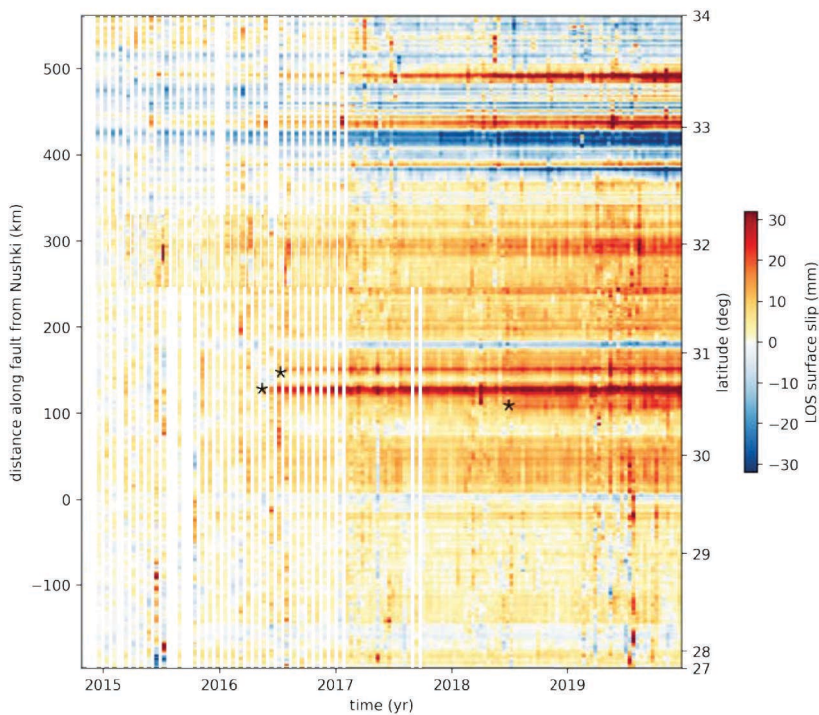


Figure A.34: Same as Figure 3.4 for creep measured for points at a distance between 1 and 5 km from the fault trace instead of 500 m and 1.5 km.

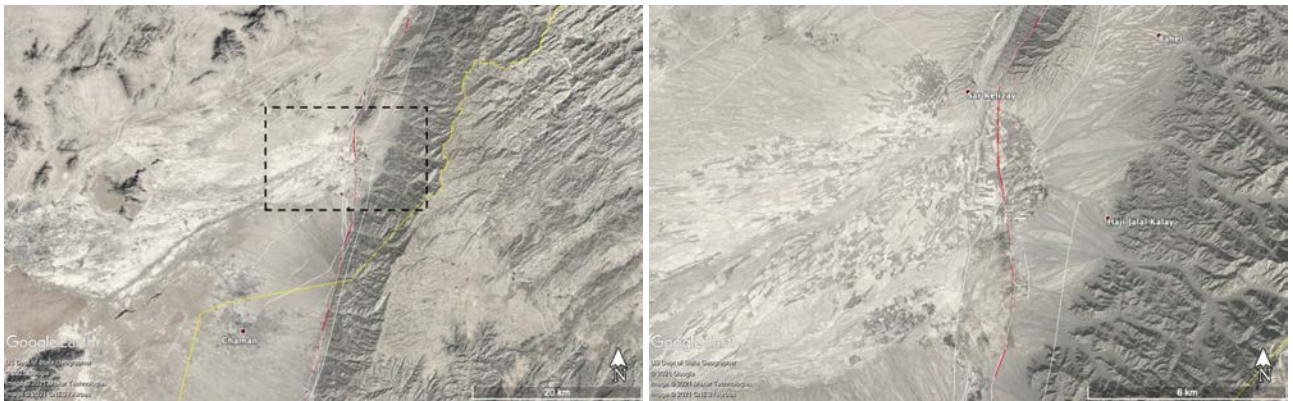


Figure A.35: Optical images of the ground near the Chaman fault main releasing bend from Google Earth. White lines are fault traces from *Ruleman et al. [2007]*, the red line is our continuous fault trace, the yellow line is the frontier between Pakistan and Afghanistan. Agricultural fields and human settlement cluster around the Dori River producing a negative anomaly in velocities west of the fault.

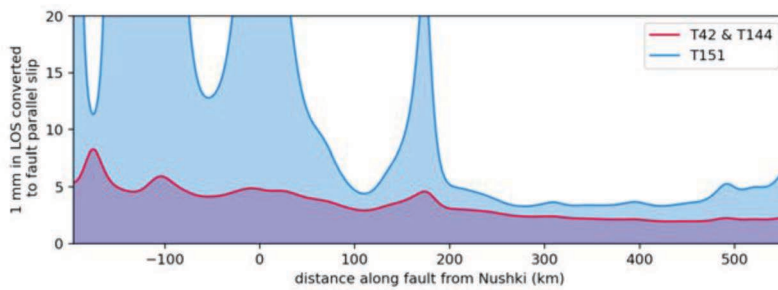


Figure A.36: Quantification of what 1 mm in satellite line of sight (LOS) is in left-lateral slip. This gives the multiplicative factor between LOS and fault parallel slip depending on local fault azimuth and LOS direction (we use interferometric wide swath acquisitions for Sentinel 1 data, which implies varying LOS azimuth). The highest it is, the larger slip in the fault parallel direction has to be in order to be detected in LOS by InSAR. The poor sensitivity of the descending track (T151) to fault slip in the southern half of the fault is obvious.

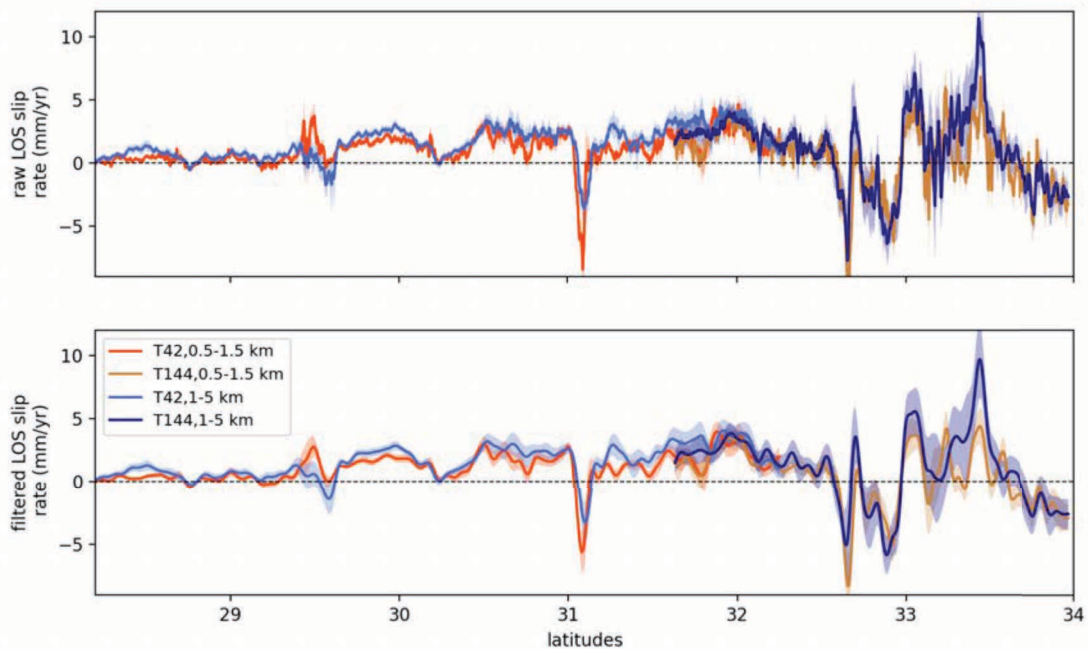


Figure A.37: More details on the line of sight (LOS) surface slip rate measures displayed in Figure 3.5b. Orange and blue lines are the raw (top) and filtered (bottom) surface slip measured along strike with two different spatial footprint of 0.1 -1 km and 1-5 km respectively. Measures from both ascending tracks are shown (track 42 and 144). The spatially low-pass filtered surface slip rate between 0.5 and 1.5 km off the fault trace are the same as in Figure 3.5b.

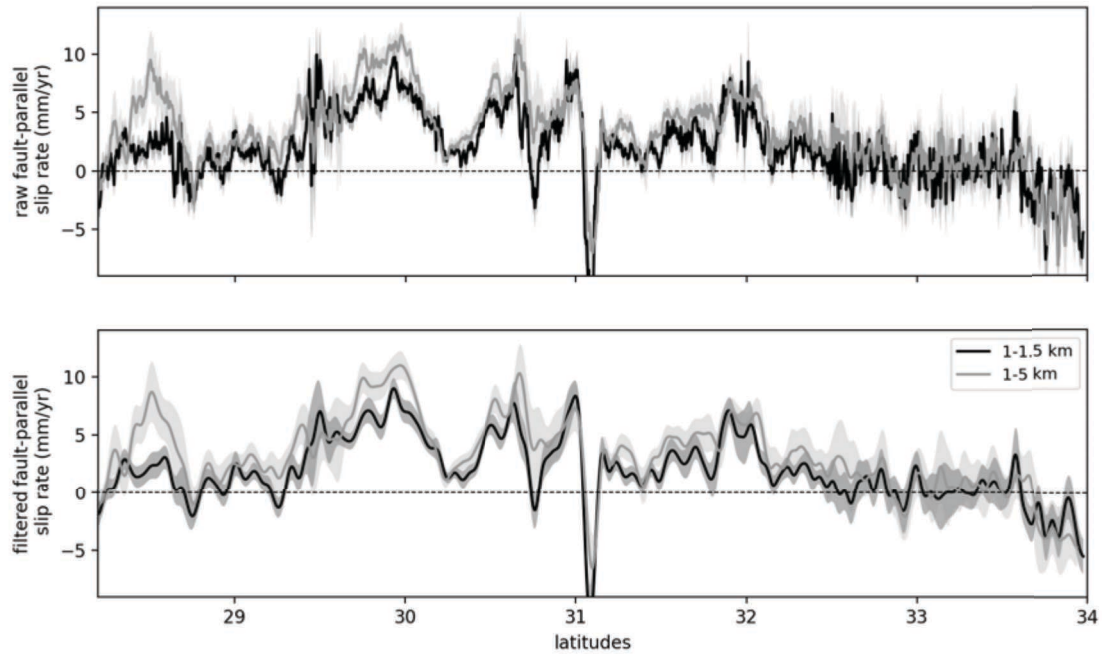


Figure A.38: More details on the slip rates projected in the fault-parallel direction displayed in Figure 3.5c. Black and gray lines are the raw (top) and filtered (bottom) strike-slip motion measured along strike with two different spatial footprint of 0.5 - 1.5 km and 1-5 km respectively. The spatially low-pass filtered strike-slip component (black curves in bottom plot) is the same as in Figure 3.5c (against latitude instead of distance).

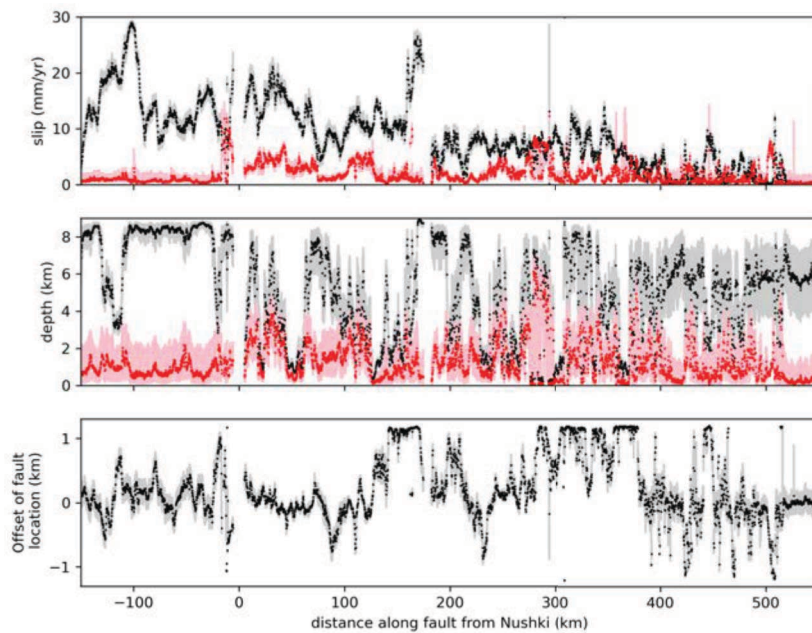


Figure A.39: Estimated median and interquartile range for the optimized parameters of our dislocation model on a vertical left-lateral fault (Equation 3.3, Section 3.3.4) along the Chaman fault trace. Parameters describing fault slip are: slip rate at depth S (top in black), creep rate C (top in red), locking depth D_S (middle in black), creep extent D_C (middle in red) and Chaman fault offset X_f (bottom). We prefer the median and interquartile range instead of the mean and standard deviation as the *posterior* probability density function is often asymmetrical, and thus not Gaussian, due to the bounded positive space explored (especially depths). The model is adjusted to 15-km-long profiles of fault-parallel velocity every 200 m along the fault (like profiles in Figure 3.3).

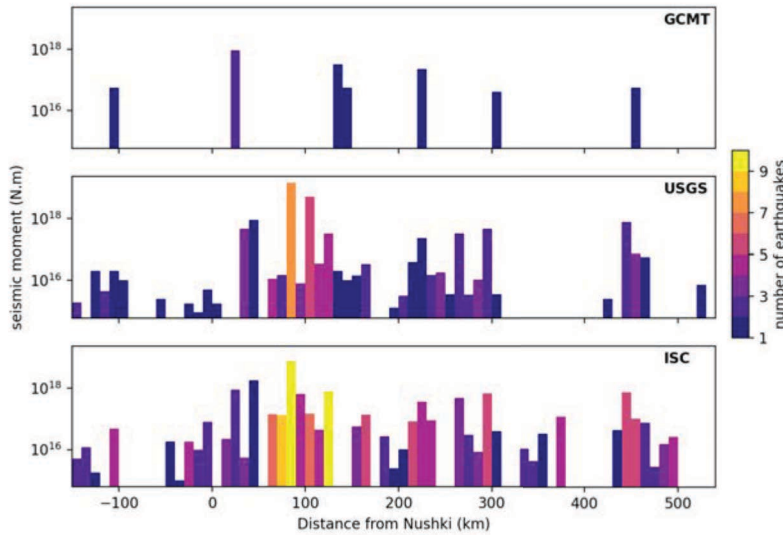


Figure A.40: Distribution of seismic moment released along the Chaman fault (including events within 30 km) according to three sources : Harvard Global Centroid Moment Tensor (top), US Geological Survey (center), International Seismological Center (bottom; same as Figure 3.5e). The 10 km wide bars have heights equal to the sum of seismic moments release on the fault segment over 1990 to 2019 (plain and outlined bars) or over 1900 to 2019 (shaded bars). Colors reflect the number of events contributing to the total moment released in each bin (see colorbar).

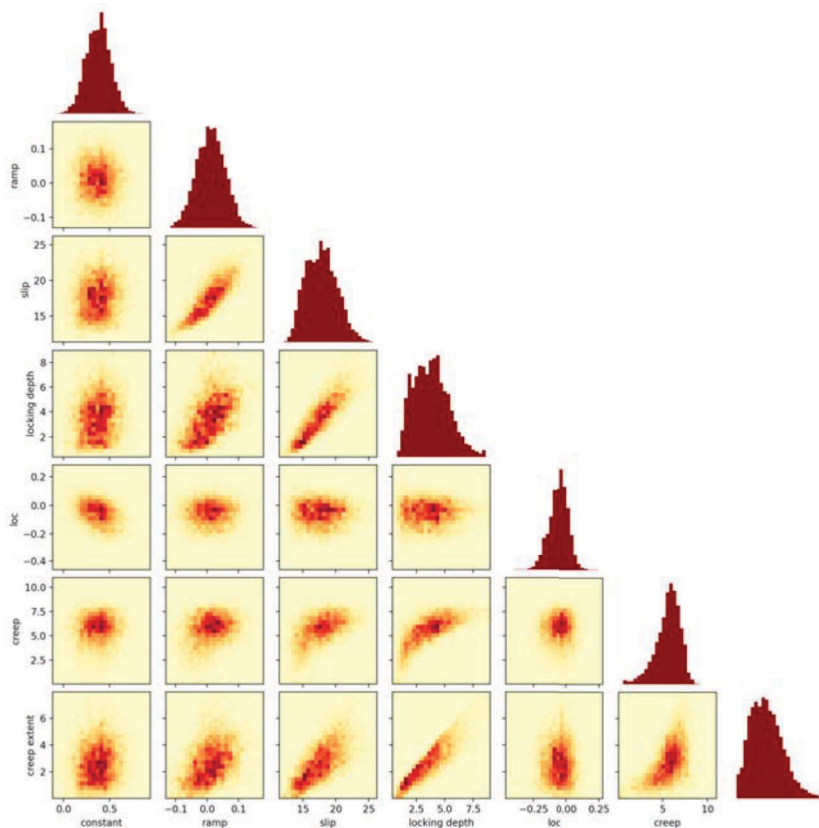


Figure A.41: Marginal posterior density distribution of model parameters (bar chart on the diagonal) and joint distributions (2D-histogram with higher sample density in dark red) for profile B in Figure 3.3 located 40 km north of Nushki. Parameters are described in Section 3.3.4 and listed in Table 3. They are a constant (A) in mm, a ramp (B) in mm/km, slip rate at depth (S) in mm/yr, locking depth (D_S) in km, fault location (X_f) in km, creep rate (C) in mm/yr, creep extent (D_C) in km. The elongated shape of the joint distribution S - D_S and S - B , exhibits a trade-off between those three parameters. The joint distributions involving C and D_C show a correlation of the creep estimate with D_S and S , showing the difficulty to distinguish shallow creep from slip at depth when D_S is close to D_C . This suggests a fault plane that slips from the surface to at least 9 km depth. The sharp bound of the D_C - D_S distribution along the $D_C = D_S$ line arises from the requirement of $D_C < D_S$.

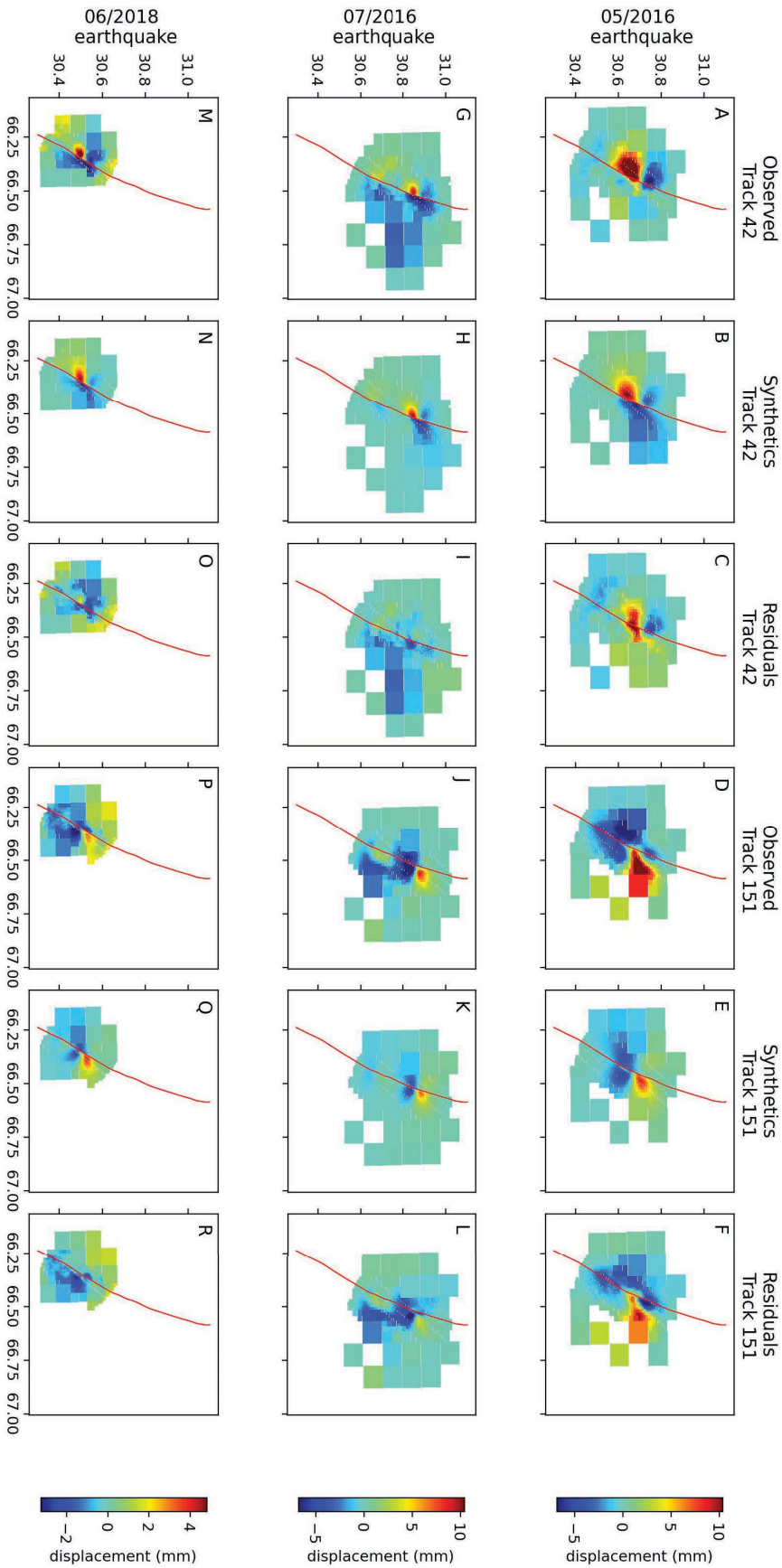


Figure A.42: Comparison of observed and modeled surface deformation due to three earthquakes on the Chaman fault. Each row is a different earthquake. The 3 columns on the left are in the ascending LOS (track 42), while the remaining columns are in descending LOS (track 151). Individual columns contain : observed deformation (A, G, M and D, J, P), synthetic deformation as predicted by modeled slip on the Chaman fault (Figure 7) (B, H, N and E, K, Q) and residual deformation in data once modeled slip is subtracted (C, I, J and F, L, R). Coarse patches far from the fault are the result of our downsampling. In red is the modeled fault trace. Colormaps apply to each row.

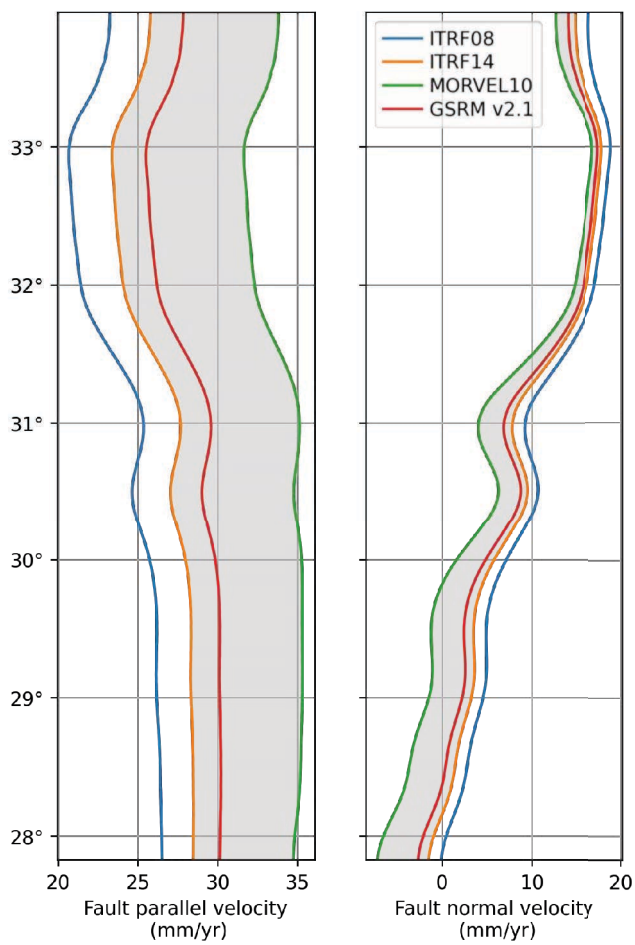


Figure A.43: Global plate motion of India with respect to Eurasia as predicted by four published models projected along our fault-parallel (left plot) and fault-perpendicular (right plot) directions of the Chaman fault. ITRFo8 is from *Altamimi et al. [2012]*, ITRF14 from *Altamimi et al. [2017]*, MORVEL10 from *DeMets et al. [2010]* and GSRM v2.1 from *Kreemer et al. [2014]*. Because ITRF14 is an update of ITRFo8, we do not consider ITRFo8 in our main text discussion. Thus, our likely relative plate motion is the region shaded in grey. ITRFo8 is used as a reference in *Szeliga et al. [2012]*'s study of the Chaman fault (their Figure 13).

A.7 Parametrisation of the partitioning model and additional results for Chapter 4

parameter	lower bound	upper bound	mean	std	unit
Constant Y	-15	15	-	-	mm/yr
Ramp V	-0.5	0.5	0	0.05	(mm/yr)/km
CF slip S_1	0	40	-	-	mm/yr
CF locking depth D_1	0.05	15	5	5	km
CF location C_1	$C_1^i - 2$	$C_1^i + 2$	C_1^i	0.25	km
CF creep A_1	0	30	-	-	mm/yr
CF creep extent E_1	0	10	1	4	km
HF slip S_2	0	50	-	-	mm/yr
HF locking depth D_2	0.05	15	5	5	km
HF location C_2	$C_2^i - 3$	$C_2^i + 3$	C_2^i	0.25	km
HF creep A_2	0	60	20	15	mm/yr
HF creep extent E_2	0	10	1	5	km
GF slip S_3	0	40	-	-	mm/yr
GF locking depth D_3	0.05	15	5	5	km
GF location C_3	-6	6	0	1	km
EF slip S_4	0	40	-	-	mm/yr
EF locking depth D_4	0.05	15	5	5	km
EF location C_4	18	65	30	4	km

Table 6: A priori distribution for all parameters. When mean and standard deviation (abbreviated std) are specified, the distribution is a truncated Gaussian function, otherwise the distribution is uniform between the lower and upper bounds. Y and V are proper to each viewing direction (ascending and descending). CF : Chaman fault; HF : Hoshab fault; GF : Ghazaband fault; EF: Eastern fault.

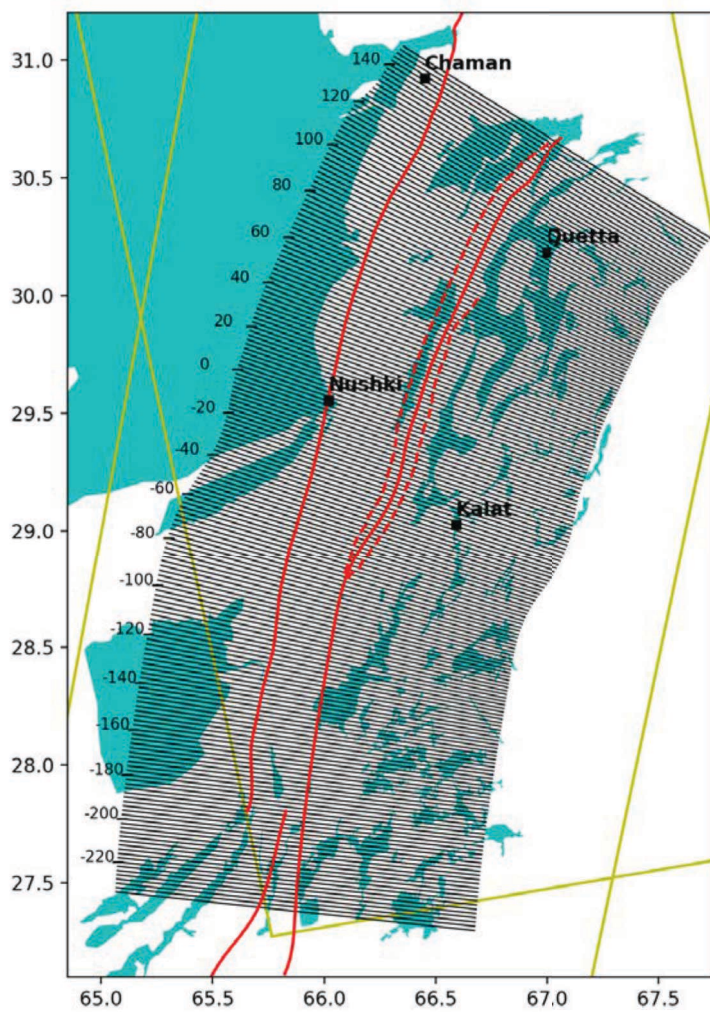


Figure A.44: Geometry of profiles (black lines) and masked zones (blue fields). Masked zones correspond to urban and agricultural area as well as sand-cover (e.g. Rigestan desert in the Northwest). Track outlines are in green and *a priori* fault location are in red. Cities are marked by black squares. The fault parallel length scale in kilometres is labelled at the western end of profiles; the origin corresponds to the profile passing through the city of Nushki.

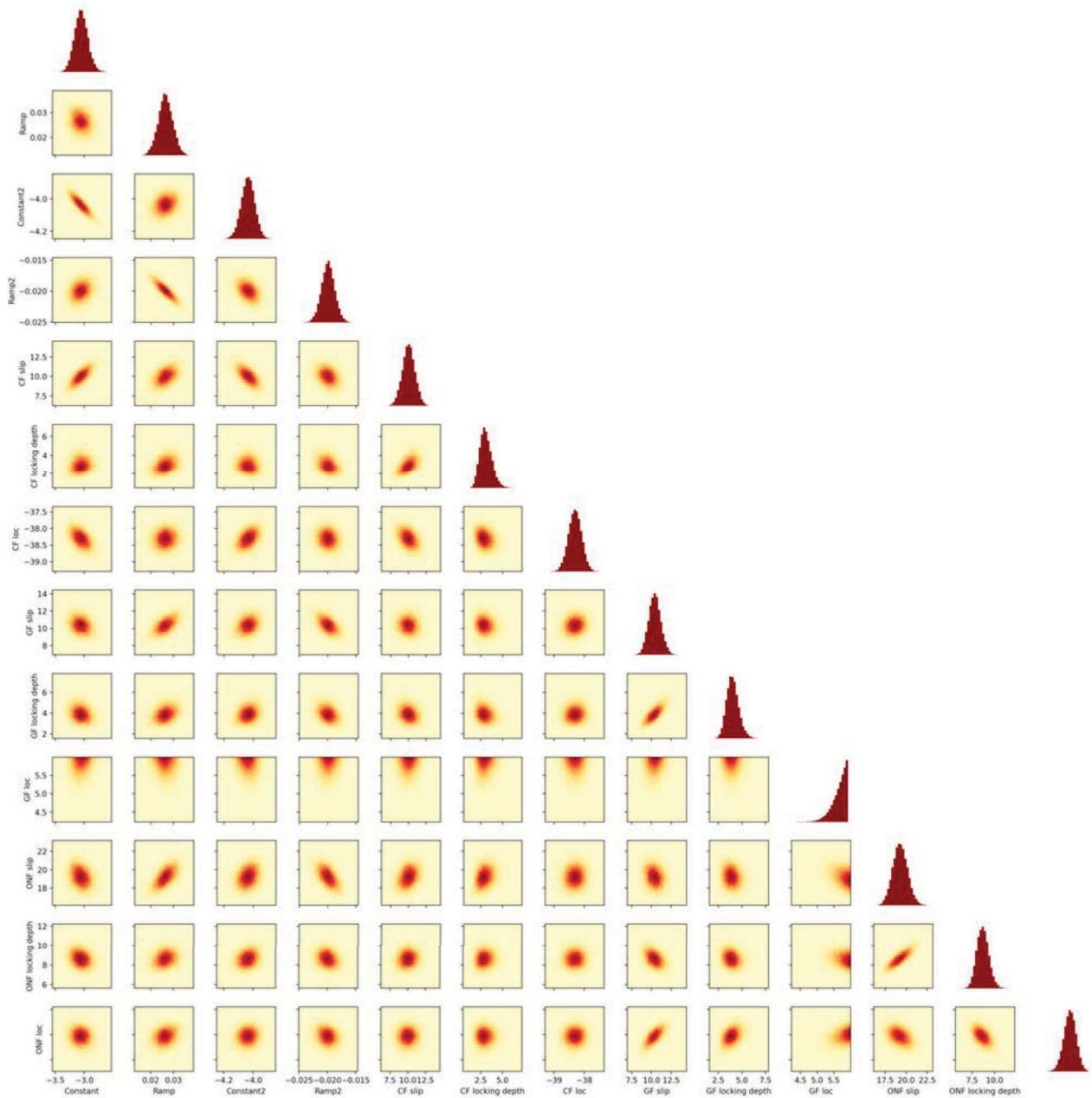


Figure A.45: Marginal PDF for profile 121

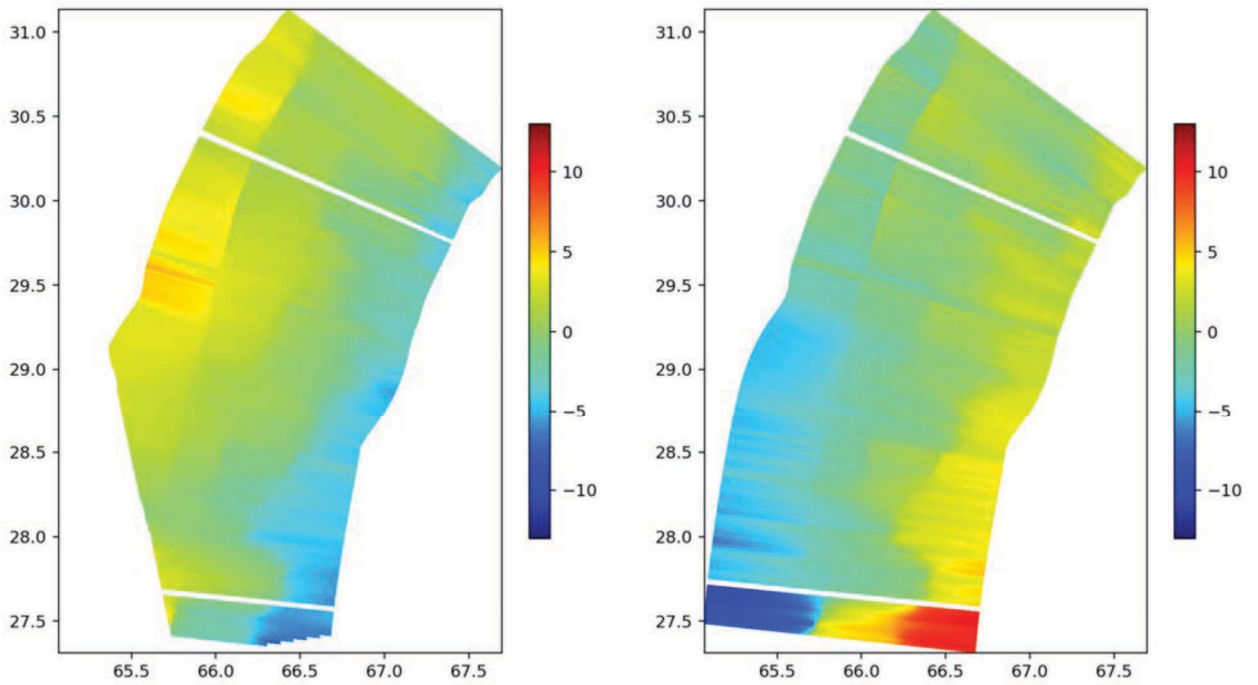


Figure A.46: Synthetic velocity field for ascending (left) and descending (right) tracks

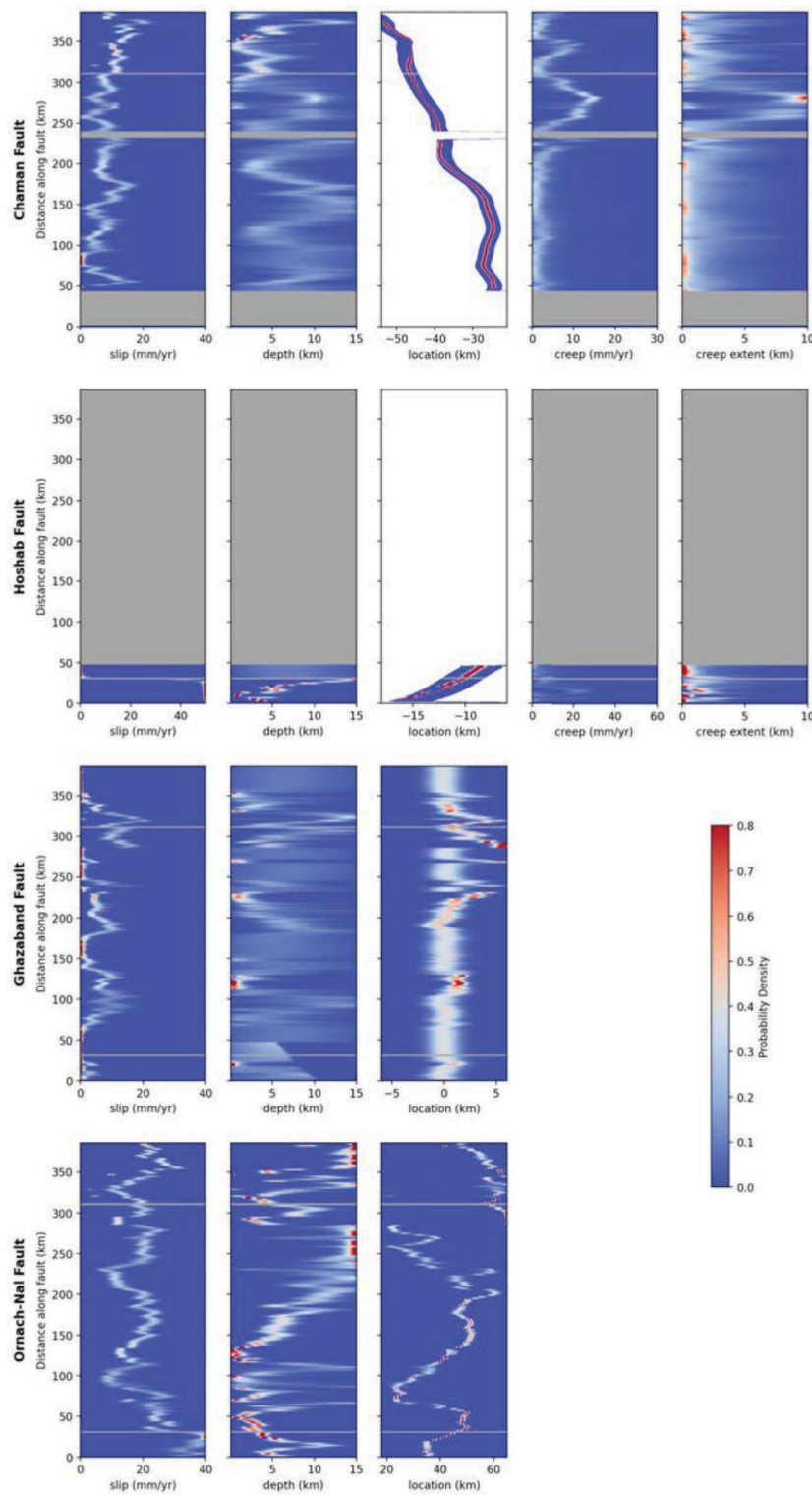


Figure A.47: Probability density of fault parameters for all profiles as a color gradient (red for high probability). Each row is a different fault, while each column is a parameter. Parameters, from left to right, are amount of slip, locking depth, fault location with respect to the center of the profiles ($x=0$) and, for the Chaman and Hoshab faults, amount of creep and creep extent. In grey are profiles for which the parameter could not be sampled because the fault is *a priori* not identified or data is insufficient. Bounds of x -axis corresponds to *a priori* bounds of the distribution (Table 6), except for Chaman and Hoshab fault locations which have a profile-dependent *a priori* based on mapped structures.

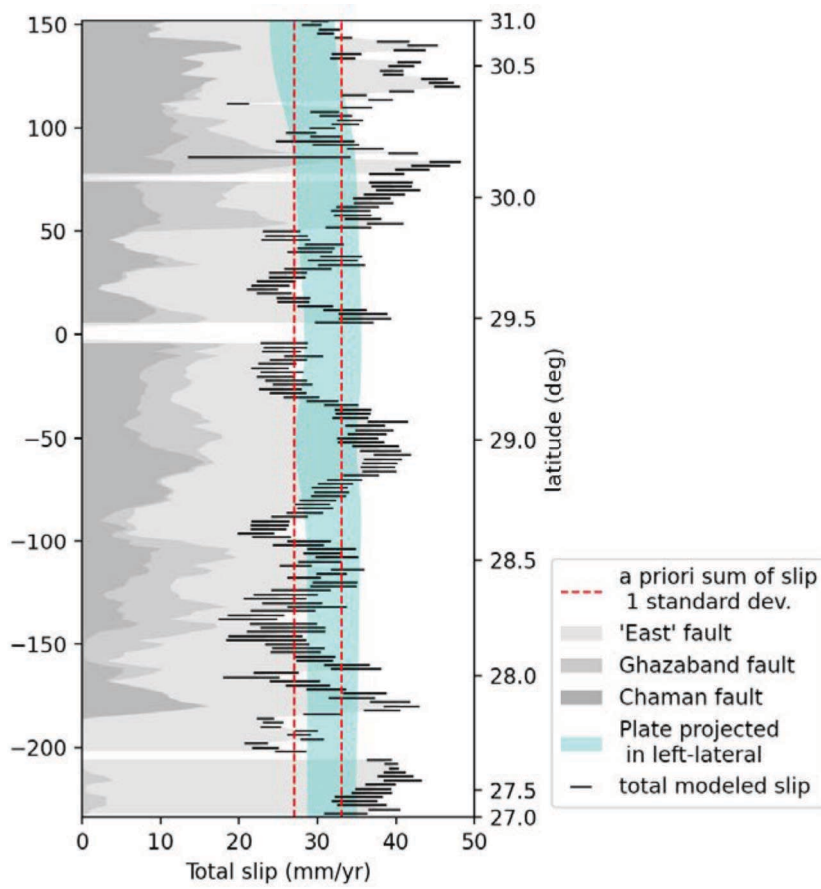


Figure A.48: Summary of measured slip with a cumulative x -scale. Total inferred left-lateral slip is consistent with the relative plate motion between India and Eurasia within uncertainty.

BIBLIOGRAPHY

(2020), ISC On-line Bulletin, DOI: 10.31905/D8o8B83o.

Agram, P., and M. Simons (2015), A noise model for InSAR time series, *Journal of Geophysical Research: Solid Earth*, 120(4), 2752–2771.

Agram, P., R. Jolivet, B. Riel, Y. Lin, M. Simons, E. Hetland, M.-P. Doin, and C. Lasserre (2013), New radar interferometric time series analysis toolbox released, *Eos, Transactions American Geophysical Union*, 94(7), 69–70.

Ahmad, W., M. Choi, S. Kim, and D. Kim (2017), Detection of land subsidence due to excessive groundwater use varying with different land cover types in Quetta valley, Pakistan using ESA-sentinel satellite data, *Nat Hazards Earth Syst Sci Discuss*, pp. 1–21.

Aki, K. (1972), Earthquake mechanism, *Tectonophysics*, 13(1-4), 423–446.

Allemann, F. (1979), Time of emplacement of the Zhob Valley ophiolites and Bela ophiolites, Baluchistan (preliminary report), *Geodynamics of Pakistan*, pp. 215–242.

Altamimi, Z., L. Métivier, and X. Collilieux (2012), ITRF2008 plate motion model, *Journal of geophysical research: solid earth*, 117(B7).

Altamimi, Z., L. Métivier, P. Rebischung, H. Rouby, and X. Collilieux (2017), ITRF2014 plate motion model, *Geophysical Journal International*, 209(3), 1906–1912.

Alwahedi, M. A., and J. C. Hawthorne (2019), Intermediate-magnitude postseismic slip follows intermediate-magnitude (Mw 4 to 5) earthquakes in California, *Geophysical Research Letters*, 46(7), 3676–3687.

Amante, C., and B. W. Eakins (2009), ETOPO1 arc-minute global relief model: procedures, data sources and analysis.

Ambraseys, N., and R. Bilham (2003a), Earthquakes and associated deformation in northern Baluchistan 1892-2001, *Bulletin of the Seismological Society of America*, 93(4), 1573–1605.

Ambraseys, N., and R. Bilham (2003b), Earthquakes in Afghanistan, *Seismological Research Letters*, 74(2), 107–123.

Ambraseys, N., and J. Douglas (2004), Magnitude calibration of north Indian earthquakes, *Geophysical Journal International*, 159(1), 165–206.

Ambraseys, N. N. (1970), Some characteristic features of the Anatolian fault zone, *Tectonophysics*, 9(2-3), 143–165.

Ambraseys, N. N. (1971), Value of historical records of earthquakes, *Nature*, 232(5310), 375–379.

Amey, R., A. Hooper, and R. Walters (2018), A Bayesian method for incorporating self-similarity into earthquake slip inversions, *Journal of Geophysical Research: Solid Earth*, 123(7), 6052–6071.

Anantrasirichai, N., J. Biggs, F. Albino, P. Hill, and D. Bull (2018), Application of machine learning to classification of volcanic deformation in routinely generated InSAR data, *Journal of Geophysical Research: Solid Earth*, 123(8), 6592–6606.

Anantrasirichai, N., J. Biggs, F. Albino, and D. Bull (2019), The application of convolutional neural networks to detect slow, sustained deformation in InSAR time series, *Geophysical Research Letters*, 46(21), 11,850–11,858.

- Anantrasirichai, N., J. Biggs, K. Kelevitz, Z. Sadeghi, T. Wright, J. Thompson, A. M. Achim, and D. Bull (2020), Detecting ground deformation in the built environment using sparse satellite InSAR data with a Convolutional Neural Network, *IEEE Transactions on Geoscience and Remote Sensing*, 59(4), 2940–2950.
- Anderson, E. M. (1905), The dynamics of faulting, *Transactions of the Edinburgh Geological Society*, 8(3), 387–402.
- Ansari, H., F. De Zan, and R. Bamler (2017), Sequential estimator: Toward efficient InSAR time series analysis, *IEEE Transactions on Geoscience and Remote Sensing*, 55(10), 5637–5652.
- Ansari, H., F. De Zan, and R. Bamler (2018), Efficient phase estimation for interferogram stacks, *IEEE Transactions on Geoscience and Remote Sensing*, 56(7), 4109–4125.
- Ansari, H., F. De Zan, and A. Parizzi (2020), Study of systematic bias in measuring surface deformation with SAR interferometry, *IEEE Transactions on Geoscience and Remote Sensing*, 59(2), 1285–1301.
- Antoine, S. L., Y. Klinger, A. Delorme, K. Wang, R. Bürgmann, and R. D. Gold (2021), Diffuse deformation and surface faulting distribution from submetric image correlation along the 2019 Ridgecrest, California, ruptures, *Bulletin of the Seismological Society of America*, 111(5), 2275–2302.
- Arshad, K., M. Imran, M. Iqbal, and A. Nazeer (2011), Structural styles and hydrocarbon potential of western Kirthar Fold belt, *Proceedings of the PAPG/SPE Annual technical conference*.
- Asrarullah, Z. A., S. G. Abbas, A. Farah, and K. DeJong (1979), Ophiolites in Pakistan: an introduction, *Geodynamics of Pakistan*, pp. 181–192.
- Auden, J. B. (1974), Afghanistan-West Pakistan, *Geological Society, London, Special Publications*, 4(1), 235–253, DOI: 10.1144/GSL.SP.2005.004.01.13.
- Avouac, J.-P. (2015), From geodetic imaging of seismic and aseismic fault slip to dynamic modeling of the seismic cycle, *Annual Review of Earth and Planetary Sciences*, 43, 233–271.
- Avouac, J.-P., and P. Tapponnier (1993), Kinematic model of active deformation in central Asia, *Geophysical Research Letters*, 20(10), 895–898.
- Avouac, J.-P., F. Ayoub, S. Wei, J.-P. Ampuero, L. Meng, S. Leprince, R. Jolivet, Z. Duputel, and D. Helmberger (2014), The 2013, Mw 7.7 Balochistan earthquake, energetic strike-slip reactivation of a thrust fault, *Earth and Planetary Science Letters*, 391, 128–134.
- Bakr, M. A., and R. O. Jackson (1964), *Geological map of Pakistan 1:2,000,000*, Geological Survey of Pakistan and U.S. Geological Survey.
- Bakun, W., B. Aagaard, B. Dost, W. Ellsworth, J. Hardebeck, R. Harris, C. Ji, M. Johnston, J. Langbein, J. Lienkaemper, et al. (2005), Implications for prediction and hazard assessment from the 2004 Parkfield earthquake, *Nature*, 437(7061), 969–974.
- Bakun, W. H., and T. V. McEvilly (1984), Recurrence models and Parkfield, California, earthquakes, *Journal of Geophysical Research: Solid Earth*, 89(B5), 3051–3058.
- Bannert, D., and H. A. Raza (1992), The Segmentation of the Indo-Pakistan Plate, *Pakistan Journal of Hydrocarbon Research*, 4(2), 5–18.
- Barbot, S. (2019), Modulation of fault strength during the seismic cycle by grain-size evolution around contact junctions, *Tectonophysics*, 765, 129–145.
- Barbot, S., Y. Hamiel, and Y. Fialko (2008), Space geodetic investigation of the coseismic and postseismic deformation due to the 2003 Mw7. 2 Altai earthquake: Implications for the local lithospheric rheology, *Journal of geophysical research: solid earth*, 113(B3).
- Barbot, S., Y. Fialko, and Y. Bock (2009), Postseismic deformation due to the Mw 6.0 2004 Parkfield earthquake: Stress-driven creep on a fault with spatially variable rate-and-state friction parameters, *Journal of Geophysical Research: Solid Earth*, 114(B7).

- Barbot, S., N. Lapusta, and J.-P. Avouac (2012), Under the hood of the earthquake machine: Toward predictive modeling of the seismic cycle, *Science*, 336(6082), 707–710.
- Barnhart, W. D. (2017), Fault creep rates of the Chaman fault (Afghanistan and Pakistan) inferred from InSAR, *Journal of Geophysical Research: Solid Earth*, 122(1), 372–386.
- Barnhart, W. D., R. D. Gold, and J. Hollingsworth (2020), Localized fault-zone dilatancy and surface inelasticity of the 2019 Ridgecrest earthquakes, *Nature Geoscience*, 13(10), 699–704.
- Bato, M. G., V. Pinel, Y. Yan, F. Jouanne, and J. Vandemeulebrouck (2018), Possible deep connection between volcanic systems evidenced by sequential assimilation of geodetic data, *Scientific reports*, 8(1), 1–13.
- Bayes, F. (1973), An essay towards solving a problem in the doctrine of chances, *Biometrika*, 45(3-4), 296–315.
- Bekaert, D., P. Segall, T. J. Wright, and A. J. Hooper (2016), A network inversion filter combining GNSS and InSAR for tectonic slip modeling, *Journal of Geophysical Research: Solid Earth*, 121(3), 2069–2086.
- Benioff, H. (1964), Earthquake source mechanisms, *Science*, 143(3613), 1399–1406.
- Benoit, A. (2020), Vers un suivi continu des faibles déplacements de surface par interférométrie radar : étude du comportement asismique le long de la faille Nord Anatolienne, Ph.D. thesis, Université Paris Sciences et Lettres.
- Benoit, A., R. Jolivet, and B. Pinel-Puysségur (2019), Correction of tropospheric effects in SAR interferometry: a comparison of ERA-Interim, ERA-5 and HRES Global Atmospheric Models.
- Benoit, A., B. Pinel-Puysségur, R. Jolivet, and C. Lasserre (2020), CorPhU: an algorithm based on phase closure for the correction of unwrapping errors in SAR interferometry, *Geophysical Journal International*, 221(3), 1959–1970, DOI: 10.1093/gji/ggaa120.
- Berardino, P., G. Fornaro, R. Lanari, and E. Sansosti (2002), A new algorithm for surface deformation monitoring based on small baseline differential SAR interferograms, *IEEE Transactions on Geoscience and Remote Sensing*, 40(11), 2375–2383.
- Bernard, M., B. Shen-Tu, W. Holt, and D. Davis (2000), Kinematics of active deformation in the Sulaiman Lobe and Range, Pakistan, *Journal of Geophysical Research: Solid Earth*, 105(B6), 13,253–13,279.
- Beroza, G. C., and S. Ide (2011), Slow earthquakes and nonvolcanic tremor, *Annual review of Earth and planetary sciences*, 39, 271–296.
- Beun, N., P. Bordet, and J.-P. Carbonnel (1979), Premières données quantitatives relatives au coulissage du décrochement de Chaman (Afghanistan du Sud-Est), *Comptes rendus hebdomadaires des séances de l'Académie des sciences*, 288, 931–934.
- Biasi, G. P., and S. G. Wesnousky (2017), Bends and ends of surface Ruptures Bends and ends of surface ruptures, *Bulletin of the Seismological Society of America*, 107(6), 2543–2560.
- Biemiller, J., C. Boulton, L. Wallace, S. Ellis, T. Little, M. Mizera, A. Niemeijer, and L. Lavier (2020), Mechanical implications of creep and partial coupling on the world's fastest slipping low-angle normal fault in southeastern Papua New Guinea, *Journal of Geophysical Research: Solid Earth*, 125(10), e2020JB020,117.
- Biggs, J., T. Wright, Z. Lu, and B. Parsons (2007), Multi-interferogram method for measuring interseismic deformation: Denali Fault, Alaska, *Geophysical Journal International*, 170(3), 1165–1179.
- Biggs, J., S. Ebmeier, W. Aspinall, Z. Lu, M. Pritchard, R. Sparks, and T. Mather (2014), Global link between deformation and volcanic eruption quantified by satellite imagery, *Nature communications*, 5, 3471.
- Bilham, R. (2004), Earthquakes in India and the Himalaya: tectonics, geodesy and history, *Annals of Geophysics*, 47(2/3).
- Bilham, R., and N. Ambraseys (2005), Apparent Himalayan slip deficit from the summation of seismic moments for Himalayan earthquakes, 1500–2000, *Current science*, pp. 1658–1663.
- Bilham, R., S. Lodi, S. Hough, S. Bukhary, A. M. Khan, and S. Rafeeqi (2007), Seismic hazard in Karachi, Pakistan: uncertain past, uncertain future, *Seismological research letters*, 78(6), 601–613.

- Bilham, R., H. Ozener, D. Mencin, A. Dogru, S. Ergintav, Z. Cakir, A. Aytun, B. Aktug, O. Yilmaz, W. Johnson, et al. (2016), Surface creep on the North Anatolian fault at Ismetpasa, Turkey, 1944–2016, *Journal of Geophysical Research: Solid Earth*, 121(10), 7409–7431.
- Bilham, R., N. U. Kakar, D. M. Kakar, K. Wang, R. Bürgmann, and W. D. Barnhart (2019), The 1892 Chaman, Pakistan, Earthquake, *Seismological Research Letters*, 90(6), 2293–2303.
- Bird, P., D. D. Jackson, Y. Y. Kagan, C. Kreemer, and R. Stein (2015), GEAR1: A global earthquake activity rate model constructed from geodetic strain rates and smoothed seismicity, *Bulletin of the Seismological Society of America*, 105(5), 2538–2554.
- Blanpied, M., C. Marone, D. Lockner, J. Byerlee, and D. King (1998), Quantitative measure of the variation in fault rheology due to fluid-rock interactions, *Journal of Geophysical Research: Solid Earth*, 103(B5), 9691–9712.
- Bletery, Q., O. Cavalié, J.-M. Nocquet, and T. Ragon (2020), Distribution of interseismic coupling along the North and East Anatolian Faults inferred from InSAR and GPS data, *Geophysical Research Letters*, 47(16), e2020GL087775.
- Blewitt, G., W. Hammond, and C. Kreemer (2018), Harnessing the GPS data explosion for interdisciplinary science, *Eos*, 99.
- Bondár, I., and D. Storchak (2011), Improved location procedures at the International Seismological Centre, *Geophysical Journal International*, 186(3), 1220–1244.
- Bouchon, M., H. Karabulut, M. Aktar, S. Özalaybey, J. Schmittbuhl, and M.-P. Bouin (2011), Extended nucleation of the 1999 Mw 7.6 Izmit earthquake, *science*, 331(6019), 877–880.
- Bouchon, M., V. Durand, D. Marsan, H. Karabulut, and J. Schmittbuhl (2013), The long precursory phase of most large interplate earthquakes, *Nature geoscience*, 6(4), 299.
- Bowman, J. (1992), The 1988 Tennant Creek, northern territory, earthquakes: A synthesis, *Australian Journal of Earth Sciences*, 39(5), 651–669.
- Boyd, O. S., C. S. Mueller, and K. S. Rukstales (2007), Preliminary earthquake hazard map of Afghanistan, *Open-File Report 1137*, U.S. Geological Survey.
- Brace, W., and J. Byerlee (1966), Stick-slip as a mechanism for earthquakes, *Science*, 153(3739), 990–992.
- Brantut, N., A. Schubnel, and Y. Guéguen (2011), Damage and rupture dynamics at the brittle-ductile transition: The case of gypsum, *Journal of Geophysical Research: Solid Earth*, 116(B1).
- Brouwer, W., and R. Hanssen (2021), An analysis of InSAR displacement vector decomposition fallacies: Facts, fiction, and the strap-down solution, in *Fringe 2021 Abstracts*.
- Burford, R., and P. Harsh (1980), Slip on the San Andreas fault in central California from alignment array surveys, *Bulletin of the Seismological Society of America*, 70(4), 1233–1261.
- Bürgmann, R. (2018), The geophysics, geology and mechanics of slow fault slip, *Earth and Planetary Science Letters*, 495, 112–134, DOI: 10.1016/j.epsl.2018.04.062.
- Bürgmann, R., and G. Dresen (2008), Rheology of the lower crust and upper mantle: Evidence from rock mechanics, geodesy, and field observations, *Annu. Rev. Earth Planet. Sci.*, 36, 531–567.
- Bürgmann, R., P. A. Rosen, and E. J. Fielding (2000), Synthetic aperture radar interferometry to measure Earth's surface topography and its deformation, *Annual review of earth and planetary sciences*, 28(1), 169–209.
- Bürgmann, R., S. Ergintav, P. Segall, E. H. Hearn, S. McClusky, R. E. Reilinger, H. Woith, and J. Zschau (2002), Time-dependent distributed afterslip on and deep below the Izmit earthquake rupture, *Bulletin of the Seismological Society of America*, 92(1), 126–137.
- Bürgmann, R., M. G. Kogan, G. M. Steblov, G. Hilley, V. E. Levin, and E. Apel (2005), Interseismic coupling and asperity distribution along the Kamchatka subduction zone, *Journal of Geophysical Research: Solid Earth*, 110(B7).
- Bürgmann, R., W. Thatcher, and M. Bickford (2013), Space geodesy: A revolution in crustal deformation measurements of tectonic processes, *Geol. Soc. Am. Spec. Pap.*, 500, 397–430.

- Byerlee, J. D. (1968), Brittle-ductile transition in rocks, *Journal of Geophysical Research*, 73(14), 4741–4750.
- Byerlee, J. D., and W. Brace (1968), Stick slip, stable sliding, and earthquakes—effect of rock type, pressure, strain rate, and stiffness, *Journal of Geophysical Research*, 73(18), 6031–6037.
- Çakir, Z., S. Ergintav, H. Özener, U. Dogan, A. M. Akoglu, M. Meghraoui, and R. Reilinger (2012), Onset of aseismic creep on major strike-slip faults, *Geology*, 40(12), 1115–1118.
- Cao, Y., S. Jónsson, and Z. Li (2021), Advanced InSAR tropospheric corrections from global atmospheric models that incorporate spatial stochastic properties of the troposphere, *Journal of Geophysical Research: Solid Earth*, 126(5), e2020JB020,952.
- Carbonnel, J.-P., and A. Blondeau (1977), Le groupe paléogène de Kerghana (Afghanistan du SW), implication paléogéographique et structurale, *Annales de la Société géologique du Nord*, 97, 107–114.
- Carrasi, A., M. Bocquet, L. Bertino, and G. Evensen (2018), Data assimilation in the geosciences: An overview of methods, issues, and perspectives, *Wiley Interdisciplinary Reviews: Climate Change*, 9(5), e535.
- Cattania, C., and P. Segall (2021), Precursory slow slip and foreshocks on rough faults, *Journal of Geophysical Research: Solid Earth*, 126(4), e2020JB020,430.
- Cavalié, O., M.-P. Doin, C. Lasserre, and P. Briole (2007), Ground motion measurement in the Lake Mead area, Nevada, by differential synthetic aperture radar interferometry time series analysis: Probing the lithosphere rheological structure, *Journal of Geophysical Research: Solid Earth*, 112(B3).
- Cavalié, O., C. Lasserre, M.-P. Doin, G. Peltzer, J. Sun, X. Xu, and Z.-K. Shen (2008), Measurement of interseismic strain across the Haiyuan fault (Gansu, China), by InSAR, *Earth and Planetary Science Letters*, 275(3-4), 246–257.
- Chang, L., R. P. Dolivoet, and R. F. Hanssen (2018), Monitoring line-infrastructure with multisensor SAR interferometry: Products and performance assessment metrics, *IEEE journal of selected topics in applied earth observations and remote sensing*, 11(5), 1593–1605.
- Chartrand, R. (2011), Numerical differentiation of noisy, nonsmooth data, *International Scholarly Research Notices*, 2011.
- Chase, C. G. (1978), Plate kinematics: The Americas, East Africa, and the rest of the world, *Earth and planetary science letters*, 37(3), 355–368.
- Chaussard, E., R. Bürgmann, M. Shirzaei, E. Fielding, and B. Baker (2014a), Predictability of hydraulic head changes and characterization of aquifer-system and fault properties from InSAR-derived ground deformation, *Journal of Geophysical Research: Solid Earth*, 119(8), 6572–6590.
- Chaussard, E., S. Wdowinski, E. Cabral-Cano, and F. Amelung (2014b), Land subsidence in central Mexico detected by ALOS InSAR time-series, *Remote sensing of environment*, 140, 94–106.
- Chen, C. W., and H. A. Zebker (2000), Network approaches to two-dimensional phase unwrapping: intractability and two new algorithms, *JOSA A*, 17(3), 401–414.
- Chen, C. W., and H. A. Zebker (2001), Two-dimensional phase unwrapping with use of statistical models for cost functions in nonlinear optimization, *JOSA A*, 18(2), 338–351.
- Cohn, S. E. (1997), An introduction to estimation theory (Special Issue "Data Assimilation in Meteorology and Oceanography: Theory and Practice"), *Journal of the Meteorological Society of Japan. Ser. II*, 75(1B), 257–288.
- Cohn, S. E., N. Sivakumaran, and R. Todling (1994), A fixed-lag Kalman smoother for retrospective data assimilation, *Monthly Weather Review*, 122(12), 2838–2867.
- Copley, A. (2012), The formation of mountain range curvature by gravitational spreading, *Earth and Planetary Science Letters*, 351, 208–214.
- Cosme, E., J. Verron, P. Brasseur, J. Blum, and D. Auroux (2012), Smoothing problems in a Bayesian framework and their linear Gaussian solutions, *Monthly Weather Review*, 140(2), 683–695.
- Crupa, W. E., S. D. Khan, J. Huang, A. S. Khan, and A. Kasi (2017), Active tectonic deformation of the western Indian plate boundary: A case study from the Chaman Fault System, *Journal of Asian Earth Sciences*, 147, 452–468.

- Dal Zilio, L., N. Lapusta, and J.-P. Avouac (2020), Unraveling Scaling Properties of Slow-Slip Events, *Geophysical Research Letters*, 47(10), e2020GL087477.
- Dalaison, M., and R. Jolivet (2020), A Kalman Filter Time Series analysis method for InSAR, *Journal of Geophysical Research: Solid Earth*, 125(7), e2019JB019150.
- Dalaison, M., R. Jolivet, E. M. van Rijsingen, and S. Michel (2021), The interplay between seismic and aseismic slip along the Chaman fault illuminated by InSAR, *submitted to Journal of Geophysical Research: Solid Earth*.
- Danciu, L., K. Şeşetyan, M. Demircioglu, L. Gülen, M. Zare, R. Basili, A. Elias, S. Adamia, N. Tsereteli, H. Yalçın, et al. (2017), The 2014 earthquake model of the Middle East: seismogenic sources, *Bulletin of Earthquake Engineering*, 16(8), 3465–3496.
- Daout, S., M.-P. Doin, G. Peltzer, C. Lasserre, A. Socquet, M. Volat, and H. Sudhaus (2018), Strain partitioning and present-day fault kinematics in NW Tibet from Envisat SAR interferometry, *Journal of Geophysical Research: Solid Earth*, 123(3), 2462–2483.
- Daout, S., H. Sudhaus, T. Kausch, A. Steinberg, and B. Dini (2019), Interseismic and postseismic shallow creep of the North Qaidam Thrust faults detected with a multitemporal InSAR analysis, *Journal of Geophysical Research: Solid Earth*, 124(7), 7259–7279.
- Davies, G. F. (1999), *Dynamic Earth: Plates, plumes and mantle convection*, Cambridge University Press.
- Davis, D. M., and T. Engelder (1985), The role of salt in fold-and-thrust belts, *Tectonophysics*, 119(1-4), 67–88.
- Davis, D. M., and R. J. Lillie (1994), Changing mechanical response during continental collision: active examples from the foreland thrust belts of Pakistan, *Journal of Structural Geology*, 16(1), 21–34.
- Davis, K., D. W. Burbank, D. Fisher, S. Wallace, and D. Nobes (2005), Thrust-fault growth and segment linkage in the active Ostler fault zone, New Zealand, *Journal of Structural Geology*, 27(8), 1528–1546.
- De Novellis, V., V. Convertito, S. Valkaniotis, F. Casu, R. Lanari, M. F. M. Tobar, and N. A. Pino (2021), Author Correction: Coincident locations of rupture nucleation during the 2019 Le Teil earthquake, France and maximum stress change from local cement quarrying, *Communications Earth & Environment*, 2(1), 1–6.
- De Zan, F., and A. Monti Guarnieri (2006), TOPSAR: Terrain observation by progressive scans, *IEEE Transactions on Geoscience and Remote Sensing*, 44(9), 2352–2360.
- De Zan, F., P. Prats-Iraola, R. Scheiber, and A. Rucci (2014), Interferometry with TOPS: Coregistration and azimuth shifts, in *EUSAR 2014: 10th European Conference on Synthetic Aperture Radar*, pp. 1–4, VDE.
- De Zan, F., M. Zonno, and P. López-Dekker (2015), Phase inconsistencies and multiple scattering in SAR interferometry, *IEEE Transactions on Geoscience and Remote Sensing*, 53(12), 6608–6616.
- Delacourt, C., P. Briole, and J. Achache (1998), Tropospheric corrections of SAR interferograms with strong topography. Application to Etna, *Geophysical Research Letters*, 25(15), 2849–2852.
- Delbridge, B. G., J. D. Carmichael, R. M. Nadeau, D. R. Shelly, and R. Bürgmann (2020), Geodetic measurements of slow-slip events southeast of Parkfield, CA, *Journal of Geophysical Research: Solid Earth*, 125(5), e2019JB019059.
- DeMets, C., R. G. Gordon, D. Argus, and S. Stein (1990), Current plate motions, *Geophysical journal international*, 101(2), 425–478.
- DeMets, C., R. G. Gordon, and D. F. Argus (2010), Geologically current plate motions, *Geophysical Journal International*, 181(1), 1–80.
- Deng, J., K. Hudnut, M. Gurnis, and E. Hauksson (1999), Stress loading from viscous flow in the lower crust and triggering of aftershocks following the 1994 Northridge, California, earthquake, *Geophysical research letters*, 26(21), 3209–3212.
- Dewey, J. W., E. A. Bergman, M. G. Hopper, and S. A. Sipkin (2006), Seismicity of Afghanistan and vicinity, *Open-File Report 1185*, U.S. Geological Survey.

- Dianala, J. D. B., R. Jolivet, M. Y. Thomas, Y. Fukushima, B. Parsons, and R. Walker (2020), The relationship between seismic and aseismic slip on the Philippine Fault on Leyte Island: Bayesian modeling of fault slip and geothermal subsidence, *Journal of Geophysical Research: Solid Earth*, 125(12), e2020JB020,052.
- Dieterich, J. (1994), A constitutive law for rate of earthquake production and its application to earthquake clustering, *Journal of Geophysical Research: Solid Earth*, 99(B2), 2601–2618.
- Dieterich, J. H. (1978), Time-dependent friction and the mechanics of stick-slip, *Pure and Applied Geophysics*, 116(4), 790–806, DOI: 10.1007/BF00876539.
- Dieterich, J. H. (1979), Modeling of rock friction: 1. Experimental results and constitutive equations, *Journal of Geophysical Research: Solid Earth*, 84(B5), 2161–2168, DOI: 10.1029/JBo84iB05p02161.
- Dietz, L. D., and W. L. Ellsworth (1990), The October 17, 1989, Loma Prieta, California, earthquake and its aftershocks: Geometry of the sequence from high-resolution locations, *Geophysical Research Letters*, 17(9), 1417–1420.
- Dodge, D. A., G. C. Beroza, and W. Ellsworth (1995), Foreshock sequence of the 1992 Landers, California, earthquake and its implications for earthquake nucleation, *Journal of Geophysical Research: Solid Earth*, 100(B6), 9865–9880.
- Doin, M.-P., S. Guillaso, R. Jolivet, C. Lasserre, F. Lodge, G. Ducret, and R. Grandin (2011), Presentation of the small baseline NSBAS processing chain on a case example: The Etna deformation monitoring from 2003 to 2010 using Envisat data, in *Proceedings of the Fringe symposium*, pp. 3434–3437, ES.
- Du, Y., A. Aydin, and P. Segall (1992), Comparison of various inversion techniques as applied to the determination of a geophysical deformation model for the 1983 Borah Peak earthquake, *Bulletin of the Seismological Society of America*, 82(4), 1840–1866.
- Duputel, Z., P. S. Agram, M. Simons, S. E. Minson, and J. L. Beck (2014), Accounting for prediction uncertainty when inferring subsurface fault slip, *Geophysical Journal International*, 197(1), 464–482.
- Duquesnoy, T., E. Barrier, M. Kasser, M. Aurelio, R. Gaulon, R. Punongbayan, and C. Rangin (1994), Detection of creep along the Philippine fault: First results of geodetic measurements on Leyte island, central Philippine, *Geophysical Research Letters*, 21(11), 975–978.
- Dziewonski, A., T.-A. Chou, and J. Woodhouse (1981), Determination of earthquake source parameters from waveform data for studies of global and regional seismicity, *Journal of Geophysical Research: Solid Earth*, 86(B4), 2825–2852.
- Ekström, G., M. Nettles, and A. Dziewoński (2012), The global CMT project 2004–2010: Centroid-moment tensors for 13,017 earthquakes, *Physics of the Earth and Planetary Interiors*, 200, 1–9.
- Elliott, J., B. Parsons, J. Jackson, X. Shan, R. Sloan, and R. Walker (2011), Depth segmentation of the seismogenic continental crust: The 2008 and 2009 Qaidam earthquakes, *Geophysical Research Letters*, 38(6).
- Elliott, J., R. Walters, and T. Wright (2016a), The role of space-based observation in understanding and responding to active tectonics and earthquakes, *Nature communications*, 7, 13,844.
- Elliott, J., R. Jolivet, P. J. González, J.-P. Avouac, J. Hollingsworth, M. Searle, and V. Stevens (2016b), Himalayan megathrust geometry and relation to topography revealed by the Gorkha earthquake, *Nature Geoscience*, 9(2), 174–180.
- Elliott, J. R., J. Biggs, B. Parsons, and T. Wright (2008), InSAR slip rate determination on the Altyn Tagh Fault, northern Tibet, in the presence of topographically correlated atmospheric delays, *Geophysical Research Letters*, 35(12).
- Ellsworth, W., and G. Beroza (1995), Seismic evidence for an earthquake nucleation phase, *Science*, 268(5212), 851–855.
- Ellsworth, W. L. (2013), Injection-induced earthquakes, *Science*, 341(6142).
- Ellsworth, W. L., and F. Bulut (2018), Nucleation of the 1999 Izmit earthquake by a triggered cascade of foreshocks, *Nature Geoscience*, 11(7), 531.
- Emardson, T., M. Simons, and F. Webb (2003), Neutral atmospheric delay in interferometric synthetic aperture radar applications: Statistical description and mitigation, *Journal of Geophysical Research: Solid Earth*, 108(B5).
- Enge, P. K. (1994), The global positioning system: Signals, measurements, and performance, *International Journal of Wireless Information Networks*, 1(2), 83–105.

- Evensen, G. (2009), *Data assimilation: the ensemble Kalman filter*, Springer Science & Business Media.
- Farr, T. G., P. A. Rosen, E. Caro, R. Crippen, R. Duren, S. Hensley, M. Kobrick, M. Paller, E. Rodriguez, L. Roth, et al. (2007), The shuttle radar topography mission, *Reviews of geophysics*, 45(2).
- Fattahi, H. (2015), Geodetic imaging of tectonic deformation with InSAR, Ph.D. thesis, University of Miami.
- Fattahi, H., and A. Amelung (2016), InSAR observations of strain accumulation and fault creep along the Chaman Fault system, Pakistan and Afghanistan, *Geophys. Res. Lett.*, 43, 8399–8406, DOI: 10.1002/2016GL070121.
- Fattahi, H., and F. Amelung (2015), InSAR bias and uncertainty due to the systematic and stochastic tropospheric delay, *Journal of Geophysical Research: Solid Earth*, 120(12), 8758–8773.
- Fattahi, H., F. Amelung, E. Chaussard, and S. Wdowinski (2015), Coseismic and postseismic deformation due to the 2007 Mw 5.5 Ghazaband fault earthquake, Balochistan, Pakistan, *Geophysical Research Letters*, 42(9), 3305–3312.
- Fattahi, H., P. Agram, and M. Simons (2017), A network-based enhanced spectral diversity approach for TOPS time-series analysis, *IEEE Transactions on Geoscience and Remote Sensing*, 55(2), 777–786.
- Fattahi, H., Z. Yunjun, X. Pi, P. S. Agram, P. Rosen, and Y. Aoki (2020), Absolute geolocation of SAR Big-Data: The first step for operational InSAR time-series analysis, in *AGU Fall Meeting Abstracts*, vol. 2020, pp. G023–05.
- Ferretti, A., C. Prati, and F. Rocca (2000), Nonlinear subsidence rate estimation using permanent scatterers in differential SAR interferometry, *IEEE Transactions on geoscience and remote sensing*, 38(5), 2202–2212.
- Ferretti, A., C. Prati, and F. Rocca (2001), Permanent scatterers in SAR interferometry, *IEEE Transactions on geoscience and remote sensing*, 39(1), 8–20.
- Ferretti, A., A. Fumagalli, F. Novali, C. Prati, F. Rocca, and A. Rucci (2011), A new algorithm for processing interferometric data-stacks: SqueeSAR, *IEEE transactions on geoscience and remote sensing*, 49(9), 3460–3470.
- Fialko, Y. (2004), Evidence of fluid-filled upper crust from observations of postseismic deformation due to the 1992 Mw 7.3 Landers earthquake, *Journal of Geophysical Research: Solid Earth*, 109(B8).
- ForM@Ter (2020), ForM@Ter (2020): FLATSIM Data Products. CNES. (Dataset), DOI: 10.24400/253171/FLATSIM2020.
- Fornaro, G., S. Verde, D. Reale, and A. Pauciuolo (2014), CAESAR: An approach based on covariance matrix decomposition to improve multibaseline–multitemporal interferometric SAR processing, *IEEE Transactions on Geoscience and Remote Sensing*, 53(4), 2050–2065.
- Fournier, M., N. Chamot-Rooke, C. Petit, O. Fabbri, P. Huchon, B. Maillot, and C. Lepvrier (2008), In situ evidence for dextral active motion at the Arabia–India plate boundary, *Nature Geoscience*, 1(1), 54–58.
- Freed, A. M., and R. Bürgmann (2004), Evidence of power-law flow in the Mojave desert mantle, *Nature*, 430(6999), 548–551.
- Frohlich, C., and S. D. Davis (1993), Teleseismic b values; or, much ado about 1.0, *Journal of Geophysical Research: Solid Earth*, 98(B1), 631–644.
- Furuya, M., and S. Satyabala (2008), Slow earthquake in Afghanistan detected by InSAR, *Geophysical Research Letters*, 35(6).
- Galehouse, J. S., and J. J. Lienkaemper (2003), Inferences drawn from two decades of alignment array measurements of creep on faults in the San Francisco Bay region, *Bulletin of the Seismological Society of America*, 93(6), 2415–2433.
- Gallovič, F., W. Imperatori, and P. M. Mai (2015), Effects of three-dimensional crustal structure and smoothing constraint on earthquake slip inversions: Case study of the Mw 6.3 2009 L’Aquila earthquake, *Journal of Geophysical Research: Solid Earth*, 120(1), 428–449.
- Gansser, A. (1979), Reconnaissance visit to the ophiolites in Baluchistan and the Himalaya, *Geodynamics of Pakistan*, pp. 193–213.
- Gardonio, B., R. Jolivet, E. Calais, and H. Leclère (2018), The April 2017 Mw 6.5 Botswana earthquake: an intraplate event triggered by deep fluids, *Geophysical Research Letters*, 45(17), 8886–8896.

- Gilbert, F. (1971), Excitation of the normal modes of the Earth by earthquake sources, *Geophysical Journal International*, 22(2), 223–226.
- Gnos, E., A. Immenhauser, and T. Peters (1997), Late Cretaceous/early Tertiary convergence between the Indian and Arabian plates recorded in ophiolites and related sediments, *Tectonophysics*, 271(1-2), 1–19.
- Goldstein, R. (1995), Atmospheric limitations to repeat-track radar interferometry, *Geophysical research letters*, 22(18), 2517–2520.
- Goldstein, R. M., and C. L. Werner (1998), Radar interferogram filtering for geophysical applications, *Geophysical research letters*, 25(21), 4035–4038.
- Goldstein, R. M., H. A. Zebker, and C. L. Werner (1988), Satellite radar interferometry: Two-dimensional phase unwrapping, *Radio science*, 23(4), 713–720.
- Gomba, G., A. Parizzi, F. De Zan, M. Eineder, and R. Bamler (2015), Toward operational compensation of ionospheric effects in SAR interferograms: The split-spectrum method, *IEEE Transactions on Geoscience and Remote Sensing*, 54(3), 1446–1461.
- Gomba, G., F. R. González, and F. De Zan (2016), Ionospheric phase screen compensation for the Sentinel-1 TOPS and ALOS-2 ScanSAR modes, *IEEE Transactions on Geoscience and Remote Sensing*, 55(1), 223–235.
- González, P. J., M. Bagnardi, A. J. Hooper, Y. Larsen, P. Marinkovic, S. V. Samsonov, and T. J. Wright (2015), The 2014–2015 eruption of Fogo volcano: Geodetic modeling of Sentinel-1 TOPS interferometry, *Geophysical research letters*, 42(21), 9239–9246.
- Grandin, R., M.-P. Doin, L. Bollinger, B. Pinel-Puysségur, G. Ducret, R. Jolivet, and S. N. Sapkota (2012), Long-term growth of the Himalaya inferred from interseismic InSAR measurement, *Geology*, 40(12), 1059–1062.
- Grandin, R., E. Klein, M. Métois, and C. Vigny (2016), Three-dimensional displacement field of the 2015 Mw8.3 Illapel earthquake (Chile) from across-and along-track Sentinel-1 TOPS interferometry, *Geophysical Research Letters*, 43(6), 2552–2561.
- Griffiths, H. (1995), Interferometric synthetic aperture radar, *Electronics & communication engineering journal*, 7(6), 247–256.
- Griggs, D. T. (1936), Deformation of rocks under high confining pressures: I. Experiments at room temperature, *The Journal of Geology*, 44(5), 541–577.
- Gu, J.-C., J. R. Rice, A. L. Ruina, and T. T. Simon (1984), Slip motion and stability of a single degree of freedom elastic system with rate and state dependent friction, *Journal of the Mechanics and Physics of Solids*, 32(3), 167–196.
- Guarnieri, A. M., and S. Tebaldini (2008), On the exploitation of target statistics for SAR interferometry applications, *IEEE Transactions on Geoscience and Remote Sensing*, 46(11), 3436–3443.
- Gurrola, E., P. Rosen, G. Sacco, W. Seliga, H. Zebker, M. Simons, and D. Sandwell (2010), InSAR scientific computing environment, in *2010 American Geophysical Union Meeting*.
- Gutenberg, B., and C. F. Richter (1936), Magnitude and energy of earthquakes, *Science*, 83(2147), 183–185.
- Gutenberg, B., and C. F. Richter (1944), Frequency of earthquakes in California, *Bulletin of the Seismological society of America*, 34(4), 185–188.
- Gutenberg, B., and C. F. Richter (1956), Magnitude and energy of earthquakes, *Annali di Geofisica*, 9(1), 1–15.
- Hamling, I. J., S. Hreinsdóttir, K. Clark, J. Elliott, C. Liang, E. Fielding, N. Litchfield, P. Villamor, L. Wallace, T. J. Wright, et al. (2017), Complex multifault rupture during the 2016 Mw 7.8 Kaikōura earthquake, New Zealand, *Science*, 356(6334).
- Hanks, T. C., and H. Kanamori (1979), A moment magnitude scale, *Journal of Geophysical Research: Solid Earth*, 84(B5), 2348–2350.
- Hanssen, R. F. (2001), *Radar interferometry: data interpretation and error analysis*, vol. 2, Springer Science & Business Media.

- Hartzell, S. H., and T. H. Heaton (1983), Inversion of strong ground motion and teleseismic waveform data for the fault rupture history of the 1979 Imperial Valley, California, earthquake, *Bulletin of the Seismological Society of America*, 73(6A), 1553–1583.
- Hauksson, E., L. M. Jones, K. Hutton, and D. Eberhart-Phillips (1993), The 1992 Landers earthquake sequence: Seismological observations, *Journal of Geophysical Research: Solid Earth*, 98(B11), 19,835–19,858.
- Hawthorne, J. C., and A. M. Rubin (2013), Short-time scale correlation between slow slip and tremor in Cascadia, *Journal of Geophysical Research: Solid Earth*, 118(3), 1316–1329.
- Helmstetter, A., and D. Sornette (2003), Foreshocks explained by cascades of triggered seismicity, *Journal of Geophysical Research: Solid Earth*, 108(B10).
- Herszterg, I., M. Poggi, and T. Vidal (2018), 2D-phase unwrapping via balanced spanning forests, *Infors Journal on Computing*, 31(3).
- Hetland, E., P. Musé, M. Simons, Y. Lin, P. Agram, and C. DiCaprio (2012), Multiscale InSAR time series (MInTS) analysis of surface deformation, *Journal of Geophysical Research: Solid Earth*, 117(B2).
- Hilley, G. E., R. Bürgmann, A. Ferretti, F. Novali, and F. Rocca (2004), Dynamics of slow-moving landslides from permanent scatterer analysis, *Science*, 304(5679), 1952–1955.
- Hofmann-Wellenhof, B., H. Lichtenegger, and J. Collins (2012), *Global positioning system: theory and practice*, Springer Science & Business Media.
- Hogenson, K., S. A. Arko, T. A. Logan, R. Gens, K. Arnoult Jr, and J. B. Nicoll (2018), Hybrid Pluggable Processing Pipeline (HyP3): A cloud-based infrastructure for generic processing of SAR data, in *AGU Fall Meeting Abstracts*, vol. 2018, pp. G32A–03.
- Hollingsworth, J., S. Leprince, F. Ayoub, and J.-P. Avouac (2012), Deformation during the 1975–1984 Krafla rifting crisis, NE Iceland, measured from historical optical imagery, *Journal of Geophysical Research: Solid Earth*, 117(B11).
- Hooper, A. (2010), A statistical-cost approach to unwrapping the phase of InSAR time series, in *Proceedings of the International Workshop on ERS SAR Interferometry, Frascati, Italy*, vol. 30.
- Hooper, A., P. Segall, and H. Zebker (2007), Persistent scatterer interferometric synthetic aperture radar for crustal deformation analysis, with application to Volcán Alcedo, Galápagos, *Journal of Geophysical Research: Solid Earth*, 112(B7).
- Hooper, A., P. Piromthong, T. Wright, J. Weiss, M. Milan Lazecky, Y. Maghsoudi, C. Rollins, Y. Morishita, J. Elliott, and B. Parsons (2021), Large-scale, high-resolution maps of interseismic strain accumulation from Sentinel-1, and incorporation of along-track measurements, in *EGU General Assembly Conference Abstracts*, pp. EGU21–15,946.
- Hooper, A. J., and K. Spaans (2016), Sentinel-1 burst overlap InSAR: north-south sensitivity at last?, in *AGU Fall Meeting Abstracts*, vol. 2016, pp. G21C–08.
- Hu, Z., and J. J. Mallorqui (2018), Comparison of InSAR atmospheric phase screen correction with Global Atmospheric Models (GAM), in *EUSAR 2018; 12th European Conference on Synthetic Aperture Radar*, pp. 1–4, VDE.
- Huang, H., L. Meng, R. Bürgmann, W. Wang, and K. Wang (2020), Spatio-temporal foreshock evolution of the 2019 M 6.4 and M 7.1 Ridgecrest, California earthquakes, *Earth and Planetary Science Letters*, 551, 116,582.
- Humayon, M., R. J. Lillie, and R. D. Lawrence (1991), Structural interpretation of the eastern Sulaiman foldbelt and foredeep, Pakistan, *Tectonics*, 10(2), 299–324.
- Hussain, E., A. Hooper, T. J. Wright, R. J. Walters, and D. P. Bekaert (2016), Interseismic strain accumulation across the central North Anatolian Fault from iteratively unwrapped InSAR measurements, *Journal of Geophysical Research: Solid Earth*, 121(12), 9000–9019.
- Hussain, E., T. J. Wright, R. J. Walters, D. P. Bekaert, R. Lloyd, and A. Hooper (2018), Constant strain accumulation rate between major earthquakes on the North Anatolian Fault, *Nature communications*, 9(1), 1–9.
- Ide, S., G. C. Beroza, D. R. Shelly, and T. Uchide (2007), A scaling law for slow earthquakes, *Nature*, 447(7140), 76.

- Ingleby, T., and T. Wright (2017), Omori-like decay of postseismic velocities following continental earthquakes, *Geophysical Research Letters*, 44(7), 3119–3130.
- Ito, Y., K. Obara, K. Shiomi, S. Sekine, and H. Hirose (2007), Slow earthquakes coincident with episodic tremors and slow slip events, *Science*, 315(5811), 503–506.
- Jacob, K., and R. Quittmeyer (1979), The Makran region of Pakistan and Iran, *Geodynamics of Pakistan*, pp. 303–317.
- Jadoon, I. A., and A. Khurshid (1996), Gravity and tectonic model across the Sulaiman fold belt and the Chaman fault zone in western Pakistan and eastern Afghanistan, *Tectonophysics*, 254(1-2), 89–109.
- Jadoon, I. A. K. (1991), Thin-skinned tectonics on continent/ocean transitional crust, Sulaiman Range, Pakistan, Ph.D. thesis, Oregon State University.
- Jaeger, J. (1959), The frictional properties of joints in rock, *Geofisica pura e applicata*, 43(1), 148–158.
- Jiang, J., Y. Bock, and E. Klein (2021), Coevolving early afterslip and aftershock signatures of a San Andreas fault rupture, *Science Advances*, 7(15), eabc1606.
- Jin, Z., and Y. Fialko (2020), Finite slip models of the 2019 Ridgecrest earthquake sequence constrained by space geodetic data and aftershock locations, *Bulletin of the Seismological Society of America*, 110(4), 1660–1679.
- Jolivet, L., P. Davy, and P. Cobbold (1990), Right-lateral shear along the northwest Pacific margin and the India-Eurasia collision, *Tectonics*, 9(6), 1409–1419.
- Jolivet, R. (2011), Déformation intersismique le long de la faille de Haiyuan, Chine - Variations spatio-temporelles contraintes par interférométrie SAR, Ph.D. thesis, Université de Grenoble.
- Jolivet, R., and W. Frank (2020), The transient and intermittent nature of slow slip, *AGU Advances*, 1(1), e2019AV000126.
- Jolivet, R., and M. Simons (2018), A multipixel time series analysis method accounting for ground motion, atmospheric noise, and orbital errors, *Geophysical Research Letters*, 45(4), 1814–1824.
- Jolivet, R., R. Cattin, N. Chamot-Rooke, C. Lasserre, and G. Peltzer (2008), Thin-plate modeling of interseismic deformation and asymmetry across the Altyn Tagh fault zone, *Geophysical Research Letters*, 35(2).
- Jolivet, R., R. Grandin, C. Lasserre, M.-P. Doin, and G. Peltzer (2011), Systematic InSAR tropospheric phase delay corrections from global meteorological reanalysis data, *Geophysical Research Letters*, 38(17).
- Jolivet, R., C. Lasserre, M.-P. Doin, S. Guillaso, G. Peltzer, R. Dailu, J. Sun, Z.-K. Shen, and X. Xu (2012), Shallow creep on the Haiyuan fault (Gansu, China) revealed by SAR interferometry, *Journal of Geophysical Research: Solid Earth*, 117(B6).
- Jolivet, R., C. Lasserre, M.-P. Doin, G. Peltzer, J.-P. Avouac, J. Sun, and R. Dailu (2013), Spatio-temporal evolution of aseismic slip along the Haiyuan fault, China: Implications for fault frictional properties, *Earth and Planetary Science Letters*, 377, 23–33.
- Jolivet, R., P. S. Agram, N. Y. Lin, M. Simons, M.-P. Doin, G. Peltzer, and Z. Li (2014a), Improving InSAR geodesy using global atmospheric models, *Journal of Geophysical Research: Solid Earth*, 119(3), 2324–2341.
- Jolivet, R., Z. Duputel, B. Riel, M. Simons, L. Rivera, S. Minson, H. Zhang, M. Aivazis, F. Ayoub, S. Leprince, et al. (2014b), The 2013 Mw 7.7 Balochistan earthquake: seismic potential of an accretionary wedge, *Bulletin of the Seismological Society of America*, 104(2), 1020–1030.
- Jolivet, R., M. Simons, P. Agram, Z. Duputel, and Z.-K. Shen (2015a), Aseismic slip and seismogenic coupling along the central San Andreas Fault, *Geophysical Research Letters*, 42(2), 297–306.
- Jolivet, R., T. Candela, C. Lasserre, F. Renard, Y. Klinger, and M.-P. Doin (2015b), The Burst-Like Behavior of Aseismic Slip on a Rough Fault: The Creeping Section of the Haiyuan Fault, China Short Note, *Bulletin of the Seismological Society of America*, 105(1), 480–488.
- Jones, A., et al. (1961), Reconnaissance geology of part of West Pakistan, *Tech. rep.*, A Colombo Plan Cooperative Project: Hunting Survey Corporation.

- Jonsson, S., P. Segall, R. Pedersen, and G. Björnsson (2003), Post-earthquake ground movements correlated to pore-pressure transients, *Nature*, 424(6945), 179–183.
- Kakar, N., D. M. Kakar, A. S. Khan, and S. D. Khan (2016), Land subsidence caused by groundwater exploitation in Quetta Valley, Pakistan, *International Journal of Economic and Environmental Geology*, 7(2), 10–19.
- Kalman, R. E. (1960), A new approach to linear filtering and prediction problems, *Journal of basic Engineering*, 82(1), 35–45.
- Kaneko, Y., and Y. Fialko (2011), Shallow slip deficit due to large strike-slip earthquakes in dynamic rupture simulations with elasto-plastic off-fault response, *Geophysical Journal International*, 186(3), 1389–1403.
- Kaneko, Y., J.-P. Avouac, and N. Lapusta (2010), Towards inferring earthquake patterns from geodetic observations of interseismic coupling, *Nature Geoscience*, 3(5), 363–369.
- Kaneko, Y., Y. Fialko, D. Sandwell, X. Tong, and M. Furuya (2013), Interseismic deformation and creep along the central section of the North Anatolian fault (Turkey): InSAR observations and implications for rate-and-state friction properties, *Journal of Geophysical Research: Solid Earth*, 118(1), 316–331.
- Kato, A., K. Obara, T. Igarashi, H. Tsuruoka, S. Nakagawa, and N. Hirata (2012), Propagation of slow slip leading up to the 2011 Mw 9.0 Tohoku-Oki earthquake, *Science*, 335(6069), 705–708.
- Kazmi, A. H. (1979), Active fault systems in Pakistan, *Geodynamics of Pakistan*, pp. 285–294.
- Kazmi, A. H., and R. A. Rana (1982), *Tectonic map of Pakistan 1: 2 000 000: Map showing structural features and tectonic stages in Pakistan*, Geological survey of Pakistan.
- Khan, M. A., R. Bendick, M. I. Bhat, R. Bilham, D. M. Kakar, S. F. Khan, S. H. Lodi, M. S. Qazi, B. Singh, W. Szeliga, et al. (2008), Preliminary geodetic constraints on plate boundary deformation on the western edge of the Indian plate from TriGGnet (Tri-University GPS Geodesy Network), *J. Himal. Earth Sci*, 41, 71–87.
- Khan, S. R., M. Q. Jan, T. Khan, and M. A. Khan (2007), Petrology of the dykes from the Waziristan Ophiolite, NW Pakistan, *Journal of Asian Earth Sciences*, 29(2-3), 369–377.
- Khoshmanesh, M., and M. Shirzaei (2018a), Episodic creep events on the San Andreas Fault caused by pore pressure variations, *Nature geoscience*, 11(8), 610.
- Khoshmanesh, M., and M. Shirzaei (2018b), Multiscale dynamics of aseismic slip on central San Andreas Fault, *Geophysical Research Letters*, 45(5), 2274–2282.
- Klinger, Y. (2010), Relation between continental strike-slip earthquake segmentation and thickness of the crust, *Journal of Geophysical Research: Solid Earth*, 115(B7).
- Klinger, Y., K. Okubo, A. Vallage, J. Champenois, A. Delorme, E. Rougier, Z. Lei, E. E. Knight, A. Munjiza, C. Satriano, et al. (2018), Earthquake damage patterns resolve complex rupture processes, *Geophysical Research Letters*, 45(19), 10–279.
- Kreemer, C., W. C. Hammond, G. Blewitt, A. A. Holland, and R. A. Bennett (2012), A geodetic strain rate model for the Pacific-North American plate boundary, western United States, in *EGU General Assembly Conference Abstracts*, p. 6785.
- Kreemer, C., G. Blewitt, and E. C. Klein (2014), A geodetic plate motion and Global Strain Rate Model, *Geochemistry, Geophysics, Geosystems*, 15(10), 3849–3889.
- Langer, L., T. Ragon, A. Sladen, and J. Tromp (2020), Impact of topography on earthquake static slip estimates, *Tectonophysics*, 791, 228,566.
- Larson, K. M. (2009), GPS seismology, *Journal of Geodesy*, 83(3), 227–233.
- Lasserre, C., G. Peltzer, F. Crampé, Y. Klinger, J. Van der Woerd, and P. Tapponnier (2005), Coseismic deformation of the 2001 Mw=7.8 Kokoxili earthquake in Tibet, measured by synthetic aperture radar interferometry, *Journal of Geophysical Research: Solid Earth*, 110(B12).
- Lauer, B., R. Grandin, and Y. Klinger (2020), Fault geometry and slip distribution of the 2013 Mw 7.7 Balochistan earthquake from inversions of SAR and optical data, *Journal of Geophysical Research: Solid Earth*, 125(7), e2019JB018,380.

- Lawrence, R. D., and R. S. Yeats (1979), Geological reconnaissance of the Chaman Fault in Pakistan, *Geodynamics of Pakistan*, pp. 351–357.
- Lawrence, R. D., R. S. Yeats, S. H. Khan, A. M. Subhani, and D. Bonelli (1981), Crystalline rocks of the Spinatizha area, Pakistan, *Journal of Structural Geology*, 3(4), 449 – 457, DOI: [https://doi.org/10.1016/0191-8141\(81\)90044-4](https://doi.org/10.1016/0191-8141(81)90044-4), tectonics.
- Lawrence, R. D., S. H. Khan, and T. Nakata (1992), Chaman Fault, Pakistan-Afghanistan, *Ann. Tectonicae*, 6, 196–223.
- Lay, T. (2018), A review of the rupture characteristics of the 2011 Tohoku-oki Mw 9.1 earthquake, *Tectonophysics*, 733, 4–36.
- Lazec̃k, M., K. Spaans, P. J. González, Y. Maghsoudi, Y. Morishita, F. Albino, J. Elliott, N. Greenall, E. Hatton, A. Hooper, et al. (2020), LiCSAR: An automatic InSAR tool for measuring and monitoring tectonic and volcanic activity, *Remote Sensing*, 12(15), 2430.
- Le Pichon, X. (1968), Sea-floor spreading and continental drift, *Journal of Geophysical Research*, 73(12), 3661–3697.
- Li, F. K., and R. M. Goldstein (1990), Studies of multibaseline spaceborne interferometric synthetic aperture radars, *IEEE Transactions on Geoscience and Remote Sensing*, 28(1), 88–97.
- Li, Y., and R. Bürgmann (2021), Partial coupling and earthquake potential along the Xianshuihe Fault, China, *Journal of Geophysical Research: Solid Earth*, 126(7), e2020JB021,406.
- Li, Z., J.-P. Muller, P. Cross, and E. J. Fielding (2005), Interferometric synthetic aperture radar (InSAR) atmospheric correction: GPS, Moderate Resolution Imaging Spectroradiometer (MODIS), and InSAR integration, *Journal of Geophysical Research: Solid Earth*, 110(B3).
- Liang, C., P. Agram, M. Simons, and E. J. Fielding (2019), Ionospheric correction of InSAR time series analysis of C-band Sentinel-1 TOPS Data, *IEEE Transactions on Geoscience and Remote Sensing*, 57(9), 6755–6773.
- Lillie, R. J., G. D. Johnson, M. Yousuf, A. S. H. Zamin, and R. S. Yeats (1987), *Sedimentary basins and basin-forming mechanisms*, chap. Structural development within the Himalayan foreland fold-and-thrust belt of Pakistan, Canadian Society of Petroleum Geologist.
- Lin, Y.-n. N., M. Simons, E. A. Hetland, P. Muse, and C. DiCaprio (2010), A multiscale approach to estimating topographically correlated propagation delays in radar interferograms, *Geochemistry, Geophysics, Geosystems*, 11(9).
- Linde, A. T., M. T. Gladwin, M. J. Johnston, R. L. Gwyther, and R. G. Bilham (1996), A slow earthquake sequence on the San Andreas fault, *Nature*, 383(6595), 65–68.
- Lindsey, E. O., Y. Fialko, Y. Bock, D. T. Sandwell, and R. Bilham (2014), Localized and distributed creep along the southern San Andreas Fault, *Journal of Geophysical Research: Solid Earth*, 119(10), 7909–7922.
- Lindsey, E. O., R. Natsuaki, X. Xu, M. Shimada, M. Hashimoto, D. Melgar, and D. T. Sandwell (2015), Line-of-sight displacement from ALOS-2 interferometry: Mw 7.8 Gorkha Earthquake and Mw 7.3 aftershock, *Geophysical Research Letters*, 42(16), 6655–6661.
- Liu, F., J. Elliott, T. Craig, A. Hooper, and T. Wright (2021), Improving the Resolving Power of InSAR for Earthquakes Using Time Series: A Case Study in Iran, *Geophysical Research Letters*, (48), e2021GL093,043.
- Liu, P., S. Custódio, and R. J. Archuleta (2006), Kinematic inversion of the 2004 M 6.0 Parkfield earthquake including an approximation to site effects, *Bulletin of the Seismological Society of America*, 96(4B), S143–S158.
- Lohman, R. B., and M. Simons (2005), Some thoughts on the use of InSAR data to constrain models of surface deformation: Noise structure and data downsampling, *Geochemistry, Geophysics, Geosystems*, 6(1).
- López-Quiroz, P., M.-P. Doin, F. Tupin, P. Briole, and J.-M. Nicolas (2009), Time series analysis of Mexico City subsidence constrained by radar interferometry, *Journal of Applied Geophysics*, 69(1), 1–15.
- Loveless, J. P., and B. J. Meade (2011), Partitioning of localized and diffuse deformation in the Tibetan Plateau from joint inversions of geologic and geodetic observations, *Earth and Planetary Science Letters*, 303(1-2), 11–24.

- Lundgren, P., S. Usai, E. Sansosti, R. Lanari, M. Tesauero, G. Fornaro, and P. Berardino (2001), Modeling surface deformation observed with synthetic aperture radar interferometry at Campi Flegrei caldera, *Journal of Geophysical Research: Solid Earth*, 106(B9), 19,355–19,366.
- Maldonado, F., J. M. Mengal, S. H. Khan, and J.-C. Thomas (2011), *Digital Geologic Map and Landsat Image Map of Parts of Loralai, Sibi, Quetta, and Khuzar Divisions, Balochistan Province, West-Central Pakistan*, US Department of the Interior, US Geological Survey.
- Manighetti, I., G. King, Y. Gaudemer, C. Scholz, and C. Doubre (2001), Slip accumulation and lateral propagation of active normal faults in Afar, *Journal of Geophysical Research: Solid Earth*, 106(B7), 13,667–13,696.
- Manighetti, I., M. Campillo, S. Bouley, and F. Cotton (2007), Earthquake scaling, fault segmentation, and structural maturity, *Earth and Planetary Science Letters*, 253(3), 429–438, DOI: <https://doi.org/10.1016/j.epsl.2006.11.004>.
- Manighetti, I., D. Zigone, M. Campillo, and F. Cotton (2009), Self-similarity of the largest-scale segmentation of the faults: Implications for earthquake behavior, *Earth and Planetary Science Letters*, 288(3-4), 370–381.
- Manighetti, I., C. Caulet, L. De Barros, C. Perrin, F. Cappa, and Y. Gaudemer (2015), Generic along-strike segmentation of Afar normal faults: Implications on fault growth and stress heterogeneity on seismogenic fault planes, *Geochemistry, Geophysics, Geosystems*, 16(2), 443–467.
- Mao, X., C. Shen, and Y.-B. Yang (2016), Image restoration using very deep convolutional encoder-decoder networks with symmetric skip connections, *Advances in neural information processing systems*, 29, 2802–2810.
- Marco, S. (2008), Recognition of earthquake-related damage in archaeological sites: Examples from the Dead Sea fault zone, *Tectonophysics*, 453(1-4), 148–156.
- Marone, C. (1997), On the rate of frictional healing and the constitutive law for time- and slip-dependent friction, *International Journal of Rock Mechanics and Mining Sciences*, 34(3-4), 187–e1.
- Marone, C. (1998), Laboratory-derived friction laws and their application to seismic faulting, *Annual Review of Earth and Planetary Sciences*, 26(1), 643–696.
- Marone, C., and C. Scholz (1988), The depth of seismic faulting and the upper transition from stable to unstable slip regimes, *Geophysical Research Letters*, 15(6), 621–624.
- Marone, C. J., C. Scholtz, and R. Bilham (1991), On the mechanics of earthquake afterslip, *Journal of Geophysical Research: Solid Earth*, 96(B5), 8441–8452.
- Marty, S., H. Bhat, J. Aubry, E. Fukuyama, R. Madariaga, and A. Schubnel (2021), Dominantly Aseismic Nucleation of Laboratory Earthquakes: A Quantitative Investigation, *arXiv preprint arXiv:2105.04298*.
- Masson, C., S. Mazzotti, and P. Vernant (2019), Precision of continuous GPS velocities from statistical analysis of synthetic time series, *Solid Earth*, 10(1), 329–342.
- Massonnet, D., and K. L. Feigl (1998), Radar interferometry and its application to changes in the Earth's surface, *Reviews of geophysics*, 36(4), 441–500.
- Massonnet, D., and J.-C. Souyris (2008), *Imaging with synthetic aperture radar*, EPFL press.
- Massonnet, D., M. Rossi, C. Carmona, F. Adragna, G. Peltzer, K. Feigl, and T. Rabaute (1993), The displacement field of the Landers earthquake mapped by radar interferometry, *Nature*, 364(6433), 138.
- Maubant, L., E. Pathier, S. Daout, M. Radiguet, M.-P. Doin, E. Kazachkina, V. Kostoglodov, N. Cotte, and A. Walpersdorf (2020), Independent component analysis and parametric approach for source separation in InSAR time series at regional scale: application to the 2017–2018 Slow Slip Event in Guerrero (Mexico), *Journal of Geophysical Research: Solid Earth*, 125(3), e2019JB018187.
- Maurer, J., and K. Johnson (2014), Fault coupling and potential for earthquakes on the creeping section of the central San Andreas Fault, *Journal of Geophysical Research: Solid Earth*, 119(5), 4414–4428.
- McCauley, J. F., G. G. Schaber, C. S. Breed, M. J. Grolier, C. V. Haynes, B. Issawi, C. Elachi, and R. Blom (1982), Subsurface valleys and geoarcheology of the eastern Sahara revealed by shuttle radar, *Science*, 218(4576), 1004–1020.

- McFarland, F. S., S. J. Caskey, and J. J. Lienkaemper (2017), Data from Theodolite Measurements of Creep Rates on San Francisco Bay Region Faults, California, *Data set*, U.S. Geological Survey, DOI: 10.5066/F76W9896.
- McGill, S. F., C. R. Allen, K. W. Hudnut, D. C. Johnson, W. F. Miller, and K. E. Sieh (1989), Slip on the Superstition Hills fault and on nearby faults associated with the 24 November 1987 Elmore Ranch and Superstition Hills earthquakes, southern California, *Bulletin of the Seismological Society of America*, 79(2), 362–375.
- McGinnis, L. (1971), Gravity fields and tectonics in the Hindu Kush, *Journal of Geophysical Research*, 76(8), 1894–1904.
- McKenzie, D. P., and W. Morgan (1969), Evolution of triple junctions, *Nature*, 224(5215), 125–133.
- McLaskey, G. C. (2019), Earthquake initiation from laboratory observations and implications for foreshocks, *Journal of Geophysical Research: Solid Earth*, 124(12), 12,882–12,904.
- Meade, B. J., and B. H. Hager (2005), Block models of crustal motion in southern California constrained by GPS measurements, *Journal of Geophysical Research: Solid Earth*, 110(B3).
- Mele Veedu, D., and S. Barbot (2016), The Parkfield tremors reveal slow and fast ruptures on the same asperity, *Nature*, 532(7599), 361–365.
- Metropolis, N., and S. Ulam (1949), The monte carlo method, *Journal of the American statistical association*, 44(247), 335–341.
- Metropolis, N., A. W. Rosenbluth, M. N. Rosenbluth, A. H. Teller, and E. Teller (1953), Equation of state calculations by fast computing machines, *The journal of chemical physics*, 21(6), 1087–1092.
- Meyer, F., R. Bamler, N. Jakowski, and T. Fritz (2006), The potential of low-frequency SAR systems for mapping ionospheric TEC distributions, *IEEE Geoscience and Remote Sensing Letters*, 3(4), 560–564.
- Michaelides, R. J., H. A. Zebker, and Y. Zheng (2019), An algorithm for estimating and correcting decorrelation phase from insar data using closure phase triplets, *IEEE Transactions on Geoscience and Remote Sensing*, 57(12), 10,390–10,397.
- Michel, R., and J.-P. Avouac (2002), Deformation due to the 17 August 1999 Izmit, Turkey, earthquake measured from SPOT images, *Journal of Geophysical Research: Solid Earth*, 107(B4), ETG–2.
- Michel, R., J.-P. Avouac, and J. Taboury (1999), Measuring ground displacements from SAR amplitude images: Application to the Landers earthquake, *Geophysical Research Letters*, 26(7), 875–878.
- Michel, S., J.-P. Avouac, N. Lapusta, and J. Jiang (2017), Pulse-like partial ruptures and high-frequency radiation at creeping-locked transition during megathrust earthquakes, *Geophysical Research Letters*, 44(16), 8345–8351.
- Michel, S., J.-P. Avouac, R. Jolivet, and L. Wang (2018), Seismic and aseismic moment budget and implication for the seismic potential of the Parkfield segment of the San Andreas fault, *Bulletin of the Seismological Society of America*, 108(1), 19–38.
- Michel, S., A. Gualandi, and J.-P. Avouac (2019), Similar scaling laws for earthquakes and Cascadia slow-slip events, *Nature*, 574(7779), 522–526.
- Mignan, A. (2015), Modeling aftershocks as a stretched exponential relaxation, *Geophysical Research Letters*, 42(22), 9726–9732.
- Minshull, T., R. White, P. Barton, and J. Collier (1992), Deformation at plate boundaries around the Gulf of Oman, *Marine Geology*, 104(1-4), 265–277.
- Minson, S., M. Simons, and J. Beck (2013), Bayesian inversion for finite fault earthquake source models I—Theory and algorithm, *Geophysical Journal International*, 194(3), 1701–1726.
- Mogi, K. (1958), 6. Relations between the eruptions of various volcanoes and the deformations of the ground surfaces around them, *Bulletin of the Earthquake Research Institute*, 36, 99–134.
- Mogi, K. (1966), 12. Pressure dependence of rock strength and transition from brittle fracture to ductile flow, *Bulletin of the Earthquake Research Institute*, 44, 215–232.

- Mohadjer, S., R. Bendick, A. Ischuk, S. Kuzikov, A. Kostuk, U. Saydullaev, S. Lodi, D. Kakar, A. Wasy, M. Khan, et al. (2010), Partitioning of India-Eurasia convergence in the Pamir-Hindu Kush from GPS measurements, *Geophysical Research Letters*, 37(4).
- Mohadjer, S., T. A. Ehlers, R. Bendick, K. Stübner, and T. Strube (2016), A Quaternary fault database for central Asia, *Natural Hazards and Earth System Sciences*, 16(2), 529–542.
- Molnar, P. (1979), Earthquake recurrence intervals and plate tectonics, *Bulletin of the Seismological Society of America*, 69(1), 115–133.
- Molnar, P., and P. Tapponnier (1975), Cenozoic tectonics of Asia: effects of a continental collision, *science*, 189(4201), 419–426.
- Monterroso, F., M. Bonano, C. D. Luca, R. Lanari, M. Manunta, M. Manzo, G. Onorato, I. Zinno, and F. Casu (2020), A global archive of coseismic DInSAR products obtained through unsupervised Sentinel-1 data processing, *Remote Sensing*, 12(19), 3189.
- Moore, D. E., and M. J. Rymer (2007), Talc-bearing serpentinite and the creeping section of the San Andreas fault, *Nature*, 448(7155), 795–797.
- Morishita, Y., M. Lazecky, T. J. Wright, J. R. Weiss, J. R. Elliott, and A. Hooper (2020), LiCSBAS: an open-source InSAR time series analysis package integrated with the LiCSAR automated Sentinel-1 InSAR processor, *Remote Sensing*, 12(3), 424.
- Murray, J., and P. Segall (2005), Spatiotemporal evolution of a transient slip event on the San Andreas fault near Parkfield, California, *Journal of Geophysical Research: Solid Earth*, 110(B9).
- Nadeau, R. M., and T. V. McEvilly (2004), Periodic pulsing of characteristic microearthquakes on the San Andreas fault, *Science*, 303(5655), 220–222.
- Nissen, E., J. Elliott, R. Sloan, T. Craig, G. Funning, A. Hutko, B. Parsons, and T. Wright (2016), Limitations of rupture forecasting exposed by instantaneously triggered earthquake doublet, *Nature Geoscience*, 9(4), 330–336.
- Noda, H., and N. Lapusta (2013), Stable creeping fault segments can become destructive as a result of dynamic weakening, *Nature*, 493(7433), 518–521.
- Okada, Y. (1992), Internal deformation due to shear and tensile faults in a half-space, *Bulletin of the seismological society of America*, 82(2), 1018–1040.
- Okubo, K., H. S. Bhat, E. Rougier, S. Marty, A. Schubnel, Z. Lei, E. E. Knight, and Y. Klinger (2019), Dynamics, radiation, and overall energy budget of earthquake rupture with coseismic off-fault damage, *Journal of Geophysical Research: Solid Earth*, 124(11), 11,771–11,801.
- Ōmori, F. (1894), *On the after-shocks of earthquakes*, vol. 7, The University.
- Pacheco, J. F., L. R. Sykes, and C. H. Scholz (1993), Nature of seismic coupling along simple plate boundaries of the subduction type, *Journal of Geophysical Research: Solid Earth*, 98(B8), 14,133–14,159.
- Palano, M., M. Aloisi, M. Amore, A. Bonforte, F. Calvagna, M. Cantarero, O. Consoli, S. Consoli, F. Guglielmino, M. Mattia, et al. (2006), Kinematics and strain analyses of the eastern segment of the Pernicana Fault (Mt. Etna, Italy) derived from geodetic techniques (1997–2005), *Annals of Geophysics*, 49(4/5), 1105–1117.
- Parsons, T. (2002), Global Omori law decay of triggered earthquakes: Large aftershocks outside the classical aftershock zone, *Journal of Geophysical Research: Solid Earth*, 107(B9), ESE–9.
- Paterson, M. (1958), Experimental deformation and faulting in Wombeyan marble, *Geological Society of America Bulletin*, 69(4), 465–476.
- Peltzer, G., and P. Tapponnier (1988), Formation and evolution of strike-slip faults, rifts, and basins during the India-Asia collision: An experimental approach, *Journal of Geophysical Research: Solid Earth*, 93(B12), 15,085–15,117.

- Peltzer, G., K. W. Hudnut, and K. L. Feigl (1994), Analysis of coseismic surface displacement gradients using radar interferometry: New insights into the Landers earthquake, *Journal of Geophysical Research: Solid Earth*, 99(B11), 21,971–21,981.
- Peltzer, G., P. Rosen, F. Rogez, and K. Hudnut (1998), Poroelastic rebound along the Landers 1992 earthquake surface rupture, *Journal of Geophysical Research: Solid Earth*, 103(B12), 30,131–30,145.
- Perfettini, H., and J.-P. Avouac (2004), Postseismic relaxation driven by brittle creep: A possible mechanism to reconcile geodetic measurements and the decay rate of aftershocks, application to the Chi-Chi earthquake, Taiwan, *Journal of Geophysical Research: Solid Earth*, 109(B2).
- Petersen, M. D., T. E. Dawson, R. Chen, T. Cao, C. J. Wills, D. P. Schwartz, and A. D. Frankel (2011), Fault displacement hazard for strike-slip faults, *Bulletin of the Seismological Society of America*, 101(2), 805–825.
- Peterson, K., and W. D. Barnhart (2017), InSAR analysis of post-seismic deformation following the 2013 Mw 7.7 Balochistan, Pakistan earthquake, in *AGU Fall Meeting Abstracts*, vol. 2017, pp. G43A–0911.
- Pinel-Puysségur, B., R. Grandin, L. Bollinger, and C. Baudry (2014), Multifaulting in a tectonic syntaxis revealed by InSAR: the case of the Ziarat earthquake sequence (Pakistan), *Journal of Geophysical Research: Solid Earth*, 119(7), 5838–5854.
- Pollard, D. D., and P. Segall (1987), Theoretical displacements and stresses near fractures in rock: with applications to faults, joints, veins, dikes, and solution surfaces, in *Fracture mechanics of rock*, pp. 277–347.
- Pollitz, F. F. (1997), Gravitational viscoelastic postseismic relaxation on a layered spherical Earth, *Journal of Geophysical Research: Solid Earth*, 102(B8), 17,921–17,941.
- Pollitz, F. F. (2003), Transient rheology of the uppermost mantle beneath the Mojave Desert, California, *Earth and Planetary Science Letters*, 215(1-2), 89–104.
- Pousse-Beltran, L., A. Socquet, L. Benedetti, M.-P. Doin, M. Rizza, and N. d'Agostino (2020), Localized afterslip at geometrical complexities revealed by InSAR After the 2016 Central Italy seismic sequence, *Journal of Geophysical Research: Solid Earth*, 125(11), e2019JB019,065.
- Powell, C. M. (1979), A speculative tectonic history of Pakistan and surroundings: Some constraints from the Indian Ocean, *Geodynamics of Pakistan*, pp. 7–22.
- Pritchard, M., and M. Simons (2004), An InSAR-based survey of volcanic deformation in the central Andes, *Geochemistry, Geophysics, Geosystems*, 5(2).
- Pritt, M. D. (1996), Phase unwrapping by means of multigrid techniques for interferometric SAR, *IEEE Transactions on Geoscience and Remote Sensing*, 34(3), 728–738.
- Pubellier, M., N. Chamot-Rooke, F. Ego, J.-C. Guezou, E. Konstantinskaya, A. Rabaute, J. Ali, J. C. Aitchison, C. Aubourg, J. Charvet, et al. (2008), Structural map of Eastern Eurasia, Scale 1/12 500 000.
- Puysségur, B., R. Michel, and J.-P. Avouac (2007), Tropospheric phase delay in interferometric synthetic aperture radar estimated from meteorological model and multispectral imagery, *Journal of Geophysical Research: Solid Earth*, 112(B5).
- Qayyum, M., A. R. Niem, and R. D. Lawrence (1996), Newly discovered Paleogene deltaic sequence in Katawaz basin, Pakistan, and its tectonic implications, *Geology*, 24(9), 835–838.
- Quittmeyer, R. C., A. Farah, and K. H. Jacob (1979), The seismicity of Pakistan and its relation to surface faults, *Geodynamics of Pakistan*, pp. 271–284.
- Radiguet, M., F. Cotton, M. Vergnolle, M. Campillo, B. Valette, V. Kostoglodov, and N. Cotte (2011), Spatial and temporal evolution of a long term slow slip event: the 2006 Guerrero Slow Slip Event, *Geophysical Journal International*, 184(2), 816–828.
- Ragon, T., A. Sladen, and M. Simons (2018), Accounting for uncertain fault geometry in earthquake source inversions—I: theory and simplified application, *Geophysical Journal International*, 214(2), 1174–1190.
- Reid, H. F. (1910), The California earthquake of April 18, 1906.

- Reid, H. F. (1911), The elastic-rebound theory of earthquakes, *Bull. Dep. Geol.*, 6(19), 413–444.
- Reynolds, K., A. Copley, and E. Hussain (2015), Evolution and dynamics of a fold-thrust belt: the Sulaiman Range of Pakistan, *Geophysical Journal International*, 201(2), 683–710.
- Rodriguez, M., N. Chamot-Rooke, P. Huchon, M. Fournier, S. Lallemand, M. Delescluse, S. Zaragosi, and N. Mouchot (2014), Tectonics of the Dalrymple trough and uplift of the Murray ridge (NW Indian Ocean), *Tectonophysics*, 636, 1–17.
- Roeloffs, E. A. (2001), Creep rate changes at Parkfield, California 1966–1999: Seasonal, precipitation induced, and tectonic, *Journal of Geophysical Research: Solid Earth*, 106(B8), 16,525–16,547.
- Roland, E., and J. J. McGuire (2009), Earthquake swarms on transform faults, *Geophysical Journal International*, 178(3), 1677–1690.
- Rollins, C., and J.-P. Avouac (2019), A geodesy-and seismicity-based local earthquake likelihood model for central Los Angeles, *Geophysical Research Letters*, 46(6), 3153–3162.
- Romanet, P., H. S. Bhat, R. Jolivet, and R. Madariaga (2018), Fast and slow slip events emerge due to fault geometrical complexity, *Geophysical Research Letters*.
- Rosen, P. A., S. Hensley, G. Peltzer, and M. Simons (2004), Updated repeat orbit interferometry package released, *Eos, Transactions American Geophysical Union*, 85(5), 47–47.
- Ross, Z. E., B. Idini, Z. Jia, O. L. Stephenson, M. Zhong, X. Wang, Z. Zhan, M. Simons, E. J. Fielding, S.-H. Yun, et al. (2019), Hierarchical interlocked orthogonal faulting in the 2019 Ridgecrest earthquake sequence, *Science*, 366(6463), 346–351.
- Rosu, A.-M., M. Pierrot-Deseilligny, A. Delorme, R. Binet, and Y. Klinger (2015), Measurement of ground displacement from optical satellite image correlation using the free open-source software MicMac, *ISPRS Journal of Photogrammetry and Remote Sensing*, 100, 48–59.
- Rouet-Leduc, B., R. Jolivet, M. Dalaison, P. A. Johnson, and C. Hulbert (2021), Autonomous extraction of millimeter-scale deformation in InSAR time series using deep learning, *accepted in Nature Communication*, XX.
- Roukounakis, N., P. Elias, P. Briole, D. Katsanos, I. Kioutsioukis, A. A. Argiriou, and A. Retalis (2021), Tropospheric correction of Sentinel-1 synthetic aperture radar Interferograms using a high-resolution weather model validated by GNSS measurements, *Remote Sensing*, 13(12), 2258.
- Rousset, B., S. Barbot, J.-P. Avouac, and Y.-J. Hsu (2012), Postseismic deformation following the 1999 Chi-Chi earthquake, Taiwan: Implication for lower-crust rheology, *Journal of Geophysical Research: Solid Earth*, 117(B12).
- Rousset, B., R. Jolivet, M. Simons, C. Lasserre, B. Riel, P. Milillo, Z. Çakir, and F. Renard (2016), An aseismic slip transient on the North Anatolian Fault, *Geophysical Research Letters*, 43(7), 3254–3262.
- Rousset, B., R. Bürgmann, and M. Campillo (2019), Slow slip events in the roots of the San Andreas fault, *Science advances*, 5(2), eaav3274.
- Rubin, A. M., and J.-P. Ampuero (2005), Earthquake nucleation on (aging) rate and state faults, *Journal of Geophysical Research: Solid Earth*, 110(B11).
- Ruina, A. (1983), Slip instability and state variable friction laws, *Journal of Geophysical Research: Solid Earth*, 88(B12), 10,359–10,370.
- Ruleman, C., A. Crone, M. Machette, K. Haller, and K. Rukstales (2007), Map and database of probable and possible Quaternary faults in Afghanistan, *Open-File Report 1103*, U.S. Geological Survey.
- Salvatier, J., T. V. Wiecki, and C. Fonnesbeck (2016), Probabilistic programming in Python using PyMC3, *PeerJ Computer Science*, 2, e55.
- Sansosti, E., P. Berardino, M. Manunta, F. Serafino, and G. Fornaro (2006), Geometrical SAR image registration, *IEEE Transactions on Geoscience and Remote Sensing*, 44(10), 2861–2870.
- Sarwar, G., and K. DeJong (1979), Arcs, oroclines, syntaxes: The curvatures of mountain belts in Pakistan, *Geodynamics of Pakistan A*, Farah, K. DeJong, pp. 341–349.

- Savage, J., and R. Burford (1973), Geodetic determination of relative plate motion in central California, *Journal of Geophysical Research*, 78(5), 832–845.
- Savage, J. C., M. Lisowski, and J. L. Svarc (1994), Postseismic deformation following the 1989 (M= 7.1) Loma Prieta, California, earthquake, *Journal of Geophysical Research: Solid Earth*, 99(B7), 13,757–13,765.
- Sborshchikov, I., L. Savostin, and L. Zonenshain (1981), Present plate tectonics between Turkey and Tibet, *Tectonophysics*, 79(1-2), 45–73.
- Scheingross, J. S., B. M. Minchew, B. H. Mackey, M. Simons, M. P. Lamb, and S. Hensley (2013), Fault-zone controls on the spatial distribution of slow-moving landslides, *Bulletin*, 125(3-4), 473–489.
- Schmidt, D. A., and R. Bürgmann (2003), Time-dependent land uplift and subsidence in the Santa Clara valley, California, from a large interferometric synthetic aperture radar data set, *Journal of Geophysical Research: Solid Earth*, 108(B9).
- Scholz, C. (1988), The brittle-plastic transition and the depth of seismic faulting, *Geologische Rundschau*, 77(1), 319–328.
- Scholz, C. H. (1998), Earthquakes and friction laws, *Nature*, 391(6662), 37–42.
- Scholz, C. H. (2002), *The mechanics of earthquakes and faulting*, 2 ed., Cambridge university press.
- Schulz, S. S., G. M. Mavko, R. O. Burford, and W. D. Stuart (1982), Long-term fault creep observations in central California, *Journal of Geophysical Research: Solid Earth*, 87(B8), 6977–6982.
- Schwartz, D. P., and K. J. Coppersmith (1984), Fault behavior and characteristic earthquakes: Examples from the Wasatch and San Andreas fault zones, *Journal of Geophysical Research: Solid Earth*, 89(B7), 5681–5698.
- Schwegmann, C. P., W. Kleynhans, J. Engelbrecht, L. W. Mdakane, and R. G. Meyer (2017), Subsidence feature discrimination using deep convolutional neural networks in synthetic aperture radar imagery, in *2017 IEEE International Geoscience and Remote Sensing Symposium (IGARSS)*, pp. 4626–4629, IEEE.
- Scordilis, E. (2006), Empirical global relations converting MS and Mb to moment magnitude, *Journal of seismology*, 10(2), 225–236.
- Scott, C., R. Lohman, and T. Jordan (2017), InSAR constraints on soil moisture evolution after the March 2015 extreme precipitation event in Chile, *Scientific reports*, 7(1), 1–9.
- Segall, P. (2010), *Earthquake and volcano deformation*, chap. 2 Dislocation models of strike-slip faults, Princeton University Press.
- Segall, P., and M. Matthews (1997), Time dependent inversion of geodetic data, *Journal of Geophysical Research: Solid Earth*, 102(B10), 22,391–22,409.
- Segall, P., A. M. Rubin, A. M. Bradley, and J. R. Rice (2010), Dilatant strengthening as a mechanism for slow slip events, *Journal of Geophysical Research: Solid Earth*, 115(B12).
- Seton, M., R. D. Müller, S. Zahirovic, C. Gaina, T. Torsvik, G. Shephard, A. Talsma, M. Gurnis, M. Turner, S. Maus, et al. (2012), Global continental and ocean basin reconstructions since 200 Ma, *Earth-Science Reviews*, 113(3-4), 212–270.
- Shakeel, A., R. Walters, N. Al Moubayed, and M. Allen (2021), Unsupervised feature learning and automatic detection of transient phenomena in InSAR time-series, in *EGU General Assembly Conference Abstracts*, pp. EGU21–1352.
- Shirzaei, M., and R. Bürgmann (2018), Global climate change and local land subsidence exacerbate inundation risk to the San Francisco Bay Area, *Science advances*, 4(3), eaap9234.
- Shirzaei, M., and T. Walter (2010), Time-dependent volcano source monitoring using InSAR time series: a combined genetic algorithm and Kalman filter approach, *J. Geophys. Res.*, 115, B10,421.
- Sieh, K. E., and R. H. Jahns (1984), Holocene activity of the San Andreas fault at Wallace creek, California, *Geological Society of America Bulletin*, 95(8), 883–896.
- Siehl, A. (2017), Structural setting and evolution of the Afghan orogenic segment—a review, *Geological Society, London, Special Publications*, 427(1), 57–88.

- Simons, M., and P. Rosen (2015), *Interferometric Synthetic Aperture Radar Geodesy*, pp. 339–385, Elsevier, DOI: 10.1016/B978-0-444-53802-4.00061-0.
- Skrine, C. (1936), The Quetta earthquake, *The Geographical Journal*, 88(5), 414–428.
- Sreejith, K., P. Sunil, R. Agrawal, A. P. Saji, D. Ramesh, and A. Rajawat (2016), Coseismic and early postseismic deformation due to the 25 April 2015, Mw 7.8 Gorkha, Nepal, earthquake from InSAR and GPS measurements, *Geophysical Research Letters*, 43(7), 3160–3168.
- Stein, R. S. (1999), The role of stress transfer in earthquake occurrence, *Nature*, 402(6762), 605–609.
- Steinbrugge, K. V., E. G. Zacher, D. Tocher, C. Whitten, and C. Claire (1960), Creep on the San Andreas fault, *Bulletin of the Seismological Society of America*, 50(3), 389–415.
- Stirling, M. W., S. G. Wesnousky, and K. Shimazaki (1996), Fault trace complexity, cumulative slip, and the shape of the magnitude-frequency distribution for strike-slip faults: A global survey, *Geophysical Journal International*, 124(3), 833–868.
- Strelitz, R. (1989), Choosing the ‘best’ double couple from a moment-tensor inversion, *Geophysical Journal International*, 99(3), 811–815.
- Sudhaus, H., and S. Jónsson (2009), Improved source modelling through combined use of InSAR and GPS under consideration of correlated data errors: application to the June 2000 Kleifarvatn earthquake, Iceland, *Geophysical Journal International*, 176(2), 389–404.
- Szeliga, W. (2010), Historical and modern seismotectonics of the Indian plate with an emphasis on its western boundary with the Eurasian plate, Ph.D. thesis, Citeseer.
- Szeliga, W., R. Bilham, D. Schelling, D. M. Kakar, and S. Lodi (2009), Fold and thrust partitioning in a contracting fold belt: Insights from the 1931 Mach earthquake in Baluchistan, *Tectonics*, 28(5).
- Szeliga, W., R. Bilham, D. M. Kakar, and S. H. Lodi (2012), Interseismic strain accumulation along the western boundary of the Indian subcontinent, *Journal of Geophysical Research: Solid Earth*, 117(B08404), DOI: 10.1029/2011JB008822.
- Tape, C., S. Holtkamp, V. Silwal, J. Hawthorne, Y. Kaneko, J. P. Ampuero, C. Ji, N. Ruppert, K. Smith, and M. E. West (2018), Earthquake nucleation and fault slip complexity in the lower crust of central Alaska, *Nature Geoscience*, 11(7), 536.
- Tapponnier, P., M. Mattauer, F. Proust, and C. Cassaigneau (1981), Mesozoic ophiolites, sutures, and Large-scale tectonic movements in Afghanistan, *Earth and Planetary Science Letters*, 52(2), 355–371.
- Tapponnier, P., X. Zhiqin, F. Roger, B. Meyer, N. Arnaud, G. Wittlinger, and Y. Jingsui (2001), Oblique stepwise rise and growth of the Tibet Plateau, *science*, 294(5547), 1671–1677.
- Tarantola, A. (2005), *Inverse problem theory and methods for model parameter estimation*, vol. 89, SIAM.
- Tarantola, A., B. Valette, et al. (1982), Inverse problems= quest for information, *Journal of geophysics*, 50(1), 159–170.
- Tarayre, H., and D. Massonnet (1996), Atmospheric propagation heterogeneities revealed by ERS-1 interferometry, *Geophysical Research Letters*, 23(9), 989–992.
- Thatcher, W. (2007), Microplate model for the present-day deformation of Tibet, *Journal of Geophysical Research: Solid Earth*, 112(B1).
- Thomas, M. Y., J.-P. Avouac, and N. Lapusta (2017), Rate-and-state friction properties of the Longitudinal Valley Fault from kinematic and dynamic modeling of seismic and aseismic slip, *Journal of Geophysical Research: Solid Earth*, 122(4), 3115–3137.
- Tong, X., and D. Schmidt (2016), Active movement of the Cascade landslide complex in Washington from a coherence-based InSAR time series method, *Remote Sensing of Environment*, 186, 405–415.
- Tong, X., D. Sandwell, and B. Smith-Konter (2013), High-resolution interseismic velocity data along the San Andreas Fault from GPS and InSAR, *Journal of Geophysical Research: Solid Earth*, 118(1), 369–389.

- Trugman, D. T., and Z. E. Ross (2019), Pervasive foreshock activity across southern California, *Geophysical Research Letters*.
- Tse, S. T., and J. R. Rice (1986), Crustal earthquake instability in relation to the depth variation of frictional slip properties, *Journal of Geophysical Research: Solid Earth*, 91(B9), 9452–9472.
- Turner, R. C., M. Shirzaei, R. M. Nadeau, and R. Bürgmann (2015), Slow and Go: Pulsing slip rates on the creeping section of the San Andreas Fault, *Journal of Geophysical Research: Solid Earth*, 120(8), 5940–5951.
- Tymofeyeva, E., Y. Fialko, J. Jiang, X. Xu, D. Sandwell, R. Bilham, T. K. Rockwell, C. Blanton, F. Burkett, A. Gontz, et al. (2019), Slow slip event on the southern San Andreas fault triggered by the 2017 Mw 8.2 Chiapas (Mexico) earthquake, *Journal of Geophysical Research: Solid Earth*, 124(9), 9956–9975.
- Udías, A., A. U. Vallina, R. Madariaga, and E. Buforn (2014), *Source mechanisms of earthquakes: theory and practice*, Cambridge University Press.
- Ul-Hadi, S., S. D. Khan, L. A. Owen, and A. S. Khan (2013a), Geomorphic response to an active transpressive regime: A case study along the Chaman strike-slip fault, western Pakistan, *Earth Surface Processes and Landforms*, 38(3), 250–264.
- Ul-Hadi, S., S. D. Khan, L. A. Owen, A. S. Khan, K. A. Hedrick, and M. W. Caffee (2013b), Slip-rates along the Chaman fault: Implication for transient strain accumulation and strain partitioning along the western Indian plate margin, *Tectonophysics*, 608, 389–400.
- Usai, S. (2003), A least squares database approach for SAR interferometric data, *IEEE Transactions on Geoscience and Remote Sensing*, 41(4), 753–760.
- Usman, M., and M. Furuya (2015), Complex faulting in the Quetta Syntaxis: fault source modeling of the October 28, 2008 earthquake sequence in Baluchistan, Pakistan, based on ALOS/PALSAR InSAR data, *Earth, Planets and Space*, 67(1), 1–11.
- Utsu, T. (1961), A statistical study on the occurrence of aftershocks, *Geophys. Mag.*, 30, 521–605.
- Utsu, T., Y. Ogata, et al. (1995), The centenary of the Omori formula for a decay law of aftershock activity, *Journal of Physics of the Earth*, 43(1), 1–33.
- Vajedian, S., and M. Motagh (2018), Coseismic displacement analysis of the 12 November 2017 Mw 7.3 Sarpol-e Zahab (Iran) earthquake from SAR Interferometry, burst overlap interferometry and offset tracking, *ISPRS Annals of the Photogrammetry, Remote Sensing and Spatial Information Sciences* 4 (2018), Nr. 3, 4(3), 205–209.
- Van Rijnsingen, E., F. Funiciello, F. Corbi, and S. Lallemand (2019), Rough subducting seafloor reduces interseismic coupling and mega-earthquake occurrence: Insights from analogue models, *Geophysical Research Letters*, 46(6), 3124–3132.
- Victor, P., O. Oncken, M. Sobiesiak, M. Kemter, G. Gonzalez, and T. Ziegenhagen (2018), Dynamic triggering of shallow slip on forearc faults constrained by monitoring surface displacement with the IPOC Creepmeter Array, *Earth and Planetary Science Letters*, 502, 57–73.
- Vidale, J. E., and P. M. Shearer (2006), A survey of 71 earthquake bursts across southern California: Exploring the role of pore fluid pressure fluctuations and aseismic slip as drivers, *Journal of Geophysical Research: Solid Earth*, 111(B5).
- Wang, H., and T. Wright (2012), Satellite geodetic imaging reveals internal deformation of western Tibet, *Geophysical Research Letters*, 39(7).
- Wang, H., T. J. Wright, J. Liu-Zeng, and L. Peng (2019), Strain rate distribution in south-central Tibet from two decades of InSAR and GPS, *Geophysical Research Letters*, 46(10), 5170–5179.
- Wang, K., and R. Bürgmann (2020), Probing fault frictional properties during afterslip updip and downdip of the 2017 Mw 7.3 Sarpol-e Zahab earthquake with space geodesy, *Journal of Geophysical Research: Solid Earth*, 125(11), e2020JB020,319.
- Wang, K., and Y. Fialko (2018), Observations and modeling of coseismic and postseismic deformation due to the 2015 Mw 7.8 Gorkha (Nepal) earthquake, *Journal of Geophysical Research: Solid Earth*, 123(1), 761–779.

- Wang, K., and Y. A. Fialko (2017), Postseismic deformation following the 2013 Mw 7.7 Balochistan (Pakistan) earthquake observed with Sentinel-1 Interferometry, in *AGU Fall Meeting Abstracts*, vol. 2017, pp. G43A–0910.
- Waseem, M., S. Khan, and M. Asif Khan (2020), Probabilistic seismic hazard assessment of Pakistan territory using an areal source model, *Pure & Applied Geophysics*, 177(8).
- Watson, A. R., J. R. Elliott, and R. J. Walters (2021), Interseismic strain accumulation across the Main Recent Fault, SW Iran, from Sentinel-1 InSAR observations, *Earth and Space Science Open Archive ESSOAr*.
- Wegmuller, U., C. Werner, T. Strozzi, and A. Wiesmann (2006), Ionospheric electron concentration effects on SAR and INSAR, in *2006 IEEE International Symposium on Geoscience and Remote Sensing*, pp. 3731–3734, IEEE.
- Wei, M., D. Sandwell, and B. Smith-Konter (2010), Optimal combination of InSAR and GPS for measuring interseismic crustal deformation, *Advances in Space Research*, 46(2), 236–249.
- Wei, M., Y. Kaneko, Y. Liu, and J. J. McGuire (2013), Episodic fault creep events in California controlled by shallow frictional heterogeneity, *Nature geoscience*, 6(7), 566–570.
- Weiss, J. R., R. J. Walters, Y. Morishita, T. J. Wright, M. Lazecky, H. Wang, E. Hussain, A. J. Hooper, J. R. Elliott, C. Rollins, et al. (2020), High-resolution surface velocities and strain for Anatolia from Sentinel-1 InSAR and GNSS data, *Geophysical Research Letters*, 47(17), e2020GL087376.
- Welch, M. D., and D. A. Schmidt (2017), Separating volcanic deformation and atmospheric signals at Mount St. Helens using Persistent Scatterer InSAR, *Journal of Volcanology and Geothermal Research*, 344, 52–64.
- Wells, D. L., and K. J. Coppersmith (1994), New empirical relationships among magnitude, rupture length, rupture width, rupture area, and surface displacement, *Bulletin of the seismological Society of America*, 84(4), 974–1002.
- Wesnousky, S. G. (1988), Seismological and structural evolution of strike-slip faults, *Nature*, 335(6188), 340–343.
- Wesnousky, S. G. (2006), Predicting the endpoints of earthquake ruptures, *Nature*, 444(7117), 358–360.
- Wessel, P., and W. H. Smith (1998), New, improved version of Generic Mapping Tools released, *Eos, Transactions American Geophysical Union*, 79(47), 579–579.
- West, W. (1935), The Baluchistan earthquake of May 31, 1935, *Current Science*, 4(2), 79–82.
- Wheeler, R. L., C. G. Bufe, M. L. Johnson, R. L. Dart, and G. Norton (2005), Seismotectonic map of Afghanistan, with annotated bibliography, *Open-File Report 1264*, U.S. Geological Survey.
- Wiemer, S., and M. Wyss (2002), Mapping spatial variability of the frequency-magnitude distribution of earthquakes, in *Advances in geophysics*, vol. 45, pp. 259–V, Elsevier.
- Williams, S., Y. Bock, and P. Fang (1998), Integrated satellite interferometry: Tropospheric noise, GPS estimates and implications for interferometric synthetic aperture radar products, *Journal of Geophysical Research: Solid Earth*, 103(B11), 27,051–27,067.
- Wright, T., B. Parsons, and E. Fielding (2001), Measurement of interseismic strain accumulation across the North Anatolian Fault by satellite radar interferometry, *Geophysical Research Letters*, 28(10), 2117–2120.
- Wright, T. J., B. E. Parsons, and Z. Lu (2004), Toward mapping surface deformation in three dimensions using InSAR, *Geophysical Research Letters*, 31(1).
- Wright, T. J., J. R. Elliott, H. Wang, and I. Ryder (2013), Earthquake cycle deformation and the Moho: Implications for the rheology of continental lithosphere, *Tectonophysics*, 609, 504–523.
- Yagüe-Martínez, N., P. Prats-Iraola, F. R. Gonzalez, R. Brcic, R. Shau, D. Geudtner, M. Eineder, and R. Bamler (2016), Interferometric processing of Sentinel-1 TOPS data, *IEEE Transactions on Geoscience and Remote Sensing*, 54(4), 2220–2234.
- Yeats, R. (2012), *Active Faults of the World*, chap. 8 India, the Himalaya, Mainland China, and Central Asia, Cambridge university press, New York.

- Yeats, R. S., R. S. Yeats, K. Sieh, K. E. Sieh, C. R. Allen, C. R. Allen, et al. (1997), *The geology of earthquakes*, Oxford University Press, USA.
- Yu, C., Z. Li, N. T. Penna, and P. Crippa (2018), Generic atmospheric correction model for Interferometric Synthetic Aperture Radar observations, *Journal of Geophysical Research: Solid Earth*, 123(10), 9202–9222.
- Yunjun, Z., H. Fattahi, and F. Amelung (2019), Small baseline InSAR time series analysis: Unwrapping error correction and noise reduction, *Computers & Geosciences*, 133, 104,331.
- Zebker, H. A., and R. M. Goldstein (1986), Topographic mapping from interferometric synthetic aperture radar observations, *Journal of Geophysical Research: Solid Earth*, 91(B5), 4993–4999.
- Zebker, H. A., and J. Villasenor (1992), Decorrelation in interferometric radar echoes, *IEEE Transactions on geoscience and remote sensing*, 30(5), 950–959.
- Zebker, H. A., P. A. Rosen, and S. Hensley (1997), Atmospheric effects in interferometric synthetic aperture radar surface deformation and topographic maps, *Journal of geophysical research: solid earth*, 102(B4), 7547–7563.
- Zhang, K., W. Zuo, Y. Chen, D. Meng, and L. Zhang (2017), Beyond a gaussian denoiser: Residual learning of deep cnn for image denoising, *IEEE transactions on image processing*, 26(7), 3142–3155.
- Zhao, B., R. Bürgmann, D. Wang, K. Tan, R. Du, and R. Zhang (2017), Dominant controls of downdip afterslip and viscous relaxation on the postseismic displacements following the Mw7.9 Gorkha, Nepal, earthquake, *Journal of Geophysical Research: Solid Earth*, 122(10), 8376–8401.
- Zheng, G., H. Wang, T. J. Wright, Y. Lou, R. Zhang, W. Zhang, C. Shi, J. Huang, and N. Wei (2017), Crustal deformation in the India-Eurasia collision zone from 25 years of GPS measurements, *Journal of Geophysical Research: Solid Earth*, 122(11), 9290–9312.
- Zhou, Y., M. Y. Thomas, B. Parsons, and R. T. Walker (2018), Time-dependent postseismic slip following the 1978 Mw 7.3 Tabas-e-Golshan, Iran earthquake revealed by over 20 years of ESA InSAR observations, *Earth and Planetary Science Letters*, 483, 64–75.
- Zhu, L., and L. A. Rivera (2002), A note on the dynamic and static displacements from a point source in multilayered media, *Geophysical Journal International*, 148(3), 619–627.
- Zongjin, M., F. Zhengxiang, Z. Yingzhen, W. Chengmin, and Z. Guomin (1990), *Earthquake prediction*, Springer-Verlag, New York.

RÉSUMÉ

Comment une faille accumule-t-elle l'énergie nécessaire à la rupture sismique ? L'Interférométrie radar à synthèse d'ouverture (InSAR) permet de mesurer avec une précision millimétrique les déplacements du sol le long des failles continentales entre les passages successifs des satellites au même endroit. Dans cette thèse, j'identifie quand et comment la déformation est accommodée à travers la frontière de plaque de Chaman entre l'Inde et l'Eurasie au Pakistan et en Afghanistan, une région touchée par de grands séismes qui reste énigmatique. De nos jours, les satellites acquièrent des images haute-résolution en continu ayant le potentiel de nous informer sur l'évolution de la déformation en temps (presque) réel, un défi pour les techniques classiques de traitement. Dans cette thèse, je présente une nouvelle méthode de calcul de séries temporelles InSAR, nommée KFTS, qui permet de mettre à jour itérativement une série temporelle préexistante par la combinaison appropriée des données, du modèle et de leurs incertitudes respectives, au fur et à mesure que les images satellite sont disponibles. La méthode est testée sur des données synthétiques ainsi que sur des réseaux d'interférogrammes sur l'Etna (Italie) et sur la frontière de plaque de Chaman. KFTS estime des délais de phase et des vitesses de déformation en accord avec les méthodes couramment utilisées et calcule également les incertitudes associées. Ensuite, j'interprète des séries temporelles InSAR le long de la frontière de plaque de Chaman entre 2014 et 2020. Je constate que la majeure partie de la faille de Chaman (FC) glisse de manière aismique et continue avec un taux de chargement compris entre 0,7 et 1,2 cm/an et trois sections qui glissent continuellement et aismiquement de 80 à 130 km de long. Je propose une nouvelle segmentation de la FC et discute de l'interaction entre les séismes, le glissement aismique et la géométrie du tracé de faille. J'étudie trois séismes de magnitude modérée, qui présentent un glissement aismique induit important. A l'aide des vitesses InSAR, je cartographie les gradients de déformation dans la ceinture de faille-plissement à l'est de la FC. Ils sont interprétés comme l'expression en surface du glissement décrochant sénestre sur trois ou quatre failles verticales. Il s'avère que la majeure partie de la déformation actuelle de la limite de plaques se concentre à l'est de la FC, dans le prolongement de la faille d'Ornach Nal au sud et le long de la faille de Quetta-Kalat qui aurait été le siège du séisme de Quetta en 1935, de magnitude 7,7. Notre description du partitionnement est en accord avec la géologie et suggère une migration vers l'est de la frontière de plaque.

MOTS CLÉS

Géodésie spatiale, Tectonique, Séisme, Glissement transitoire, Failles actives, Déformation

ABSTRACT

How does a fault accumulate the energy necessary for seismic rupture? Synthetic Aperture Radar Interferometry (InSAR) can measure with a millimetre-precision ground displacements along continental faults between successive passes of satellites at the same location. In this thesis, I identify when and how strain is accommodated across the Chaman plate boundary between India and Eurasia in Pakistan and Afghanistan, a region struck by large earthquakes that remains enigmatic. Nowadays, satellites acquire continuous high-resolution images with the potential to inform us about the evolution of deformation in (almost) real time, a challenge for classic processing techniques. In this thesis, I present a new method for computing InSAR time series, named KFTS, which allows us to iteratively update a pre-existing time series through the appropriate combination of data, models and their respective uncertainties, as satellite images become available. The method is tested on synthetic data as well as interferometric networks on Etna (Italy) and on the Chaman plate boundary. KFTS estimates phase delays and strain rates in agreement with commonly used methods and also computes associated uncertainties. Subsequently, I interpret InSAR time series along the Chaman plate boundary between 2014 and 2020. I find that most of the Chaman fault (CF) slides aseismically and continuously with a loading rate between 0.7 and 1.2 cm/yr and three 80-130 km-long creeping sections. I propose a new segmentation of the CF and discuss the interplay between earthquakes, aseismic slip and fault trace geometry. I image three moderate magnitude earthquakes, which exhibit significant induced aseismic slip. Using InSAR velocities, I map deformation gradients in the fault and fold belt east of the CF. They are interpreted as the surface expression of left-lateral strike-slip on three to four vertical faults. It turns out that most of the current plate boundary deformation focusses to the east of the CF, along the continuation of the Ornach Nal fault to the south and along the Quetta-Kalat fault which is thought to have hosted the 1935 Quetta earthquake of magnitude 7.7. Our description of partitioning is consistent with the geology and suggests an eastward migration of the plate boundary.

KEYWORDS

Spatial geodesy, Tectonics, Earthquake, Slow slip, Active faults, Deformation